

Optical spin-mechanics quantum interface:
entanglement and back-action evasion

PhD Thesis

Rodrigo A. Thomas

This thesis has been submitted to
the PhD School of The Faculty of Science,
University of Copenhagen

Center for Quantum Optics
Niels Bohr Institute
Faculty of Science
University of Copenhagen
Copenhagen, Denmark
2020

Academic Supervisor	Prof. Eugene S. Polzik
Evaluation committee	
External referees	Prof. Dr. Klaus Mølmer Prof. Dr. Philipp Treutlein
Local referee	Prof. Dr. Per Hedegård
Thesis submitted	August 27th, 2020
Date of defense	October 1st, 2020

Abstract

The experimental control of physical systems to their ultimate quantum limits has advanced tremendously in the last couple of decades. Parallel advancements in the theoretical descriptions allowed for better understanding the performance requirements needed for using quantum-enabled technologies in real world applications. With that, it has also become more and more clear that a single platform might not be able to realize all the protocols needed, for example, in a future quantum information processing network. Hybrid quantum devices attempt to combine fundamentally different systems with high efficiency, harnessing the advantages from its constituent elements.

In this thesis, we report the recent developments on the hybrid interface between a mechanical oscillator prepared in dielectric membrane and a spin oscillator prepared in an atomic ensemble. The mechanical oscillator, a drum-like stressed silicon nitride membrane, is placed inside a high finesse cavity and mounted in a cryostat operating at 4 K. The spin oscillator is prepared in the ground state manifold of an optically pumped cesium vapor, placed in a homogeneous static magnetic field and confined in a glass vapor cell at approximately 330 K. Each subsystem is coupled to light, operating in the quantum back-action limited regime, that is, at the limit in which the measurement disturbs the dynamics of the oscillator significantly. The optical interface is established by coupling the systems in a cascaded fashion. We show that the measurement induced quantum back-action can be destructively interfered when preparing the spin ensemble in an effective negative mass regime. In the experiments, we show up to 4.6 dB reduction of the quantum back-action contribution. Furthermore, we show that the back-action evasion, along with the information acquired via the measurement, allows for preparing the hybrid system in an entangled continuous variables Einstein-Podolsky-Rosen-like state with variance below the inseparability limit, $0.83 \pm 0.03 < 1$.

The established quantum link constitutes a new milestone in the hybrid systems landscape and paves the road towards measurement of motion beyond the standard quantum limits of sensitivity, as well as towards teleportation-based protocols in hybrid quantum networks.

Sammenfatning

Over de sidste par årtier er den eksperimentelle kontrol over mange fysiske systemer nået helt ned til deres kvanteniveau. Parallelle fremskridt indenfor teoretiske beskrivelser af disse systemer har gjort det muligt at opnå en bedre forståelse af de tekniske krav for fuldt at kunne udnytte disse kvante-klare systemer som brugbare teknologier. Dertil er det blevet mere og mere tydeligt, at ét enkelt system muligvis ikke vil kunne realisere samtlige protokoller nødvendige i fremtidens kvanteinformationprocesseringsnetværk. Hybride kvanteenheder sammensætter forskellige kvante-klare systemer på effektiv vis og kan dermed udnytte fordelene af de individuelle systemer, således at helheden er mere end summen af delene.

I denne afhandling rapporterer vi om de seneste fremskridt på den hybride grænseflade mellem en mekanisk resonator i form af en dielektrisk membran og en spin oscillator forberedt i et atomart ensemble. Den mekaniske oscillator, en udspændt tromme-lignende silicium nitrid membran, er placeret i en optisk kavitet med høj finesse og er monteret i en kryostat der opererer ved 4 K. Spin oscillatoren er forberedt i grundtilstandsmanifolden af en optisk pumpet damp af cæsium atomer, der er fanget i en glas celle ved omtrent 330 K og placeret i et homogent statisk magnetfelt. Hvert delsystem er koblet til lys og opererer i det kvantetilbagevirkningsbegrænsede regime, hvilket vil sige i grænsen hvor målingen skaber en signifikant forstyrrelse i oscillatorens dynamik. Den optiske grænseflade er etableret ved at koble de to systemer i en kaskaderet konfiguration. Vi viser at den måleinducerede kvantetilbagevirkning kan interferere destruktivt når det atomare spinensemble er forberedt i en effektiv negativ-masse tilstand. I eksperimenterne viser vi op imod 4.6 dB reduktion af bidraget fra kvantetilbagevirkningen. Ydermere viser vi at undvigelsen af tilbagevirkningen, samt informationen anskaffet gennem målingen, muliggør at forberede det hybride system i en sammenfiltret kontinuerlig-variabel Einstein-Podolsky-Rosen-lignende tilstand med en varians under grænsen for uadskillelighed, $0.83 \pm 0.03 < 1$.

Den etablerede kvanteforbindelse er en ny milepæl indenfor hybride kvanteenheder og baner vejen for målinger af bevægelser under den konventionelle kvantegrænse, samt protokoller baseret på teleportation i hybride kvantenetværk.

List of Publications

Peer-reviewed articles:

Authors marked with * contributed equally to given the work.

Rodrigo A. Thomas*, Michał Parniak*, Christoffer Østfeldt*, Christoffer B. Møller*, Christian Bærentsen, Yeghishe Tsaturyan, Albert Schliesser, Jürgen Appel, Emil Zeuthen, and Eugene S. Polzik. *Entanglement between distant macroscopic mechanical and spin systems*. arXiv preprint, arXiv:2003.11310 (2020). Accepted for publication in *Nature Physics*.

Christoffer B Møller*, Rodrigo A. Thomas*, Georgios Vasilakis, Emil Zeuthen, Yeghishe Tsaturyan, Mikhail Balabas, Kasper Jensen, Albert Schliesser, Klemens Hammerer, and Eugene S Polzik. *Quantum back-action-evading measurement of motion in a negative mass reference frame*. *Nature* 547, 191-195 (2017).

Kasper Jensen, Rima Budvytyte, Rodrigo A. Thomas, Tian Wang, Annette M. Fuchs, Mikhail V. Balabas, Georgios Vasilakis, Lars D. Mosgaard, Hans C. Stærkind, Jörg H. Müller, Thomas Heimburg, Søren-Peter Olesen, and Eugene S. Polzik. *Non-invasive detection of animal nerve impulses with an atomic magnetometer operating near quantum limited sensitivity*. *Scientific Reports* 6, 29638 (2016).

Articles in preparation:

Rodrigo A. Thomas, et al. *Atomic Spin System Calibrations by Coherently Induced Faraday Rotation*.

List of abbreviations

AOM	acousto-optic modulator
CIFAR	Coherently Induced Faraday rotation
EPR	Einstein-Podolsky-Rosen
EOM	electro-optic modulator
FID	free induction decay
FWHM	full width at half maximum
HWP	half waveplate
LIGO	Laser Interferometer Gravitational-Wave Observatory
LO	local oscillator
MORS	Magneto-optical resonance signal
NBI	Niels Bohr Institute
PBS	polarizing beam splitter
PSD	power spectral density
QBA	quantum back-action
QND	quantum non-demolition
QWP	quarter waveplate
SN	shot noise
TN	thermal noise

Preface

Getting to the start of the PhD was a long haul flight. From there to here, the end of it, it was a journey. I have crossed paths with several people who, in one way or another, contributed with much more than can possibly be described in the following words. Hereby I express my gratitude for the support.

I start by thanking Eugene Polzik for the opportunity of taking part in his research activities. His strive for greatness, guidance, advice and criticism, have been precious during these years of supervision. Thank you for giving me the freedom to explore ideas independently and flourish my own version of a researcher.

All the learning during the PhD would not have been possible without Jörg Helge Müller and Jürgen Appel. The effortless and clear way the two communicate their vast knowledge on basically anything we encountered in the lab has been fundamental to my growth. Kasper Jensen introduced me to the cell experiments and guided me through the first years in Denmark. Georgios Vasilakis took over when we started the hybrid experiments, and I have learned much from him. It has been a privilege to work with you all!

Down at the labs, I have encountered amazing people, eager to share not only ideas and knowledge about the experiments, but also about life in general. Christoffer Møller, Yeghishe Tsaturyan, Michael Zugenmaier, and Andreas Barg have been fundamental in making me feel welcome from day zero. With the years, Karsten Dideriksen, Yannick Seis, Boris Albrecht, Emil Zeuthen, Ivan Galinskiy, Christoffer Østfeldt, and Michal Parniak joined the lab efforts and much contributed in keeping the welcoming environment. The work experience at Blegdamsvej is also greatly enhanced by the close contact we have with the quantum optics groups, the Quantum Photonics, the Theoretical Quantum Optics, and the Schliesser lab. It has been a great honor to be part of this environment.

Back at home base, pai, mãe, and mano provided unconditional love and caring, essential to cope with the quarter-world separation. Lola, you are amazing. Thanks for being there always for me!

PhD work and thesis structure

My PhD started in the summer of 2014. During the first year I worked in the optical detection of animal nerve impulses using an atomic magnetometer. The results are published in Jensen et al. (2016) and will not be covered in this manuscript. From 2015 onwards I started working with the development of a hybrid experiment atomic part. The challenges involved in running and calibrating the atomic ensemble in a continuous wave mode, along with its performance in the hybrid configuration, is the work that constitutes my PhD. The optomechanical cavity designs and implementation presented in this thesis are part of Christoffer Møller's and of Christoffer Østfeldt's PhD work, while the fabrication of the mechanical oscillator has been done in Yeghishe Tsaturyan's PhD work. Many of the techniques involved in testing the mechanical devices are described in Andreas Barg's PhD thesis. Although I describe them to some degree throughout the manuscript, the full credit for the achievements goes to them.

In this thesis, I present a summary of the back-action evasion and entanglement experiments in the optical interface between a cesium spin ensemble and a nanomechanical device. I also present a set of spin oscillator calibration techniques and state preparation analysis. The emphasis of the is primarily in the experimental realization, with theoretical framework introduced as needed.

Readers with varied degree of background should read this manuscript differently. Some chapters display a more pedagogical and bottom-up structure. Other chapters are built upon knowledge previously described in the previous thesis in the group, being—in the opinion of the writer—most useful when connected to the discussions presented by Julsgaard (2003), Sherson (2006), Krauter (2011), Jensen (2011), and Møller (2018).

The manuscript is divided in four parts. The structure goes as follows

- Part I. The initial chapters lay the foundations of the hybrid system and describe the implementation of the mechanical and spin oscillators.
- Chapter 1. We give a general introduction to the goals of the experiment and its context in the broader quantum optics community. We also present a general picture negative mass reference frame and how back-action evasion and entanglement come about.
 - Chapter 2. We describe the membrane-in-the-middle optomechanical system. Starting with a short overview of the device’s design—both the mechanics and the optics—we focus on presenting the input-output relations for the light interacting with the mechanical oscillator.
 - Chapter 3. We describe the atomic ensemble and its mapping to a spin oscillator, along with its interaction with light, with emphasis in describing the input-output relations.
- Part II. In a rather different set of gears, we dive in a technical accounting of the experimental configuration, spin oscillator calibration techniques, and performance of the spin ensemble in free space and in an optical cavity are discussed.
- Chapter 4. We give a detailed accounting of the various experimental components used in our hybrid platform: the bits and pieces of the vapour cell and the optomechanical cavity, the hardware used for transforming the optical spin response into the desired light quadratures, and the software used for controlling the apparatus.
 - Chapter 5. The continuous wave operation of the spin ensemble at relatively high temperature introduces particular challenges not previously described in our group. The techniques used for spin state preparation, detection, and characterization are presented. At last, we present the connecting of spin polarization to effective thermal occupation.
 - Chapter 6. A technique for measuring the Faraday angle in experimental conditions is presented, along with its modeling and measurements. We finish by linking the Faraday angle to the quantum cooperativity parameter.
 - Chapter 7. The spin noise observed via light has signatures of the motional averaging of the spins over the beam during the interaction. We study its dependence on laser beam parameters and present an effective model to the total noise.
 - Chapter 8. We present CIFAR (Coherently Induced Faraday Rotation), a technique for calibrating the spin readout rate and compare it to a model based in the input-output relations presented on Chapter 3.
 - Chapter 9. We present the initial results on studying the optodynamical effects of the spin ensemble in an optical cavity. Similar to the optomechanical system, the cavity acts as a feedback that can dampen/excite the positive/negative mass oscillator motion.

- Part III. We return to the hybrid system, discussing the back-action evasion and entanglement experiments.
- Chapter 10. The back-action evasion scheme is presented both theoretically and experimentally, summarizing the advances harvested in the last experimental update.
 - Chapter 11. The EPR entanglement between the spin and mechanical oscillators is discussed. We also present a simplified picture of the Wiener filtering and apply it to the hybrid system.
 - Chapter 12. We finish up concluding the work and presenting some of the possible next steps, along with envisioned updates.
- Part IV. The supplementary information is a set of technical chapters with additional information on various lengthy topics that did not covered in the main text. Many of the results can be found in atomic physics and quantum optics textbooks, and are reproduced here as a matter of convenience.
- Appendix A. This chapter contains a set of relations useful for treating the theoretical derivation of the equations of motion.
 - Appendix B. We consider the effect of optical losses in the double pass spin readout.
 - Appendix C. The method for calculating the an effective ground state Hamiltonian and non-Hamiltonian operators for arbitrary atomic level structures is presented.
 - Appendix D. The white noise drive method for calibrating the spin quantum cooperativity is presented.
 - Appendix E. We relate the absorption profile of moving and stationary atoms, considering the Doppler effect on the atomic motion.
 - Appendix F. The relation of κ^2 , the atoms-light interaction strength parameter used in the early QUANTOP experiments, is linked to the quantum cooperativity and spin readout rate parameters, language utilized in the hybrid experiments.
 - Appendix G. We present the spin ensemble coherence time measurements in an unshielded environment.
 - Appendix H. A reference table for estimating the cesium vapor density according to the vapor cell temperature.
 - Appendix I. A summary of the experimental parameters extracted from the experiments presented in Møller et al. (2017) and in Thomas et al. (2020).

Contents

Abstract	i
Sammenfatning	ii
List of Publications	iii
List of abbreviations	iv
Preface	v
I Overview	1
1 Introduction	2
1.1 Atomic Spin Ensembles	3
1.2 Mechanical resonators	3
1.3 Hybrid systems	4
1.4 Motivational outline	5
2 Membrane in-the-middle optomechanics	11
2.1 Membranes as mechanical oscillators	11
2.2 Cavity optomechanics	13
2.3 Input-output relations	16
2.3.1 Simplified relations	19
3 Room temperature spin oscillator	23
3.1 The cesium atom and magnetic fields	23
3.2 Interaction with light	26
3.3 Atomic Polarizability	30
3.4 Input-output relations	32
3.5 Noise spectrum	34
3.6 Spectral response and quantum cooperativity	36
II Experimental methods and characterizations	38
4 Experimental methods	39
4.1 Laser systems and optical pumping	39
4.2 Vapour cell	40
4.2.1 Anti-relaxation coating and cell performance	41
4.2.2 Characterization	42
4.3 Optomechanical system	42
4.3.1 Cavity	43
4.3.2 Sample holder	43
4.4 Hybrid setup	45

Contents

5 Spin State Preparation	47
5.1 Magneto Optical Resonance Signal	47
5.2 Optical pumping transition	50
5.3 Density dependent optical pumping	51
5.4 Microwave assisted optical pumping	52
5.5 Effective thermal occupation	54
6 AC Faraday Angle	59
6.1 Model	60
6.2 Measurement and calibrations	63
6.3 Connection to spin noise	66
7 Spin Noise	68
7.1 Modelling	68
7.2 Beam size dependence	71
7.3 Power dependence	72
7.4 Conclusions	74
8 Coherently Induced Faraday Rotation	75
8.1 Introduction	75
8.2 General CIFAR expression	77
8.3 Experiments	78
8.3.1 Broadband spin noise	80
9 Spin optodynamics in a warm cesium ensemble	82
9.1 Cell cavity characterizations	82
9.2 Experiments	84
9.3 Spin dynamics in a cavity	87
III Hybrid implementation	90
10 Back-action evasion	91
10.1 Full model	91
10.2 QND limit	94
10.3 Non-QND noise interference	96
10.4 Losses	97
10.5 Running the experiment	98
10.6 Calibrations	100
10.7 Results	101
10.7.1 The 2017 experiments	101
10.7.2 The 2020 experiments	104
11 Hybrid entanglement	108
11.1 Background	108
11.2 Hybrid entanglement	109
11.3 Filtering	112
11.4 Wiener Filtering	113
11.5 Filtering, QND readout	115
11.5.1 Single oscillator	115
11.5.2 Hybrid system	118
11.5.3 A discrete Wiener filter	119
11.6 Experiments	120
11.7 Estimation of uncertainties	122
11.8 Conclusions	125
12 Conclusions and Outlook	126

IV Supplementary Information	128
A Mathematical Methods	129
A.1 Commutators and power spectral densities	129
A.2 Angular momentum operators	130
A.3 Stokes operators	131
A.4 1st order non-homogeneous differential equation	132
B Losses in the double-pass atomic readout	133
C Effective hamiltonian evolution and decay	136
D Quantum cooperativity calibration via white noise drive	138
E Doppler broadening and two-level system absorption	140
F Connection with pulsed experiments	147
F.1 Modelling	147
F.2 Faster than (bad) decoherence	148
F.3 Including decoherence	150
G Unshielded measurements	152
H Cesium vapor density	154
I Experimental parameters	155
Bibliography	158

Part I

Overview

Chapter 1

Introduction

In the last couple of decades, remarkable progress has been made in controlling physical systems near their quantum limits. The advances in the fabrication of miniaturized electronic, optical, and mechanical structures, along with respective mathematical and theoretical understandings, has prompted a technological revolution. The advances in the control of micro- and nano-sized structures allowed for engineering of devices that could fit the specific needs in various fields of scientific research, helping push the boundaries of the respective fields.

The research on both single and ensembles of atoms, ions, and spins, to nano- and micro-fabricated superconducting and mechanical devices, has matured so much that it will allow these advances to go beyond the scope of fundamental research, reaching industry and society (Riedel et al., 2019). Although still advancing in baby steps, the *second quantum revolution* is happening (MacFarlane et al., 2003).

From harnessing the supremacy in computing, simulating complex molecular configurations, to cryptography and communication (Kimble, 2008), the landscape of possible applications of quantum technologies is vast. Nonetheless, given the specificities of every experimental setup, it has become more and more clear that a single platform might not be able to realize all the protocols needed in a future quantum information processing network (Kurizki et al., 2015). Hybrid quantum devices attempt to combine fundamentally different systems with high efficiency, harnessing the advantages from its constituent elements (Wallquist et al., 2009).

Let us consider quantum information protocols for a moment. In many of these protocols, entanglement is a key resource in ensuring that these protocols outperform their classical counterparts (if such exist). Entangled states share very specific correlations, which due to their de-localized features, can be shared among multiple parties. Given that quantum states cannot be copied with arbitrary fidelity, information encoded in entangled states can be used as a way to communicate with intrinsic fundamental security. In an envisioned quantum-enabled network, the transmission of quantum information over long distances (Duan et al., 2001), for example, can be realized by using optical photons as quantum information carriers about its source to distant nodes. The task of developing quantum-enabled communication protocols is a topic under major development (Wehner et al., 2018).

Another area that can harness advantages from the development of quantum technologies is metrology. In this field of research, the task is to prepare the measurement device in states with reduced uncertainties or increased sensitivity to parameters of interest. The uncertainty in the estimation of parameters, such as position, velocity, or frequency, are limited by the disturbance induced by measurements and/or the Heisenberg uncertainty principle. There is a great effort towards developing technologies that can exploit quantum effects to improve precision past classical limits. Here, perhaps the most striking application up-to-date is in the Laser Interferometer Gravitational-Wave Observatory

(LIGO). There, the sensitivity to gravitational waves (Abbott et al., 2016) is limited by both the light shot noise and quantum back-action. The former arises from quantum fluctuations in the arrival of photons at the photo-detector and the latter induces quantum fluctuations in the motion of the tens-of-kilograms scale mirrors by way of a fluctuating radiation pressure force. Recently, the sensitivity of LIGO has been enhanced by probing the detector using squeezed laser light, a quantum state of light with reduced noise over the sensitive bandwidth of the measurement device (Tse et al., 2019). Other major topics of research orbit around the effects of quantized gravity on massive objects (Bose et al., 2017; Marletto and Vedral, 2017) and test the fundamental symmetries (Lee et al., 2018) with table top experiments.

In the next sections, we will introduce the two platforms we are interested in developing and use to interact with light, and preview the subjects covered in this manuscript.

1.1 Atomic Spin Ensembles

The interaction of light with atomic ensembles, in its various forms, dates from the early 1950's with the studies from Brossel (Brossel and Bitter, 1952), Kastler (Kastler, 1954), and Franzen (Franzen and Emslie, 1957). Other works worth noting are related to the development of paraffin coated vapor cells (Bouchiat and Brossel, 1966) and the optical pumping, summarized in Happer (1972).

Throughout the following decades, with the development of quantum optics and quantum electrodynamics, the non-classical features of photons interacting with few atoms or even a single atom (Kimble et al., 1977) have been explored, setting the stage for experimentally studying entanglement (Aspect et al., 1981) and other features of the atom-light interface (Kimble, 1998). Despite the tremendous progress in this direction, the technical challenges associated with these implementations called for alternative platforms to realize strong interactions between atoms and photons.

The late 1990's and early 2000's came with a new approach to the interface of light and matter. The understanding was that a large collection of atoms could also offer an efficient platform for quantum optics experiments if a collective superposition state of the ensemble could be used for the coupling. A variety of proposals for preparing the ensemble in non-classical states (Kuzmich et al., 1997, 1998) and for establishing quantum communication protocols (Duan et al., 2001) showed the feasibility of the platform. Since then, strong light-matter coupling and various proof-of-principle experiments have been realized using room temperature (Julsgaard et al., 2001) and laser cooled ensembles (Chou et al., 2005), along with solid state atomic mediums (Simon et al., 2007).

The interface of collective atomic ground state coherences with light, be it involving Zeeman or hyperfine levels, has shown particularly high performance due to its long T_2 coherence times, enabling long memory times (Kozhekin et al., 2000; Julsgaard et al., 2004) for input light states. Alkali atoms as potassium, rubidium and cesium, are the most popular choice of species. Several groups around the world have been pursuing improved performance of this type of systems, with Morgan Mitchell's at ICFO¹, Mike Romalis at Princeton, Mikhail Lukin's group at Harvard, Vladan Vuletic at MIT², and Eugene Polzik's group here at the Niels Bohr Institute, to name a few.

1.2 Mechanical resonators

The mechanical effects of light on objects and their motion has long attracted attention, with the earliest known accountings dating from Kepler in the 17th century, observing that transiting comets have dust tails pointing away from

¹The Institute of Photonic Sciences

²Massachusetts Institute of Technology

the Sun. It took, however, a few additional centuries and the works of Newton, Maxwell, Einstein and many others, to develop a theory of electromagnetic radiation and interactions that could account for the observed phenomena (Mansuripur, 2011).

In its most simple form, radiation pressure coupling is due to light transferring momentum to the object. According to Quantum Mechanics, each photon carries a momentum p , proportional to the photon energy E or, equivalently, its angular frequency ω , and inversely proportional to the speed of light c ,

$$p = \frac{E}{c} = \frac{\hbar\omega}{c}. \quad (1.1)$$

Upon incidence on an object, momentum is transferred and a force is generated. The forces exerted by light on objects are very small, and therefore observing this effect often requires looking at the small length scales. The development of Quantum Mechanics in the early 20th century, along with rapid technological developments in various fields, has allowed tailoring interactions to be more susceptible to such small actions. More generally, cavity optomechanical coupling can be achieved when electromagnetic radiation leads to a change on its own optical path length, either by changing the index of refraction or by modifying the object's boundary condition (Midolo et al., 2018). It can be realized by any dispersive non-linear interaction, being direct momentum transfer, shifting a cavity frequency or by optical near field effects (Aspelmeyer et al., 2014).

The interest in affecting motion with electromagnetic radiation has attracted renewed attention during the 1960's, with the advent of experimental gravitational wave detection systems, as resonant Weber bars (Weber, 1967) and optical interferometry (Forward, 1978). Due to the extremely high measurement sensitivity needed to detect gravitational waves, techniques that go beyond classical measurement approaches have appeared (Braginsky et al., 1980).

In the 1990's, techniques for preparing non-classical motional states in ions (Meekhof et al., 1996) were developed, setting the scene for controlling motion at and even below ground state levels. The interest in controlling larger mechanical systems with light has gained a new breath with the predictions and experiments on ground state cooling via dynamical back-action, in Wilson-Rae et al. (2007) and Chan et al. (2011), respectively. As the coupling of mechanical degrees of freedom to light does not require the use of naturally occurring resonances, the application and design span many orders of magnitude in overall mass and dimensions (Aspelmeyer et al., 2014).

1.3 Hybrid systems

As we discussed in the beginning of the chapter, a given platform for studies of light-matter interaction will likely not be able to perform an arbitrary number of different protocols. Reasons for such limitations might arise from which degrees of freedom the platform is sensitive to, or be due to a wavelength mismatch between the constituent parties. For example, one might need to transduce an optical signal into the microwave regime, requiring an electrically tunable system. This is where hybrid systems are meant to harness the best of all possible worlds involved in a more general quantum-linked hybrid network Wehner et al. (2018). Here, we will focus on the hybrid implementations involving atomic ensembles interacting with mechanical systems via light.

On the experimental side, apart from the activities in Eugene Polzik's group at NBI, there has been activities in Philip Treutlein's group in Basel³, Dan Stamper Kurn's at UC Berkeley⁴, and more recently at Christoph Becker's in Hamburg⁵. Due to the different physical processes involved in the realizations, it is useful to classify the experiments according to implementation. There have been experiments coupling

³University of Basel, Basel, Switzerland.

⁴University of California, Berkeley, USA.

⁵Universität Hamburg, Hamburg, Germany.

Motivational outline

- *external degrees of freedom of the atomic ensemble and a mechanical oscillator.* In this implementation, the center-of-mass degree of freedom of an optically trapped atomic ensemble is coupled to a distant mechanical oscillator via light. Early implementations had both systems in free space (Camerer et al., 2011), that have been updated to place the membrane in an optical resonator (Jöckel et al., 2015; Vochezer et al., 2018; Christoph et al., 2018), enhancing the effects of the light onto the mechanical device. Here, the experiments were mostly focused on optically cooling the membrane via the signal written onto the light by the atomic ensemble.
- *internal degrees of freedom of the atomic ensemble and mechanical oscillator.* Instead of the atomic motion, one can use the ground state angular momentum of the atomic ensemble to mediate interactions with light, and consequently with the mechanical oscillator. Our implementation at NBI fits into this category. The polarization of the light, modulated by the spin ensemble, is converted into amplitude/phase modulation and directed to a distant mechanical device in a cascaded fashion. We have demonstrated quantum back-action evasion (Møller, 2018) and, more recently, entanglement (Thomas et al., 2020) between the systems. In this implementation, the spin oscillator can be prepared in an effective negative mass state, significantly altering the landscape of interactions. We also note that it is possible to increase the number of passes by the systems, interfacing the parts with light which has already seen both systems once back to the spin ensemble, as demonstrated in Karg et al. (2020).
- *external and internal degrees of freedom of the atomic ensemble coupled to each other.* Finally, one can also implement both spin and mechanical degrees of freedom in the same physical ensemble (Kohler et al., 2018). The ensemble is positioned inside an optical cavity, interacting multiple times with the systems and intra-cavity field. It has been observed that the systems can exchange energies, amplifying the coupled mode as in a self-driven parametric oscillator.

The backbone of the hybrid implementation presented in this manuscript comes from the initial proposal for interfacing the spin and mechanics (Hammerer et al., 2009), which aimed to prepare the collective system in an entangled EPR state. Since then, it has been perfected (Huang et al., 2018) to include dynamical cooling effects for improved performance with realistic parameters.

The origins of our implementation date to previous experiments involving two spin systems, (Julsgaard et al., 2001), which already realized the intriguing negative mass harmonic oscillator in the spin system. It was soon realized that quantum mechanics free dynamics could be achieved in the positive-negative mass configuration of harmonic oscillators (Tsang and Caves, 2012). The trajectories of the joint oscillator in this subspace is free of quantum uncertainties (Polzik and Hammerer, 2015). New regimes of light-matter interaction can also be encountered when interacting the optical degrees of freedom multiple times with the stationary systems (Karg et al., 2019).

Having introduced the systems, we move on to the topic of the present work.

1.4 Motivational outline

If you have reached this far, you might be wondering what we are going to deal with in this manuscript. In this section, we will provide an overview of the goals we pursue, along with some of the concepts used throughout our implementation.

We start by asking the question: how precisely can one estimate the position of an object? More generally, what are the effects of measurement on the dynamics of a quantum object?

These questions have been asked multiple times, in one way or another, throughout the last century. To name a few, physicists such as Einstein, Podolsky, and Rosen (Einstein et al., 1935), John Bell (Clauser and Shimony, 1978),

Braginsky and Thorne (Braginsky et al., 1980), and Caves (Caves, 1980) have contributed to the understanding and experimental developments. The latter approach, by Caves, is formulated around the question of gravitational waves and their detection.

The backbone of the quantum back-action effects we observe stems from the quantized nature of photons and its effects when interacting with different objects (Caves, 1980). For example, an ideal laser source outputs light with photons that obey Poissonian distribution $p(n)$ of the photon number (Davidovich, 1996)

$$p(n) = e^{-\langle n \rangle} \frac{\langle n \rangle^n}{n!}, \quad (1.2)$$

with $\langle n \rangle$ as the mean photon number. In an ideal laser, photons are emitted independently from each other and arrive at random times at a given location, for instance at a photo-detector. Therefore, the flux of photons fluctuates in time, even when the ideal laser maintains a constant average output flux. This fluctuation, of true quantum mechanical origin, manifests itself in a multitude of effects. The transfer of momentum from light to a massive object, which is the basis of radiation pressure coupling, will set the object in a respectively fluctuating motion. Nonetheless, before talking about the forces of light on objects, let us define the states of light we deal with.

The quantum mechanical analysis of a single mode electromagnetic radiation with frequency ω , at time t , tells us that the total energy can be described by the Hamiltonian

$$\hat{H}(t) = \hbar\omega \left(\hat{a}^\dagger(t)\hat{a}(t) + \frac{1}{2} \right), \quad (1.3)$$

where $\hat{a}(t)$ and $\hat{a}^\dagger(t)$ are the photon annihilation and creation operators satisfying $[\hat{a}(t), \hat{a}^\dagger(t')] = \delta(t - t')$. The quantity $\hat{a}^\dagger(t)\hat{a}(t)$ is also defined as the number operator \hat{n} , which follows from $\hat{n}|n\rangle = n|n\rangle$ with $|n\rangle$ as the photon state with occupation n . The photon state with lowest energy is the vacuum state $|0\rangle$, the state with null average occupation, whose energy is $\langle 0|\hat{H}(t)|0\rangle = \hbar\omega/2$.

Instead of the total energy of the field, we are mostly interested in the electric field of the electromagnetic wave. For example, the quantized electric field of a wave in a resonator follows (Gerry and Knight, 2004)

$$\hat{E}_x(z, t) = iE_0 \left[\hat{a}e^{i(kz - \omega t)} - \hat{a}^\dagger e^{-i(kz - \omega t)} \right] \quad (1.4)$$

with $E_0 = (\hbar\omega/2\epsilon_0 V)^{1/2}$ being the field amplitude, which depends on the resonator volume V . Here we assume that the medium within this volume is vacuum, with a permittivity ϵ_0 . The electric field expression given above resembles the one seen in Classical Electromagnetism books (Griffiths et al., 1999), with the electric field amplitudes substituted by the creation and annihilation operators. Although the $|n\rangle$ photon states do not accurately capture the output state of a laser (Gerry and Knight, 2004), the coherent states $|\alpha\rangle$, presented in the next paragraph, represent a suitable description. The electric field has a non-zero variance, that is

$$\Delta E_x \equiv \langle 0|(\hat{E}_x - \langle 0|\hat{E}_x|0\rangle)^2|0\rangle^{1/2} = E_0, \quad (1.5)$$

a consequence of the non-commutability between \hat{a} and \hat{a}^\dagger . The electric field fluctuations has observable consequences in many light-matter interactions, as in spontaneous emission of excited atoms and molecules.

Further analysis of the field and energies is done by defining a sensible state for the electromagnetic radiation. We know that in free space the classical electric field is a periodic function. The ideal laser source outputs light in a *coherent state*, which follows from $\hat{a}|\alpha\rangle = \alpha|\alpha\rangle$, for $\alpha = |\alpha|e^{i\theta}$ as the the state eigenvalue.

Motivational outline

The coherent states are the states that describes the classical expectations of a laser field, as they match the classical expectation of an electric field

$$\langle \alpha | \hat{E}_x(z, t) | \alpha \rangle = 2E_0 |\alpha| \sin(kz - \omega t), \quad (1.6)$$

but also displays vacuum fluctuations

$$\langle \alpha | (\hat{E}_x - \langle \alpha | \hat{E}_x | \alpha \rangle)^2 | \alpha \rangle^{\frac{1}{2}} = E_0. \quad (1.7)$$

Therefore, the coherent state is also a state with minimum fluctuations.

Instead of the using the creation and annihilation operators, it will be more convenient to write the electric field in terms of the *optical quadrature operators*

$$\hat{E}_x(z, t) = iE_0(\hat{X}_L \cos(kz - \omega t) + \hat{P}_L \sin(kz - \omega t)), \quad (1.8)$$

in which

$$\hat{X}_L = \frac{\hat{a} + \hat{a}^\dagger}{2} \quad \hat{P}_L = -i \frac{\hat{a} - \hat{a}^\dagger}{2}, \quad (1.9)$$

as the amplitude and phase quadrature operators, satisfying $[\hat{X}_L, \hat{P}_L] = \frac{i}{2}$. They are the real and imaginary part of the electric field, but also play the role of effective position and momentum operators of light. With the quadrature operators we can write the Hamiltonian (1.3) as

$$\hat{H}(t) = \frac{\hbar\omega}{2} (\hat{X}_L^2 + \hat{P}_L^2), \quad (1.10)$$

which resembles the harmonic oscillator, the favorite description of 10/10 physicists. The mapping to harmonic variables allows us to visualize the coherent state in a phase space picture, as shown in Figure 1.1. A given coherent state $|\alpha\rangle$ with average amplitude $|\alpha|$ and phase ϕ occupies a certain area in phase space, demonstrating that the vacuum level of energy and uncertainty. In particular, the amplitude and phase have standard deviations $\Delta X_L = \Delta P_L = \frac{1}{2} |[\hat{X}_L, \hat{P}_L]| = \frac{1}{4}$.

We now return to the discussion of estimating the position of a given object with maximum precision. We will here consider an interferometer, as in the concrete case of LIGO, whose end-mirrors, which behave like suspended pendula, are probed by light. Imagine an end-mirror having a mass m and resonant frequency ω_M . In general, any external excitation will set the mass in an oscillatory motion and the instantaneous mirror position will be given by

$$\hat{X}_M(t) = \hat{X}_M(0) \cos \omega_M t + \hat{P}_M(0) \sin \omega_M t, \quad (1.11)$$

where $\hat{X}_M(0)$ and $\hat{P}_M(0)$ are the position and momentum of the mirror at time $t = 0$. The harmonic motion is captured by the Hamiltonian

$$\hat{H}_M = \frac{\hbar\omega_M}{2} (\hat{X}_M^2 + \hat{P}_M^2). \quad (1.12)$$

As the mass moves, it will alter the path length difference between the two interferometer arms, imprinting the object's motion onto the phase of light \hat{P}_L . The task here is to determine the presence of a minute force F_{gwd} originating from some far-away gravitational wave source. For isolated mirrors, the object is on average at its equilibrium position. Because of that, the spectral analysis of the oscillator motion will be the most interesting, as it gives information about the Fourier frequency Ω of the motion. A change in the end-mirror position is imprinted onto the phase of light, which can be described as follows

$$\hat{P}_L^{\text{out}}(\Omega) = \hat{P}_L^{\text{in}}(\Omega) + \sqrt{\Gamma_M} \hat{X}_M(\Omega), \quad (1.13)$$

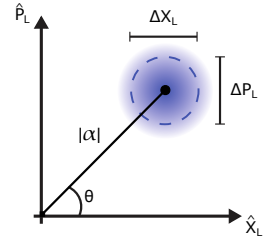


Figure 1.1: Phase space representation of a coherent state. The coherent state with average amplitude $|\alpha|$ and phase θ has non-zero variances, leading to an uncertainty area defined by the standard deviations ΔX_L and ΔP_L .

for Γ_M as the parameter that gauges the how much motion is mapped into light, which is often referred to as the *readout rate*. The parameter Γ_M , being proportional to the photon flux $\langle n \rangle$, also has the complementary role of gauging how much the light affects the objects motion. More precisely, the position of the mirror behaves as

$$\hat{X}_M(\Omega) = \chi_M(\Omega)[2\sqrt{\Gamma_M}\hat{X}_L(\Omega) + \sqrt{\gamma_M}\hat{F}_M(\Omega) + F_{\text{gwd}}]. \quad (1.14)$$

Before explaining the various terms of the equation above, we should point out that the dynamics of the light quadratures and the mirror's position and momentum are inherently connected. A precise measurement of the objects position, according to equation (1.13), requires a large coupling parameter Γ_M . Nonetheless, the large coupling rate will also set the mirror in motion with the same rate. If too large, it can spoil the detection of the force F_{gwd} . The physics of optimum coupling and detection performance is vast (Braginsky et al., 1992). Here it suffices to say that there is an optimum for the coupling strength, in which the input phase fluctuations \hat{P}_L^{in} balance the effect of light on the object, the measurement *quantum back-action*. This point of optimal coupling is often referred to as the *standard quantum limit* (SQL).

Equation (1.14) contains the *mechanical susceptibility* χ_M

$$\chi_M(\Omega) = \omega_M / (\omega_M^2 - \Omega^2 - 2i\Omega\gamma_M), \quad (1.15)$$

which sets the responsivity of the mirror to all forces acting upon it. If the external force acts at $\Omega \sim \omega_M$, the corresponding induced motion will be maximum. The overall displacement is just limited by the damping mechanisms that spoil otherwise perfect mirror oscillation. The damping is lumped in the quantity γ_M . An example of the oscillator response to an external force is shown in Figure 1.2 (blue points). The susceptibility is represented in polar coordinates, $R \propto |\chi_M|$ and the phase ϕ as the phase of the object response with respect to the drive.

The other term in equation (1.14) is the thermal force \hat{F}_M , here present due to inevitable coupling of the mirror to the environment thermal bath with occupation n_M . Here we assume that we can describe the coupling of the mirror to its surroundings via a Langevin equation, in which the damping term γ_M is due to the overall viscosity experienced by the mirror motion during its motion.

An important quantity to be defined at this moment is the *quantum cooperativity* of the optical measurement

$$C_q = \frac{\Gamma_M}{2\gamma_M(n_M + \frac{1}{2})}, \quad (1.16)$$

which is the ratio of the motion induced by the light, the quantum back-action, Γ_M , to the thermal forces. A high $C_q \gg 1$ would indicate that the motion of the object is mostly due to the interaction with the laser light. In general, a small quantum cooperativity leads to a decrease in sensitivity to external forces of interest.

At this point, a central question arises: can we do anything to get around the measurement noise induced by the optical probing? The answer is "yes", and there are many different approaches to circumvent quantum back-action. One can engineer a different scheme of coupling to light (Kimble et al., 2001; Woolley and Clerk, 2013; Ockeloen-Korppi et al., 2016) or stroboscopically modulate the probe beam (Vasilakis et al., 2015), for example. Other proposals involve coherent feed-forward (Tsang and Caves, 2010) and diverse atomic systems (Zhang et al., 2013; Bariani et al., 2015).

Here, we take a different approach. We prepare another auxiliary oscillator, insensitive to the force F_{gwd} , with canonical variables \hat{X}_S and \hat{P}_S , which will couple to light in the same way as given in equation (1.13)

$$\hat{P}_{L,S}^{\text{out}}(\Omega) = \hat{P}_{L,S}^{\text{in}}(\Omega) + \sqrt{\Gamma_S}\hat{X}_S(\Omega). \quad (1.17)$$

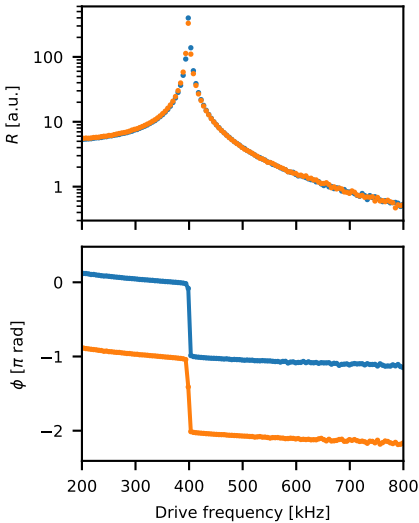


Figure 1.2: Spin oscillator susceptibility. The response of a positive (blue) and a negative mass (yellow) spin oscillator to an external magnetic field force with constant magnitude. Although the oscillators respond with the same strength, there is a π phase shift delay, characteristic of a system responding oppositely to the drive.

Motivational outline

This time the oscillator will be coupling to the external forces as follows

$$\hat{X}_S(\Omega) = -\chi_S(\Omega)[2\sqrt{\Gamma_S}\hat{X}_{L,S}^{\text{in}}(\Omega) + \sqrt{\gamma_S}\hat{F}_S(\Omega)]. \quad (1.18)$$

Note the minus sign before the susceptibility. This minus sign manifests itself as a π phase shift on the response to external forces, as seen in Figure 1.2 (orange points), with the absolute value of the response unchanged. The auxiliary oscillator is prepared in the magnetic coherences of the cesium ground state levels. The minus sign in susceptibility is the consequence of the spin oscillator Hamiltonian being

$$\hat{H}_S = -\frac{\hbar\omega_S}{2} (\hat{X}_S^2 + \hat{P}_S^2), \quad (1.19)$$

achieved when preparing the atomic system in its highest energy as a ground state. In this configuration, the system behaves as an effective negative mass oscillator, responding oppositely to external forces when compared to a canonical harmonic oscillators. That is to say, pushing it leads to the motion in the opposite direction to the input force (Baker and Bowen, 2017). The other terms in equation (1.18) are analogous to the ones encountered in the equation (1.14), with γ_S and $\hat{F}_S(\Omega)$ as the spin oscillator damping rate and effective thermal spin bath force.

The back-action evasion measurement happens when we connect the output light of the readout of the first oscillator as the input for the second, that is

$$\hat{p}_L^{\text{in}}(\Omega) = \hat{p}_{L,S}^{\text{out}}(\Omega), \quad (1.20)$$

such that we can re-write equation (1.13) as

$$\begin{aligned} \hat{p}_L^{\text{out}}(\Omega) &= \hat{p}_{L,S}^{\text{in}}(\Omega) + \sqrt{\Gamma_M}\hat{X}_M(\Omega) + \sqrt{\Gamma_S}\hat{X}_S(\Omega) \\ &= \hat{p}_{L,S}^{\text{in}}(\Omega) + 2[\Gamma_M\chi_M(\Omega) - \Gamma_S\chi_S(\Omega)]\hat{X}_{L,S}^{\text{in}}(\Omega) \\ &\quad + \sqrt{\Gamma_M}\chi_M(\Omega)[\hat{F}_M(\Omega) + F_{\text{gwd}}] - \sqrt{\gamma_S}\chi_S(\Omega)\hat{F}_S(\Omega). \end{aligned} \quad (1.21)$$

The first term in the right hand side, $\hat{p}_{L,S}^{\text{in}}(\Omega)$, stands for the measurement shot noise. The second term, proportional to $\hat{X}_{L,S}^{\text{in}}(\Omega)$, is the quantum back-action contribution from each oscillator. The terms $\hat{F}_M(\Omega)$ and $\hat{F}_S(\Omega)$ are the thermal noise contributions. By setting

$$\Gamma_M\chi_M(\Omega) = \Gamma_S\chi_S(\Omega), \quad (1.22)$$

we can effectively remove all measurement induced back-action, recovering the limit in which the quantum mechanics of the measurement is not present (Polzik and Hammerer, 2015). The price paid here is the added spin thermal noise. Nonetheless, this contribution should be vanishingly small compared to the overall noise cancellation due to the back-action interference.

Interestingly, we notice an additional consequence of the light-matter interaction in this hybrid cascaded system. From equation (1.11), the light is now carrying information about the overall position

$$\hat{X}_M(t) + \hat{X}_S(t) = [\hat{X}_M(0) + \hat{X}_S(0)] \cos \omega_0 t + [\hat{P}_M(0) - \hat{P}_S(0)] \sin \omega_0 t, \quad (1.23)$$

in the case with $\omega_M = -\omega_S \equiv \omega_0$. The joint position operator has unique property that the quantity measured carries no measurement induced back-action due to the commutability of the measured quantities

$$[\hat{X}_M + \hat{X}_S, \hat{P}_M - \hat{P}_S] = 0. \quad (1.24)$$

Therefore, measuring the hybrid system induces no quantum back-action, as already seen in the discussion about equation (1.21). The state involving sum of

position $\hat{X}_M + \hat{X}_S$ and difference in momenta $\hat{P}_M - \hat{P}_S$ is the Einstein-Podolsky-Rosen state, theorized by authors with the same names (Einstein et al., 1935).

In this thesis, light plays the role of probing and linking two distant systems. Locally, at each site, the optical probe measures and accordingly disturbs the system dynamics. Subsequently, light travels to the next site, interacting with the second system. By engineering the overall interaction we can not only remove the quantum back-action, enhancing the sensitivity of position measurements, but also generate entanglement between the distant and disparate quantum systems.

The generation of entanglement is connected to a complementary view of the measurement disturbance. The quantum back-action induced by the probe light is not bad in and of itself. On the contrary, it indicates that the light and probed object are becoming highly correlated. In the high cooperativity limit, for $C_q \gg 1$, significant correlations between light and object can be created, allowing to reconstruct the trajectory of the system in phase space. Furthermore, for strong measurements induced by light, the system can be tracked back to its ground state uncertainty (Rossi et al., 2019).

Here we recompose the thinking by incorporating the information extracted by measurement. More precisely, we filter the measured optical phase quadrature using the Wiener filter K_X , which incorporates the acquired knowledge in an efficient manner. From the Wiener filter K_X for \hat{X}_{EPR} , the conditional quadrature is

$$X_{\text{EPR}}^c(t) = \int_0^t dt' K_X(t' - t, t) \hat{P}_L^{\text{out}}(t'). \quad (1.25)$$

In the simplest (ideal) case, the Wiener filter envelope is an exponential with a time constant defined by its decoherence and readout processes.

Including all complexities not discussed in the reasoning presented above, we prepare the hybrid system with generalized coordinates \hat{X}_{EPR} and \hat{P}_{EPR}

$$\hat{X}_{\text{EPR}} = (\hat{X}_M - a\hat{X}_S^\beta) / \sqrt{1 + a^2} \quad (1.26)$$

$$\hat{P}_{\text{EPR}} = (\hat{P}_M + a\hat{P}_S^\beta) / \sqrt{1 + a^2}, \quad (1.27)$$

for a as an arbitrary weight scalar parameter and

$$\hat{X}_S^\beta = \hat{X}_S \cos \beta + \hat{P}_S \sin \beta \quad (1.28)$$

$$\hat{P}_S^\beta = \hat{P}_S \cos \beta - \hat{X}_S \sin \beta, \quad (1.29)$$

as generalized spin operators, accounting for a phase rotation β . The conditional variance of the system for classical systems is bounded from below by (Duan et al., 2000)

$$V_c = \text{Var}_c[\hat{X}_{\text{EPR}}] + \text{Var}_c[\hat{P}_{\text{EPR}}] = 1. \quad (1.30)$$

Establishing $V_c < 1$ therefore demonstrates entanglement in the hybrid system.

In this chapter we have introduced the constituents of the hybrid system, the mechanical and spin oscillators, and discussed how its performance can lead to quantum back-action evasion and entanglement. In the next chapters, we will consider in more detail the implementation as far as the individual systems are concerned.

Chapter 2

Membrane in-the-middle optomechanics

We start the main body of this by thesis devoting a chapter to the cavity optomechanical system. We present some of the basic design principles of the mechanical oscillators used in the hybrid experiments, defining the motional eigenfrequencies and associated linewidths, the optical resonator and the membrane in the middle configuration, and finish with the input-output relations for the optical field.

2.1 Membranes as mechanical oscillators

In the field of cavity optomechanics a multitude of mechanical oscillators and geometries for optical mode confinements are under study (Aspelmeyer et al., 2014). Here, we work with a thin dielectric membrane embedded in an optical cavity. This particular geometry allows us to partially decouple the mechanical resonator and optical cavity considerations and optimizations.

The optical cavity is a high-finesse Fabry-Perot resonator and the mechanical resonator is based on a tensioned silicon nitride membrane. This configuration was initially proposed in Jayich et al. (2008), and has been utilized in various groups ever since (Thompson et al., 2008; Wilson et al., 2009; Yu et al., 2012; Purdy et al., 2013; Nielsen et al., 2017).

The interest in silicon nitride (SiN) membranes dates back to 2008, where studies on the mechanical quality of commercially available devices first appeared (Zwickl et al., 2008). An example of such device is shown in Figure 2.1 (a). A thin (~ 50 nm) silicon nitride membrane (in white) is suspended on top of a silicon frame (in yellow), and supports a multitude of high-quality vibrational modes. The mechanical quality factors $Q > 10^6$ for modes with frequencies $\omega_m/2\pi \sim 130$ kHz and low optical round trip loss, allowing for cavities with finesse $\mathcal{F} > 10^4$ —which are indeed quite promising numbers for an optomechanical interface. The macroscopic size of the structure, on the order of 5 mm, allows the experimenter to rigidly clamp the supporting silicon frame, which is important in ensuring proper thermalization of the oscillator in cryogenic experiments. The catch, and there is always a catch, is that the SiN mechanical modes couple to the lossy frame modes, heavily influencing the performance of the oscillator.

The loss of mechanical energy to the supporting frame and losses associated with bending near the clamping points of the membrane to the supporting frame have been reported in (Jöckel et al., 2011; Yu et al., 2012). Typically, the energy damping mechanisms present in the membrane mechanical oscillators are summarized as

$$Q^{-1} = Q_{\text{gas}}^{-1} + Q_{\text{rad}}^{-1} + Q_{\text{mat}}^{-1}, \quad (2.1)$$

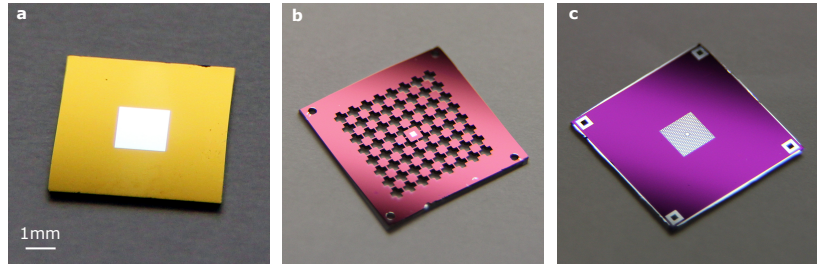


Figure 2.1: Different generations of silicon nitride-based drum mechanical oscillators. The engineering complexity of the mechanical oscillator (central light-colored patches) has been built up from the (a) relatively simple drum resonator, adding a (b) 2D phononic structure in the silicon frame. In (c), the soft clamping idea is applied, making the phononic bandgap in the same material of the central pad. Figure reproduced from (Møller, 2018).

with Q_{gas} as the gas damping, Q_{rad} as the mechanical radiation (anchoring/-mounting) losses and Q_{mat} as the material losses. The gas damping losses are due to collision of air molecules with the membrane and can be reduced by placing the device in a low air pressure p environment $Q_{\text{gas}} \propto p$. The radiation losses Q_{rad} are due to the anchoring/mounting of the material to the surrounding structure, leading to a spatial overlap between the modes of interest with the frame modes and allowing phonons to dissipate to the environment. The final loss mechanism, Q_{mat} , is due to imperfections in the mechanical device material, as defects in the bulk and in the surface.

An important step towards better control of membrane modes was the development of a phononic bandgap shield in the supporting silicon frame (Yu et al., 2014; Tsaturyan et al., 2014), inspired by studies of phononic structures in optomechanical crystals (Safavi-Naeini and Painter, 2010). The design of the two-dimensional phononic crystal structure, along with the central pad, within which the membrane resonator is embedded, can be seen in Figure 2.1 (b). By introducing a phononic bandgap within the frequency range of the membrane modes of interest, the whole outer region of the silicon frame could be tightly clamped to a sample holder without affecting the Q-factors of membrane modes within the phononic bandgap. The shield is composed of a periodic structure consisting of large square silicon pads, connected with narrow silicon tethers, forming a Bragg reflector for phonons within a frequency range of several hundred kilohertz, suppressing excitations and couplings from the outside world to affect the inner silicon pad, within which the membrane resonator resides. The finitude of the bandgap in the membranes used locally at NBI leads to a finite mechanical noise suppression, e.g. ~ 20 dB to 40 dB on a ~ 200 kHz bandwidth centered on the defect mode in work of (Tsaturyan et al., 2014). Locally, the performance of these devices in a cryogenic environment was first presented in (Nielsen et al., 2017).

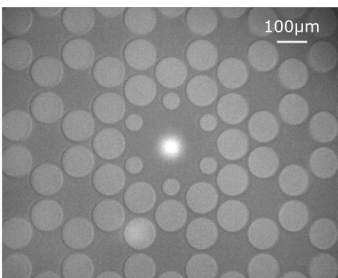


Figure 2.2: Image of the membrane with an optical mode placed at the center of the defect. The hexagonal structure of the phononic shield surrounds the defect, the central pad. Bright spot in the center is the optical beam.

With anchoring/mounting losses removed by the presence of the phononic crystal structure in the silicon frame, a new step towards improving the mechanical quality factors was set by having closer look on the geometry of the mechanical device (Tsaturyan et al., 2017). In the devices presented in the panels (a) and (b) of Figure 2.1, the central pad is directly attached to the silicon frame. It turns out that tensioned membranes lose most of their mechanical energy at the boundary of the silicon nitride membrane and the supporting frame. During the membrane oscillations the displacement fields associated with different vibrational modes of the membrane have large mode curvatures near the clamped edges of the membrane (Yu et al., 2012), leading to a considerable amount of bending related losses of elastic energy.

The strategy employed in Tsaturyan et al. (2017) was to tailor the boundary condition of the mode of interest, such that its amplitude would be vanishingly small at the hard silicon clamp. Images of these devices are shown in Figure 2.1 (c), and also in the zoom in Figure 2.2. The phononic crystal structure is now patterned in the silicon nitride membrane, rather than the silicon frame, as discussed previously. The *soft clamping* of the mechanical mode significantly reduced the bending losses, improving the quality factors by approximately $\times 10^2$ times compared to the previous best, reaching $Q = 1.555 \times 10^9$ at its highest (Tsaturyan, 2019). At cryogenic temperatures the high Q factors, along with the MHz mechanical frequencies, leads to coherence times on the order of $T_2 \sim 1$ ms. This allows for coherent processes between light and the device to happen with high efficiency.

2.2 Cavity optomechanics

The interaction between light and a mechanical object is traditionally idealized as shown in Figure 2.3 (a). There we see the most important constituents of the canonical optomechanical system: an optical cavity composed of two mirrors, one of which is allowed to move, and the intra-cavity field.

The interaction between the light and mirror can be illustrated as follows. The optical field (red oscillating line) exerts a force on a small suspended mirror, setting it in motion. As the mirror moves, the cavity length changes, and so does the cavity resonance condition. The change in resonance condition leads to a different intra-cavity number of photons on a timescale of the cavity lifetime $\tau = 2\pi/\kappa$, changing the force on the mirror, and restarting the cycle of mirror-light interaction. Here, $\kappa/2\pi$ is the cavity bandwidth (FWHM), set by the total losses (e.g. transmissivity) of the cavity mirrors. The cavity is also defined to have length L_c and longitudinal mode spacing $\text{FSR} = c/2L_c$.

In a more formal language, the intracavity optical mode and the mechanical mode are assumed to be harmonic, with frequencies ω_{cav} and ω_M . Following equation (1.3), the total Hamiltonian, without the mirror-light interaction, can be expressed as

$$\hat{H}/\hbar = \omega_{\text{cav}}\hat{a}^\dagger\hat{a} + \omega_M\hat{b}^\dagger\hat{b}, \quad (2.2)$$

in which we have disregarded the $\frac{1}{2}$ contributions from the vacuum energies. The operators \hat{a} and \hat{b} , along with their conjugates, are the operators related to the destruction/creation of optical and motional quanta, with $[\hat{a}^\dagger, \hat{a}] = [\hat{b}^\dagger, \hat{b}] = 1$. The position and momentum operators of the motional degrees of freedom are

$$\hat{x}_M = x_{\text{zpf}}(\hat{b} + \hat{b}^\dagger) \quad \hat{X}_M = (\hat{b} + \hat{b}^\dagger)/\sqrt{2} \quad (2.3)$$

$$\hat{p}_M = -ip_{\text{zpf}}(\hat{b} - \hat{b}^\dagger) \quad \hat{P}_M = -i(\hat{b} - \hat{b}^\dagger)/\sqrt{2}, \quad (2.4)$$

with $x_{\text{zpf}} = \sqrt{\hbar/2M\omega_M}$ and $p_{\text{zpf}} = \sqrt{\hbar M\omega_M/2}$ as the zero-point motion and zero-point momentum of the movable mirror with effective mass M . The capital letter variables are the dimensionless version of the dimensioned variables.

We now allow the interaction to change the end-mirror position, such that cavity frequency becomes $\omega_{\text{cav}}(x)$. For small fluctuations around the equilibrium position, the cavity resonance will be only weakly modulated. Expanding the frequency to first order and quantizing the position we find

$$\omega_{\text{cav}}(\hat{x}) \sim \omega_{\text{cav}} + \hat{x} \frac{\partial}{\partial x} \omega_{\text{cav}} = \omega_{\text{cav}} + \hat{x}G, \quad (2.5)$$

with the quantity G defining the frequency shift per displacement. With the interaction, the Hamiltonian becomes

$$\hat{H}/\hbar = \omega_{\text{cav}}\hat{a}^\dagger\hat{a} + \omega_M\hat{b}^\dagger\hat{b} + G\hat{x}\hat{a}^\dagger\hat{a} \quad (2.6)$$

$$= \omega_{\text{cav}}\hat{a}^\dagger\hat{a} + \omega_M\hat{b}^\dagger\hat{b} + g_0(\hat{b} + \hat{b}^\dagger)\hat{a}^\dagger\hat{a} \quad (2.7)$$

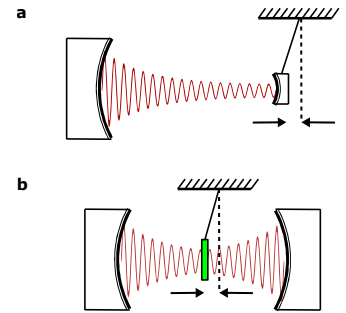


Figure 2.3: Canonical and membrane-in-the-middle optomechanical systems. (a) The movable end-mirror optical resonator is the canonical version of the experimental sketch. (b) In our experiments, the movable part is sitting inside the optical resonator. Figure adapted from (Wilson, 2012).

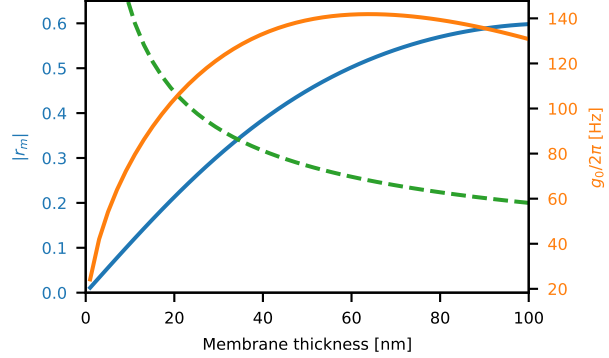


Figure 2.4: Single photon optomechanical coupling g_0 and reflectivity $|r_m|$. The single photon optomechanical coupling rate g_0 (orange) is a product of the membrane reflectivity (blue) and the zero-point fluctuation amplitude x_{zpf} (green). The x_{zpf} goes as $1/\sqrt{t}$ (scale not shown) and has been rescaled such that $x_{zpf} = 1$ fm for $t = 60$ nm. The curves are calculated for $\lambda = 852$ nm, $n = 2$ and $L_c = 2.5$ mm. Figure adapted from (Barg, 2018).

in which $g_0 = Gx_{zpf}$ is the single-photon optomechanical coupling rate.

In the experiments we deal with, g_0 is typically smaller than any other coupling rates involved in the optomechanical interaction. To boost the coupling rate, we work in the regime of large intra-cavity field amplitudes $\langle \hat{a} \rangle = \sqrt{\langle \hat{n} \rangle}$. The dynamics of interest will therefore be happening around the steady state

$$\hat{a} \rightarrow \langle \hat{a} \rangle + \hat{a}, \quad (2.8)$$

transforming equation (2.6), to the first order in fluctuations, as

$$\hat{H}/\hbar \sim \omega_{\text{cav}} \hat{a}^\dagger \hat{a} + \omega_M \hat{b}^\dagger \hat{b} + g(\hat{b} + \hat{b}^\dagger)(\hat{a} + \hat{a}^\dagger), \quad (2.9)$$

in which we have disregarded static and second order terms, and define the optomechanical coupling rate $g = g_0 \langle \hat{a} \rangle$.

The linearized hamiltonian presented in equation (2.9) is the basis of the optomechanical effects involved in this thesis. In particular, two basic types of photon-phonon couplings are presented there (Vasilyev et al., 2013): the beam splitter interaction $\hat{b} \hat{a}^\dagger + \hat{b}^\dagger \hat{a}$ exchanges excitations between the two fields, while the entanglement interaction $\hat{b} \hat{a} + \hat{b}^\dagger \hat{a}^\dagger$ is responsible for the pair-wise particle creation/destruction. The relative weight of these processes can be tuned by the cavity bandwidth κ , which acts as a frequency selector for intra-cavity processes. In particular, when the cavity is tuned to resonance $\Delta = 0$, the two interactions presented above are balanced, and a QND interaction proportional to $\hat{X}_M \hat{X}_L$ comes about.

However, the simple picture presented above, the movable end-mirror system, is not really what we work with. A more accurate version of the experimental situation is sketched in Figure 2.3 (b). The movable "mirror" is now placed inside the optical resonator. As discussed earlier in this chapter, decoupling of the movable part of the optomechanical cavity from the end-mirrors allows for optimization of the individual parts independently, which is a great feature for an experimental system.

The presence of the membrane, a dielectric slab with a finite reflectivity coefficient, inside of the cavity leads to a different physical picture, which, as it turns out, can be readily mapped to the canonical optomechanical system (Jayich et al., 2008; Wilson, 2012), which is what we do in our approach. Now, the triple stack composed of the membrane sandwiched by the mirrors forms two coupled cavities (Genes and Dantan, 2017). The coupling between the two

Cavity optomechanics

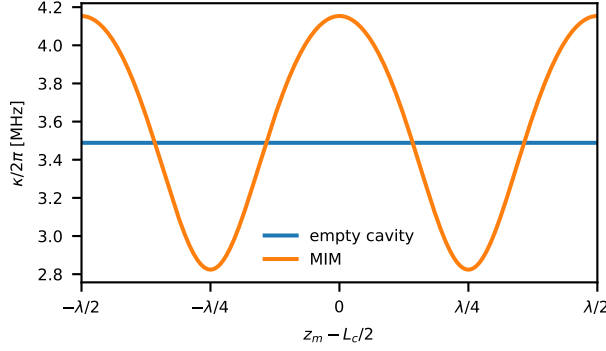


Figure 2.5: Cavity decay rate versus membrane position. The cavity linewidth is modulated according to the membrane position in the cavity standing wave pattern (orange). The empty cavity has length $L_c = 2.6 \text{ mm} \sim 6104\lambda/2$ and mirror transmissions $T_1 = 20 \text{ ppm}$ and $T_2 = 360 \text{ ppm}$, respectively. The membrane thickness is 20 nm. The curve in blue stands for the empty cavity configuration.

cavities depends on the membrane position in a given standing wave, which is what we call its "2kz position" (more on this later). Maximum sensitivity to the membrane motion happens at the biggest slope of the optical standing wave.

The amplitude reflectivity of a membrane with index of refraction n and thickness t is (Tsaturyan, 2019)

$$r_m = \frac{(n^2 - 1) \sin(knh)}{2in \cos(knh) + (n^2 + 1) \sin(knh)}, \quad (2.10)$$

for $k = 2\pi/\lambda$ as the wavenumber of the incident light field. The reflectivity is a periodic function of thickness t . In Figure 2.4 (blue curve) we show the reflectivity over the thickness range of interest. It can be shown that the maximum single photon coupling rate g_0 for the membrane-in-the-middle configuration is (Barg, 2018)

$$\max(|g_0|) = 4\text{FSR}x_{\text{zpf}}k|r_m|, \quad (2.11)$$

which we show in orange in Figure 2.4. The green curve in Figure 2.4 is there as a reminding that the zero-point fluctuations are inversely proportional to the mass of the mode.

Overall, all the optomechanically related parameters can be obtained numerically from the transfer matrix model (Wilson, 2012). Here, for completeness, we reproduce the analytical expressions for the cavity frequency shift and decay rate for the membrane at x_M from (Dumont et al., 2019)

$$\omega_{\text{cav}} = q\text{FSR} + \frac{\text{FSR}}{\pi} \left(\arccos \left[(-1)^{q+1} |r_m| \cos(2k_q x_M) \right] - \phi_r \right) \quad (2.12)$$

$$\kappa/2\pi = \frac{c}{2\pi} \frac{(1 - |r_m|^2) |t_1|^2 + (1 + 2|r_m| \cos(2k x_M + \phi_r) + |r_m|^2) |t_2|^2}{2x_M(1 - |r_m|^2) + 2(L_c - x_M)(1 + 2|r_m| \cos(2k x_M + \phi_r) + |r_m|^2)}, \quad (2.13)$$

for k_q as the q -th empty cavity resonance, $|t_1|^2$ and $|t_2|^2$ as the cavity mirror power transmissivities and ϕ_r as the phase change for light reflected from the membrane, here assumed to be $\phi_r = 0$, for simplicity. In Figure 2.5 we show the cavity decay rate versus the membrane position inside the cavity. Here we use experimental observed values – an empty cavity with length $L_c = 2.6 \text{ mm} \sim$

$6104\lambda/2$ and mirror transmissions $T_1 = 20$ ppm and $T_2 = 360$ ppm, respectively. The membrane thickness is set to be 20 nm. Note how the membrane alters the cavity decay rate, as it moves across the $\lambda/2$ standing wave period and couples the two internal cavities with different rates. The position of the membrane in the standing wave period is called the $2kz$ position.

Here, having introduced the basics of the optomechanical system, along with the modifications introduced by the membrane-in-the-middle configuration, we move on to describe how the optical field and the mechanical degree of freedom couple.

2.3 Input-output relations

In cavity optomechanical experiments, we only have access to the light field after the interaction with the optomechanical system. Establishing the relation between the observed light field and the mechanical degree of freedom is therefore of great importance. The *input-output relations* for the light-mechanics system therefore relates how the input light field, prior to the optical resonator, and forces acting on the mechanics, are transduced to the output light field.

Although the radiation pressure changes the cavity resonance according to the position of the moving object, in equation (2.9) we saw that, in our operating regime, the intra-cavity amplitude $\hat{X}_L \propto \hat{a} + \hat{a}^\dagger$ couples to the membrane position $\hat{X}_M \propto \hat{a} + \hat{a}^\dagger$. How the intra-cavity field is mapped to the outer world depends on the whole optomechanical interaction.

In Figure 2.6, we sketch how the mechanical motion is mapped to light according to the cavity detuning Δ . In this picture it becomes clear that due to the phase dependent cavity response, shown as R_{cav} and ϕ_{cav} , both amplitude \hat{X}_L and phase quadrature \hat{P}_L of the output light field can carry information mechanical motion depending on the detuning. The effects shown also apply for the input light, that is, incoming amplitude and phase fluctuations will be mixed according to the cavity detuning.

The journey through the input-output relations starts by writing the optomechanical Hamiltonian (2.9) in terms of the optical and mechanical quadrature operators, as

$$\begin{aligned} \hat{H}_M = & \frac{\omega_M}{2} (\hat{X}_M^2 + \hat{P}_M^2) - \Delta (\hat{X}_{L,M}^{\text{cav}2} + \hat{P}_{L,M}^{\text{cav}2}) \\ & - 4g (\hat{X}_{L,M}^{\text{cav}} \cos \psi_{\text{in}} + \hat{P}_{L,M}^{\text{cav}} \sin \psi_{\text{in}}) \hat{X}_M, \end{aligned} \quad (2.14)$$

where $\Delta = \omega_L - \omega_c$ is the detuning of the laser with respect to the cavity resonance ω_c . Note that we are here in a rotating frame with the laser frequency ω_L . Assuming you are detecting and probing through the same port, the cavity linewidth κ can be decomposed into contributions from the in-and-out-coupling mirror (κ_{in}), the highly-reflective (HR) back mirror ($\kappa_{\text{ex}}^{\text{HR}}$), and intracavity losses ($\kappa_{\text{ex}}^{\text{loss}}$) such that $\kappa = \kappa_{\text{in}} + \kappa_{\text{ex}}$, with $\kappa_{\text{ex}} = \kappa_{\text{ex}}^{\text{HR}} + \kappa_{\text{ex}}^{\text{loss}}$, the subscript ex signifies any extra loss mechanism not related to the input/output coupler. Losses due to the HR mirror and due to intracavity scattering are mathematically equivalent. Finally, $\psi_{\text{in}} = \arctan(2\Delta/\kappa)$ denotes the phase of the intracavity field relative to input field.

The time evolution of the optical and mechanical variables must include, apart from the dynamics induced by the Hamiltonian (2.14), coupling to the environment, and associated decay and fluctuations. We use the Heisenberg-Langevin formalism to account the various contributions. In this formalism, The *Heisenberg-Langevin equation* for a generic variable \hat{A} , evolving due to the \hat{H} and decay to its environment via \hat{L} , is defined as

$$\frac{d}{dt} \hat{A} = i[\hat{H}, \hat{A}] + (\hat{L}^\dagger/2 + \hat{F}^\dagger)[\hat{A}, \hat{L}] - [\hat{A}, \hat{L}^\dagger](\hat{L}/2 + \hat{F}). \quad (2.15)$$

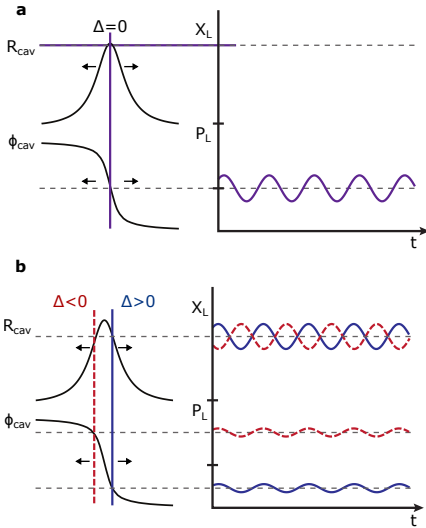


Figure 2.6: Optomechanical transduction of motion. (a) A resonant optical field gets modulated in phase due to the membrane motion. (b) A detuned optical field carries information about mechanical motion both in its amplitude and phase quadratures. Figure adapted from (Kohler, 2018).

Input-output relations

The first term on the right-hand side recalls the Schrödinger equation in the Heisenberg picture, in which the time evolution is incorporated in the operators. The other terms involve \hat{L} and \hat{F} and represent the stochastic evolution of the system interacting with the environment (?).

In the frequency domain and in the steady-state regime, the equations of motion, using the Hamiltonian (2.14), is¹

$$\begin{pmatrix} \kappa/2 - i\Omega & \Delta & 2g \sin \psi_{\text{in}} \\ -\Delta & \kappa/2 - i\Omega & -2g \cos \psi_{\text{in}} \\ -4g \cos \psi_{\text{in}} & -4g \sin \psi_{\text{in}} & \chi_{\text{M00}}^{-1} \end{pmatrix} \begin{pmatrix} \hat{X}_{\text{L,M}}^{\text{cav}} \\ \hat{p}_{\text{L,M}}^{\text{cav}} \\ \hat{X}_{\text{M}} \end{pmatrix} = \begin{pmatrix} \sqrt{\kappa_{\text{in}}} \hat{X}_{\text{L,M}}^{\text{in}} + \sqrt{\kappa_{\text{ex}}} \hat{X}_{\text{L,M}}^{\text{ex}} \\ \sqrt{\kappa_{\text{in}}} \hat{p}_{\text{L,M}}^{\text{in}} + \sqrt{\kappa_{\text{ex}}} \hat{p}_{\text{L,M}}^{\text{ex}} \\ \hat{F}_{\text{M}} \end{pmatrix}, \quad (2.16)$$

in which $\hat{X}_{\text{L,M}}^{\text{in}}$ ($\hat{X}_{\text{L,M}}^{\text{ex}}$) is the input quantum field leaking in via the port ‘in’ (‘ex’). The port ‘in’ corresponds to the main in/outcoupler, while mathematically port ‘ex’ corresponds to both the HR mirror and intra-cavity loss, which act in the same way since no light is present at the input of HR. The natural linewidth of the mechanical mode is γ_{M0} , and the mean occupation due to the thermal reservoir at temperature T is $n_{\text{M0}} = \hbar\omega_{\text{M0}}/k_{\text{B}}T$. The quantity $\chi_{\text{M00}}^{-1} \equiv (\omega_{\text{M0}}^2 - \Omega^2 - i\Omega\gamma_{\text{M0}})/\omega_{\text{M0}}$ is the natural mechanical susceptibility.

Given the optical and mechanical couplings, the system of equations presented in (2.16) is all we need to solve. There are multiple ways to tackle the problem, from a numerical (Nielsen, 2016; Møller et al., 2017) to analytical solutions. We present both in the coming pages.

We are interested both in the effect of the mechanical mode on the light variables and in the dynamics of the oscillator itself. By defining the matrices

$$\mathbf{A} = \begin{pmatrix} \kappa/2 - i\Omega & \Delta \\ -\Delta & \kappa/2 - i\Omega \end{pmatrix}, \quad \mathbf{O}_{\psi} = \begin{pmatrix} \cos \psi & -\sin \psi \\ \sin \psi & \cos \psi \end{pmatrix}, \quad (2.17)$$

$$\mathbf{B} = \begin{pmatrix} 0 \\ -2g \end{pmatrix}, \quad \mathbf{C} = (-4g \quad 0), \quad \hat{\mathbf{X}}_{\text{L,M}}^j = \begin{pmatrix} \hat{X}_{\text{L,M}}^j \\ \hat{p}_{\text{L,M}}^j \end{pmatrix}, \quad (2.18)$$

with the index $j \in \{\text{cav}, \text{in}, \text{ex}\}$ for optical fields, we write (2.16) in a more compact form, as system of matrix equations

$$\begin{pmatrix} \mathbf{O}_{\psi} & 0 \\ 0 & 1 \end{pmatrix} \begin{pmatrix} \mathbf{A} & \mathbf{B} \\ \mathbf{C} & \chi_{\text{M00}}^{-1} \end{pmatrix} \begin{pmatrix} \mathbf{O}_{\psi}^{\text{T}} & 0 \\ 0 & 1 \end{pmatrix} \begin{pmatrix} \hat{\mathbf{X}}_{\text{L,M}}^{\text{cav}} \\ \hat{\mathbf{X}}_{\text{M}} \end{pmatrix} = \begin{pmatrix} \sqrt{\kappa_{\text{in}}} \hat{\mathbf{X}}_{\text{L,M}}^{\text{in}} + \sqrt{\kappa_{\text{ex}}} \hat{\mathbf{X}}_{\text{L,M}}^{\text{ex}} \\ \hat{F}_{\text{M}} \end{pmatrix} \quad (2.19)$$

From here, we show two ways of solving the problem: the first being more suited for analytical expressions, and the second for numerical procedures.

The analytical method is useful for separating the effects of the drive terms on the intra-cavity field and mechanical degree of freedom; it will be particularly handy when dealing with the conditional entanglement procedure presented on Chapter 11. We start by multiplying the three square matrices on the left hand side of (2.19). Noting that the cavity response matrix \mathbf{A} is invariant under quadrature rotations, $\mathbf{O}_{\psi} \mathbf{A} \mathbf{O}_{\psi}^{\text{T}} = \mathbf{A}$, the intra-cavity field and the mechanical variable are found by simple substitution, such that

$$\hat{\mathbf{X}}_{\text{L,M}}^{\text{cav}} = \mathbf{A}^{-1} \left(\sqrt{\kappa_{\text{in}}} \hat{\mathbf{X}}_{\text{L,M}}^{\text{in}} + \sqrt{\kappa_{\text{ex}}} \hat{\mathbf{X}}_{\text{L,M}}^{\text{ex}} \right) - \mathbf{A}^{-1} \mathbf{O}_{\psi_{\text{in}}} \mathbf{B} \hat{\mathbf{X}}_{\text{M}}, \quad (2.20)$$

$$\hat{\mathbf{X}}_{\text{M}} = \chi_{\text{M}} \left[-\mathbf{C} \mathbf{A}^{-1} \mathbf{O}_{\psi_{\text{in}}}^{\text{T}} \left(\sqrt{\kappa_{\text{in}}} \hat{\mathbf{X}}_{\text{L,M}}^{\text{in}} + \sqrt{\kappa_{\text{ex}}} \hat{\mathbf{X}}_{\text{L,M}}^{\text{ex}} \right) + \hat{F}_{\text{M}} \right], \quad (2.21)$$

¹The dynamics of the membrane momentum are calculated from the relation $-i\Omega \hat{X}_{\text{M}} = \omega_{\text{M0}} \hat{p}_{\text{M}}$.

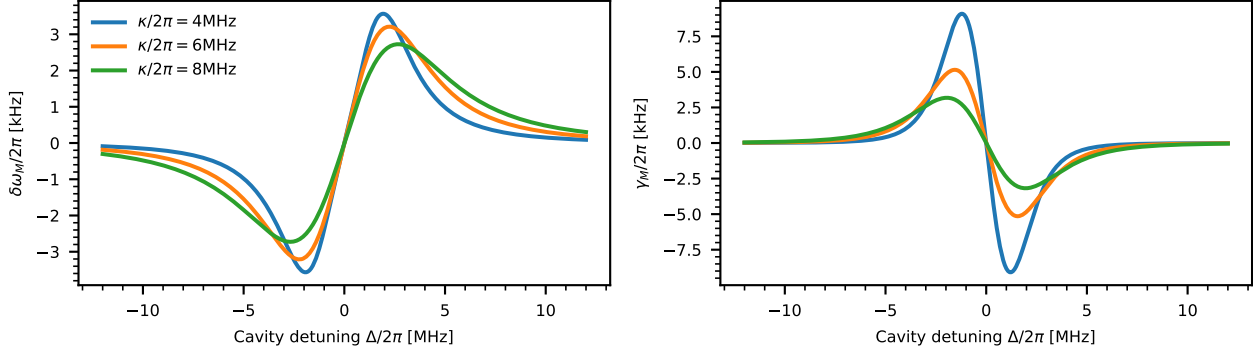


Figure 2.7: Optical modification of the mechanical susceptibility. The mechanical susceptibility is modified due to the presence of intracavity optical field: the observed mechanical resonance is going to be shifted (left) and broadened/narrowed (right). Curves are calculated for $\omega_M/2\pi = 1.4$ MHz and various κ . The coupling rate value $g/2\pi = 76$ kHz is set for $\Delta = 0$ and scaled according to the detuning dependence of the intracavity photon number.

for the input fluctuations and thermal bath. The quantity $\chi_M = (\chi_{M00}^{-1} - \mathbf{CA}^{-1}\mathbf{B})^{-1}$ is the *effective mechanical susceptibility* in the presence of optomechanical coupling. We can rewrite it as

$$\chi_M^{-1} = \chi_{M00}^{-1} - \mathbf{CA}^{-1}\mathbf{B} \quad (2.22)$$

$$= (\omega_M^2 + 2\Omega\delta\omega_M - \Omega^2 - i\Omega\gamma_M)/\omega_{M0} \quad (2.23)$$

where $\gamma_M = \gamma_{M0} + \delta\gamma_M$ and

$$\delta\omega_M(\Omega) = \frac{4g^2\omega_M}{\kappa\Omega} \left[\frac{(\Delta + \Omega)\kappa/2}{(\Delta + \Omega)^2 + (\kappa/2)^2} + \frac{(\Delta - \Omega)\kappa/2}{(\Delta - \Omega)^2 + (\kappa/2)^2} \right] \quad (2.24)$$

$$\delta\gamma_M(\Omega) = \frac{8g^2\omega_M}{\kappa\Omega} \left[\frac{(\kappa/2)^2}{(\Delta + \Omega)^2 + (\kappa/2)^2} - \frac{(\kappa/2)^2}{(\Delta - \Omega)^2 + (\kappa/2)^2} \right]. \quad (2.25)$$

In the limit we operate our optomechanical system, $g \ll \kappa$, the expressions above can be evaluated at the natural resonant frequency $\Omega = \omega_M$; in this limit, the effect of light is to shift and broaden/narrow the resonance, as can be seen in Figure 2.7. Due to the small, of order 1 mHz, natural linewidth γ_{M0} , the blue detuning ($\Delta > 0$) section of the figures cannot be accessed due to mechanically induced parametric instabilities (Kippenberg et al., 2005).

The equation (2.21) described how the mechanical mode is coupled to the external light and thermal forces. By substituting (2.21) in (2.20), we solve for the intra-cavity field

$$\hat{\mathbf{X}}_{L,M}^{\text{cav}} = \mathbf{A}^{-1} \left(\mathbf{1}_2 + \chi_M \mathbf{O}_{\psi_{\text{in}}} \mathbf{BCA}^{-1} \mathbf{O}_{\psi_{\text{in}}}^{\text{T}} \right) \left(\sqrt{\kappa_{\text{in}}} \hat{\mathbf{X}}_{L,M}^{\text{in}} + \sqrt{\kappa_{\text{ex}}} \hat{\mathbf{X}}_{L,M}^{\text{ex}} \right) - \chi_M \mathbf{A}^{-1} \mathbf{O}_{\psi_{\text{in}}} \mathbf{B} \hat{\mathbf{F}}_M. \quad (2.26)$$

The field that leaks out of the cavity must respect the cavity input-output relations

$$\begin{aligned} \hat{\mathbf{X}}_{L,M}^{\text{out}} &= \mathbf{O}_{\psi_{\text{in}} + \psi_{\text{out}}}^{\text{T}} \left\{ \hat{\mathbf{X}}_{L,M}^{\text{in}} - \sqrt{\kappa_{\text{in}}} \hat{\mathbf{X}}_{L,M}^{\text{cav}} \right\} \\ &= \mathbf{O}_{\psi_{\text{in}} + \psi_{\text{out}}}^{\text{T}} \left\{ \left(-\mathbf{1}_2 + \kappa_{\text{in}} \mathbf{A}^{-1} \left(\mathbf{1}_2 + \chi_M \mathbf{O}_{\psi_{\text{in}}} \mathbf{BCA}^{-1} \mathbf{O}_{\psi_{\text{in}}}^{\text{T}} \right) \right) \hat{\mathbf{X}}_{L,M}^{\text{in}} \right. \\ &\quad + \mathbf{A}^{-1} \left(\mathbf{1}_2 + \chi_M \mathbf{O}_{\psi_{\text{in}}} \mathbf{BCA}^{-1} \mathbf{O}_{\psi_{\text{in}}}^{\text{T}} \right) \sqrt{\kappa_{\text{in}} \kappa_{\text{ex}}} \hat{\mathbf{X}}_{L,M}^{\text{ex}} \\ &\quad \left. - \sqrt{\kappa_{\text{in}}} \chi_M \mathbf{A}^{-1} \mathbf{O}_{\psi_{\text{in}}} \mathbf{B} \hat{\mathbf{F}}_M \right\}. \end{aligned} \quad (2.27)$$

Input-output relations

This solution marks the end, for now, of the derivation involving the to-be-analytical solution. We will return to it in the end of this section.

The numerical approach was initially presented in this particular form in (Møller et al., 2017). As all square matrices on the left hand side are invertible, we can basically multiply both sides by the total inverse matrix, such that the system of equations (2.19) becomes

$$\begin{pmatrix} \hat{\mathbf{X}}_{L,M}^{\text{cav}} \\ \hat{\mathbf{X}}_M \end{pmatrix} = \begin{pmatrix} \mathbf{O}_{\psi} & 0 \\ 0 & 1 \end{pmatrix} \begin{pmatrix} \mathbf{A} & \mathbf{B} \\ \mathbf{C} & \chi_{M00}^{-1} \end{pmatrix}^{-1} \begin{pmatrix} \mathbf{O}_{\psi}^{\top} & 0 \\ 0 & 1 \end{pmatrix} \begin{pmatrix} \sqrt{\kappa_{\text{in}}} \hat{\mathbf{X}}_{L,M}^{\text{in}} + \sqrt{\kappa_{\text{ex}}} \hat{\mathbf{X}}_{L,M}^{\text{ex}} \\ \hat{f}_M \end{pmatrix}. \quad (2.28)$$

The non-trivial part of solution is calculating the inverse of the central block matrix. As the determinant of \mathbf{A} is non-zero, $\det \mathbf{A} = \Delta^2 + (\kappa/2 - i\Omega)^2 \neq 0$ for any $\{\Delta, \Omega\}$, \mathbf{A} is invertible. Therefore, we can use the Schur complements of a block matrix to write the inverse in two ways

$$\begin{pmatrix} \mathbf{A} & \mathbf{B} \\ \mathbf{C} & \chi_{M00}^{-1} \end{pmatrix}^{-1} = \begin{pmatrix} \mathbf{A}^{-1} + \mathbf{A}^{-1} \mathbf{B} \chi_{M00} \mathbf{C} \mathbf{A}^{-1} & -\mathbf{A}^{-1} \mathbf{B} \chi_{M00} \\ -\chi_{M00} \mathbf{C} \mathbf{A}^{-1} & \chi_{M00} \end{pmatrix} \quad (2.29)$$

$$= \begin{pmatrix} \mathbf{Y}^{-1} & -\mathbf{Y}^{-1} \mathbf{B} \chi_{M00} \\ -\chi_{M00} \mathbf{C} \mathbf{Y}^{-1} & \chi_{M00} + \chi_{M00} \mathbf{C} \mathbf{Y}^{-1} \mathbf{B} \chi_{M00} \end{pmatrix} \quad (2.30)$$

Notice how the solution (2.29) resembles the result from the analytical method, equation (2.26). With the relation (2.30), multiplying the matrices in (2.28), we get the intra-cavity field

$$\hat{\mathbf{X}}_{L,M}^{\text{cav}} = \mathbf{O}_{\psi_{\text{in}}} \mathbf{Y}^{-1} \mathbf{O}_{\psi_{\text{in}}}^{\top} \left(\sqrt{\kappa_{\text{in}}} \hat{\mathbf{X}}_{L,M}^{\text{in}} + \sqrt{\kappa_{\text{ex}}} \hat{\mathbf{X}}_{L,M}^{\text{ex}} \right) - \mathbf{O}_{\psi_{\text{in}}} \mathbf{Y}^{-1} \mathbf{B} \chi_{M00} \hat{f}_M, \quad (2.31)$$

where, in this formulation, $\mathbf{Y} = \mathbf{A} - \mathbf{B} \chi_{M00} \mathbf{C}$ is the effective cavity response matrix in the presence of optomechanical coupling. The last step is connecting the intra-cavity field to the outside world via the input-output relations

$$\begin{aligned} \hat{\mathbf{X}}_{L,M}^{\text{out}} &= \mathbf{O}_{\psi_{\text{out}}}^{\top} (\kappa_{\text{in}} \mathbf{Y}^{-1} - \mathbf{1}_2) \mathbf{O}_{\psi_{\text{in}}}^{\top} \hat{\mathbf{X}}_{L,M}^{\text{in}} \\ &+ \sqrt{\kappa_{\text{in}} \kappa_{\text{ex}}} \mathbf{O}_{\psi_{\text{out}}}^{\top} \mathbf{Y}^{-1} \mathbf{O}_{\psi_{\text{in}}}^{\top} \hat{\mathbf{X}}_{L,M}^{\text{ex}} \\ &- \sqrt{\kappa_{\text{in}}} \mathbf{O}_{\psi_{\text{out}}}^{\top} \mathbf{Y}^{-1} \mathbf{B} \chi_{M00} \hat{f}_M. \end{aligned} \quad (2.32)$$

The formulation presented above is our favourite for numerical implementations. In order to faithfully reproduce the elements of a real experiment, optical losses and finite detection effects must be included. We will discuss them in detail in Chapter 10, when we present the implementation of the hybrid experiment.

2.3.1 Simplified relations

We now return to the derivation of an analytical solution for the optomechanical input-output relations. The basis of this formulation follows from the equation (2.26). We would like to simplify the final result, which, due to the presence of many matrices, fails to convey what is really going on. The description presented here is also described in the Supplementary Information of Thomas et al. (2020). We will focus on the limit of a lossless cavity, $\kappa_{\text{ex}} = 0$, and weak optomechanical coupling ($g \ll \kappa$). Within these assumptions, a rather simple input-output relation will emerge.

We start by writing \mathbf{A} , the cavity response matrix, in terms of the complex Lorentzian sideband amplitude and phase, defined as

$$L(\Omega) = \frac{\kappa/2}{\kappa/2 - i(\Omega + \Delta)}. \quad (2.33)$$

As the matrix \mathbf{A} and its inverse appear many times throughout the derivations, $L(\Omega)$ will allow us to rewrite

$$\mathbf{A}^{-1} = \frac{1}{\kappa} \begin{pmatrix} L(\Omega) + L^*(-\Omega) & i(L(\Omega) - L^*(-\Omega)) \\ -i(L(\Omega) - L^*(-\Omega)) & L(\Omega) + L^*(-\Omega) \end{pmatrix}. \quad (2.34)$$

It is particularly useful to decouple the amplitude and phase of the complex Lorentzian sideband function; in the polar form, $L(\Omega) = |L(\Omega)|e^{i\Theta(\Omega)}$ and $L^*(-\Omega) = |L^*(-\Omega)|e^{-i\Theta(-\Omega)}$, with

$$|L(\Omega)| = \frac{\kappa/2}{\sqrt{(\kappa/2)^2 + (\Delta + \Omega)^2}} \quad (2.35)$$

$$|L^*(-\Omega)| = \frac{\kappa/2}{\sqrt{(\kappa/2)^2 + (\Delta - \Omega)^2}} = |L(-\Omega)| \quad (2.36)$$

$$\text{Arg}[L(\Omega)] = \arctan \frac{\Delta + \Omega}{\kappa/2} = \Theta(\Omega) \quad (2.37)$$

$$\text{Arg}[L^*(-\Omega)] = -\arctan \frac{\Delta - \Omega}{\kappa/2} = -\Theta(-\Omega) \quad (2.38)$$

With that, the decomposition is possible

$$\mathbf{A}^{-1} = \frac{|L(\Omega)| + |L(-\Omega)|}{\kappa} e^{i(\Theta(\Omega) - \Theta(-\Omega))/2} \mathbf{O}_{(\Theta(\Omega) + \Theta(-\Omega))/2} \times \left[\mathbf{1}_2 + i \frac{|L(\Omega)| - |L(-\Omega)|}{|L(\Omega)| + |L(-\Omega)|} \mathbf{O}_{-\pi/2} \right]. \quad (2.39)$$

We proceed assuming that the dependence of $L(\Omega)$ on the Fourier frequency Ω is negligible over the bandwidth of interest and that $L(\pm\Omega) \sim L(\pm\omega_M)$ and $\Theta(\pm\Omega) \sim \Theta(\pm\omega_M)$. This approximation is not needed to perform the calculation per se, but within this limit, the interpretation of the optomechanical broadening and frequency shift will become clear. In equation (2.21), we have

$$-\mathbf{C}\mathbf{A}^{-1}\mathbf{O}_{\psi_{\text{in}}}^{\text{T}} \left(\sqrt{\kappa_{\text{in}}}\hat{\mathbf{X}}_{L,M}^{\text{in}} + \sqrt{\kappa_{\text{ex}}}\hat{\mathbf{X}}_{L,M}^{\text{ex}} \right) \sim 2\sqrt{\Gamma_M} \begin{pmatrix} 1 \\ i\zeta_M \end{pmatrix}^{\text{T}} \left(\sqrt{\kappa_{\text{in}}/\kappa}\hat{\mathbf{X}}_{L,M}^{\text{in}'} + \sqrt{\kappa_{\text{ex}}/\kappa}\hat{\mathbf{X}}_{L,M}^{\text{ex}'} \right), \quad (2.40)$$

in which the input/extra field has been redefined to include the phase the cavity induced phases as

$$\mathbf{X}_{L,M}^{\text{in(ex)'}} = e^{i[\Theta(\omega_m) - \Theta(-\omega_m)]/2} \mathbf{O}_{[\Theta(\omega_m) + \Theta(-\omega_m)]/2} \mathbf{O}_{\psi_{\text{in}}}^{\text{T}} \mathbf{X}_{L,M}^{\text{in(ex)}}. \quad (2.41)$$

Notably, we have also introduced the *mechanical readout rate* and *sideband asymmetry parameter* as

$$\Gamma_M \equiv \frac{4g^2}{\kappa} (|L(\omega_M)| + |L(-\omega_M)|)^2 \quad (2.42a)$$

$$\zeta_M \equiv \frac{|L(\omega_M)| - |L(-\omega_M)|}{|L(\omega_M)| + |L(-\omega_M)|}, \quad (2.42b)$$

respectively. With these two parameters, we have created a common language with the spin oscillator description, to be discussed in Chapter 3. The readout rate Γ_M is related to the effect of the perturbation the light field produces on the mechanical system, which is by itself linked to the extraction of information about the mechanical degree of freedom. The asymmetry parameter ζ_M is related to the sideband imbalance induced by the possibly detuned optical

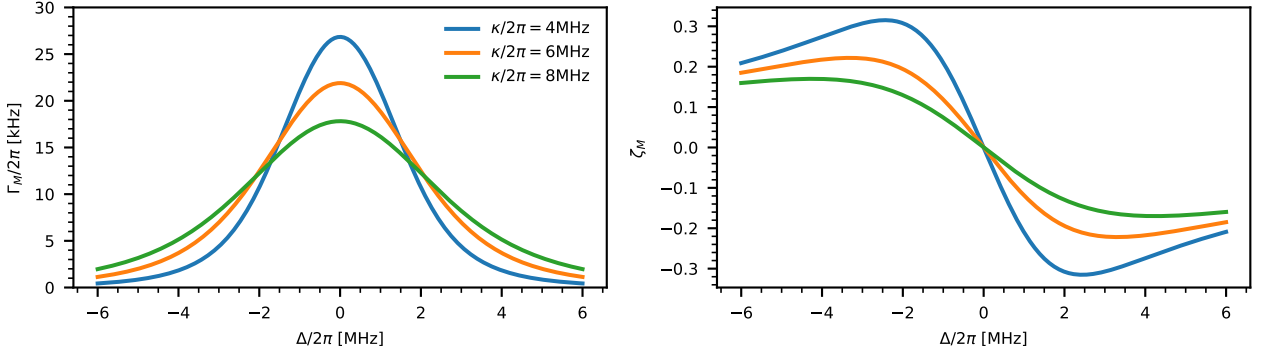


Figure 2.8: Optomechanical readout rate and sideband asymmetry parameter. Detuning dependence of the readout rate and sideband asymmetry as defined by equation (2.42). We have set $\omega_M/2\pi = 1.4$ MHz and varied κ . The coupling rate value $g/2\pi = 76$ kHz is set for $\Delta = 0$ and scaled according to the detuning dependence of the intracavity photon number.

drive. The dependence of the parameters on the cavity detuning Δ can be seen in Figure 2.8. In the limit of $\omega_M \ll \kappa$, the parameters reduce to

$$\Gamma_M \sim \frac{4g^2}{\kappa} \frac{(\kappa/2)^2}{(\kappa/2)^2 + \Delta^2} \quad (2.43)$$

$$\zeta_M \sim -\frac{\Delta\omega_M}{\Delta^2 + (\kappa/2)^2}, \quad (2.44)$$

limit which is not perfectly valid for the parameter regime in our latest experiment ($\omega_M/\kappa \sim 0.3$), it serves a good initial guess for gauging the experimental expectations. As it will become more clear by the end of this chapter, the parameter ζ_M , being sensitive to the sideband amplitudes at ω_M , represents the conversion between optical phase and amplitude, and vice-versa.

As a last step, we set the cavity overcoupling to unity, by choosing $\kappa_{\text{in}} = \kappa$ (and hence $\kappa_{\text{ex}} = 0$). The mechanical degree of freedom

$$\hat{X}_M \sim \chi_M \left[2\sqrt{\Gamma_M} \begin{pmatrix} 1 \\ i\zeta_M \end{pmatrix}^\top \hat{X}_{L,M}^{\text{in}} + \hat{F}_M \right] \quad (2.45)$$

The field outside the cavity, following the input-output relations

$$\hat{X}_{L,M}^{\text{out}} = \mathbf{O}_{\psi_{\text{in}}+\psi_{\text{out}}}^\top \left(\hat{X}_{L,M}^{\text{in}} - \sqrt{\kappa_{\text{in}}} \hat{X}_{L,M}^{\text{cav}} \right), \quad (2.46)$$

becomes

$$\mathbf{O}_{\psi_{\text{in}}+\psi_{\text{out}}} \hat{X}_{L,M}^{\text{out}} = (\mathbf{1}_2 - \kappa \mathbf{A}^{-1}) \hat{X}_{L,M}^{\text{in}} + \sqrt{\kappa} \mathbf{A}^{-1} \mathbf{O}_{\psi_{\text{in}}} \mathbf{B} \hat{X}_M \quad (2.47)$$

$$\mathbf{X}_{L,M}^{\text{out}} = \mathbf{X}_{L,M}^{\text{in}} + \sqrt{\Gamma_M} \begin{pmatrix} i\zeta_M \\ 1 \end{pmatrix} \hat{X}_M, \quad (2.48)$$

in which we have used (2.20) and

$$-\mathbf{1}_2 + \kappa \mathbf{A}^{-1} = e^{i[\Theta(\omega_m) - \Theta(-\omega_m)]} \mathbf{O}_{\Theta(\omega_m) + \Theta(-\omega_m)} \quad (2.49)$$

$$\mathbf{X}_{L,M}^{\text{out}} = e^{-i[\Theta(\omega_m) - \Theta(-\omega_m)]/2} \mathbf{O}_{[\Theta(\omega_m) + \Theta(-\omega_m)]/2}^\top \mathbf{O}_{\psi_{\text{out}}} \mathbf{X}_{L,M}^{\text{out}}. \quad (2.50)$$

The equation (2.48) shows that the information about the mechanical oscillator is not only written in the phase quadrature of light, but also in the amplitude quadrature via the asymmetry parameter ζ_M . Moreover, the choice of phases

indicated by the primed optical variables highlights that the relation is only valid for a particular configuration of parameters.

With the simplified input-output relations, we conclude this chapter. Further details on the optomechanical implementation can be found in Chapter 4 and in the Part IV of the manuscript.

Chapter 3

Room temperature spin oscillator

Following the optomechanical system, we present some of the basic concepts of preparing a cesium atomic ensemble as a spin oscillator. We present the implementation of the oscillator and the concept of effective mass. From there, we discuss its time evolution due to coupling with light and its environment. We finish with the input-output relations for spin-light interaction, presenting the spectrum of the light carrying information about the spin system and its relation with the quantum cooperativity parameter.

3.1 The cesium atom and magnetic fields

In the atomic physics part of our experiment, we use cesium. More specifically, cesium-133, the only stable isotope of this species. Due to a relatively simple level structure, wide availability of laser sources and high room temperature vapor density, this neutral atom is a rather common¹ choice in room-temperature-based atomic physics experiments. Other alkali, as potassium (K) and rubidium (Rb), are also popular choices.

We briefly comment now on the electronic level structure of cesium. For a more detailed discussion on cesium and other alkali, we refer to Seltzer (2008) and Steck (2019). The electronic transitions we deal with are components of the fine structure doublet, see Figure 3.1. In spectroscopic notation, the transitions are $6^2S_{1/2} \rightarrow 6^2P_{1/2}$ (D_1 line) and $6^2S_{1/2} \rightarrow 6^2P_{3/2}$ (D_2 line). This doublet is further split by hyperfine interaction, giving rise to the levels $F = 3, 4$ in the ground state, and $F' = 3, 4$ and $F' = 2, 3, 4, 5$ in the D_1 and D_2 excited states, respectively.

At room temperature, where the atoms are almost exclusively in the ground state manifold $6^2S_{1/2}$, we are particularly interested in how the atoms interact with external magnetic fields. The nucleus, the electronic spin, and the orbital angular momentum have their own magnetic moment μ contributing to the total magnetic moment of the atom. The moments interact with each other via the fine and hyperfine coupling. For the ground state manifold, if the energy shift due to the magnetic field \mathbf{B} is small compared to the hyperfine splitting, the good quantum numbers are the total angular momentum F and its projection on the quantization axis m_F . The energy² E_{Fm} of a given level is described by the *Breit-Rabi formula* (Steck, 2019)

$$E_{Fm} = -\frac{h\nu_{\text{hfs}}}{2(2I+1)} + g_I\mu_B mB \pm \frac{h\nu_{\text{hfs}}}{2} \sqrt{1 + \frac{4m}{2I+1}x + x^2}. \quad (3.1)$$

in which \pm is used for $F = I \pm 1/2$, $B = |\mathbf{B}|$ is the magnetic field magnitude, ν_{hfs} is the hyperfine splitting, and $\mu_B = h \cdot 1.4 \text{ MHz G}^{-1}$ is the Bohr Magneton. The parameter x describes the strength of the Zeeman effect in respect to the

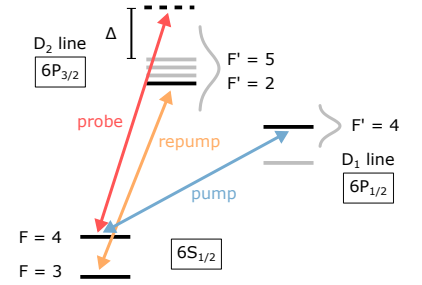


Figure 3.1: Optical pumping and laser configuration. Optical pumping lasers, pump and repump, are frequency stabilized to certain transitions in the D_1 and D_2 lines, respectively. The probe laser is stabilized off resonant with respect to the electronic transition, with detuning Δ from the $F = 4 \rightarrow F' = 5$ transition. See text for details.

¹Note that since 1967 the definition of the second is based in a cesium microwave transition. More precisely, (Newell and Tiesinga, 2019) “the unperturbed ground state hyperfine transition frequency of the cesium-133 atom $\Delta\nu_{\text{hfs}} = 9\,192\,631\,770 \text{ Hz}$ ”. The widespread availability of optical and electronic control resources for time keeping purposes is certainly a contributor for the popularity of cesium in atomic physics experiments.

²A more consistent notation for the projection of total spin on the quantization axis would be m_F . As the total angular momentum is the focus of study we drop the subscript, for brevity.

hyperfine splitting, defined as

$$x = \frac{(g_J - g_I)\mu_B B}{h\nu_{\text{hfs}}}. \quad (3.2)$$

Here, $g_J \sim 2$ and $g_I \sim -4 \times 10^{-4}$ are the spin-orbit and nuclear g-factors, respectively; we refer to (Steck, 2019) for exact values. For our experiments, we rarely go above $B \sim 10$ G (or 1 mT), leaving $x \sim 10^{-3}$.

Expanding equation (3.1) around $x = 0$ gives us the energy values in the limit of small perturbation by the magnetic field. Given the typical resolution of the energy levels in the experiments, we consider the effects up to second order³. The Zeeman level energies in the $F = 4$ hyperfine manifold follow (Julsgaard et al., 2003)

$$E_m = \hbar\omega_S m + \hbar\omega_{\text{qzs}} m^2, \quad (3.3)$$

where the Larmor frequency ω_S and quadratic Zeeman splitting ω_{qzs} are defined as

$$\frac{\omega_S}{2\pi} = \nu_S = \frac{g_F \mu_B B}{h} \quad (3.4)$$

$$\frac{\omega_{\text{qzs}}}{2\pi} = \nu_{\text{qzs}} = \frac{2\nu_S^2}{\nu_{\text{hfs}}}. \quad (3.5)$$

The frequencies above are first and second order contribution to the Zeeman energy levels due to the presence of an external magnetic field. The hyperfine Landé g-factor is

$$g_F = g_J \frac{F(F+1) - I(I+1) + J(J+1)}{2F(F+1)} + g_I \frac{F(F+1) + I(I+1) - J(J+1)}{2F(F+1)} \\ = \begin{cases} 0.250390 & \text{for } F = 4 \\ -0.251194 & \text{for } F = 3 \end{cases} \quad (3.6)$$

The Larmor frequency scales as approximately 350 kHz G^{-1} , being of order 1 MHz throughout the most experiments described here. Due to the sign in g_F , the two hyperfine levels shift oppositely with the external magnetic field. The $F = 3$ manifold energies scale 0.3% faster with the applied magnetic field.

In our experiments, the laser light will induce transitions between ground state Zeeman levels. The most common transitions are those fulfilling $\Delta m = m' - m = \pm 1$, where energy goes as

$$\frac{E_{m'} - E_m}{\hbar} = \omega_S + \omega_{\text{qzs}} m. \quad (3.7)$$

Therefore, we will be inducing magnetic excitations when driving the system satisfying the resonant condition $\omega_{\text{rf}} \sim \omega_S$. On the other hand, in the limit the quadratic Zeeman splitting is much larger than the transition linewidth, $\omega_{\text{qzs}} \gg \gamma_S$, the ground state response will be split in $2F$ resonances. This split is particularly important for characterizing the spin state in Chapter 5.

As we start talking about transitions within the ground state manifold, it is useful to write the energies in the Hamiltonian description. In particular, the Zeeman shifts induced by the external magnetic field given in equation (3.3), are equivalently given by the Hamiltonian

$$\hat{H}_B = \hbar \sum_m \left[\omega_S m |m\rangle \langle m| + \omega_{\text{qzs}} m^2 |m\rangle \langle m| \right] \quad (3.8)$$

in which $|m\rangle$ is the ket state associated with the m -th Zeeman level⁴.

³The selectivity of energy levels is set by its linewidth. Typical linewidths values are on the order of 10 Hz to 100 Hz. The 3rd order term is $\nu_L^3/\nu_{\text{hfs}}^2 \sim 10$ mHz, much smaller than the transition linewidth.

⁴Here we consider only one ground state manifold. In the experiments, optical pumping will transfer all atoms to a single manifold.

The cesium atom and magnetic fields

The Hamiltonian written as above motivates us to map, or rotate, the Zeeman level basis into an angular momentum description. A complete angular momentum basis for a collection of N spin- F atoms is

$$\begin{aligned}
\hat{F}_x &\equiv \sum_N \hat{f}_x^{(i)} = \sum_N \sum_m m A_{mm}^{(i)} \\
\hat{F}_y &\equiv \sum_N \hat{f}_y^{(i)} = \frac{1}{2} \sum_N \sum_m c(F, m) \left(A_{m+1, m}^{(i)} + A_{m, m+1}^{(i)} \right) \\
\hat{F}_z &\equiv \sum_N \hat{f}_z^{(i)} = \frac{1}{2i} \sum_N \sum_m c(F, m) \left(A_{m+1, m}^{(i)} - A_{m, m+1}^{(i)} \right) \\
\hat{F}_0 &\equiv \sum_N \hat{f}_0^{(i)} = \sum_N \sum_m A_{mm}^{(i)}.
\end{aligned} \tag{3.9}$$

The (capitalized) \hat{F} spin operators are related the total ensemble spin. Strictly speaking, the total interaction energy must be the weighted sum/integral over all atoms in the ensemble given an interaction strength⁵, although for the case of homogeneously coupled atoms the discrete summation agrees with the continuous model. Including the continuous description of the spin variables was done in Julsgaard (2003). From here on, we will drop the atom number index.

The set of angular momentum operators from equation (3.9) is itself spanned from the action of \hat{F}_x and \hat{F}_\pm , the spin projection in the quantization axis and the ladder operators, respectively⁶. Note that we follow the *QUANTOP school of non-trivial quantization axis*, in which the energies are quantized along the x -axis. The coefficients $c(F, m) = \sqrt{F(F+1) - m(m+1)}$ and the atomic operators $\hat{A}_{a,b}^{(i)} \equiv |a\rangle\langle b|^{(i)} = |F, a\rangle\langle F, b|^{(i)}$ define the relative weights of the atomic coherences in the angular momentum operator description. The definitions fulfill the standard commutation relations $[\hat{F}_i, \hat{F}_j] = i\epsilon_{ijk}\hat{F}_k$, with ϵ_{xyz} as the Levi-Civita symbol. The anticommutation rules are $\{\hat{F}_x, \hat{F}_y\} = 2\delta_{xy}1_2$, with 1_2 as the identity matrix.

Within the angular momentum basis, the energy of the ground state level due to the external field B_{DC} given in equation (3.8), disregarding the quadratic component⁷, is written as

$$\hat{H}_B = \hbar\omega_S \hat{F}_x, \tag{3.10}$$

resembling the magnetic dipole interaction, $\propto \mathbf{B} \cdot \mathbf{F}$, for a static field in the x -axis direction.

In the hybrid experiments, we will work in the limit of a constant and high spin polarization, that is, in the limit in which the ensemble magnetization is large $F_x \sim |\langle \hat{F}_x \rangle|$, valid for an ensemble polarized close to $|F = 4, m_F = \pm 4\rangle$. For that, we can make use of the *Holstein-Primakoff transformation* to map the spin variables, $\hat{F}_\pm = \hat{F}_y \pm i\hat{F}_z$, to bosonic creation and annihilation operators \hat{b} and \hat{b}^\dagger , respectively, satisfying $[\hat{b}, \hat{b}^\dagger] = 1$. We follow the approach described in Hammerer (2006). According to the transformation, the spin component \hat{F}_x can be written as

$$\hat{F}_x = F_x - \frac{\hat{b}^\dagger \hat{b}}{2}. \tag{3.11}$$

In the low excitation limit $\langle \hat{b}^\dagger \hat{b} \rangle \ll F_x$, the ladder operators are given by $\hat{F}_+ \sim \sqrt{F_x} \hat{b}$ and $\hat{F}_- \sim \sqrt{F_x} \hat{b}^\dagger$. In this limit, the number of bosonic excitations in the system is given by

$$\hat{b}^\dagger \hat{b} = \frac{\hat{F}_- \hat{F}_+}{F_x} \sim \frac{\hat{F}_y^2 + \hat{F}_z^2}{F_x}, \tag{3.12}$$

⁵Here, we assume the atoms to interact homogeneously with light. See Chapter 7 for the inclusion of inhomogeneous coupling.

⁶See Appendix A for further details

⁷Including the quadratic magnetic field contribution is more naturally written as

$$\hat{H}_B = \hbar\omega_S \hat{F}_x + \hbar\omega_{qzs} (\hat{J}_m + F(F+1)1_F)/3,$$

with $\hat{J}_m = 2\hat{F}_z^2 - \hat{F}_x^2 - \hat{F}_y^2$, as the effective quadrupole moment (Colangelo et al., 2013).

allowing us to finally write equation (3.10) as

$$\hat{H}_B/\hbar = \omega_S \hat{F}_x \sim \omega_S F_x - \frac{\omega_S}{2} (\hat{X}_S^2 + \hat{P}_S^2). \quad (3.13)$$

We have redefined the spin variables as $\hat{X}_S = \hat{F}_z/\sqrt{\hbar F_x}$ and $\hat{P}_S = \pm \hat{F}_y/\sqrt{\hbar F_x}$, with respect to F_x , the steady-state spin polarization, and $[\hat{X}_S, \hat{P}_S] = i$. The \pm refers to a positive (+) and negative (-) mass spin scenario. The operators $\{\hat{X}_S, \hat{P}_S\}$ are the effective spin variables, describing the spin oscillator dynamics. The term proportional the mean ensemble spin polarization F_x contributes only as an offset to the dynamics and will be disregarded from here on.

To grant the Holstein-Primakoff approximation and map the dynamics of the cesium spin ensemble to a harmonic oscillator, the atoms must be optically pumped such that $\langle \hat{b}^\dagger \hat{b} \rangle / |F_x| \ll 1$. The pumping can be set in a way that the atoms are transferred to a Zeeman level with maximal value of angular momentum, here the $|0\rangle = |F=4, m_F=4\rangle$ state, a situation sketched in Figure 3.2 (a). In this configuration, the static magnetic field and the macroscopic spin are aligned, and the ground state has the maximum Zeeman energy. Exciting the system, that is, transferring energy to it, will lead to a decrease in total energy of the system. This is the case described by equation (3.13), the case of an effective negative mass oscillator.

On the other hand, one could have chosen to pump the atoms towards the other extreme Zeeman level, or even invert the direction of the static magnetic field, as depicted in Figure 3.2 (b). In this case, the final state would have been $|F=4, m_F=-4\rangle$ and exciting the system would have increased the total magnetic energy. In this case, a positive mass oscillator with Hamiltonian

$$\hat{H}_B/\hbar = \frac{\omega_S}{2} (\hat{X}_S^2 + \hat{P}_S^2), \quad (3.14)$$

would have been created.

3.2 Interaction with light

Within a single atom, the light fields \mathbf{E} couple to the atomic dipole moment \mathbf{d} , via the electric dipole coupling

$$\hat{H}_{\text{int}} = \mathbf{d} \cdot \mathbf{E}. \quad (3.15)$$

The cesium atom, shown in Figure 3.1, has 16 magnetic sub-levels in its ground state manifolds ($F=3$ and $F=4$) and, considering the D_2 line, 27 more in the excited states. Electric dipole interaction couples the ground states to the excited states via exchange of photons. For dealing with such complex energy level structures, effective formalisms are particularly powerful. Especially, as we work in a regime in which atoms spend most of their time in the ground states and in a time scale much longer than the decay time of the excited states, we can adiabatically eliminate the excited states, as described in Julsgaard (2003), leading to an Hamiltonian that contains only the ground state levels. We will deal with this approach in Section 3.3.

For now, we take an alternative route, using the approach developed by Reiter and Sørensen (2012). By driving the atomic subsystem in subspaces according to their effects and related time scales, the authors develop a self-consistent procedure for eliminating the excited state manifolds of weakly driven arbitrary level structures via adiabatic elimination, including the effects of decoherence and decay induced by light. The description is valid in the limit of a weakly coupled system to a Markovian reservoir. We will consider an ensemble of atoms with level structure seen in Figure 3.3. We abstract this atomic system to have a single ground state manifold and an excited state manifold, each with total angular momentum $F = \frac{1}{2}$.

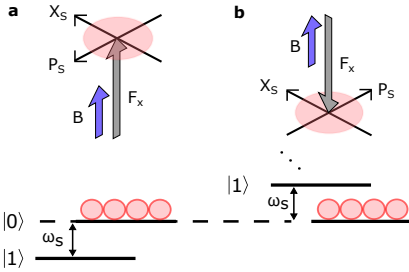


Figure 3.2: Spin oscillators. The relative direction of the magnetic field \mathbf{B} with respect to the macroscopic spin \mathbf{F} defines the sign of the spin oscillator's effective mass. Here we use the x coordinate as quantization axis. If both spin and magnetic field are aligned **a**, a negative mass oscillator is prepared and the ground state $|0\rangle$ has bigger energy than the first excited state $|1\rangle$. On the other hand, if both are anti-aligned **b**, a positive mass oscillator is prepared. Note that the spin mass also sets the energy levels ladder and spin variables \hat{X}_S and \hat{P}_S .

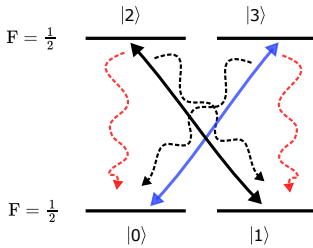


Figure 3.3: Simplified level structure. The ground state, composed of the states $|0\rangle$ and $|1\rangle$ is coupled by a single laser (solid lines) to the excited state manifold, spanned by $|2\rangle$ and $|3\rangle$. Dashed lines show the spontaneous decay channels. Color coding for Clebsch-Gordan coefficients: black for $\sqrt{2/3}$, red for $\sqrt{1/3}$ and blue for $-\sqrt{2/3}$.

Interaction with light

The four level system is written in the angular momentum basis $|F, m_F\rangle$, here compactly written as $\{|0\rangle, |1\rangle, |2\rangle, |3\rangle\}$ ⁸. A quantized electric field described by the operators \hat{a}_R, \hat{a}_L of a traveling laser beam with frequency ω_L and transverse mode are A_B (Julsgaard, 2003), is

$$\mathbf{E} = E_0(\hat{a}_R \mathbf{e}_R + \hat{a}_L \mathbf{e}_L + \text{h.c.}). \quad (3.16)$$

The laser's electric field couples the ground to the excited states via electric dipole interaction, given in equation (3.15), with $\mathbf{e}_R, \mathbf{e}_L$ as the polarization unit vectors and h.c. as the Hermitian conjugate. The proportionality constant $E_0 = \sqrt{\omega_L \hbar / 2\epsilon_0 A}$ is the single photon coupling rate per atom. For a laser beam traveling along the z quantization axis, circularly polarized light couples the ground and excited state manifolds via $\Delta m \equiv m' - m = \pm 1$ transitions. Once in the excited state, the atoms return to the ground state by spontaneously emitting a photon.

The total energy of the atom-light system is a combination of the atomic, optical and interaction terms. In the rotating wave approximation and in the laser frequency rotating frame (Sherson, 2006), is

$$\begin{aligned} \hat{H} &= \hat{H}_{\text{atoms}} + \hat{H}_{\text{int}} \quad (3.17) \\ \hat{H}_{\text{atoms}} &= \hbar\Delta(\hat{A}_{22} + \hat{A}_{33}) \\ \hat{H}_{\text{int}} &= \hbar g_0(-\hat{a}_R \hat{A}_{30} + \hat{a}_L \hat{A}_{21} + \text{h.c.}), \end{aligned}$$

with $\Delta = \omega_0 - \omega_L$ as the detuning from the atomic resonance, $\hat{A}_{ij} = |i\rangle\langle j|$ as a general operator in the atomic basis, and $g_0 = E_0 d_{ge} / \hbar$. The atomic basis follows $\hat{A}_{ab} \hat{A}_{cd} = \hat{A}_{ad} \delta_{bc}$ and $[\hat{A}_{ab}, \hat{A}_{cd}] = \hat{A}_{ad} \delta_{bc} - \hat{A}_{ad} \delta_{da}$. The magnitude of the atomic dipole moment d_{ge} includes the Clebsch-Gordan coefficients. The interaction Hamiltonian \hat{H}_{int} is derived from equation (3.15).

Following Reiter and Sørensen (2012), we divide the Hamiltonian (3.17) according to the atomic subspaces. The ground state and excited state levels evolve according to \hat{H}_g and \hat{H}_e . The interaction \hat{H}_{int} mixes the two subspaces, in principle independent from each other, via \hat{V}_+ and \hat{V}_- . Namely

$$\hat{H}_g = 0 \quad (3.18a)$$

$$\hat{H}_e = \hbar\Delta(\hat{A}_{22} + \hat{A}_{33}) \quad (3.18b)$$

$$\hat{V}_+ = \hbar g_0(-\hat{a}_R \hat{A}_{30} + \hat{a}_L \hat{A}_{21}) \quad (3.18c)$$

$$\hat{V}_- = (\hat{V}_+)^\dagger, \quad (3.18d)$$

Couplings among the ground state levels can be added directly to \hat{H}_g . Once in the excited state, the atoms decay spontaneously following the four possible decay paths

$$\hat{L}_{03} = \sqrt{2\gamma_e/3} \hat{A}_{03} \quad (3.19a)$$

$$\hat{L}_{02} = \sqrt{\gamma_e/3} \hat{A}_{02} \quad (3.19b)$$

$$\hat{L}_{13} = \sqrt{\gamma_e/3} \hat{A}_{13} \quad (3.19c)$$

$$\hat{L}_{12} = \sqrt{2\gamma_e/3} \hat{A}_{12}, \quad (3.19d)$$

where γ_e is the excited state decay rate. The \hat{L} operators are the jump operators associated with a given reservoir coupling.

Having introduced the systems and interactions we proceed to apply the effective formalism. According to Reiter and Sørensen (2012), the dynamics of

⁸The full spelling of the basis is

$|0\rangle \equiv |F = 1/2, m_F = -1/2\rangle$
 $|1\rangle \equiv |F = 1/2, m_F = +1/2\rangle$
 $|2\rangle \equiv |F' = 1/2, m_{F'} = -1/2\rangle$
 $|3\rangle \equiv |F' = 1/2, m_{F'} = +1/2\rangle.$

a system operator \hat{A} is given by the *Heisenberg-Langevin equation* of the form⁹

$$\begin{aligned} \frac{d}{dt} \hat{A} = & i[\hat{H}_{\text{eff}}, \hat{A}] + \sum_k \left[\hat{L}_{k,\text{eff}}^\dagger \hat{A} \hat{L}_{k,\text{eff}} - \frac{1}{2} \{ \hat{L}_{k,\text{eff}}^\dagger \hat{L}_{k,\text{eff}}, \hat{A} \} \right] \\ & + \sum_k \left[\hat{F}^\dagger [\hat{A}, \hat{L}_{k,\text{eff}}] - [\hat{A}, \hat{L}_{k,\text{eff}}^\dagger] \hat{F} \right], \end{aligned} \quad (3.20)$$

where the effective Hamiltonian and decay processes parametrized are the operators $\hat{L}_{k,\text{eff}}$ and \hat{H}_{eff} , respectively. Being an equation of the Langevin type, the decay processes have the respective Langevin noise forces \hat{F} . The effective Hamiltonian and decays are given by

$$\hat{H}_{\text{eff}} = -\frac{1}{2} \hat{V}_- \left(\hat{H}_{\text{NH}}^{-1} + \hat{H}_{\text{NH}}^{-1,\dagger} \right) \hat{V}_+ + \hat{H}_g \quad (3.21a)$$

$$\hat{L}_{k,\text{eff}} = \hat{L}_k \hat{H}_{\text{NH}}^{-1} \hat{V}_+ \quad (3.21b)$$

$$\hat{H}_{\text{NH}} = \hat{H}_e - \frac{i}{2} \sum_k \hat{L}_k^\dagger \hat{L}_k, \quad (3.21c)$$

see Appendix C for further details. Inserting the quantities defined in equations (3.18) and (3.19), the effective interaction Hamiltonian becomes

$$\hat{H}_{\text{eff}} = \frac{\hbar g_0^2 \Delta}{\Delta^2 + (\gamma_e/2)^2} \left(\hat{a}_R^\dagger \hat{a}_R \hat{A}_{00} + \hat{a}_L^\dagger \hat{a}_L \hat{A}_{11} \right). \quad (3.22)$$

In this picture, we see that the interaction is due to *ac Stark shifts*, that is, the state $|0\rangle$ ($|1\rangle$) is shifted in energy according to the number of photons $\hat{n}_R = \hat{a}_R^\dagger \hat{a}_R$ ($\hat{n}_L = \hat{a}_L^\dagger \hat{a}_L$).

For understanding the interaction presented in equation (3.22), we introduce relevant polarization degrees of freedom. Polarized light plays an important role in the interaction, as it is the source of the Stark shifts presented above. The *Stokes operators*, given as

$$\begin{aligned} \hat{S}_x &= \frac{\hat{n}_x - \hat{n}_y}{2} \\ \hat{S}_y &= \frac{\hat{n}_{+45^\circ} - \hat{n}_{-45^\circ}}{2} \\ \hat{S}_z &= \frac{\hat{n}_R - \hat{n}_L}{2}, \end{aligned} \quad (3.23)$$

where $\hat{n}_i = \hat{a}_i^\dagger \hat{a}_i$ is the number operator, characterize the polarization of light. The indices $x, y, \pm 45^\circ$, and R, L , describe the photons in linear, diagonal and circular basis. The fourth and last operator is $\hat{S}_0 = (\hat{n}_R + \hat{n}_L)/2$, giving information about the total amount of photons in the circular basis, for example. The Stokes operators relate to each other via $[\hat{S}_x, \hat{S}_y] = i\epsilon_{xyz} \hat{S}_z$, with ϵ_{xyz} as the Levi-Civita symbol. The operators can be related to each other via basis transformations, as shown in Section A.3.

The ac Stark shift interaction (3.22) is also equivalent to the Faraday paramagnetic rotation Hamiltonian (Hammerer et al., 2010). Writing the atomic degrees of freedom in the angular momentum basis and the light operators in terms of Stokes operators¹⁰ from equation (3.22), we get to

$$\hat{H}_{\text{eff}} = \hbar g (\hat{F}_0 \hat{S}_0 - \hat{F}_z \hat{S}_z), \quad (3.25)$$

as previously shown by Sherson (2006), with $g = 2g_0^2 \Delta / (\Delta^2 + (\gamma_e/2)^2)$. The term $\hat{F}_z \hat{S}_z$ represents the mutual rotation of polarization of light and atomic spins. The other term, proportional to $\hat{F}_0 \hat{S}_0$, is an overall energy shift added

⁹To be more precise, in Reiter and Sørensen (2012) the authors give an effective master equation for the system density operator ρ . Here, it has been phrased in terms of the analogous operator equation following $\langle \hat{A} \rangle = \text{Tr}[\rho \hat{A}]$.

¹⁰The angular momentum operators for spin-1/2 in the z-quantization basis are defined as

$$\begin{aligned} \hat{F}_x &= \frac{\hat{A}_{10} + \hat{A}_{01}}{2} \\ \hat{F}_y &= \frac{i(\hat{A}_{10} - \hat{A}_{01})}{2} \\ \hat{F}_z &= \frac{\hat{A}_{00} - \hat{A}_{11}}{2} \\ \hat{F}_0 &= \frac{\hat{A}_{00} + \hat{A}_{11}}{2} = \frac{1_z}{2}. \end{aligned} \quad (3.24)$$

Interaction with light

to the system, not influencing the internal degrees of freedom or altering the polarization of the light. It will be disregarded in most cases in this thesis.

The ac Stark shift Hamiltonian (3.22) is therefore equivalent to the Faraday interaction (3.25). In general, the larger the excursions of the spin component from its equilibrium coordinates, the larger the effect on the polarization of light. We will, in general, utilize the Faraday interaction throughout. It allows, when using the Holstein-Primakoff approximation, to map the spin system to a canonical harmonic oscillator language.

Having calculated the Hamiltonian evolution, we proceed to the incoherent contributions. As an example, we calculate the decay rate $\hat{L}_{03}^{\text{eff}}$. According to (3.21a), the effective decay channel is calculated by using (3.18), (3.19) and (3.21c), such that

$$\hat{L}_{03}^{\text{eff}} = \frac{\sqrt{2\gamma_e/3}g_0}{\Delta - i\gamma_e/2} \hat{A}_{00}\hat{a}_R. \quad (3.26)$$

The same procedure¹¹ can be applied to the other decay channels from equation (3.19).

At this point, having both effective Hamiltonian (3.25) and the associated decay processes, we can calculate the dynamics of the system using equation (3.20). The angular momentum time evolution is

$$\begin{aligned} \frac{d}{dt}\hat{F}_x &= g\hat{S}_z\hat{F}_y - \gamma S_0\hat{F}_x + \hat{F}_{Fx} \\ \frac{d}{dt}\hat{F}_y &= -g\hat{S}_z\hat{F}_x - \gamma S_0\hat{F}_y + \hat{F}_{Fy} \\ \frac{d}{dt}\hat{F}_z &= -\gamma\hat{S}_z\hat{F}_0 - \gamma S_0\hat{F}_z + \hat{F}_{Fz} \\ \frac{d}{dt}\hat{F}_0 &= 0, \end{aligned} \quad (3.28)$$

in which we have lumped the Langevin forces as the generic \hat{F}_{Fi} . It is not crucial to write the term explicitly, it is only important to know the diffusion associated with it. The diffusion is calculated using the generalized Einstein relations, presented in Chapter 5.

The light variables evolve as¹²

$$\begin{aligned} c\frac{d}{dz}\hat{S}_x &= -g\hat{S}_y\hat{F}_z \\ c\frac{d}{dz}\hat{S}_y &= g\hat{S}_x\hat{F}_z \\ c\frac{d}{dz}\hat{S}_z &= 0 \\ c\frac{d}{dz}\hat{S}_0 &= 0. \end{aligned} \quad (3.29)$$

The according decay and induced fluctuations have been neglected as absorption is negligible (Vasilyev et al., 2012).

The equations (3.28) show that the interaction rotates the spin around the z-axis with rate g . Simultaneously, the light polarization also rotates around the z-axis. The interaction is of the quantum non-demolition type, as the z-components of the light and spins is conserved in the interaction¹³. Due to coupling of the ground states to the short-lived excited states, the spin components decay with rate γS_0 . The detuning dependence of the decay constant $\gamma \equiv g_0^2\gamma_e/2/(\Delta^2 + (\gamma_e/2)^2)$ is to be compared with the coupling constant g . If $\Delta \gg \gamma$, coupling and decay scale as $g \sim 1/\Delta$ and $\gamma \sim 1/\Delta^2$, just like dispersion and absorption (Foot, 2005), respectively.

¹¹The remaining effective decays are

$$\begin{aligned} \hat{L}_{02}^{\text{eff}} &\propto \hat{a}_L\hat{A}_{01} \\ \hat{L}_{13}^{\text{eff}} &\propto \hat{a}_R\hat{A}_{10} \\ \hat{L}_{12}^{\text{eff}} &\propto \sqrt{2}\hat{a}_L\hat{A}_{11}. \end{aligned} \quad (3.27)$$

The operators above have $\frac{\sqrt{\gamma_e/3}g_0}{\Delta - i\gamma_e/2}$ as proportionality constant.

¹²In a more complete description, the light variables evolve as the Maxwell-Bloch equations (Julsgaard, 2003, Appendix C)

$$\left(\frac{d}{dt} + c\frac{d}{dz}\right)\hat{a}_i = \frac{i}{\hbar}[\hat{H}, \hat{a}_i].$$

For the case that $\tau \gg L/c$, that is, when the time scales of interest τ are much longer than the interval of time needed for a given pulse of light travel across the atomic ensemble, we can disregard the time evolution.

¹³Although we derive the equations of motion asserting spatial directions to the operators, we note that the interaction is more generally defined when taking the propagation of the optical probe and the respective polarization components as defining coordinates. See Deutsch and Jessen (2010) for a detailed accounting.

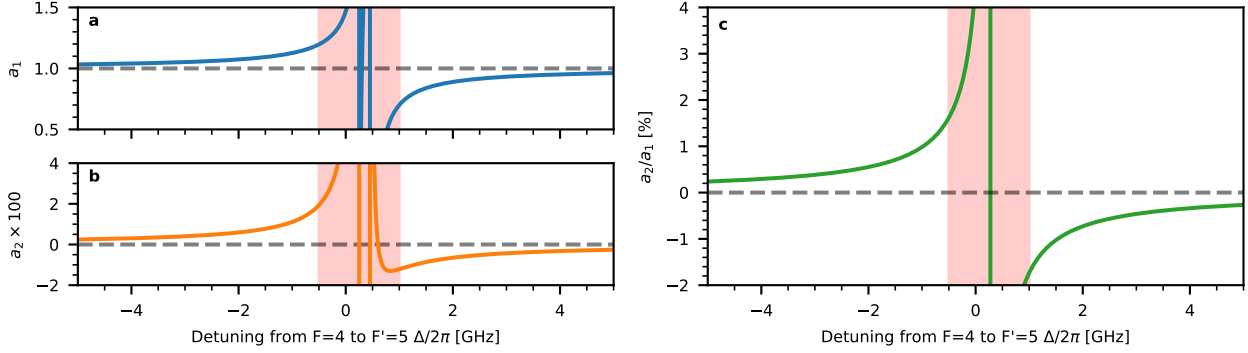


Figure 3.4: Detuning dependence of the interaction parameters. The coefficients a_1 and a_2 dependence on the detuning from the $F = 4 \rightarrow F' = 5$ transition are shown in **a** and **b**, respectively. The dashed lines present the asymptotic limit $\Delta \rightarrow \pm\infty$. In **c**, we plot the ratio a_2/a_1 . For reference, the red shaded region is the frequency band in which significant optical absorption might be present.

It is important to notice that the decay terms in equation (3.28) are proportional to the total photon flux S_0 , irrespective of the photon polarization. The only term that does not follow this rule is $-\gamma \hat{S}_z \hat{F}_0$, which shows that if the laser is circularly polarized, there will be optical pumping and a spin component along the quantization axis that is non-zero. Having the effects of optical pumping directly included in the dynamical equations highlight the self-consistency of the adiabatic elimination method here used.

Summing up, the simplified description given by the level structure presented in Figure 3.3 allowed us to introduce the concepts of polarization rotation and optically induced decay. In the next section we will increase the level of complexity, discussing the effects on the electronic structure of cesium.

3.3 Atomic Polarizability

The cesium structure, presented in Figure 3.1, contains many more levels than the case discussed above. The experimental configuration and hierarchy of processes, nonetheless, is still valid. We operate the laser rather far detuned from the atomic resonance, away from electronic transitions. Thus, by using a low laser power, we operate far below the transition saturation, we make sure the excited states will not be populated on average. The dynamics of our interest will happen on a timescale much longer than the optical coherences' lifetime. As the ground state evolves ~ 3 orders of magnitude slower than the fast decaying excited states¹⁴, the excited states can be adiabatically eliminated.

Along the same lines of the derivation performed in the previous section, an effective Hamiltonian governing the ground state dynamics can be found (Juls-gaard, 2003; Sherson, 2006). For the cesium D_2 level structure, here particularly for the $F = 4$, the effective Hamiltonian is

$$\hat{H}/\hbar = g_{\text{Cs}}(a_0 \hat{S}_0 \hat{1}_9 + a_1 \hat{S}_z \hat{F}_z + a_2 [\hat{S}_0 \hat{F}_z^2 - 2\hat{S}_x(\hat{F}_x^2 - \hat{F}_y^2) - 2\hat{S}_y(\hat{F}_x \hat{F}_y + \hat{F}_y \hat{F}_x)]), \quad (3.30)$$

where the single photon and single atom coupling rate are

$$g_{\text{Cs}} = -\frac{c\gamma_{\text{Cs}}}{8A_B\Delta} \frac{\lambda_{\text{Cs}}^2}{2\pi}, \quad (3.31)$$

¹⁴Typical scales for the decay of the ground states is in the order of $50 \mu\text{s}$, while the optical coherence decays in the order of 10 ns .

valid for $\Delta \gg \gamma_{\text{Cs}}$. Note the similarities between g_{Cs} and g , from equation (3.25).

Atomic Polarizability

The a_i -parameters are coefficients that set the relative weights of the interaction terms, which for the present case are

$$\begin{aligned} a_0 &= \frac{1}{4} \left(\frac{1}{1 - \Delta_{35}/\Delta} + \frac{7}{1 - \Delta_{45}/\Delta} + 8 \right) \rightarrow 4 \\ a_1 &= \frac{1}{120} \left(-\frac{35}{1 - \Delta_{35}/\Delta} - \frac{21}{1 - \Delta_{45}/\Delta} + 176 \right) \rightarrow 1 \\ a_2 &= \frac{1}{240} \left(\frac{5}{1 - \Delta_{35}/\Delta} - \frac{21}{1 - \Delta_{45}/\Delta} + 16 \right) \rightarrow 0, \end{aligned} \quad (3.32)$$

with asymptotic values valid for $\Delta \rightarrow \pm\infty$. The offset Δ_{35} (Δ_{45}) is the frequency difference between $F' = 3$ ($F' = 4$) and $F' = 5$. In Figure 3.4 (a) and (b), we present the detuning dependence of a_1 and a_2 . The region in red represents the frequency band in which the Doppler broadened ensemble might absorb light significantly, and should therefore be avoided.

The form of the Hamiltonian (3.30) is familiar. The contributions proportional to a_0 and a_1 are similar to the ones presented in equation (3.25), representing an overall phase shift and the Faraday rotation. The term proportional to a_2 appears as the ground state total angular momentum is $F > \frac{1}{2}$. The laser light, detuned from the electronic transition, now interacts with the whole excited state hyperfine structure. The parameter a_2 tends to zero in the far detuned limit, with overall interaction strength related with the parameter scaling as $1/\Delta^2$. Notice that the a_2 parameter scales with detuning in the same way as the light induced decoherence rate γ . The effectiveness of the atom-light interaction will therefore be a balance between the desired coherent effects and the decoherence induced by the coupling.

It is also useful to break down the interactions presented in equation (3.30) according to their physical origin (Deutsch and Jessen, 2010). The interaction induces the ac Stark shifts, a change on the energy levels, of the atom, which is by itself polarizable. The terms proportional to a_0 , a_1 and a_2 are the scalar, vector and tensor light shifts. Although not in its more explicit form, the Hamiltonian (3.30) is written into its irreducible tensor components (Vasilyev et al., 2012). The scalar term couples to the total number of atoms, here as an identity matrix. The vector term, as the name goes, couples to the vectorial part of the interaction and is maximized in media with a large spin polarization. The tensor part, on the other hand, couples to the quadrupole spin components (Di Domenico et al., 2006).

The spin-light interaction given in equation (3.30) describes a plethora of physical effects. We point to de Echaniz et al. (2008) and Hammerer et al. (2010) for the review of some of them. For us, particularly important are the *tensor Stark shifts* ω_{tss} , the ac Stark shifts induced by a_2 terms. The tensor Stark shifts will induce a m_F dependent energy shift, which will change the spectral response of the ensemble. We can calculate the shifts as described in Julsgaard (2003). For an linearly polarized input field propagating along the z -axis, the electric field is

$$E/E_0 = \cos \alpha \mathbf{e}_x + \sin \alpha \mathbf{e}_y,$$

where $\{\mathbf{e}_x, \mathbf{e}_y\}$ are the polarization unit vectors, and α as the angle between the polarization vector and the static magnetic field $\mathbf{B} = B_{\text{DC}} \mathbf{e}_x$. The average Stokes parameters, in the linear basis, are

$$\begin{aligned} S_x/S_0 &= E_x E_x - E_y E_y = \cos 2\alpha \\ S_y/S_0 &= 2\text{Re}[E_x E_y^*] = \sin 2\alpha \\ S_z/S_0 &= 0. \end{aligned}$$

Substituting these values in equation (3.30) and performing first order perturbation theory, it is possible to show that the Zeeman transition frequencies are

affected as

$$\omega_{\text{tss}} = \frac{E_{m+1} - E_m}{\hbar} = \frac{\gamma_{\text{cs}}}{8A_B\Delta} \frac{\lambda_{\text{cs}}^2}{2\pi} a_2 S_0 \frac{1 + 3 \cos 2\alpha}{2}. \quad (3.33)$$

In particular, the shifts can be zeroed by choosing $\alpha \sim 54.7^\circ$. In our experiments, we will routinely use the tensor Stark shifts to cancel the quadratic Zeeman splitting induced by the external magnetic field.

In the next section, we head to describe the physical effects we observe in our light spins interface.

3.4 Input-output relations

Spin polarizing the ground state manifold allows for simplification of the Hamiltonian in equation (3.30). In the limit of all atoms being in one of the stretched states $|F = 4, m_F = \pm 4\rangle$, using the relations given in Appendix A, the terms quadratic on angular momentum operators, \hat{F}_z^2 , $\hat{F}_x^2 - \hat{F}_y^2$ and $\hat{F}_x\hat{F}_y + \hat{F}_y\hat{F}_x$, can be approximated in a spin- $\frac{1}{2}$ description, such that equation (3.30) becomes

$$\hat{H}/\hbar = \omega_S \hat{F}_x + g_{\text{CS}} (a_0 \hat{S}_0 \hat{1}_2 + a_1 \hat{S}_z \hat{F}_z + a_2 [2\hat{S}_0 \hat{1}_2 - 14\hat{S}_x (\hat{F}_x - 2\hat{1}_2) - 14\hat{S}_y \hat{F}_y]). \quad (3.34)$$

The static magnetic field contribution, assuming the quadratic Zeeman splitting has been canceled by the tensor light shifts, is given by equation (3.10). Given the energy introduced by the magnetic field, the terms proportional to \hat{F}_x and $\hat{1}_2$, are inducing frequency shifts that can be compensated by the external magnetic field, we are then left with

$$\hat{H}_{1/2}/\hbar = \omega_S \hat{F}_x + g_{\text{CS}} (a_1 \hat{S}_z \hat{F}_z \pm 14a_2 \hat{S}_y \hat{F}_y). \quad (3.35)$$

From here we proceed to map the Hamiltonian above to the quadrature operators language. The quantum Stokes operators as $\hat{S}_x, \hat{S}_y, \hat{S}_z, \hat{S}_0$ are redefined as $\{\hat{S}_\parallel = \hat{S}_x \cos 2\alpha - \hat{S}_y \sin 2\alpha, \hat{S}_\perp = \hat{S}_x \sin 2\alpha + \hat{S}_y \cos 2\alpha, \hat{S}_z, \hat{S}_0\}$, for α as the angle between polarization of the probe laser with respect to the static magnetic field B_{DC} . Defining the Stokes operators as $\{\hat{S}_\parallel, \hat{S}_\perp, \hat{S}_z\}$ allow us to reference an arbitrary linear polarization state according to its decomposition along and perpendicular to the referenced magnetic field.

For mapping the polarization variables into quadrature variables, we choose the parallel component as the classical variable – the local oscillator LO_1 with the photon flux $\langle \hat{S}_\parallel \rangle = \langle \hat{S}_0 \rangle = S_\parallel$, leaving \hat{S}_\perp, \hat{S}_z as quantum variables. We define the light quadratures as $\hat{X}_L = \hat{S}_z / \sqrt{S_\parallel}$ and $\hat{P}_L = -\hat{S}_\perp / \sqrt{S_\parallel}$, such that $[\hat{X}_L, \hat{P}_L] = \frac{i}{2}$. The negative mass spin oscillator variables are redefined as $\hat{X}_S = \hat{F}_z / \sqrt{F_x}$ and $\hat{P}_S = -\hat{F}_y / \sqrt{F_x}$, with F_x as the steady-state spin polarization $F_x = \langle \hat{F}_x \rangle$, and $[\hat{X}_S, \hat{P}_S] = i$.

In the quadrature language, after employing the Holstein-Primakoff approximation, the Hamiltonian according to equations (3.13) and (3.35) is

$$\hat{H}_S/\hbar = \frac{\omega_S}{2} (\hat{X}_S^2 + \hat{P}_S^2) - 2\sqrt{\Gamma_S} (\hat{X}_S \hat{X}_L + \zeta_S \hat{P}_S \hat{P}_L), \quad (3.36)$$

where $\zeta_S = -14 \frac{a_2}{a_1} \cos 2\alpha$ as the tensor interaction strength. We have also introduced the spin readout rate

$$\Gamma_S = g_{\text{CS}}^2 S_x F_x. \quad (3.37)$$

The Hamiltonian (3.36) is the starting point of our theoretical understanding of the spin ensemble, and will be analyzed in its various forms in the next chapters. For our standard detuning $\Delta/2\pi = 3 \text{ GHz}$ and polarization of the probe

Input-output relations

$\alpha = 60^\circ$, the tensor interaction strength is rather small $\zeta_S \sim 0.01$, the light-matter coupling is approximately of the QND-type. Notice the similarity of equation (3.36) with the harmonic oscillator description presented in the last chapter for the optomechanical system. The physics of atoms driven much below the saturation being mapped to mechanical oscillators is also vast (Souza et al., 2015).

Given the system Hamiltonian, equation (3.36), and by the Heisenberg-Langevin equations (3.20), the spin and optical operators¹⁵ evolve as

$$\frac{d}{dt} \begin{pmatrix} \hat{X}_S \\ \hat{P}_S \end{pmatrix} = \begin{pmatrix} -\gamma_{S0}/2 & \omega_S \\ -\omega_S & -\gamma_{S0}/2 \end{pmatrix} \begin{pmatrix} \hat{X}_S \\ \hat{P}_S \end{pmatrix} + 2\sqrt{\Gamma_S} \begin{pmatrix} -\zeta_S \hat{P}_L \\ \hat{X}_L \end{pmatrix} + \begin{pmatrix} \hat{F}_S^X \\ \hat{F}_S^P \end{pmatrix} \quad (3.38)$$

$$\begin{pmatrix} \hat{X}_{L,S}^{\text{out}} \\ \hat{P}_{L,S}^{\text{out}} \end{pmatrix} = \begin{pmatrix} \hat{X}_{L,S}^{\text{in}} \\ \hat{P}_{L,S}^{\text{in}} \end{pmatrix} + \sqrt{\Gamma_S} \begin{pmatrix} 0 & -\zeta_S \\ 1 & 0 \end{pmatrix} \begin{pmatrix} \hat{X}_S \\ \hat{P}_S \end{pmatrix}, \quad (3.39)$$

with \hat{F}_S^X, \hat{F}_S^P as the effective Langevin forces acting on the spin oscillator. The first term in equation (3.38) shows that the oscillator variables are coupled due to the presence of the static magnetic field. The spin components decay with rate γ_{S0} . The total bandwidth of the spin resonance in the absence of dynamical processes is $\gamma_{S0} = \gamma_{S0,\text{dark}} + \gamma_{\text{pb}} + \gamma_{\text{op}}$, summing the contributions from the decay in the dark, power broadening and optical pumping, respectively. For an accounting of the different decay processes, see Krauter (2011). The decay in the dark contribution will be discussed in Chapter 4. The last two terms in equation (3.38) are the optical and effective spin thermal forces, respectively. In the absence of extraneous couplings—as classical external magnetic fields—these are the only two components that couple to the spins.

The last ingredient on the dynamics is accounting for the ensemble average of the light variables. Due to atomic motion, the optical signal seen by the spins is an average over the whole ensemble, that is

$$\begin{pmatrix} \hat{X}_L \\ \hat{P}_L \end{pmatrix} \rightarrow \frac{1}{2} \left\langle \begin{pmatrix} \hat{X}_{L,S}^{\text{out}} \\ \hat{P}_{L,S}^{\text{out}} \end{pmatrix} + \begin{pmatrix} \hat{X}_{L,S}^{\text{in}} \\ \hat{P}_{L,S}^{\text{in}} \end{pmatrix} \right\rangle = \left\langle \begin{pmatrix} \hat{X}_{L,S}^{\text{in}} \\ \hat{P}_{L,S}^{\text{in}} \end{pmatrix} \right\rangle + \frac{\sqrt{\Gamma_S}}{2} \begin{pmatrix} 0 & -\zeta_S \\ 1 & 0 \end{pmatrix} \left\langle \begin{pmatrix} \hat{X}_S \\ \hat{P}_S \end{pmatrix} \right\rangle. \quad (3.40)$$

Inserting this equation in the term related to the optical quadratures in (3.38), we get to

$$\begin{aligned} \frac{d}{dt} \begin{pmatrix} \hat{X}_S \\ \hat{P}_S \end{pmatrix} &= \begin{pmatrix} -\gamma_{S0}/2 - \zeta_S \Gamma_S & \omega_S \\ -\omega_S & -\gamma_{S0}/2 - \zeta_S \Gamma_S \end{pmatrix} \begin{pmatrix} \hat{X}_S \\ \hat{P}_S \end{pmatrix} \\ &+ 2\sqrt{\Gamma_S} \begin{pmatrix} -\zeta_S \hat{P}_L^{\text{in}} \\ \hat{X}_L^{\text{in}} \end{pmatrix} + \begin{pmatrix} \hat{F}_S^X \\ \hat{F}_S^P \end{pmatrix}. \end{aligned} \quad (3.41)$$

The extra decay term $2\zeta_S \Gamma_S$ is the tensor (dynamical) broadening. Depending on the choice of ζ_S , this term can be positive or negative.

We are interested in work in the steady state regime. Furthermore, the dynamics are best seen in frequency space, in which we have used the Fourier transform definition $\mathcal{F}(\hat{X}_S) = -i\Omega \hat{X}_S$, see Appendix A. In a shorthand matrix notation, the spin evolution (3.41), in frequency space, is

$$\hat{X}_S = 2\sqrt{\Gamma_S} \mathbf{Z} \mathbf{L} \hat{X}_{L,S}^{\text{in}} + \mathbf{L} \hat{F}_S, \quad (3.42)$$

with

$$\mathbf{Z} = \begin{pmatrix} 0 & -\zeta_S \\ 1 & 0 \end{pmatrix}, \quad \mathbf{L} = \begin{pmatrix} \gamma_{S0}/2 + \zeta_S \Gamma_S - i\Omega & -\omega_S \\ \omega_S & \gamma_{S0}/2 + \zeta_S \Gamma_S - i\Omega \end{pmatrix}^{-1},$$

$$\hat{X}_{L,S}^{\text{in(out)}} = \begin{pmatrix} \hat{X}_{L,S}^{\text{in(out)}} \\ \hat{P}_{L,S}^{\text{in(out)}} \end{pmatrix}, \quad \hat{X}_S = \begin{pmatrix} \hat{X}_S \\ \hat{P}_S \end{pmatrix}, \quad \hat{F}_S = \begin{pmatrix} \hat{F}_S^X \\ \hat{F}_S^P \end{pmatrix}. \quad (3.43)$$

¹⁵Here we use the sub-indices L, S as for the light variables related to the spin oscillator. In the hybrid implementation, such indices become important.

The matrix \mathbf{L} contains the spin oscillator dynamics in frequency space. Element-by-element, \mathbf{L} is

$$\mathbf{L} = \begin{pmatrix} \varrho_S(\Omega) & \chi_S(\Omega) \\ -\chi_S(\Omega) & \varrho_S(\Omega) \end{pmatrix}, \quad (3.44)$$

in which the general spin susceptibilities χ_S and ϱ_S are defined as

$$\chi_S(\Omega) = \frac{\omega_S}{\omega_S^2 - \Omega^2 - i\Omega\gamma_S + (\gamma_S/2)^2} \quad (3.45)$$

$$\varrho_S(\Omega) = \frac{\gamma_S/2 - i\Omega}{\omega_S^2 - \Omega^2 - i\Omega\gamma_S + (\gamma_S/2)^2} \quad (3.46)$$

with $\gamma_S = \gamma_{S0} + 2\zeta_S\Gamma_S$ as the total spin linewidth. As seen in equation (3.42), the matrix \mathbf{L} maps the input optical and thermal forces into the oscillator dynamics.

In the limit of $\gamma_S \ll \omega_S$, when only the dynamics around the resonance ($\Omega \sim \omega_S$) are significant, the susceptibilities from equation (3.45) get the more familiar form

$$\chi_S(\Omega) \sim \frac{1}{2} \frac{1}{\omega_S - \Omega - i\gamma_S/2} \quad (3.47)$$

$$\varrho_S(\Omega) \sim -i\chi_S(\Omega). \quad (3.48)$$

The absolute squared of equation (3.47) $|\chi_S|^2$ is a Lorentzian function. In this case, an approximate versions of equation (3.42) can be written. The effective thermal forces \hat{F}_S^X and \hat{F}_S^P can be combined into the single thermal force term $\hat{F}_S \approx i\hat{F}_S^X + \hat{F}_S^P$, and

$$\hat{X}_S = \chi_S \left[\hat{F}_S + 2\sqrt{\Gamma_S} \begin{pmatrix} 1 \\ -i\zeta_S \end{pmatrix}^\top \hat{X}_{L,S}^{\text{in}} \right] = \chi_S \left[2\sqrt{\Gamma_S} (\hat{X}_{L,S}^{\text{in}} - i\zeta_S \hat{P}_{L,S}^{\text{in}}) + \hat{F}_S \right]. \quad (3.49)$$

The light variables, from equation (3.39), read

$$\hat{X}_{L,S}^{\text{out}} = \hat{X}_{L,S}^{\text{in}} + \sqrt{\Gamma_S} \mathbf{Z} \hat{X}_S = (\mathbf{1}_2 + 2\Gamma_S \mathbf{Z} \mathbf{L} \mathbf{Z}) \hat{X}_{L,S}^{\text{in}} + \sqrt{\Gamma_S} \mathbf{Z} \mathbf{L} \hat{F}_S, \quad (3.50)$$

in which $\mathbf{1}_2$ is the 2×2 identity matrix, and we have already plugged in the the expression for the spin dynamics. Approximate expressions for the output light field in the limit $\gamma_S \ll \omega_S$ can also be written. In Noting that $\hat{P}_S \approx -\text{sign}(\omega_{S0})i\hat{X}_S$, the simpler input-output are

$$\hat{X}_{L,S}^{\text{out}} = \hat{X}_{L,S}^{\text{in}} + \sqrt{\Gamma_S} \begin{pmatrix} -i\zeta_S \\ 1 \end{pmatrix} \hat{X}_S. \quad (3.51)$$

This is the final result of this section. The equation (3.50) will be used in depth throughout the next chapters.

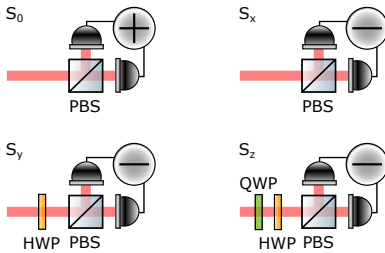


Figure 3.5: Measurement of the Stokes parameters. The configurations required for detecting the Stokes parameters. The half waveplates (HWP) are set to $\pi/8$ and the quarter waveplate (QWP) to $\pi/4$. Plus and minus are for sum and difference of the photodiode's electrical signals.

3.5 Noise spectrum

The output light field, after interacting with the spin oscillator, is directed towards a photo-detection setup. As the spin ensemble rotates the polarization of light, to use standard photodiodes we need to convert the polarization signal into an intensity signal. The simplest experimental setups uses waveplates and polarizing beam splitters (Seltzer, 2008). We use the balanced detection-like configuration shown in Figure 3.5 and described in Bowen et al. (2002), and in Julsgaard (2003). We can select the measured Stokes parameter \hat{S}_i , or optical quadrature $\hat{X}_{L,S}, \hat{P}_{L,S}$ in the linearized language, by adjusting the quarter and

Noise spectrum

half waveplates, setting the light field's polarization ellipticity. In this way, we adjust the homodyning the angle φ , as

$$\hat{\mathbf{X}}_L^{\text{det}} = \begin{pmatrix} \hat{X}_L^{\text{det}} \\ \hat{P}_L^{\text{det}} \end{pmatrix} = \mathbf{M}_\varphi \hat{\mathbf{X}}_{L,S}^{\text{out}} = \begin{pmatrix} \cos \varphi \hat{X}_{L,S}^{\text{out}} - \sin \varphi \hat{P}_{L,S}^{\text{out}} \\ \sin \varphi \hat{X}_{L,S}^{\text{out}} + \cos \varphi \hat{P}_{L,S}^{\text{out}} \end{pmatrix}. \quad (3.52)$$

An arbitrary angle φ leads to the measurement of a combination of the output quadratures. As we will see in Chapter 4, the angle φ can be controlled via balanced polarimetry, as described above, or using standard interferometric homodyning techniques. In the noise analysis, we need to consider only one of the vector entries, as \hat{P}_L^{det} for φ is the same as \hat{X}_L^{det} for $\varphi + \pi/2$.

Similarly to the previous chapter, we are mostly interested in the power spectral density (PSD) of the detected output field. As the PSD is proportional to the symmetrized correlation function¹⁶, the detected power spectral density matrix is

$$\begin{aligned} \bar{S}_{\mathbf{X}\mathbf{X}}^{\text{det}} \delta(\Omega - \Omega') &\equiv \frac{1}{2} \langle \hat{\mathbf{X}}_L^{\text{det}} \hat{\mathbf{X}}_L^{\text{det},\dagger} + \hat{\mathbf{X}}_L^{\text{det},*} \hat{\mathbf{X}}_L^{\text{det},\top} \rangle \\ &= \mathbf{M}_\varphi \bar{S}_{\mathbf{X}\mathbf{X}}^{\text{out}} \mathbf{M}_\varphi^\top, \end{aligned} \quad (3.53)$$

where $\bar{S}_{\mathbf{X}\mathbf{X}}^{\text{det}} \delta(\Omega - \Omega')$ is the PSD of the output field, from equations (3.50) and (3.52). The input power spectral density of the light field and thermal bath are

$$\bar{S}_{\mathbf{X}\mathbf{X}}^{\text{in}} = \frac{1}{4} \begin{pmatrix} 1 & 0 \\ 0 & 1 \end{pmatrix} \delta(\Omega - \Omega') \quad (3.54)$$

$$\bar{S}_{\mathbf{F}\mathbf{F}} = \begin{pmatrix} 0 & 0 \\ 0 & 1 \end{pmatrix} \gamma_S (n_S + \frac{1}{2}) \delta(\Omega - \Omega'). \quad (3.55)$$

The symbol $*$ represents the complex conjugate, while \top stands for the transpose matrix. The expressions from the matrix equation (3.53) can be used to fit experimental data.

An important case is the QND interaction, $\zeta_S = 0$. In this regime, equation (3.53) for $\varphi = 0$ simplifies to

$$\bar{S}_{\mathbf{X}\mathbf{X}}^{\text{out}} = \frac{1}{4} \begin{pmatrix} 1 & 2\Gamma_S \chi_S^* \\ 2\Gamma_S \chi_S & 1 + 4\Gamma_S^2 |\chi_S|^2 \end{pmatrix} + \Gamma_S (|\chi_S|^2 + |\varrho_S|^2) \begin{pmatrix} 0 & 0 \\ 0 & 1 \end{pmatrix} \gamma_{S0} (n_S + \frac{1}{2}). \quad (3.56)$$

This matrix contains all the correlations written into light via the QND interaction with the spin ensemble. The diagonal terms represent the PSD of the auto-correlation functions. The off-diagonal terms represent the PSD of the cross-correlation between the optical quadratures.

Note that the coupling of light to the spins leads to non-zero off-diagonal elements in the first matrix to the right hand side of (3.56), a consequence of the spin-light interaction. The input light fluctuations $\hat{X}_{L,S}^{\text{in}}$ induce spin fluctuations \hat{F}_z , which are written back into light in the orthogonal quadrature $\hat{P}_{L,S}^{\text{out}}$ according to the spin susceptibility χ_S . In this way, the amplitude and phase fluctuations get correlated according to the coupling rate Γ_S .

Including a detection angle φ , according to equation (3.53), means multiplying the expression (3.56) by the rotation matrix \mathbf{M}_φ , as indicated in equation (3.53). The rotation of the detected quadrature will give us access to the spin induced optical correlations. The phase quadrature component, that is, the (2,2) element of equation (3.53), is

$$\begin{aligned} S_{\text{PP}}^{\text{det}} / \text{SN} &= 1 + 4\Gamma_S^2 |\chi_S|^2 \cos^2 \varphi + \\ &4\Gamma_S \text{Re}[\chi_S] \sin \varphi \cos \varphi + 4\gamma_{S0} \Gamma (|\chi_S|^2 + |\varrho_S|^2) \cos^2 \varphi (n_S + \frac{1}{2}). \end{aligned} \quad (3.57)$$

¹⁶See Appendix A for more details.

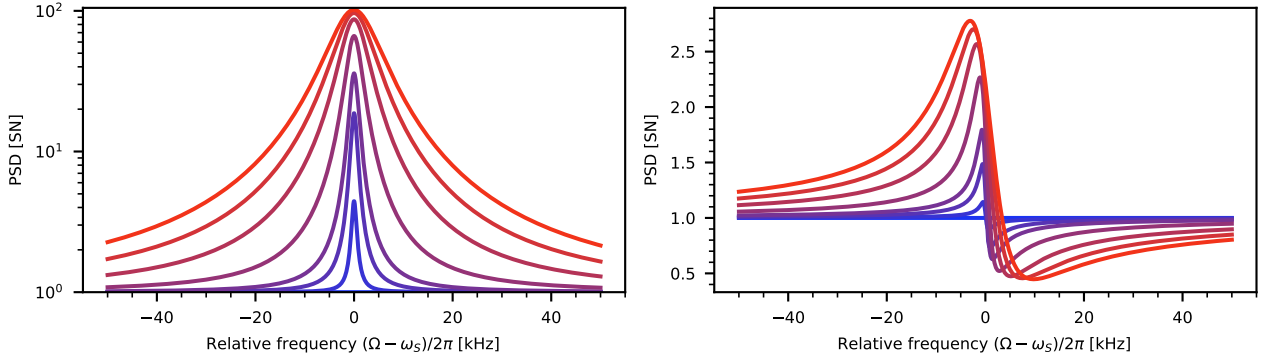


Figure 3.6: Spin noise for an increasing probe power. The power spectral densities of \hat{P}_S^{out} for $\varphi_0 = 0^\circ$ (left) and $\varphi_1 = 84^\circ$ (right), for increasing probe powers (from blue to red). The detection angle φ_1 has been optimized for maximum squeezing, given the chosen parameters. The quantum cooperativity is set to $C_q^S = 5$. Other parameters are $\gamma_{S,\text{dark}}/2\pi = 1$ kHz and $n_S = 0$. From blue to red, the linewidth and readout rate were scaled as $\gamma_S/2\pi = \gamma_{S,\text{dark}}/2\pi + [0, 0.125, 0.5, 1, 2.5, 5, 7.5, 10]$ kHz and $\Gamma_S/2\pi = [0, 0.125, 0.5, 1, 2.5, 5, 7.5, 10] \times 5$ kHz.

The PSD has been normalized to the shot-noise level, which is $\frac{1}{4}$ according to equation (3.54). Here, we include the effective spin occupancy n_S for generality. If $n_S = 0$, we say that the spin is at its ground state. The associated noise is also usually called *projection noise*. We will discuss its origin in Chapter 5.

For demonstrating the detected light fluctuations and their dependence on the spin parameters, we present in Figure 3.6 the spin noise for increasing optical drive S_x . We show the PSD of equation (3.57) for $\varphi_0 = 0$ (left). Increasing the light power leads to a higher spin readout rate Γ_S and linewidth γ_{S0} . Overall, the spin noise grows with respect to the shot noise level up to the point in which the linewidth is dominated by power broadening. From there on, the spin response gets only broader.

When detecting a combination of the output amplitude and phase quadratures, we will be able to measure the correlations induced by the readout on the spin response. Setting $\varphi_1 = 84^\circ$, in Figure 3.6 (right), we see a dispersive-like feature. It is the measurement induced back-action that induces an asymmetric response, due to the interference of the optical drive and its respective response induced on light. The interference is related to the off-diagonal terms in equation (3.56). Being driven by the vacuum fluctuations of the light field, the destructive interference leads to a frequency dependent squeezing feature, here reaching approximately 50% below the SN level. In the limit of $\Gamma_S/\gamma_S \rightarrow \infty$, the minimum of Figure 3.6 (right) tends to zero. This indicates the feasibility of using a spin ensemble as a non-linear gain media.

Had we set $\varphi = 90^\circ$, plotting equation (3.57) would have given us no spin noise contribution. This is a consequence of the QND interaction, which leaves the $\hat{X}_{L,S}$ optical quadrature unaffected. In the case of $\zeta_S \neq 0$, the coupling induced by tensor effects would also be manifested as extra atomic noise in the $\varphi = 90^\circ$ measurement.

3.6 Spectral response and quantum cooperativity

The detected light field, having interacted with the spin oscillator, carries information about its dynamics. Therefore, for a calibrated spin readout, it is possible to characterize the measurement strength, that is, the quantum cooperativity C_q^S .

Let us examine the equation (3.57) for $\varphi = 0$. The total detected noise is

$$S_{\text{pp}}^{\text{det}}/\text{SN} = 1 + 4\Gamma_S^2|\chi_S|^2 + 4\gamma_{S0}\Gamma(|\chi_S|^2 + |\varrho_S|^2)(n_S + \frac{1}{2}). \quad (3.58)$$

Spectral response and quantum cooperativity

The three contributions to the right-hand side of the equation above are: shot noise, back-action, and spin thermal noise, respectively. When evaluated at the Larmor frequency $\Omega = \omega_S$, it becomes

$$S_{\text{PP}}^{\text{det}}/\text{SN} = 1 + \frac{4\Gamma_S^2}{\gamma_S^2} + \frac{8\Gamma_S(n_S + \frac{1}{2})}{\gamma_S}, \quad (3.59)$$

in which we have used the narrowband approximation for q_S , given in equation (3.47), such that $|\chi_S|^2 + |q_S|^2 \sim 2|\chi_S|^2$. From here, by taking the ratio of the back-action and thermal noise components

$$\frac{\text{BA}}{\text{TH}} \equiv C_q^S = \frac{\Gamma_S}{2\gamma_{S0}(n_S + 1/2)}, \quad (3.60)$$

we arrive at the definition of the spin quantum cooperativity C_q^S .

Including the tensor contribution in the spectral response leads to more complicated expressions, as now there will also be correlations induced by coupling to \hat{P}_S . The spectra can be calculated from equations (3.53). We note that the total noise can still be divided between back-action and thermal noise, allowing for an estimation of the light induced noise.

It is meaningful to rewrite the quantum cooperativity in terms of fundamental light-matter interaction parameters. From simplicity, let us consider the case of the ideal two-level system described in Section 3.2. Given the definition of the spin readout rate, $\sqrt{\Gamma_S} = \sqrt{F_x S_x} g$, the effective decay rate γ_{S0}

$$g = 2g_0^2 \frac{\Delta}{\Delta^2 + (\gamma_e/2)^2} \quad (3.61)$$

$$\gamma_{S0} = g_0^2 \frac{\gamma_e S_0/2}{\Delta^2 + (\gamma_e/2)^2}, \quad (3.62)$$

and the quantities (Steck, 2007)

$$g_0 = \sqrt{\frac{\omega_e}{2\hbar\epsilon_0 A_L}} d_{eg} \quad (3.63)$$

$$\gamma_e = \frac{d_{eg}^2 \omega_{cs}^3}{3\pi\hbar\epsilon_0 c^3}, \quad (3.64)$$

we are able to write equation (3.60) as

$$C_q^S = \frac{S_x F_x g^2}{\gamma_{S0}} = \frac{\Delta^2}{\Delta^2 + (\gamma_e/2)^2} \frac{4N_a g_0^2}{\gamma_e} \sim \frac{4N_a g_0^2}{\gamma_e}, \quad (3.65)$$

in which we have assumed a perfectly spin polarized ensemble ($F_x = FN_a = N_a/2, n_S = 0$), a linearly polarized drive ($S_x = S_0$) and a large detuning $\Delta \ll \gamma_e$. We can give one step further to show that the quantum cooperativity is related to the optical depth as

$$C_q^S = \frac{4N_a g_0^2}{\gamma_e} = \rho\sigma_0 L, \quad (3.66)$$

for $\sigma_0 = \frac{3\lambda^2}{2\pi}$ as the absorption cross section (Jackson, 1999). Therefore, increasing the quantum cooperativity can be made by increasing the density of the vapor and/or by increasing the length of the ensemble.

Here, we finish the introduction of the hybrid system components and move on to the experimental section.

Part II

Experimental methods and characterizations

Chapter 4

Experimental methods

In this chapter we present the general experimental aspects of our hybrid implementation. On the atomic physics side, this includes details on laser systems, vapor cells and fabrication thereof, and testing on unshielded environment. On the optomechanics side, we talk about the cavity design, the cryostat and cavity locking. We finish presenting the operation of the hybrid setup.

4.1 Laser systems and optical pumping

Running the hybrid experiment requires the probe beam, and optical pumping beams. Optical pumping is performed by one or two lasers, depending on the particular experiment. The cesium electronic level structure was discussed on Chapter 3 and is reproduced in Figure 4.1 for completeness.

The probe laser is a titanium-sapphire laser¹, pumped by a Sprout semiconductor laser. For the standard pump power value of 2.5 W the Ti-Sapph provides ~ 150 mW of laser light, tunable from ~ 760 nm to 900 nm. The laser control interface allows us to readily tune the laser wavelength around the cesium D_1 and D_2 lines, 852 nm and 894 nm. A small portion of the output power is picked off and directed to a wavelength meter, which along a feedback loop give us ~ 40 MHz long term wavelength stability. The most common operation wavelength is 852.3490 nm, corresponding to a detuning $\Delta/2\pi = 3$ GHz from the $F = 4 \rightarrow F' = 5$ electronic transition. The titanium-sapphire amplitude and phase laser noise are shot-noise limited in Fourier frequencies of interest $\Omega > 1$ MHz for optical powers up to 100 μ W. The polarization components, whose noise performance depends mostly on good polarizers to clean out unwanted polarization components, are shot noise limited up to the levels of power commonly used in the experiments, about 10 mW.

The probe laser, along with optics for power distribution, is positioned on its own breadboard stands with passive isolation on the main optical table. Isolating the laser from mechanical vibrations caused by interaction with the optical table allows for stable operation throughout the workday. For fast light intensity/phase control, an AOM² and an EOM³ are installed in the optical path. A polarization maintaining optical fiber delivers light from the laser breadboard to the experiment. A typical hybrid experiment run requires ~ 50 mW of laser power, measured at the laser breadboard.

The pump and repump diode lasers are installed on a separate breadboard. The output powers are 20 mW and 50 mW. Both lasers are frequency stabilized via *polarization spectroscopy* (Pearman et al., 2002; Harris et al., 2006). The technique uses a counter-propagating pump-probe configuration, with the optical pumping created by the pump inducing birefringence on the weak probe beam. Balanced polarimetry of the transmitted signal gives access to a Doppler-free dispersive signal. The detected polarization rotation is directly used as error signal in a slow feedback circuit, stabilizing the laser frequency. The pump

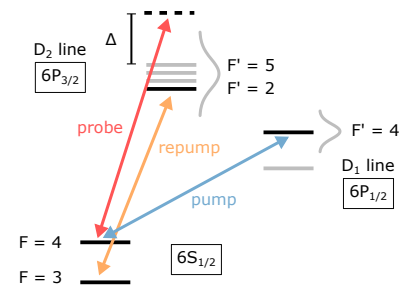


Figure 4.1: Optical pumping and laser configuration. Optical pumping lasers, pump and repump, are frequency stabilized via polarization spectroscopy to certain transitions in the D_1 and D_2 lines, respectively. The probe laser is stabilized off resonantly, with detuning Δ from the $F = 4 \rightarrow F' = 5$ transition. See text for details.

¹MSquared SolsTiS 7W-SRX-F

²IntraAction ATM-A2 Series

³LINOS PM0202

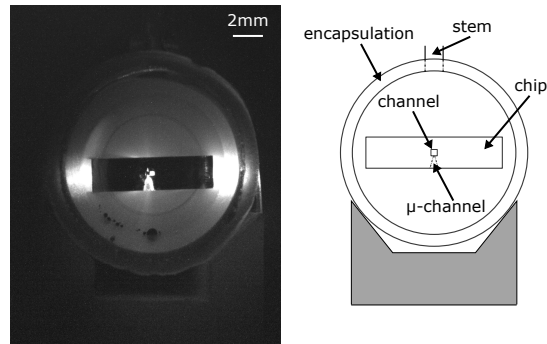


Figure 4.2: Front view of the J18 encapsulated vapour cell. The cell is mounted in a wedged plastic holder and illuminated by the optical pumping beam, crossing the chip from left to right. Light scattering shows the microchannel and its conical connection to the encapsulation. Image taken with Flir BFLY-PGE-12A2M-CS.

laser is locked on the $F = 4 \rightarrow F' = 4$ electronic transition of the D_1 line; the repump laser is locked on the $F = 3 \rightarrow F' = 2$ electronic transition of the D_2 line. Details on the choice of locking transitions are given on Chapter 5.

Both pump and repump lasers are combined in a polarizing beam splitter and sent to an AOM. The AOM is activated when the pumping lasers need to be switched on and off. After the AOM the beams are projected in the same polarization and sent to a polarization maintaining optical fiber. On the experiment, the output laser beam is polarization controlled by achromatic waveplates. The beam is reshaped by a pair of cylindrical lenses and focused at the vapour cell, with a beam diameter in the vertical direction ($1/e^2$) $2w_0 = 400 \mu\text{m}$ and in the horizontal direction $2w_0 = 8 \text{mm}$.

4.2 Vapour cell

The vapour cell contains the cesium atomic ensemble. The cell used in the hybrid experiments is presented on Figure 4.2. This type of construction is commonly referred to as *encapsulated vapour cell*, or simply *cell*. The encapsulating Pyrex cylinder and the flat windows are sealed by glass blowing. The flat windows are anti-reflection coated, reflecting $\sim 0.2\%$ (in power) per window.

The cylindrical glass encapsulation is mainly responsible for making the cell vacuum tight. The stem is a narrow tube glass-blown to the encapsulation, allowing connection to different equipment during the fabrication of the cell. When ready for use, it is in the stem that a small drop of metallic cesium sits.

The glass encapsulation contains a perforated rectangular glass rod⁴ and alignment/holding pieces. The rectangular glass rod, the *glass chip*, is ($L \times H \times W$) $10 \text{mm} \times 2.5 \text{mm} \times 8 \text{mm}$ and contain a $300 \mu\text{m} \times 300 \mu\text{m}$ through hole, the *channel*, see Figure 4.3. The channel is connected to the housing via a femtosecond laser⁵ drilled *microchannel*, measuring $\sim 30 \mu\text{m}$ to $50 \mu\text{m}$ in diameter.

Using a cell with such a small transverse cross-section allows for faster spin motional averaging (Borregaard et al., 2016), vital for an efficient interaction of the spin ensemble with light. It also allows for reducing the overhead in optical probing power, further reducing the contributions of excess classical optical noise.

In the experiment, the cell sits on non-magnetic post and holder, usually made on machinable glass-ceramic *Macor* or 3D printed *ABS* thermoplastic. The choice of material is also based on its thermal expansion coefficients, with the former being much less affected by changes in temperature. A thermal cy-

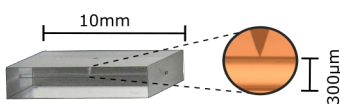


Figure 4.3: Glass chip. The glass chip is a small slab with a rectangular cross-section channel crossing its length. The access of atoms from the encapsulation to the channel is done via the microchannel, shown in the zoomed inset.

⁴Purchased from VitroCom Inc

⁵The microchannel perforation has been performed at the Technical University of Denmark (DTU) Danchip facilities.

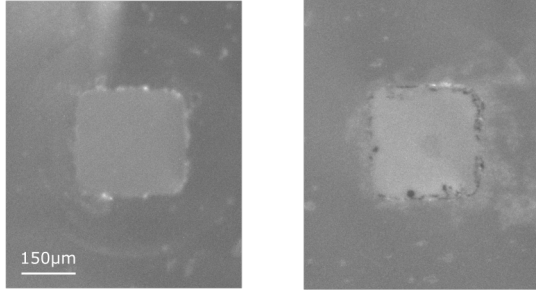


Figure 4.4: Effects of long term curing on the vapour cell. Close-up in the microchannel: (left) cell *J19*, kept in storage at room temperature for ~ 1 year; (right) cell *J18*, kept at 55°C for the same period of time. Spots appear on the channel edges and a misty layer covers the whole cross-section. Optical transmission decreased by 5% (from 92% to 87%) over the year in which the cell was heated up.

cle between room temperature and 60°C usually leads to misalignments on the order of $100\ \mu\text{m}$, that are corrected when reaching stable operation temperature.

4.2.1 Anti-relaxation coating and cell performance

The microcell fabrication, anti-relaxation coating and alkali filling is performed by Mikhail Balabas, from the St Petersburg State University, a expert in the science of paraffin coated vapor cells (Balabas et al., 2010b). Most of the cells used in the hybrid experiment have been fabricated at the in-house workshop. The workshop is equipped with glass-blowing equipment, vacuum pumps and an oven for anti-relaxation coating deposition. The procedure employed for characterization of the various steps of the process, see Zugenmaier (2018, Chapter 4).

Over the period of 2015 – 2020, four cells have been used in the hybrid experiment: *G4*, *J11*, *J18* and *J19*. The cell *J11* was used in the back-action evasion experiments presented in Møller et al. (2017), while the cell *J19* has been used in the entanglement experiments Thomas et al. (2020).

Operating the experiment at elevated temperatures for extended periods of time has shown that the vapour cells continue to cure with time. We observed that the Zeeman T_2 of the all cells improved over the course of 1 year time-scales on the order of 50 Hz to 100 Hz; we have also observed the optical transmission decrease on the order of 5% to 10%. The effects of the high-temperature exposure can be seen in Figure 4.4. On the two panels, we show (left) the cell *J19*, which kept in storage at room temperature for ~ 1 year, and (right) the cell *J18*, kept at 55°C for the same period of time. Various spots appear on the channel edges and a misty layer covers the whole cross-section. The dark spots are most likely cesium droplets that migrated from the stem to the cell body. Optical transmission decreased by 5% (from 92% to 87%) over the year in which the cell was heated up.

We have also experienced the sudden disappearance of atoms, as described in Zugenmaier (2018). The reason for this sudden loss of atomic density is correlated with the microchannel clogging, nonetheless we have not established the conditions that lead to such effect.

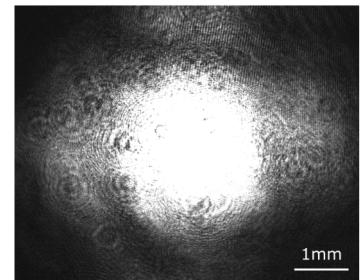


Figure 4.5: Imaging of the transmitted optical mode in the far field. A $w_0 = 60\ \mu\text{m}$ $1/e^2$ diameter Gaussian beam propagates through the microcell. The characteristic diffraction pattern is observed. Notice that the sensor is saturated and relative brightness is not a measure of the beam quality. Circular diffraction-like spots are due to dust particles on the camera sensor.

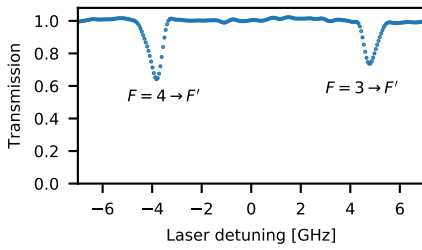


Figure 4.6: The optical transmission of linearly polarized light through a Cs ensemble. A 10 mm long, room temperature (at 20 °C) ensemble, probed by a laser scanning through the D_2 line. The two labeled transmission dips are related to the transitions of a given ground state hyperfine manifold to the allowed excited states.

4.2.2 Characterization

Once a vapour cell has been fabricated, filled, and cured (Balabas et al., 2010a), it is ready for characterization. Three parameters are of great importance: optical transmission, vapour density and transverse coherence time. These parameters are responsible for the important part of the overall photon detection efficiency, optical depth and operating bandwidth, respectively.

The optical transmission might simply be measured by comparing how much light passes through the cell with respect to the input⁶. However, given the square transverse geometry of the channel, the input Gaussian optical mode can be modified, see Figure 4.5. Therefore, a more precise method for estimating the optical losses, that is sensitive to both intensity and optical mode, involves positioning the cell in a Fabry-Perot resonator and comparing the cavity bandwidth with respect to the calibrated empty resonator. For detailed description on the cavity characterization method, see Zugenmaier et al. (2018).

The vapour density is estimated by measuring optical absorption and relating it to the absorption cross section. For a 10 mm long ensemble at room temperature (20 °C), about 30% of the light is absorbed on the D_2 resonances, see Figure 4.6⁷. At this temperature, typical cesium volume densities⁸ are on the order of 10^{16} m^{-3} . We refer to Stærkind (2016); Schmieg (2018) for detailed methods of absorption measurement and calibration. It is also important to notice that for anti-relaxation coated cells, the equilibrium cesium vapour density also depends on the complex coating dynamics with temperature and time. As studied in Li et al. (2017), the measured alkali density for a given temperature is often smaller than in uncoated cells.

The transverse coherence time measurement is perhaps the most involved part of the characterization. At times that cell production is being performed⁹, a quick measurement procedure is valuable. The coherence time measurement involves positioning the cell in a well-controlled homogeneous magnetic field and optically pumping the ensemble along the same direction. Experimentally, we have found that both conditions can be relaxed in our laboratory environment for typical encapsulated microcells: the observed transverse decay at room temperature is the same, regardless of magnetic shielding or optimal spin state preparation. The finding was shown to be valid both for 10 mm and 25 mm encapsulated cells. For encapsulations with bigger volume and increased spin lifetimes, the effects of magnetic field generated by nearby electronic components in the Free Induction Decay (FID) signal become evident. The maximum coherence time observed in unshielded environment is 15 ms. See Appendix G for details on the unshielded measurements.

⁶Due to diffraction of light through the channel aperture, the measured transmitted power might be position dependent. A ~ 30 cm distance should be enough to let the fast diverging contributions die out.

⁷See Appendix E for details on the absorption measurements, and Appendix H for cesium density parameters.

⁸See Appendix H for vapor density considerations

⁹We also note that, as far as vapour cell characterization goes, simpler laser configurations can be used, as the collinear method presented in (Chalupczak et al., 2010).

¹⁰Janis ST-100

4.3 Optomechanical system

As described in Chapter 2, the optomechanical system is implemented in a membrane-in-the-middle configuration. In this section, we briefly describe the construction of the cavity and sample holder. Here, we briefly point out some basic design principles. For a detailed description of the two generations of the cavity sample holders used in the hybrid experiments, we point out to Nielsen (2016), Møller (2018) and Mathiassen (2019). For extensive description of membrane fabrication and characterization, see Barg (2018) and Tsaturyan (2019).

The optomechanical system is positioned in a flow cryostat¹⁰, evacuated to 10^{-6} mbar residual pressure and connected to a liquid Helium-4 dewar. The cryostat contains two 0.5 inch diameter windows for optical access and feed-through connectors for electrical cables. Typical operation brings the mechanical mode of interest to a temperature of 7 K to 10 K.

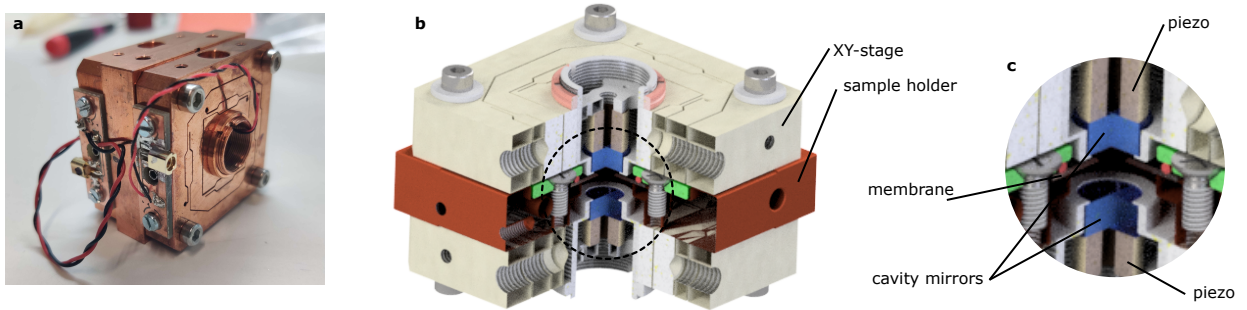


Figure 4.7: Hybrid experiment high-degree of freedom sample holder. The full construction is shown in **a**, along with the piezo control electric connections. In **b** we show a side cut of the holder and in **c** a zoom around the optomechanical cavity region. This figure has been adapted from Mathiassen (2019).

4.3.1 Cavity

The optomechanical cavity design considerations also involve the quality of the laser source in the experiment. As we wish to operate with shot noise limited light statistics, limiting the added classical laser noise to 1%, the maximum amount input photon flux is limited to order $100 \mu\text{W}$ at the 1 MHz Fourier frequency range, for a 2.5 W laser pump power (Møller, 2018). With the photon flux set, the cavity parameters can be adjusted to the experimental requirements. In general, the cavity length must be small for maximizing single photon coupling rate, as $g_0 \propto 1/L_{\text{cav}}$. On the other hand, an efficient optical cooling, required by hybrid matching conditions, works best for a cavity bandwidth on the same order of magnitude of ω_M , setting the total mirror transmissivity (including optical losses as scattering and absorption) to order 0.1%. The loss budget are set for single sided cavity, with the input mirror being much more transmissive than the back mirror. In the experiments presented in Møller et al. (2017), the cavity length is 1.3 mm and the cavity decay rate is $\kappa/2\pi = 25 \text{ MHz}$; in the entanglement experiments (Thomas et al., 2020) $L_{\text{cav}} = 2.6 \text{ mm}$ and $\kappa/2\pi = 3 \text{ MHz}$. The cavity over-coupling, the fractional leakage of intra-cavity photons in the optical mode of interest, is usually 90% to 95%.

4.3.2 Sample holder

The sample holder employed in the optomechanics setup is shown in Figure 4.7. The noble role of the sample holder is to keep a fixed relative position of the mirrors in respect to the membrane chip and to provide thermal contact between the cold bath and the mechanical oscillator. The specific design and configuration of the parts have been in constant development since the first cryogenic optomechanical experiments realized in the early 2010's, and that have been summarized in Nielsen (2016).

The basic philosophy of the early sample holder design employed in the optomechanics experiments orbited around passive stability. The various components are to be pressed and bolted down together, forming a solid piece that leaves minimal room for misalignments as the construction is cooled down. Having all components in close contact also ensures that thermalization to the cold bath temperature is possible. Lastly, as the motional noise of interest displays a order femtometer scale zero point fluctuations, the external vibrations must be efficiently damped to scales smaller than that at the Fourier frequency range of interest. In the latest sample holder design used in the hybrid ex-

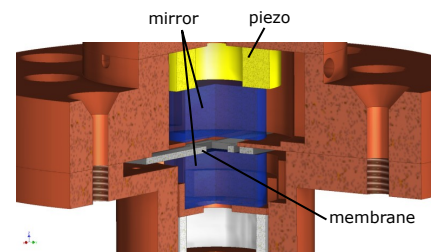


Figure 4.8: Sample holder design used in Møller et al. (2017). Here, one of the mirrors is glued to a piezo, allowing for cavity length tunability. The second mirror and the membrane are tightly clamped to the copper mount.

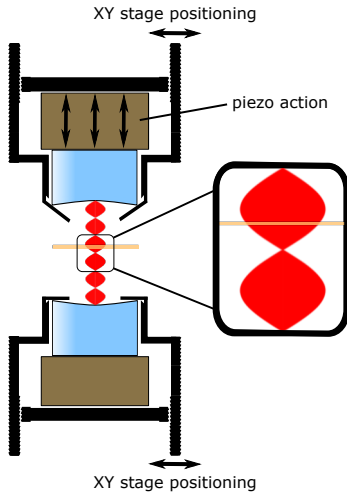


Figure 4.9: Controlling the membrane positioning and cavity length. Two piezoelectric elements actively control the cavity length and the membrane position in the intra-cavity standing wave pattern (see inset). This figure is not in scale. The membrane tilt adjustment is done moving the XY stages sideways. As both cavity mirrors are concave, lateral movements can tilt the optical mode to match the membrane's tilt. This figure has been adapted from Mathiassen (2019).

periment, the number of parts independently bolted to each other increased significantly, as we will see in the next pages. Nonetheless, passive stability is still a fundamental part of the design in use.

Let's now dive in the sample holder design. The designs used throughout the hybrid experiments require significantly more degrees of freedom than optomechanics-only experiment. As the spin ensemble requires a rather specific laser wavelength, set withing a couple of GHz, a hybrid-ready optomechanical system must be able to fulfil the conditions

condition 1: *a variable cavity length* L_{cav} . With a fixed laser wavelength, the cavity length must be externally controlled to ensure the incoming light will be allowed to couple into the cavity. Therefore, L_{cav} must be adjustable by order $\lambda/2 \sim 0.5 \mu\text{m}$ in order to reach the closest cavity resonance. Once close to the resonance condition, relatively fast small adjustment of its position must be possible to ensure a stable cavity detuning.

condition 2: *a variable membrane position in the intracavity standing wave pattern*. Given a fixed laser wavelength, the membrane position within the standing wave pattern will determine the optomechanical coupling and related effects, described in Chapter 2. Therefore, optimal performance will require the membrane to sit in a rather specific region of the $\lambda/2$ pattern. This degree of freedom also requires a control range on the order of $0.5 \mu\text{m}$, for arbitrary control of the coupling rate.

Another important feature of a good sample holder is the ability to control the membrane tilt in respect to the cavity mode. For all intents and purposes, the membrane is a piece of dielectric with non-zero reflectivity sitting in between two very good mirrors. Any tilt of the membrane plane from normal beam incidence will reflect light off the cavity mode, leading to an increase in optical cavity losses.

In the experiments presented in Møller et al. (2017), the cavity had a plano-concave cavity geometry, see Figure 4.8. The curved mirror was glued to a piezoelectric element, which itself was glued to one of the sample holder parts; this fulfilled the condition 1. The membrane was positioned $\sim 500 \mu\text{m}$ away from the flat mirror, separated by a tailor made silicon spacer. The position of the curved mirror in respect to the membrane-flat mirror construction could be adjusted to remove tilt losses. Although no other degree of freedom was introduced to fulfil the condition 2, we noticed that we could effectively randomly reshuffle the membrane position in the $2kz$ by thermal cycling the sample holder from 4 K to 80 K. Once back at base temperature, the membrane position was fixed. Achieving ideal position usually required a couple of thermal cycles. Although workable, depending on thermal cyclings for controlling $2kz$ position, one of the most important optomechanical parameters, is sub-optimal and has lead to a new sample holder design.

The new design, presented on Figure 4.7, has been used in the entanglement experiments. A completely new cavity and holder design were employed. The cavity, composed by two concave mirrors, has the membrane positioned at the beam waist position. Conditions 1 and 2 are fulfilled by clamping the mirrors between piezoelectric elements and a small lever, bending according to the force exerted by the piezo. Typically, one of the mirrors is used for cavity length feedback control and the other for $2kz$ adjustment. See Mathiassen (2019) for further details.

The sample holder update happened simultaneously with the update in membrane design, from a silicon 2D bandgap style to the new generation soft-clamped silicon nitride generation. Due to the relatively small defect in the new generation membranes, the higher order transverse cavity modes experience higher diffraction and optical losses due to the phononic structure. A tilted membrane mixes the TEM_{00} mode of interest to the lossy modes, increasing the decay rate of the mode of interest¹¹. The tilt alignment is done by series of screws and adjusters that move the mirrors transverse to the membrane plane, see Figure 4.9. In cryogenic experimental conditions, one of the piezos is

¹¹The coupling of different transverse cavity modes by a tilted membrane, in the membrane-in-the-middle configuration, has been studied in Sankey et al. (2010). Here, we are mostly interested in getting rid of the coupling, minimizing the overlap between the various modes.

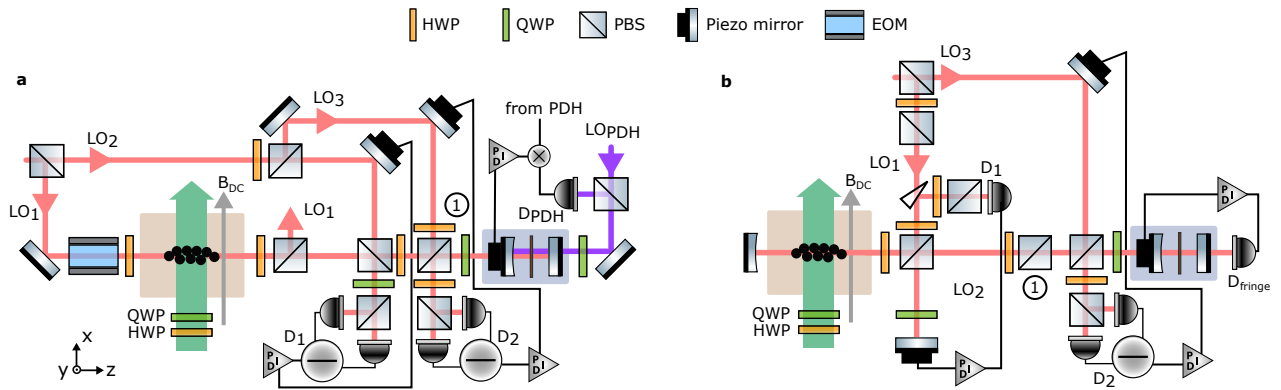


Figure 4.10: Experimental setups. The simplified representation of the hybrid experiment, including, local oscillators, polarization/power control, and detection. The piezo mirrors are the actuators for relative path length control. The setup in **a** was used in Møller et al. (2017), while **b** was implemented for Thomas et al. (2020). The numbered PBS 1 marks the element in which the spin response and LO₂ are projected into the same polarization mode. The purple line in **a** marks the cavity locking optical path. See Chapter 10 for further discussion and details.

fed with DC voltage, setting the membrane position in the intra-cavity standing wave pattern. The other piezo is actively controlled to stabilize the cavity length to a given detuning in respect to the incoming laser frequency.

4.4 Hybrid setup

The last part of hybrid setup to be described is the conversion between the optical modes the spins couple to the modes the optomechanics couple to. A simplified version of experimental setups are presented in Figure 4.10.

A major section of the hybrid experiment setup is related to the filtering of the spin response and addition of new local oscillators for optomechanical drive and final homodyning. In Figure 4.10, we see them as a set of nested interferometers and different local oscillators. Historically, we have been calling the strong spin classical drive LO₁; the mechanical analogous is LO₂, and the final homodyning local oscillator as LO₃. The local oscillators are manipulated using polarization optics such as wave plates and polarizing beam splitters throughout the entirety of the setup.

After the light has interacted with the spin ensemble, it is sent through a polarizing beam splitter for suppressing the local oscillator, here LO₁. As the spins scatter light in the orthogonal polarization to the drive, we can remove the carrier with extinction ratio on the order of 1 : 500, with minimal loss to the scattered light.

A new local oscillator LO₂, having a controllable path length difference in respect to LO₁, is overlapped with the light output from the atoms. This mode is sub-sequentially coupled to the optomechanical cavity, whose output is homodyned with a final local oscillator, LO₃. Note how we use polarization optics to direct light in the desired direction. Details on the operation of the hybrid setup are presented in Chapter 10.

While the 2017 experiments used mostly analog feedback to control the path length differences, which were detected interferometrically in the detectors D₁, D₂, D_{fringe}, and D_{PDH}, in the 2020 experiments it is made mostly digitally¹², with the aid of the PyRPL interface¹³. The interface provides low noise processing of signals and modules for locking interferometers and Fabry-Perot cavities. The processed signals are amplified via homemade amplifiers and sent to piezoelectric elements for feedback.

¹²Red Pitaya STEMLab 125-14

¹³documentationpyrpl.readthedocs.io

The data acquisition is made via a 30 MHz 4-channel analog-to-digital converter¹⁴, with $1 \times 10^{-14} \text{ V}^2 \text{ Hz}^{-1}$ dark noise from Fourier frequencies above 1 kHz.

With this, we finish the chapter describing the hardware and move on to the characterization discussions.

¹⁴Spectrum M2i.4931

Chapter 5

Spin State Preparation

The concept of effective spin mass — positive or negative — relies on the preparation of the ensemble in a given atomic state. Loosely speaking, the mapping from spin to harmonic oscillator physics relies only on a large collective spin polarization along the DC magnetic field. In our experiment, optical pumping towards the stretched Zeeman level $|F, m_F = \pm F\rangle$ creates spin polarization of the ground state manifold.

In this chapter, we describe the optical pumping stage and the spin state characterization via the Magneto Optical Resonance Signal (MORS) (Julsgaard et al., 2003). The MORS method allows extraction of the Zeeman decoherence rates and populations, as well as the Stark shifts induced by the laser beams, in a general spin- F system. We start by discussing the MORS modelling, along with the procedure to extract information from it. Focusing on the continuous wave operation, we consider the effects of selecting the optimal frequency for optical pumping beams and varying the vapor density. We also present the principles of a power-broadening-free optical pumping technique using microwave tones. Finally, we finish by studying the intrinsic noise related to a given Zeeman population distribution.

5.1 Magneto Optical Resonance Signal

The experimental setup is presented in Figure 5.1. Optical pumping lasers, as described in Chapter 4, prepare the spin state to be studied. As discussed in Chapter 3, due to the Faraday interaction, the spin ensemble induces optical polarization rotation proportional to the length of the spin in the probe direction.

In the MORS experiments, the spin component along the probe is induced by a weak RF magnetic field, orthogonal to the DC magnetic field, setting the mean spin to precess about its equilibrium position. A weak probe beam, far detuned from atomic resonance, probes the induced polarization rotation. In cw-MORS experiments, as the lasers and RF field are ran continuously, the information extracted is related to steady state dynamics. In pulsed experiments, the optical pumping, RF drive, and probe stages happen subsequently. The current chapter is devoted to the cw version; pulsed experiments are only used for estimating the spin state under the hybrid experiment conditions and is discussed in Chapter 11.

The magnetic field B_{dc} sets the Larmor frequency ω_S and the non-linear Zeeman splitting ω_{qzs} . The spin response is split in $2F$ resonances with natural frequency $\omega_{m+1,m}$, each with linewidth $\gamma_{m+1,m}$. For a linearly polarized input light field, the optimum signal-to-noise ratio for detecting Faraday rotation is achieved when detecting the orthogonal direction to the input in the polarization sphere (Deutsch and Jessen, 2010). In the Stokes parameter language, for a S_x input, detecting S_y is optimum. For an ensemble with N atoms, the MORS

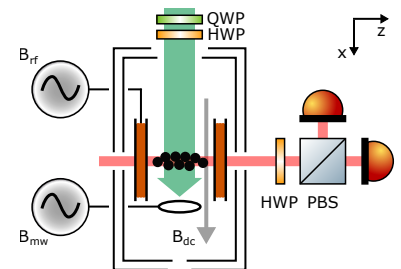


Figure 5.1: Experimental setup for atomic state characterization, including microwave drive. The atomic ensemble is positioned inside a magnetically shielded environment. Inside the magnetic shield, different sets of coils produce magnetic fields: the static field B_{dc} , and the oscillating B_{rf} ($\omega_{RF}/2\pi \sim$ MHz) and B_{mw} ($\omega_{MW}/2\pi \sim$ 9 GHz), RF field and microwave field, respectively. The microwave field is only used on experiments in Section 5.4.

(Julsgaard et al., 2003) response is

$$\text{MORS}(\omega) = c_0 \left| N \sum_{m=-F}^{F-1} \frac{(F(F+1) - m(m+1))(P_{m+1} - P_m)\gamma_{m+1,m}}{(\omega_{m+1,m} - \omega_{\text{rf}}) - i\gamma_{m+1,m}/2} \right|^2, \quad (5.1)$$

for P_m as the mean population of the m -th Zeeman level and c_0 as the proportionality constant relating the magnitude of the polarization rotation to the detected electrical signal¹. Due to the phase coherent drive, the detected signal is a phase sensitive quantity and can therefore be analysed in the polar form, with magnitude squared as presented (5.1), and phase extracted from the function before squaring. The expression (5.1) is valid for both continuous and pulsed probing.

Although general in result, the expression (5.1) contains many parameters that need to be extracted from the fitting procedure: populations P_m , frequencies ω_m , widths γ_m and c_0N . As discussed in (Julsgaard, 2003; Julsgaard et al., 2003), the practical effectiveness of the MORS method relies on a model with few free variables describing a complex structure. The commonly used version of (5.1) is

$$\text{MORS}_0(\omega) = c_0 \left| N \sum_{m=-F}^{F-1} \frac{(F(F+1) - m(m+1))(e^{\beta(m+1)} - e^{\beta m})\gamma_0}{(\omega_S + m\omega_{\text{vqs}} - \omega_{\text{rf}}) - i\gamma_0/2} \right|^2, \quad (5.2)$$

for β as the reciprocal spin temperature. This version reduces the number of free fitting variables from 26 to 5 and is extensively used in the group (Julsgaard, 2003; Sherson, 2006; Jensen, 2011; Krauter, 2011). The assumptions that lead to (5.2) are

1. **spin temperature distribution.** The steady state population distribution among the Zeeman levels is determined by the various decay and decoherence processes the atoms experience within the vapour cell. In general, contributions are alkali collisions with other alkali atoms, with buffer gases, with the container walls and interaction with laser beams/optical pumping. As initially shown in the early '60s (Anderson and Ramsey, 1963) and discussed in Appelt et al. (1998), if the rate of spin exchange collisions is much bigger than any other spin relaxation rate, the Zeeman level populations follows the *spin temperature distribution*, with density matrix

$$\rho_{\text{th}} = \frac{e^{\beta\hat{F}_x}}{Z}, \quad (5.3)$$

for $Z = \text{Tr}[e^{\beta\hat{F}_x}]$ as the partition function. In this case, the populations follow an exponential function $P_m = e^{\beta m}$ and the only parameter to be determined is $\beta = 1/k_B T_S$, with T_S as the *spin temperature*.

2. **equal linewidths γ_m .** The decay of the spin coherence² is affected by collisions and dephasing, e.g. due to inhomogeneous magnetic fields. Some of the population decay contributions described affect Zeeman coherences differently (Savukov and Romalis, 2005). Spin exchange and optical pumping interactions follow conservation rules which lead to m_F dependent linewidths. The collision of alkali-atoms with the anti-relaxation coating leads to electron spin flips, conserving the nuclear spin state, and total spin randomization collisions (Corsini et al., 2013). The relative weight of these contributions are highly vapor cell dependent and need to be characterized for each case individually.
3. **uniform line separation.** Off-resonant interaction with laser light leads to Stark shifts in the ground state levels. In the limit of vanishing optical power, the resonances are equally spaced $\omega_{m+1,m} = \omega_S + m\omega_{\text{qzs}}$. The presence of light induces shifts to the lines in respect to each other, competing with the quadratic Zeeman splitting.

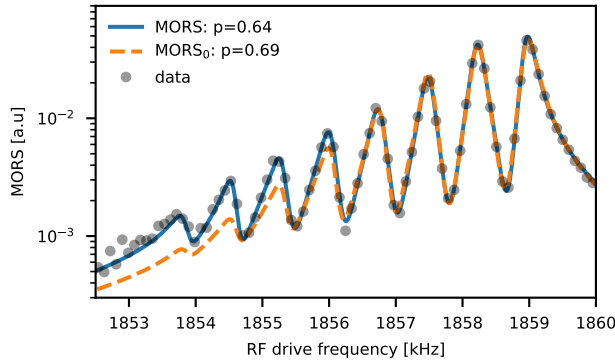


Figure 5.2: Comparing MORS models. The models presented equations (5.1) (blue) and (5.2) (orange) are fitted to signal (see Section 5.3 for details) from a 30 °C spin ensemble. The fitting procedure weighs residuals linearly. Data is downsampled for clarity.

Given the assumptions described above, the choice of fitting model is a function of the experimental conditions. In our experimentally available alkali densities, nonetheless, spin exchange is not the most dominant contribution. In the absence of light, interaction with the container walls contribute as much as atomic collisions. Moreover, in the hybrid experiments, the transverse decay and population relaxation are dominated by the lasers, decay processes which also affect some levels more than others. As it will be clear from the discussion in the next sections, the Zeeman populations P_m are free parameters. Further improvements of the agreement of fits with the data can be achieved by setting the linewidths $\gamma_{m+1,m}$ as free parameters. There are usually ~ 10 to 15 free parameters in a MORS fit.

Using MORS_0 , and therefore the spin temperature distribution, not only reduces the number of free variables in a fit, but also gives a rather simple way of calculating the spin polarization p : given the parameter β , the spin polarization is the relative size of the mean spin along the magnetic field axis

$$p = \frac{\langle F_x \rangle}{F} = \frac{1}{F} \text{Tr}[\rho_{\text{th}} F_x] = \frac{1}{F} \sum_m m e^{\beta m}. \quad (5.4)$$

When the spin temperature distribution is not valid, as in equation (5.1), the simplicity is lost and a new issue appears: the number of parameters P_m is bigger than the number of independent variables obtained from the fitting procedure, that is $P_{m+1} - P_m$, being nine versus eight in total. This system of equations has no unique solution. To solve this issue, we therefore assume that one of the extreme $m_F = \pm F$ levels is unpopulated, allowing for a unique solution. This assumption should be valid already for moderate spin polarization values (on the order $p \sim 0.5$), cases in which the population in one of the extreme m_F levels is negligible.

In Figure 5.2, we compare the curve fitting of the two MORS models, equations (5.1) and (5.2). It is clear that the spin temperature assumption does not reproduce the experimental result faithfully. Note how the MORS_0 model fails to account for population distribution in the smallest peaks³. On the range of temperature and laser powers used throughout, the extracted spin polarization absolute errors are commonly up to 5% off when using the MORS_0 model. Given the importance of this parameter—it is directly linked to the effective spin bath occupation and Faraday angle—systematic errors of this kind are potentially of great consequence.

With the model introduced, we proceed to the study the Zeeman population distribution with respect to optical pumping transitions and vapor density.

¹Although the procedure to derive (5.1) presented in (Julsgaard, 2003) includes the quadratic Zeeman splitting by hand in the final result, it can also be taken into account in the Hamiltonian formulation presented on Chapter 3.

²In analogy to the Nuclear Magnetic Resonance (NMR) experiments, we define the relation of the decay rate (FWHM) to the coherence time as $\gamma_m/2\pi = 1/(\pi T_2)$. We typically do not differentiate between single particle and ensemble decay rate.

³The fitting procedure and residuals' weighing plays a big role on extracting parameters faithfully. As the magnitude of the data varies by approximately 2 orders of magnitude, weighing residuals linearly will focus on the features with biggest absolute value. Weighing them logarithmically gives bigger importance for small values. We have tried both strategies for the data on Figure 5.2: the procedure returns $p = 0.59$ in the case of log weighing of the MORS_0 model (result not shown).

5.2 Optical pumping transition

Optical pumping is the process of exciting electrons from a low to a higher electronic energy level via coupling to light. It has been used throughout the atomic physics community to study and prepare atoms and molecules in the most diverse electronic states. We refer to Franz (1966) and Happer (1972) for the seminal description of the various physical concepts involved; to Happer and Van Wijngaarden (1987) for a pedagogical introduction, and to Atoneche and Kastberg (2017) for numerical implementation of the problem.

In a great deal of experiments shown in this document, the optical pumping involves only a circularly polarized repumping beam. The repump laser is responsible for the hyperfine pumping, that is, transferring atoms from the $F = 3$ to $F = 4$. Traditionally, a circularly polarized pumping beam is also used to ensure atoms are in the stretched state $|F = 4, m_F = 4\rangle$. As it acts directly on the coherences of interest, it causes broadening of the Zeeman line. In the hybrid experiments, the total spin bandwidth is required to approximately the mechanical oscillator, the pump beam use is rather limited. We are therefore left to optimize the optical pumping with a single repump laser.

The choice of optical repumping transition greatly affects the $F = 4$ steady state population distribution. In Figure 5.3 we show the MORS for different repump laser locking points. While all the transitions are well within the Doppler broadened absorption profile, the prepared steady spin state has a bigger spin polarization for the case $F = 3 \rightarrow F' = 2$.

The best state preparation performance being achieved for the $F = 3 \rightarrow F' = 2$ transition might seem puzzling, given that considering the electric dipole selection rules atoms in the $F' = 2$ manifold can not decay to $F = 4$. Although a complete modelling of the effect has not yet been performed, we argue that the seemingly non-trivial optimum involves off-resonant optical transitions, atomic motion and alkali spin-exchange interaction, and goes as follows.

Although the $F' = 2 \rightarrow F = 4$ decay channel is forbidden, repumping to the $F' = 3, 4$ excited state manifolds is possible: resonantly for some, those moving towards the beam in a certain velocity class, off-resonantly for the remaining. There are, therefore, two processes happening in parallel: (i) atoms are cycling within the $F = 3$ manifold via the excited state $F' = 2$, and (ii) atoms off-resonantly coupling to $F' = 3, 4$ and decaying back to the ground states. As the former process is stronger than the latter, atoms will experience a number of repumping cycles moving on average up in m_F , due to the absorption of circularly polarized photons. Eventually, when they do end up going to $F = 4$, they will have an angular momentum projection that is closer to maximum allowed.

Atoms within the $F = 4$ manifold will distribute themselves according to the Zeeman population decay rates, which happen due to interaction with the walls, other alkali and the probing laser. It has been shown that spin-exchange collisions are an important factor for the steady state population distribution in paraffin coated vapour cells. The collisions preserve total electron spin and all states apart from $|4, \pm 4\rangle$ are affected by it. With the aid of a repumping beam, spin polarizations of up to 92% have been observed when the spin exchange collision rate dominates over the total Zeeman population decay rates (Chalupczak et al., 2012).

Coupling the long lived ground state to an excited electronic state with lifetime limited by spontaneous emission causes decoherence, here called *power broadening*. The repump laser power, for example, although ~ 9 GHz detuned from $F = 4$, can also induce power broadening. In the experiments, the repump power is adjusted such that the $F = 3$ manifold is emptied and no significant broadening is observed in the coherences of interest.

Improving the spin polarization above $p \sim 0.7$ requires coupling to atoms in the $F = 4$ manifold. While effective in transferring atoms to a stretched state, for example, optical pumping comes with the cost of dampening the ground level coherence. The standard approach is to use a circularly polarized light resonant with $F = 4 \rightarrow F' = 4$ on the D_1 line, directly coupling to the $|4, 4\rangle \rightarrow$

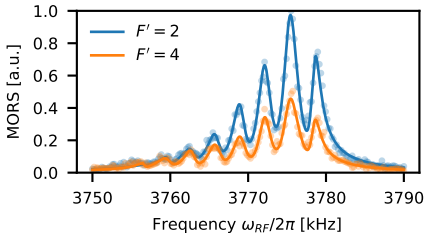


Figure 5.3: Optical pumping efficiency for different D_2 line repump locking transitions. The spin polarization increases from $p = 0.54$, when the repump laser is tuned from $F = 3 \rightarrow F' = 4$, to $p = 0.65$ for $F = 3 \rightarrow F' = 2$.

$|4, 3\rangle$ transition as a side effect. Alternatively, pumping on the $F = 4 \rightarrow F' = 3$ spares the aforementioned coherence. Nonetheless, perfect stretched state preparation is not possible, as $|4, 2\rangle$ is also a dark state for circularly polarized light. The effect is strong when using a pump laser, see Figure 5.4.

The ideal optical pumping cycle would move atoms from unwanted Zeeman levels to the stretched state with no added broadening. In Section 5.4, we discuss the usage of microwave fields to selectively couple levels across hyperfine manifolds, therefore controllably introducing decoherence.

5.3 Density dependent optical pumping

The temperature affects the alkali vapor pressure inside the glass cell. As shown in Appendix H, the increase in vapor pressure leads to a higher density and more frequent atomic collisions. The physics of atomic collisions are rich, and we do not intend to cover them here. For an extensive review of alkali collisions on vapor cells, we point to Happer (1972), Happer and Van Wijngaarden (1987) and Appelt et al. (1998). It suffices to say that one of these collision processes is the *spin exchange collisions*, a process in which alkali atoms interact as they get in close proximity.

In Figure 5.5 we show the density dependent MORS signal, as the cell temperature is varied from $\sim 55^\circ\text{C}$ to $\sim 30^\circ\text{C}$. The curves have been fitted to the model on equation (5.1). The decrease in atomic density leads to a signal scaled by the total number of atoms, the resonant features that become narrower, and the frequencies shift. This is a signature of spin collisions, which is further explored in Figure 5.6. The broadening of the resonances with atomic density can be seen in Figure 5.5 (right), in which we have compared the signals with 55°C to $\sim 30^\circ\text{C}$. The change in linewidths is evident on the depth of the signal in between consecutive resonances. Up to this moment, we do not have a clear explanation for the observed effects.

In Figure 5.6 (left) we show the change in linewidth of the four extreme-most lines, labelled according to the m_F coherences. It is noticeable how the $|4, 4\rangle \rightarrow |4, 3\rangle$ coherence is more resilient to density changes. From the atomic density series it is also possible to extract the linewidth in the dark and in the absence of spin-spin collisions, being $\gamma_{S0}/2\pi = 250$ Hz. The change in density is followed by a change in spin polarization, increasing by $\sim 5\%$ over the range explored.

According to Appelt et al. (1999), the spin exchange collision contribution to the Zeeman decay rate γ_{F,m_F} of the coherence $|F, m_F\rangle\langle F, m_F - 1|$ for an ensem-

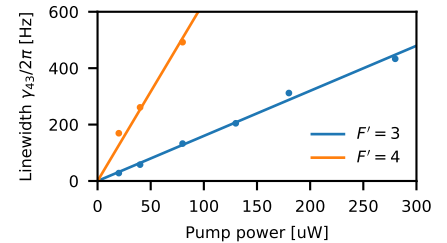


Figure 5.4: D₁ pump induced power broadening. A pump laser directly couples to the Zeeman coherence of interest, here shown as the induced broadening on the $|4, 4\rangle\langle 4, 3|$ coherence. Pumping on the D₁ line, $F = 4 \rightarrow F' = 4$ transition, directly couples to this coherence; tuning the laser to the $F = 4 \rightarrow F' = 3$ reduces the effect.

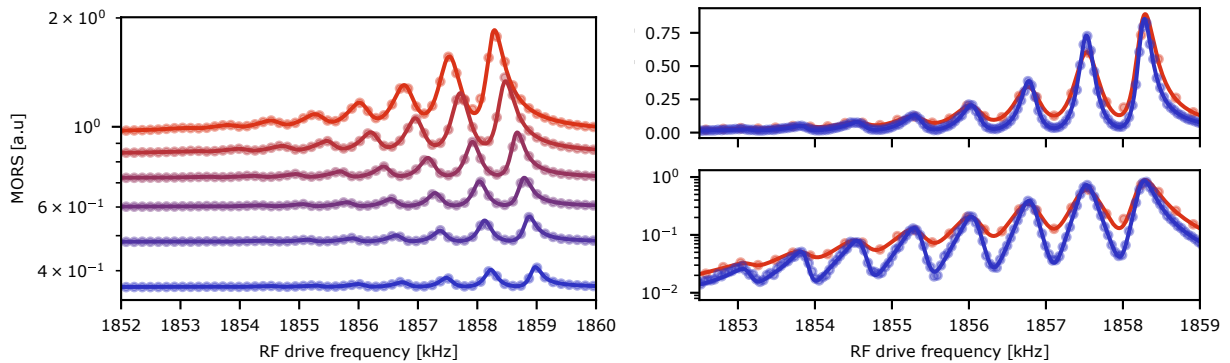


Figure 5.5: Density dependent MORS signal. (left) As the temperature of the cell is decreased from $\sim 55^\circ\text{C}$ to $\sim 30^\circ\text{C}$ (top to bottom), the signal decreases in size and shifts in frequency. (right) Comparison of the signal at the maximum and minimum measured density. Data has been shifted, rescaled, and resampled for clarity.

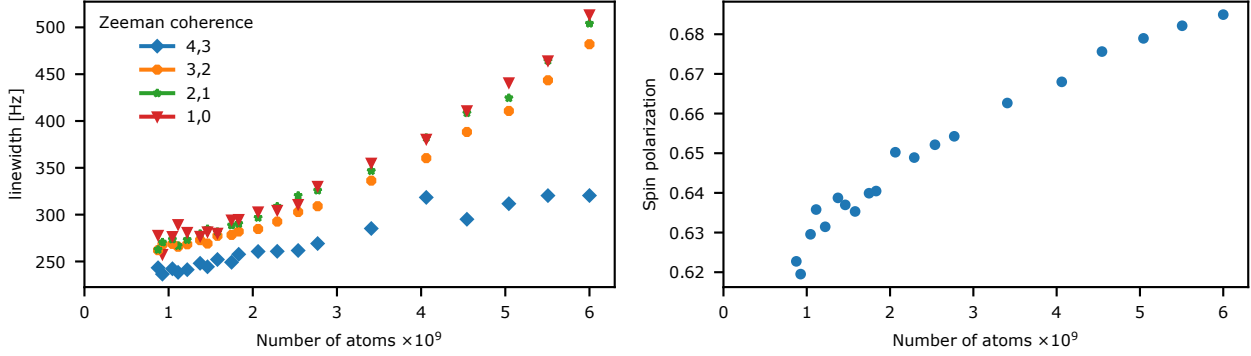


Figure 5.6: Density dependent spin polarization and transverse coherence time. (left) Increasing with the number of atoms leads to more frequent collisions between atoms and/or other buffer gasses, increasing the decoherence rate. (right) The collisions do not only change the decoherence rate, but also affect the population distribution.

ble with spin polarization p , is

$$\gamma_{Fm_F}/2\pi = 2R_{\text{ex}} \left(\frac{3[I]^2 + 1 - 4\bar{m}_F^2}{4[I]^2} - p \frac{\bar{m}_F}{[I]} - Q_{\bar{m}_F} \frac{[F]^2 - 4\bar{m}_F^2}{4[I]^2} \right) \quad (5.5)$$

where $[F] = 2F + 1$, $[I] = 2I + 1$, $\bar{m}_F = m_F - \frac{1}{2}$ and

$$Q_{\bar{m}_F} = \frac{2p(1+p)^{I+\bar{m}_F}(1-p)^{I-\bar{m}_F}}{(1+p)^{[I]} - (1-p)^{[I]}}.$$

Here, $R_{\text{ex}} = \rho v_{\text{th}} \sigma_{\text{se}}$ is the spin exchange collision rate, set by the atomic density ρ , the Cesium atom mean thermal velocity $v_{\text{th}} = \sqrt{8k_B T / \pi m}$ and the spin-exchange cross section $\sigma_{\text{se}} = 2 \times 10^{-14} \text{ cm}^2$ (Seltzer, 2008).

The expression (5.5) is valid for spin-exchange limited dynamics, that is, the same limit in which the spin-temperature distribution applies. As we already seen from the model discussion, and also from with linewidths presented on Figure 5.6, there are other collision processes that play important roles in our case. Nonetheless, we use equation (5.5) as a guiding rule for estimating the effects of spin exchange in the experiments and show that it provides qualitative agreement.

Let us examine equation (5.5). First of all, in the limit of perfect spin polarization, $p \rightarrow 1$, $Q_{\bar{m}_F} \rightarrow \delta_{\bar{m}_F, I}$ and $\gamma_{44} \rightarrow 0$. Therefore, in this limit spin exchange collisions cause no broadening. For all other values of spin polarization, the decay rate is m_F dependent and linear on the atomic density. The spin collision rate at 60°C is $R_{\text{SE}} \sim 500 \text{ Hz}$, which for $p = 0.7$ would give $\gamma_{44}/2\pi \sim 50 \text{ Hz}$, close to the increase observed in Figure 5.6. The coherences that include smaller m_F 's are more affected by the collisions, differing from the prediction. We also observe a rather non-linear scaling of the widths, for which up to now we have not found a satisfactory explanation.

5.4 Microwave assisted optical pumping

The ideal optical pumping method for our cw hybrid experiments would be a process that increases spin polarization with minimal added power broadening. We have seen that a pump laser resonant with $F = 4$ adds significant broadening to the Zeeman lines. Here, we show that microwave radiation can be used to improve the spin polarization of the ensemble, adding negligible broadening.

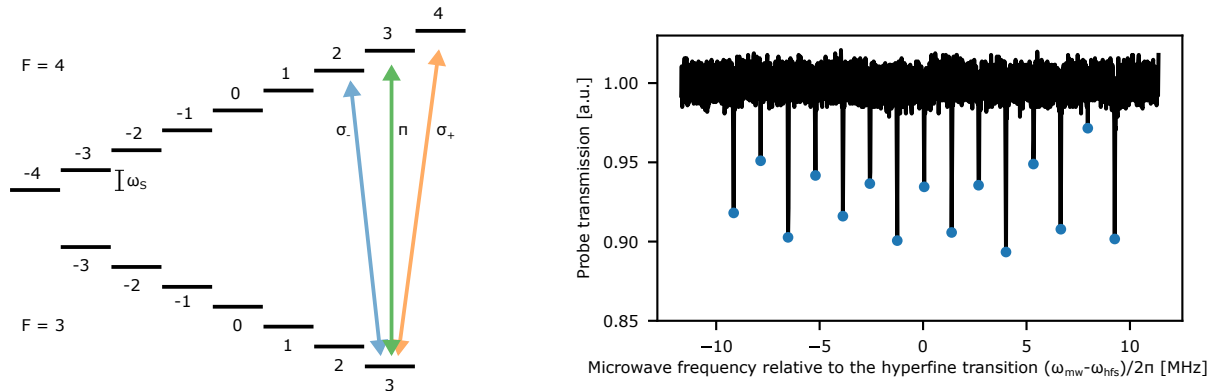


Figure 5.8: Hyperfine microwave spectroscopy. (left) The Zeeman levels are split in the presence of a static magnetic field. Due to opposite gyromagnetic ratios, the $F = 3$ and $F = 4$ energy ladder have opposite slopes. A microwave tone can couple the hyperfine manifolds according to its polarization with respect to the magnetic field: $\Delta m = -1(1)$ for left (right) handed circular polarization in blue (yellow), and $\Delta m = 0$ for π polarized photons. (right) Optical absorption measurement with a microwave tone scanned over the ground state transitions, around the $0 - 0$ hyperfine transition frequency ω_{hfs} . The polarization of the microwave field is a mixture of π and σ_{\pm} . The 15 possible transitions, separated by a Larmor energy unit $\omega_S/2\pi = 1.32$ MHz are excited.

The basic idea of the microwave assisted optical pumping is presented in Figure 5.8. In the first step, a circularly polarized repump laser empties the $F = 3$ manifold. Shortly after, a microwave drive, with a given frequency and polarization, couples Zeeman levels from different hyperfine manifolds, $|4, 2\rangle \rightarrow |3, 3\rangle$ for example. The intensity of the microwave field is chosen such the population is transferred via a π pulse to $|3, 3\rangle$. The repump laser then immediately optically pumps the atom back to the $F = 4$ manifold, reshuffling the population according to the spontaneous decay branching. This technique is specially suited for cases in which the DC magnetic field splits the Zeeman levels by many hundreds of kHz, allowing for addressing any pair of levels (which are allowed by the selection rules) via suitably polarized microwave fields.

In the experiments, decay processes reshuffle the atomic distribution, both within and across the hyperfine levels, with order $\gamma_{1,\text{hf}}/2\pi = 1/\pi T_1 \sim 200$ Hz⁴, in the dark. An efficient population transfer requires microwave and optical pumping rates being much bigger than the population decay rates. The microwave power is delivered by a microwave antenna, positioned approximately at 5 cm from the vapor cell, pointing along the static magnetic field direction.

We start by characterizing the microwave transitions. The microwave spectroscopy experiment are similar to (Budker et al., 2005), and described in detail in (Zugenmaier et al., 2018) for vapour cells with geometry and characteristics close to the used here. The total transmission of a weak probe beam, 1 μ W in power and on resonance with the $F = 4 \rightarrow F'$ transition ($\lambda = 852.3560$ nm), is monitored. The transmission signal, normalized to the signal without microwave pumping, is shown in Figure 5.8. The microwave tone, scanned around the ground hyperfine Zeeman transitions, alters the equilibrium population distribution, leading to change in absorption. The observed 15 peaks correspond to the all possible $\Delta F = 1, \Delta m = 0, \pm 1$ microwave transitions, all separated by $\omega_S/2\pi = 1.32(1)$ MHz, the Larmor energy splitting induced by the static magnetic field in this experiment. The linewidths were similar for all the transitions, $\gamma_{2,\text{hf}}/2\pi = 19(1)$ kHz.

The effect of the microwave drive on the steady state population distribution can be measured via MORS. Setting the probe power to 10 μ W and a weak repump power of 10 μ W, we probe the ensemble with and without the mi-

⁴This rate is typical for a high-temperature C30 paraffin coated cells. Alkene coated cells with the same geometry, on the other hand, can show much slower population decay $\gamma_{1,\text{hf}}/2\pi \sim 20$ Hz (Shen, 2014).

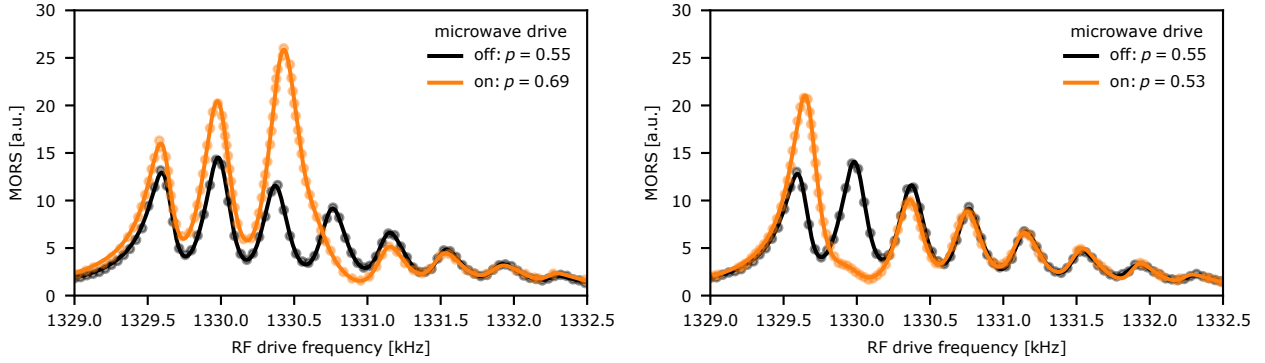


Figure 5.9: MORS with microwave drive. Depending on the chosen microwave transition, the populations are going to be affected differently. Setting the microwave frequency to $\omega_{\text{mw}}/2\pi = 9195.31$ MHz (right) has a smaller effect on the spin polarization than the setting $\omega_{\text{mw}}/2\pi = 9199.29$ MHz (right).

crowave tone. In Figure 5.9, the frequency $\omega_{\text{mw}}/2\pi = 9195.31$ MHz (left) and $\omega_{\text{mw}}/2\pi = 9199.29$ MHz (right), corresponding to the transitions $|4, 1\rangle \rightarrow |3, 1\rangle$ and $|4, 3\rangle \rightarrow |3, 2\rangle + |4, 2\rangle \rightarrow |3, 3\rangle$, respectively. The microwave coupling alters significantly the population distribution, increasing the spin polarization from $p = 0.55$ to $p = 0.69$ for the data shown on Figure 5.9 (left).

For Figure 5.9 (right), even though one of the Zeeman resonances is almost fully suppressed, the spin polarization is quite unchanged. This curious effect is can be seen directly from the MORS theoretical model, in equation (5.1). The peak heights are proportional to the population differences squared, $|P_m + 1 - P_m|^2$. Therefore, if the population of two neighbouring levels is brought to similar levels, there will be no peak, even though there is a potentially high number of atoms on those Zeeman levels.

Although the microwave assisted optical pumping showed possibility of increasing the spin polarization without broadening the coherences of interest in the first principles experiments shown above, it failed to give meaningful results in the parameter regime of interest. In the hybrid experiment conditions, overcoming the optical pumping and decoherence induced by the probe beam required more microwave power than the available at the time. The maximum available power was 30 dBm. Alternatively, instead of the microwave drive, an optical Raman transition could be used.

5.5 Effective thermal occupation

The Zeeman state population distribution defines not only the spin polarization p , but also sets the effective excitation temperature T_s and the related extra spin noise. As we will see in the end of this section, we like to define the extra spin noise as giving an effective thermal occupation n_s to the spin oscillator.

Consider, for example, a spin- $\frac{1}{2}$ ensemble with ground and excited states g and e with populations $P_g = e^{-\beta/2}$ and $P_e = e^{\beta/2}$, respectively. The state populations and the spin temperature are linked via equation (5.3).

$$P_e/P_g = e^\beta, \quad (5.6)$$

where $\beta = 1/k_b T_s$. The temperature of the spin system is determined by the ensemble population distribution.

Notice that the concept of spin temperature must not be confused with the thermodynamic concept of temperature, established via the equipartition theorem. While the latter relates to the average energies of the system's degrees of

Effective thermal occupation

freedom, the former is solely defined by the average occupation of the energy levels, as given by equation (5.6). This definition can lead to seemingly absurd results. The spin temperature in a laser gain medium, for example, is negative due to population inversion⁵

The aspects of finite temperature in the spin system are captured within the Heisenberg-Langevin formalism, which has been used to describe the dynamics of the spin system in Chapter 3. For a spin- F system, described by the set of operators $\hat{A}_1, \dots, \hat{A}_N$, the time evolution will be governed by (Davidovich, 1996)

$$\frac{d}{dt} \hat{A}_i = \text{function}[\hat{A}_1, \dots, \hat{A}_N] + \hat{F}_i(t).$$

In our case, the function of the system operators $\hat{A}_1, \dots, \hat{A}_N$ is determined by the coupling to light and magnetic fields, as described in Chapter 3, equation (3.28). We picture the spin oscillator precession being driven externally by forces that act on the transverse spin state components, which themselves play the role of generalized position and velocity. Upon interaction with the environment, the trajectory is affected by random Langevin forces \hat{F}_i , leading to a diffusion-like dynamics of the spin states. Similar approaches, in the context of spin oscillators, were studied in Vasilyev et al. (2012) and in Vasilyev et al. (2013).

Given that we are monitoring the noise properties of spin dynamics continuously over time, we are interested in how the correlations of spins evolve with time. In the limit of a memoryless bath, the forces $\hat{F}_i(t)$ satisfy

$$\langle \hat{F}_i(t) \rangle = 0 \quad (5.7)$$

$$\langle \hat{F}_i^\dagger(t) \hat{F}_i(t') \rangle = 2D_{ij} \delta(t - t'), \quad (5.8)$$

with D_{ij} as the diffusion coefficient. To calculate D_{ij} we use the *generalized Einstein relations* (Davidovich, 1996)

$$2D_{ij} = \left\langle \frac{d}{dt} (\hat{A}_i^\dagger \hat{A}_j) - \left(\frac{d}{dt} \hat{A}_i \right)^\dagger \hat{A}_j - \hat{A}_i^\dagger \frac{d}{dt} \hat{A}_j \right\rangle. \quad (5.9)$$

We would like to calculate the noise related to the evolution of our spin system. For that we will need the equations of motion described in Chapter 3. The dynamics of the spin system is presented in equations (3.28). The mean spin component $\langle \hat{F}_x \rangle = F_x$ is here assumed to be a classical variable, in connection to the Holstein-Primakoff approximation. For the case of a spin- $\frac{1}{2}$ description of the spin ensemble, the diffusing operators \hat{A}_i are the transverse spin components \hat{F}_y and \hat{F}_z . The diffusion coefficients are calculated as

1. $2D_{yy}$. For this case $A_i, A_j \rightarrow \hat{F}_y$. From equation (5.9), we have

$$\left\langle \frac{d}{dt} (\hat{F}_y \hat{F}_y) - \left(\frac{d}{dt} \hat{F}_y \right) \hat{F}_y - \hat{F}_y \frac{d}{dt} \hat{F}_y \right\rangle. \quad (5.10)$$

Using the equations of motion, each of the terms in the equation above are

$$\begin{aligned} \frac{d}{dt} \hat{F}_y^2 &= 0 \\ \left(\frac{d}{dt} \hat{F}_y \right) \hat{F}_y &= -\omega_S \hat{F}_z \hat{F}_y + g \hat{F}_x \hat{F}_y - \gamma \hat{F}_y^2 / 2 \\ \hat{F}_y \left(\frac{d}{dt} \hat{F}_y \right) &= -\omega_S \hat{F}_y \hat{F}_z + g \hat{F}_y \hat{F}_x - \gamma \hat{F}_y^2 / 2. \end{aligned}$$

⁵As Abragam and Proctor point out: “there does not seem to exist among physicists a universal agreement as to the validity of the concept of spin temperatures, positive or negative. While some consider this concept as perfectly natural and requiring no more justification than, say, the temperature of a crystal lattice or a gas, others think that it lacks the deep physical meaning of thermodynamic temperature and is at best useless and often greatly misleading” (Abragam and Proctor, 1958).

Plugging the results above in equation (5.10), we have

$$2D_{yy} = \gamma \langle \hat{F}_y^2 \rangle. \quad (5.11)$$

2. $2D_{zz}$. For this case $A_i, A_j \rightarrow \hat{F}_z$. Applying same reasoning of the previous case, the diffusion constant is

$$2D_{zz} = \gamma \langle \hat{F}_z^2 \rangle \quad (5.12)$$

The diffusion coefficient of the spin variable is proportional to the variance of the transverse spin component. In particular, using the angular momentum relations (A.9) we can write (5.16) as

$$\begin{aligned} 2D_{zz} &= \gamma \text{Tr}[\rho \hat{F}_z^2] \\ &= \frac{\gamma}{2} (\text{Tr}[\rho \hat{F}_x] + \text{Tr}[\rho \hat{F}_- \hat{F}_+]), \end{aligned} \quad (5.13)$$

with the same relations applying for $2D_{yy}$.

The spin state variance can be calculated with the knowledge of the density matrix. The relations for the diffusion coefficients shown above also valid for spin systems with total angular momentum $F > \frac{1}{2}$ (Appelt et al., 1998). If the population distribution follows the spin temperature density matrix (5.3), we can calculate analytical expressions. For $2D_{zz}$, for example, a spin temperature distribution ρ_{th} gives

$$\text{Tr}[\rho_{\text{th}} \hat{F}_x] = \sum_m \langle m | \rho_{\text{th}} \hat{F}_x | m \rangle = \sum_m m \langle m | \rho_{\text{th}} | m \rangle = \frac{1}{Z} \sum_m m e^{\beta m} \quad (5.14)$$

$$\text{Tr}[\rho_{\text{th}} \hat{F}_- \hat{F}_+] = \sum_m \langle m | \rho_{\text{th}} \hat{F}_- \hat{F}_+ | m \rangle = \frac{1}{Z} \sum_m c(F, m)^2 e^{\beta m}, \quad (5.15)$$

such that the diffusion coefficients are

$$2D_{yy} = 2D_{zz} = \frac{\gamma}{2Z} \sum_m e^{\beta m} (F(F+1) - m^2). \quad (5.16)$$

We also note that the equation (5.14) gives the mean spin component for a given inverse temperature β . The decay constant γ_S is a proportionality constant relating the spin dependent summation and the diffusion, so we will drop it for now. Note how we have already used a similar result in Chapter 3, when discussing about the spectral components of the spin noise, see Section 3.5.

For clarity of the derivation presented above for the diffusion coefficients and their connection to the spin temperature, let us consider a couple of examples of different spin systems. For the case of

1. a *spin- $\frac{1}{2}$ system*, the diffusion coefficients from equation (5.16) are

$$2D_{yy} = 2D_{zz} = \frac{1}{4Z} \sum_m e^{\beta m} = \frac{1}{4} \quad (5.17)$$

Therefore, the diffusion coefficients for the spin- $\frac{1}{2}$ system are not affected by the spin temperature parameter. The spin polarization of the ensemble, that is

$$p \equiv \frac{\hat{F}_x}{F} = \frac{1}{F} \text{Tr}[\rho \hat{F}_x] = \frac{1}{ZF} \sum m e^{\beta m} = \tanh \frac{\beta}{2}, \quad (5.18)$$

is a function of the spin temperature.

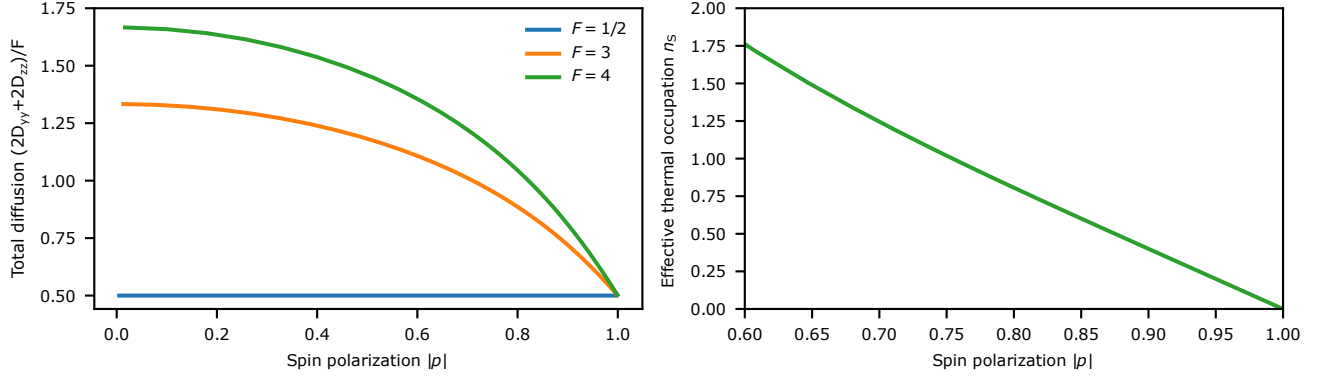


Figure 5.10: Total diffusion and effective thermal occupation n_S as a function of spin polarization. (left) The total diffusion coefficient (in units of γ) induced by coupling the spin ensemble to a spin thermal reservoir depends on the total spin F . In general, the bigger the total angular momentum F , the bigger is the incremental effect of a small spin polarization change. For perfect spin polarization, the ensemble has minimum variance. (right) When the Holstein-Primakoff mapping is performed, we transform the transverse spin noise into an effective occupation of the harmonic position and momentum variables.

2. *a spin- F system*, the overall situation gets more complicated. The expressions for spin polarization (5.14) and diffusion coefficients (5.16) get more complicated, due to the weighted sum of exponential functions. In Figure 5.10 (left), we show the dependency of the diffusion as a function of the spin polarization for various spin- $\frac{1}{2}$, discussed above, and spin-3 and spin-4, the total angular momentum of the ground state manifolds in cesium. Overall, the limiting cases can be worked out directly from quantum angular momentum relations (see Appendix A). For example, for

- for $|p| = 1$, all spins are aligned and we are in the state of minimum variance, the ground state. This state is also called a coherent spin state. At the ground state, we can use the Heisenberg Uncertainty relation

$$\langle \hat{F}_y^2 \rangle \langle \hat{F}_z^2 \rangle = \frac{1}{4} |\langle [\hat{F}_y, \hat{F}_z] \rangle|^2 = \frac{1}{4} |\langle \hat{F}_x \rangle|^2 = \frac{F^2}{4}. \quad (5.19)$$

The minimum uncertainty state has equal variances in its both variables, that is, $\langle \hat{F}_y^2 \rangle = \langle \hat{F}_z^2 \rangle = \frac{F}{2}$, which is $\frac{1}{2}$ when normalized to F .

- for $|p| = 0$, we are in a completely mixed state. From the total angular momentum relation $\langle \hat{\mathbf{F}}^2 \rangle = F(F+1)$, we obtain

$$\langle \hat{F}_x^2 \rangle + \langle \hat{F}_y^2 \rangle + \langle \hat{F}_z^2 \rangle = F(F+1). \quad (5.20)$$

For a completely mixed state, we expect equal variances in all possible directions, which lead to $\langle \hat{F}_x^2 \rangle = \langle \hat{F}_y^2 \rangle = \langle \hat{F}_z^2 \rangle = \frac{F(F+1)}{3}$, which is $\frac{F+1}{3}$ when normalized to F .

3. *mapping the diffusion coefficient to effective thermal occupancy n_S* . Having calculated the diffusion coefficients, which are shown in Figure 5.10 (left), we would like to map the extra diffusion into an effective thermal occupancy of the effective position and momentum spin operators. For notation symmetry, when comparing to the case of a mechanical oscillator coupled to a thermal bath, we call the extra spin occupancy n_S . This is the case we deal with in the hybrid experiments, discussed in Chapter

11. In the same limit of the Holstein-Primakoff approximation, in which we map the spin transverse variables $\{\hat{F}_z, \hat{F}_y\}$ into $\{\hat{X}_S, \hat{P}_S\}$, as already shown in Section 3.1. In terms of total variance, the mapping is

$$n_S \equiv \frac{2D_{yy} + 2D_{zz}}{F|p|} - \frac{1}{2} = \frac{\langle \hat{F}_y^2 \rangle + \langle \hat{F}_z^2 \rangle}{\gamma \langle |\hat{F}_x| \rangle} - \frac{1}{2}, \quad (5.21)$$

that is, the effective thermal occupancy n_S is the total diffusion coefficient normalized to the spin polarization.

Chapter 6

AC Faraday Angle

Besides characterizing the internal state of the spin ensemble, we are interested in characterizing the strength with which the ensemble interacts with light. Given the description presented in Chapter 3, the polarization rotation light experiences due to interaction with the ensemble is parametrized by the Faraday angle θ_F . For a given detuning Δ from the atomic resonance with wavelength λ_{Cs} and width γ_{Cs} , vapor density ρ and dimensions $A_c \times L$ (transverse area and length), the rotation angle for light propagating in the z -direction is given by (Sherson, 2006)

$$\theta_F = \frac{a_1 \gamma_{Cs} \lambda_{Cs}^2 \rho L}{32\pi A_c \Delta} \langle \hat{F}_z \rangle, \quad (6.1)$$

that is, it is proportional to the mean spin component in the propagation direction.

The standard approach for measuring θ_F is based on the measurement of the *DC Faraday rotation*. The experiment goes as follows. In a pulsed pump/probe cycle, optical pumping beams spin polarize the ensemble and a linearly polarized probe beam travels along the bias magnetic field direction. Subsequently to the preparation stage, the weak probe beam experiences the birefringence induced by the ensemble, generating a non-zero signal in the probing polarimeter. As time evolves, the macroscopic mean spin decays and so does the signal. The maximum polarization rotation detected is related directly to the DC Faraday angle.

There are two complications with this Faraday angle measurement method: (i) it relies on the knowledge of ensemble spin polarization and (ii) requires setting up optics and extra magnetic coil systems. Notice that the MORS technique, presented in Chapter 5, and basically any other experiment in this group utilizes a different laser/magnetic field configuration. While the latter complication is of more technical nature, the former, lack of knowledge about the prepared atomic spin, can lead to systematic errors in the estimated coupling parameters.

To solve this technical issue, in this chapter we use the *AC Faraday rotation* to measure θ_F . This method uses the same experimental apparatus as the MORS technique, relying only on (i) a RF pulse to realize a $\pi/2$ -pulse in the spin polarization, (ii) a photodetector with calibrated frequency response and (iii) conversion of the detected electrical signal in optical rotation.

In the next pages, we present the idea, a model to describe the observed signal and the link between Faraday angle and other coupling parameters. We finish the chapter linking θ_F to other quantities as the ratio of back-action to projection noise and optical depth.

6.1 Model

Similar to the MORS method, the basic idea can be described in terms of the Bloch equations and is the following. Consider an ensemble of spin- $\frac{1}{2}$ particles, in the presence of a static \mathbf{B} field in the x -direction, prepared with macroscopic spin F coordinates $\{F_x/F, F_y/F, F_z/F\} = \{1, 0, 0\}$, that is, on the north pole of the Bloch sphere. The presence of the magnetic field leads to a Larmor frequency ω_0 . At time t_0 , a transverse RF magnetic field with frequency $\omega_{\text{rf}} = \omega_0$ is turned on. This magnetic field will drive the magnetization out of the initial state, precessing down the sphere towards the equator. When the magnetization reaches the equatorial plane, the RF field is turned off, allowing the system to relax towards the thermal state.

A linearly polarized probe beam, traveling in the z -direction probes the transverse magnetization of the sample. If the duration τ of the RF pulse is much shorter than the coherence times $\{T_1, T_2\}$, the initial magnetization is efficiently rotated to the equator, allowing the measurement of the total length of the spin, as required to define the Faraday angle via equation (6.1).

For keeping the description simple, we will describe the spin ensemble in the regime of a small bias magnetic field¹, probed in the weak readout limit, that is $\Gamma_S/\gamma_S \ll 1$, by a far detuned laser beam. Fulfillment of these conditions allows us to describe the ensemble dynamics as an effective spin- $\frac{1}{2}$ system coupled to light via Faraday rotation.

We proceed now to the modeling of the AC Faraday angle measurements. Consider a spin- $\frac{1}{2}$ ensemble in the presence of a static magnetic field in the x -direction, leading to an energy splitting ω_0 , and an oscillating RF magnetic field in the z -direction, with a constant amplitude B_{RF} and frequency ω_d . The magnetic fields couple to the spin via its magnetic dipole, such that the total energy² of the coupled system reads

$$\hat{H} = \omega_0 \hat{F}_x + A \hat{F}_z \cos \omega_d t, \quad (6.2)$$

with $A = \mu_B g_4 B_{\text{RF}}$ as the coupling Rabi frequency, with $\mu_B g_4 = 350 \text{ kHz G}^{-1}$. The time evolution³ of the mean spin variables components $\langle \hat{F}_i \rangle = F_i$, including the phenomenological spin decay rate γ

$$\begin{aligned} \frac{d}{dt} F_x &= -A \cos \omega_d t F_y - \gamma F_x \\ \frac{d}{dt} F_y &= -\omega_0 F_z + A \cos \omega_d t F_x - \gamma F_y \\ \frac{d}{dt} F_z &= \omega_0 F_y - \gamma F_z. \end{aligned} \quad (6.3)$$

¹We understand the bias magnetic field as being small when the quadratic Zeeman splitting ν_{qzs} can not be resolved, that is, $\nu_{\text{qzs}} \ll \gamma_S$.

²Notice that treating the spin-magnetic field interaction quantum mechanically is not required to understand the experiment: as long as fluctuations of the spins and field are negligible, the dynamics can be mapped to the classical description of magnetic moments interacting with a classic \mathbf{B} field. Nonetheless, for consistency of notation, I keep the operatorial notation.

³Using the Heisenberg picture

$$\frac{d}{dt} \hat{A} = i[\hat{H}, \hat{A}].$$

The decay terms are added by hand assuming, for simplicity, equal decay rates for all components.

As the right hand side of the system of equations (6.3) contains a periodic time dependency, it doesn't look particularly simple to be solved analytically in the most general case. Nonetheless, in the weak RF coupling limit, in which $A \ll \omega_0$, the spin variables will evolve slowly. Furthermore, in the frame which evolves with ω_0 , the approximate evolution will not contain an explicit time dependence.

Let us move to the rotating frame. As described in Appendix A, for $T = \omega_d \hat{J}_x$ and $\hat{U} = e^{-i\hat{T}t}$, the rotating frame Hamiltonian \hat{H}^{R} is given by

$$\hat{H}^{\text{R}} = \Delta \hat{J}_x^{\text{R}} + A(\hat{J}_z^{\text{R}} \cos \omega_d t + \hat{J}_y^{\text{R}} \sin \omega_d t) \cos \omega_d t \quad (6.4)$$

where $\Delta \equiv \omega_0 - \omega_d$ is the detuning from the spin resonance. We proceed to eliminate the fast evolving dynamics. If the RF coupling A is small compared

Model

to ω_0 , the fast oscillating terms will not dominate the dynamics, that is, the $2\omega_d$ terms in (6.4) can be dropped,

$$\begin{aligned}\cos^2 \omega_d t &= \frac{1}{2}(1 + \cos 2\omega_d t) \sim \frac{1}{2} \\ \cos \omega_d t \sin \omega_d t &= \frac{1}{2} \sin 2\omega_d t \sim 0,\end{aligned}$$

which is equivalent to a rotating wave approximation. Therefore, in the small coupling regime, equation (6.4) is rewritten as

$$H^R = \Delta F_x^R + A F_z^R / 2.$$

The new equations of motion, using the Hamiltonian above, are

$$\begin{aligned}\frac{d}{dt} F_x &= -A F_y / 2 - \gamma F_x \\ \frac{d}{dt} F_y &= -\Delta F_z + A F_x / 2 - \gamma F_y \\ \frac{d}{dt} F_z &= \Delta F_y - \gamma F_z,\end{aligned}\tag{6.5}$$

to be compared with the equations (6.3). We have dropped the superscript R for simplicity. The system of equations (6.5), now with right hand side time independent, can be solved using simpler techniques⁴.

We start by focusing on a simple, but illustrative example. Consider the spin ensemble prepared with maximum projection along the x -axis, the initial condition is $(F_x, F_y, F_z)_0 = (J, 0, 0)$. The solution to (6.5) is

$$\frac{F_x(t)}{J} = \frac{e^{-\gamma t}}{\tilde{A}^2} \left[\cos\left(\frac{\tilde{A}t}{2}\right) A^2 + 4\Delta^2 \right]\tag{6.6}$$

$$\frac{F_y(t)}{J} = \frac{A e^{-\gamma t}}{\tilde{A}} \sin\left(\frac{\tilde{A}t}{2}\right)\tag{6.7}$$

$$\frac{F_z(t)}{J} = \frac{4A\Delta e^{-\gamma t}}{\tilde{A}^2} \sin^2\left(\frac{\tilde{A}t}{4}\right),\tag{6.8}$$

in which $\tilde{A}^2 \equiv A^2 + 4\Delta^2$ is the generalized Rabi frequency, governing the strength of the transition. The equations (6.6) are quite general, and some limits are discussed in the following. For a

1. **weak, resonant drive:** $\Delta = 0$ & $At \ll 1$. The dynamics is similar to a driven damped harmonic oscillator

$$\begin{aligned}\frac{F_x(t)}{J} &\sim e^{-\gamma t} \\ \frac{F_y(t)}{J} &\sim A t e^{-\gamma t} \\ \frac{F_z(t)}{J} &\sim 0,\end{aligned}$$

that is, the transverse component of the spin will grow in amplitude as long as the drive is on, being only damped by the natural dephasing of the oscillator.

2. **strong, resonant drive:** *i.e.*, $\Delta = 0$, $\gamma t \ll 1$. In this limit, the spin is rotated about the z -axis from pole to pole, reminding the *Rabi cycling*.

⁴The system of equations can be rewritten in the matrix form and solved as

$$\frac{d}{dt} \mathbf{J} = \mathbf{M} \mathbf{J}, \quad \mathbf{J}(t) = e^{\mathbf{M}t} \mathbf{J}(0),$$

for \mathbf{J} as the column vector with the spin components and \mathbf{M} as the matrix of coefficients; $\mathbf{J}(0)$ is the initial spin condition.

The spin components evolve as

$$\begin{aligned}\frac{F_x(t)}{J} &= \cos\left(\frac{At}{2}\right) \\ \frac{F_y(t)}{J} &= \sin\left(\frac{At}{2}\right) \\ \frac{F_z(t)}{J} &= 0.\end{aligned}$$

By choosing the correct time duration of the driving field, one can realize $\pi/2$ and π -pulses, leaving the spin along the equator and opposite pole of the Bloch sphere, respectively.

3. **strong, off-resonant drive:** *i.e.*, $\Delta \neq 0$ & $\gamma t \ll 1$. In this limit, the spin fails to reach the equator or the other pole, as in the cases of the $\pi/2$ and π -pulses, respectively. The spin components evolve as

$$\begin{aligned}\frac{F_x(t)}{J} &= \frac{1}{\tilde{A}^2} \left[\cos\left(\frac{\tilde{A}t}{2}\right) A^2 + 4\Delta^2 \right] \\ \frac{F_y(t)}{J} &= \frac{A}{\tilde{A}} \sin\left(\frac{\tilde{A}t}{2}\right) \\ \frac{F_z(t)}{J} &= 0.\end{aligned}$$

As can be seen in the equation for $F_y(t)/J$, the error in reaching the equator plane, that is $F_y(t) = J$, is of the order

$$A/\tilde{A} = 1/\sqrt{1 + 4\Delta^2/A^2} \sim 1 - 2\Delta^2/A^2$$

for small Δ/A .

For the more general case, in which the initial conditions are unknown, *i.e.*, the initial spin state is $(F_x(0), F_y(0), F_z(0)) = (F_{x0}, F_{y0}, F_{z0})$, the solution is

$$\begin{aligned}F_x(t) &= \frac{e^{-t\gamma}}{\tilde{A}^2} \left[\left(\cos\left(\frac{\tilde{A}t}{2}\right) A^2 + 4\Delta^2 \right) F_{x0} - \tilde{A}A \sin\left(\frac{\tilde{A}t}{2}\right) F_{y0} + 4A\Delta \sin^2\left(\frac{\tilde{A}t}{4}\right) F_{z0} \right] \\ F_y(t) &= \frac{e^{-t\gamma}}{\tilde{A}} \left[\sin\left(\frac{\tilde{A}t}{2}\right) (AF_{x0} - 2\Delta F_{z0}) + \tilde{A} \cos\left(\frac{\tilde{A}t}{2}\right) F_{y0} \right] \\ F_z(t) &= \frac{e^{-\gamma t}}{\tilde{A}^2} \left[2\Delta \cos\left(\frac{\tilde{A}t}{2}\right) (2\Delta F_{z0} - AF_{x0}) + A(AF_{z0} + 2\Delta F_{x0}) + 2\Delta \tilde{A} F_{y0} \sin\left(\frac{\tilde{A}t}{2}\right) \right].\end{aligned}\tag{6.9}$$

These are the expressions used for fitting the experimental data and extracting the parameters of interest, such as the Rabi frequency A and initial spin components.

The optical signal couples to the spin dynamics via the atomic polarizability, as discussed on Chapter 3. In the case of a weak far detuned probe, the Faraday interaction $\hat{H} = g\hat{S}_z\hat{J}_z$ describes the spin dynamics mapping to light. In the current case, we employed a rotating frame, leading to

$$\hat{H}^R = g\hat{S}_z(\hat{J}_z^R \cos \omega_d t + \hat{J}_y^R \sin \omega_d t),$$

Measurement and calibrations

for g as the coupling constant. The Stokes operators \hat{S}_i evolve according to the Maxwell-Bloch equations, see Chapter 3. For the mean value of the Stokes parameters $S_i = \langle \hat{S}_i \rangle$ for $i = x, y, z$, the solution is

$$\begin{pmatrix} S_x \\ S_y \\ S_z \end{pmatrix} = \begin{pmatrix} S_x^{\text{in}} \cos \theta(t) - S_y^{\text{in}} \sin \theta(t) \\ S_y^{\text{in}} \sin \theta(t) + S_x^{\text{in}} \cos \theta(t) \\ S_z^{\text{in}} \end{pmatrix}, \quad (6.10)$$

in which the rotation angle is

$$\theta(t) = \frac{g\rho A_B L}{2c} (F_z \cos \omega_d t + F_y \sin \omega_d t) = -\frac{a_1 \gamma \rho L}{16\Delta} \frac{\lambda^2}{2\pi} (F_z \cos \omega_d t + F_y \sin \omega_d t).$$

Note that the constant outside the parenthesis is the Faraday angle defined in equation (6.1). Most commonly, we operate in the regime $2\theta(t) \ll 1$. To the first order, equation (6.10) is

$$\hat{S}_x^{\text{out}} = \hat{S}_x^{\text{in}} + \hat{S}_y^{\text{in}} \theta(t) \quad (6.11)$$

$$\hat{S}_y^{\text{out}} = \hat{S}_y^{\text{in}} - \hat{S}_x^{\text{in}} \theta(t) \quad (6.12)$$

$$\hat{S}_z^{\text{out}} = \hat{S}_z^{\text{in}}. \quad (6.13)$$

Using the relations above, the Faraday angle can be directly extracted from the detection of the suitable Stokes operator.

Summing up the discussion presented up to now, we see that if an RF pulse with Rabi frequency A is applied to the spins for a duration $\tau = \pi/A$, the macroscopic spin is going to be pointing at the probing direction, as required from equation 6.1. A calibrated detector would give the Faraday angle as the maximum polarization rotation, $\theta_F = \max(\theta(t))$. This description is valid as long as the spin is coherent ($\gamma t \ll 1$) and the Rabi frequency is smaller than the natural frequency $A \ll \omega_0$.

In the next section we present measurements and study the validity of the model.

6.2 Measurement and calibrations

Having discussed the model, we move to the experimental section. As for the optical signal, a few parameters must be known to convert the detected signal (in units of voltage V) into rotation angle (in the units of *radians* or *degrees*). If the internal state of the ensemble is of interest, there are more parameters involved, as the RF drive, amplitude, frequency, and pulse timing also matter.

The experiment is set as shown in Figure 6.1 (a). The configuration of lasers and magnetic fields is similar to the used in MORS experiments, discussed in Chapter 5. The lasers in the experiments can be run in pulsed or continuous mode. In general, the pulsed version is preferred when there is significant decoherence induced by the laser beams. For the results presented in this chapter, the data in Figures 6.2 to 6.4 were taken in continuous wave operation, as represented in Figure 6.1 (c). The data presented in Figure 6.5 involved the pump beam and used pulsed operation, as in Figure 6.1 (b). Regardless of the laser intensity profile, the RF drive⁵ is always pulsed: while on, the RF drive is a sine wave with constant amplitude. All data presented here is a single-shot result, that is, multiple traces have not been averaged to generate the data shown. The data, nonetheless, have been band-passed around the Larmor frequency with a second order Butterworth filter with 50 kHz bandwidth.

The polarization rotation signal due to the RF drive is shown in Figure 6.2. A 10 μW probe beam, detuned $\Delta = 3$ GHz from the atomic resonance, couples to the spin ensemble at $T = 29$ °C which is being repumped; the spin polarization is ~ 0.6 . At time $t = 0$, a resonant drive field with Rabi frequency A is turned

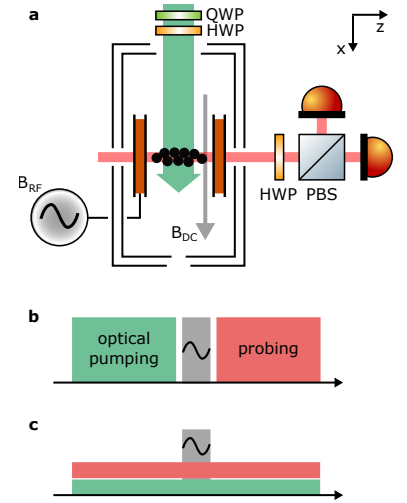
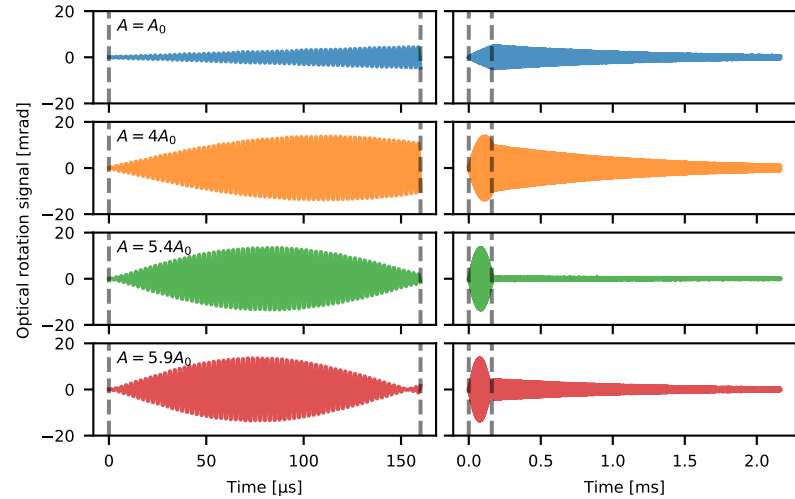


Figure 6.1: Setup for the AC Faraday angle measurements. a Optical pumping (green arrow) generates spin polarization and probe beam (red line) measures the ensemble positioned in a magnetic shielded region. A DC bias field (B_{DC}) sets the Larmor frequency and the RF field (B_{RF}) forces the magnetization out of the equilibrium position. The experiment can be run in a (b) pulsed or (c) continuous fashion. See text for more details

⁵Rigol DG1032Z

Figure 6.2: Time dependence of the polarization rotation signal for increasing RF field coupling rate. At time $t = 0$, a sinusoidal RF field drive with Rabi frequency A and frequency $\omega_d/2\pi = 400$ kHz is turned on. Up to $t = 160$ μ s (left column), the atomic system is forced to oscillate at the drive frequency. When drive field is turned off, the ensemble evolves freely, with transverse spin components decaying towards their steady state values. (right column) The complete time trace, including excitation and decay.



on. For small $A = A_0$, the amplitude of the oscillating signal increases linearly with time until the end of the drive pulse. From this moment onwards, the spin magnetization oscillates down to zero, with envelope decaying exponentially with time.

Increasing the Rabi frequency to $A = 4A_0$ shows that the rotation is bigger than $\pi/2$, as the signal already passed its maximum. For $A = 5.4A_0$, a π -pulse is achieved: the spin has been rotated from north to south pole. Setting $A = 5.9A_0$ makes the precession start to return to the starting pole. We observe that the spin can sustain several π rotations before significant decay happens.

For fitting the model to the measured data, we use the expressions from equations (6.9) and a non-linear least squares function. To reduce the extensive list of free parameters, knowledge and/or educated guesses of a few more parameters is advisable.

In Figure 6.3 (left) we show a fitting result, here for the curve with drive $A = 4A_0$. The model agrees rather well with the data. Disagreement happens mostly in the beginning of the driving period, as the current is loading the coil and is therefore time dependent. Of the parameters returned by the fitting, the RF Rabi frequency is of great interest and it is shown in Figure 6.3 (left). There is a linear relationship between the applied voltage to the coil and the observed Rabi frequency, as expected from equation (6.2).

The quality of the fit can be judged better when removing the fast oscillation. In Figure (6.4), we show the absolute value of detected signal envelope as processed by a Hilbert transform⁶. The Hilbert transform is specially useful for determining the instantaneous amplitude and phase/frequency of a fast oscillating signal. The lines are calculated from the fitted parameters and calculated as $R = \sqrt{F_y^2 + F_z^2}$, for the spin components defined in equation (6.9).

The calibration of the detected signal from electrical units to rotation units is described as follows. Consider a linearly polarized input beam, passing through a half-wave plate. We can rotate this plate around its axis by an angle θ . Chosen θ in a way that if $\theta = 0$, then the light polarization is unaltered.

⁶As computed by the Python function `scipy.signal.hilbert`.

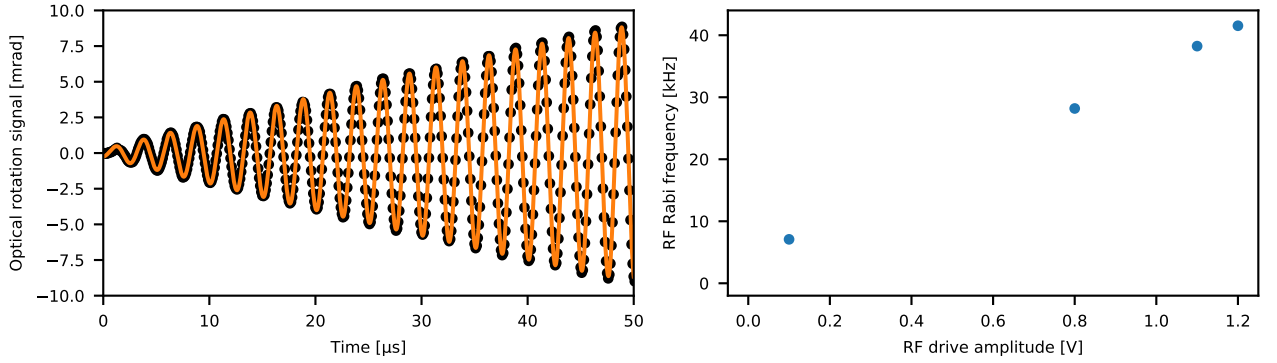


Figure 6.3: AC Faraday rotation signal. (left) Close up on the first 50 μs of the forced precession for $A = 4A_0$ and comparison between the data (black points) and the fitted theory (orange line); (right) linear dependence of the RF Rabi frequency versus applied RF field amplitude, as extracted from fits.

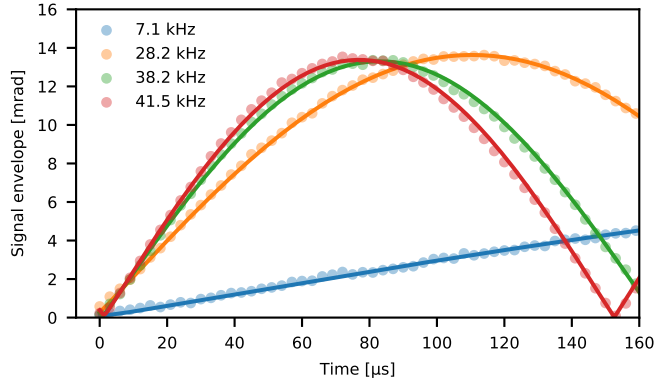


Figure 6.4: AC Faraday signal envelope. The absolute value of the measured signal Hilbert Transform from the data presented in Figure 6.2 is shown as points. The curves are labelled according to RF Rabi frequency. Lines are the absolute value of spin on the probe direction, using the fitted parameters obtained from the lab frame fitting procedure.

The output polarization, using matrix notation, is

$$\begin{aligned} \begin{bmatrix} S_x^{\text{out}} \\ S_y^{\text{out}} \end{bmatrix} &= \begin{bmatrix} \cos 2\theta & -\sin 2\theta \\ \sin 2\theta & \cos 2\theta \end{bmatrix} \begin{bmatrix} S_x^{\text{in}} \\ S_y^{\text{in}} \end{bmatrix} \\ &= \begin{bmatrix} S_x^{\text{in}} \cos 2\theta - S_y^{\text{in}} \sin 2\theta \\ S_x^{\text{in}} \sin 2\theta + S_y^{\text{in}} \cos 2\theta \end{bmatrix} \end{aligned} \quad (6.14)$$

for an unchanged \hat{S}_z component. Notice the similarity between the equation above and (6.10). The spin ensemble behaves as a rotator with a time dependent rotation angle.

To calibrate the rotation angle, one needs to know (i) the input polarization state, (ii) the total available power, that is, S_0 , (iii) the change in the Stokes parameters of interest. With this information in hand, given an input $S_x^{\text{in}} = S_0$

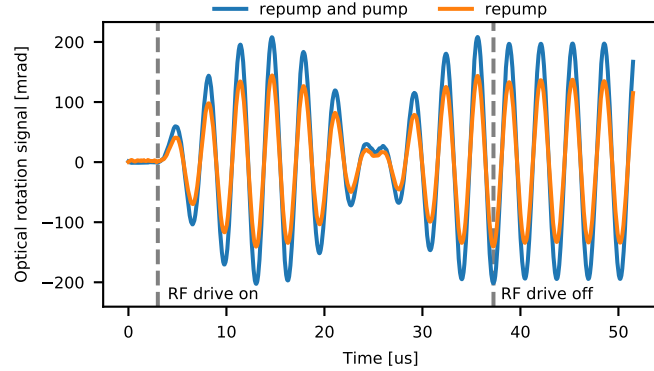


Figure 6.5: Calibrated AC Faraday signal and spin polarization dependence. A pumping-probing pulsed experiment with optical pumping using repump only (orange) and repump+pump (blue). The amplitude of the signal grows from ~ 280 mrad to ~ 400 mrad, which roughly agrees with the independently measured spin polarization values increasing from 0.7 to 0.97.

and measuring S_y^{out} , the rotation angle can be calculated from (6.14), as

$$\theta = \frac{1}{2} \arcsin \frac{S_y^{\text{out}}}{S_0} \sim \frac{1}{2} \frac{S_y^{\text{out}}}{S_0}, \quad (6.15)$$

the approximation being valid for small changes in the polarization state, ie $\theta \ll 1$.

The effect of the optical pumping on the AC Faraday signal is shown in Figure 6.5. For the data shown there, a probe beam with power $10 \mu\text{W}$ and $\Delta/2\pi = 3 \text{GHz}$ was used. The Larmor frequency was $\omega_0/2\pi = 300 \text{kHz}$ and the cell temperature $T = 55^\circ\text{C}$. The RF Rabi frequency is chosen such a π pulse is achieved in a reasonably short time. The effect of the pump beam is clearly seen as an increase in polarization rotation. This increase leads to a bigger F_x , with the polarization rotation following the same relationship. The amplitude of detected signal increases from ~ 280 mrad to ~ 400 mrad. The spin polarization was measured independently, going from ~ 0.7 to ~ 0.97 with the addition of the pump beam, roughly matching the observed increase in signal.

6.3 Connection to spin noise

The Faraday interaction described above also describes the polarization fluctuations induced by the probe. In this section we relate θ_F to the observed spin noise and the optical depth.

The description of the spin fluctuations follows the derivations by Julsgaard (2003). There, quite similarly to the discussions presented in this chapter, a linearly polarized, far-detuned beam with mean photon flux S_x interacts with the ensemble with mean spin F_x and coupling constant a . Disregarding tensor effects, $\xi_S = 0$, and decoherence in the dark, $\gamma_{S0} = 0$, the output optical response can be broken down according to source, decorrelating the light and spin variables. Within the aforementioned limits, the integrated *Back-Action Noise Area* (here BANA) and the *Projection Noise Area* (here PNA) of the detected light sig-

Connection to spin noise

nal are⁷

$$\begin{aligned} \text{BANA} &= \frac{\pi a^4 |F_x|^2}{\gamma_S} \left(\frac{S_x}{2} \right)^3 \\ \text{PNA} &= 2\pi a^2 |F_x| \left(\frac{S_x}{2} \right)^2. \end{aligned} \quad (6.18)$$

These relations are valid for the spins interacting with light via an ideally homogeneous Faraday interaction. It is also assumed that the spins are perfectly spin polarized. Although quite restrictive, the areas above serve as a good order of magnitude estimation for the quantity of interest, which is the ratio of rates in which the spins couple to light, the quantum back-action, to the thermal environment. In Chapter 3, we also define the ratio (6.18) as the quantum cooperativity C_q^S .

For large detuning Δ from the atomic resonance in respect to the absorption profile width, the parameter $a \rightarrow 1$, and the ratio of BANA to PNA is

$$\frac{\text{BANA}}{\text{PNA}} \approx \frac{\lambda^2}{2\pi} \frac{F_x}{256A_c}, \quad (6.19)$$

for λ_{Cs} as the wavelength of the optical transition and A_c as the cell transverse area. We now wish to express this ratio in terms of the Faraday angle. Combining equations (6.1) and (6.19), we get to

$$\frac{\text{BANA}}{\text{PNA}} \approx \frac{\theta_F \Delta}{16\gamma_{Cs}}. \quad (6.20)$$

As an example, for the data presented on Figure 6.5, $\theta_F \sim 200$ mrad for optical pumping with pump and repump. Given the detuning $\Delta/2\pi = 3$ GHz, we have $\text{BANA}/\text{PNA} = C_q^S \sim 7$. The estimation is in the right ballpark. For the ensemble operated in similar conditions, it agrees with other calibration techniques (see Chapter 8).

⁷For convenience, we remind the reader the definitions of a and γ

$$a = -\frac{\gamma}{8A_c\Delta} \frac{\lambda_{Cs}^2}{2\pi} a_1 \quad (6.16)$$

$$\gamma = \frac{\lambda_{Cs}^2 \gamma_{Cs}^2}{2\pi\Delta^2} \frac{S_x}{A_c}, \quad (6.17)$$

the Faraday interaction coupling coefficient and the decoherence rate induced by the probe; A_c is the vapor cell transverse area and γ_{Cs} is the excited state spontaneous decay rate, here $\gamma_{Cs}/2\pi = 5.22$ MHz for the D_2 line. The expressions above are valid only for a QND interaction. The mean value of the classical drive in terms of the Stokes operator language can be written in terms of the incoming power P or intensity I as $I = P/A = \hbar\omega_L n_{ph}/A_c = 2\hbar\omega_L S_x/A_c$, for ω_L as the frequency of the laser, n_{ph} is the number of photons per unit time and P is the power.

Chapter 7

Spin Noise

In this chapter we experimentally study the averaging effects on the time-dependent spin-light coupling. We observe the polarization rotation noise dependence on the beam profile and on the optical power and discuss about modeling the contributions.

The interaction presented in Chapter 3, based on the polarizability of the cesium atom due to coupling to the optical field, focusing on the effects of light on the internal atomic degrees of freedom. In reality, the situation in our experiments is more complex. We sketch the problem in Figure 7.1. Atoms move around the optical field, interacting with the laser light in a time dependent fashion, eventually also colliding with the glass walls. Upon interaction with the wall, which is coated with paraffin-like material, the atoms return in different trajectories across the cell. The dependence of the internal degrees of freedom on the external degrees of freedom, as position and velocity, force us to think about the ensemble properties of the interaction¹: what are the effects of atomic motion on the light-matter interaction?

In most of the experiments presented here, Cs atoms are moving on the order of $\sim 100 \text{ m s}^{-1}$ across $50 - 200 \mu\text{m}$ (diameter) Gaussian beams in channels with $300 - 500 \mu\text{m}$ side length. The atomic transit time across the beam is on the order of $\sim 0.75 \mu\text{s}$; the collective spin readout time, as described in Chapter 10, is on the order of $\sim 15 \mu\text{s}$, indicating that the ensemble spin state is read rather slowly in comparison to the fly-through time. Given the stochastic nature of the atomic motion, we can say that the spin noise and the corresponding degrees of freedom we are interested in is somewhat the *average* in time and space of the spin ensemble.

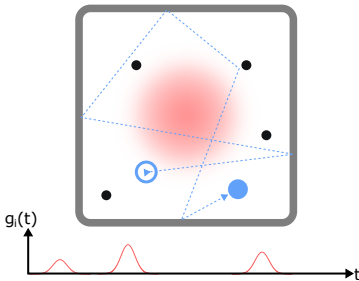


Figure 7.1: Time dependent coupling . The cell is illuminated by a laser with a transverse Gaussian beam profile (in red). Atoms move across the cell, colliding with the container walls and background gasses (black dots), experiencing a time dependent coupling. Here, we sketch the dynamics of the i -th atom, for simplicity. The coupling experienced by the atom over time is given by $g_i(t)$ and is sketched in the graph below.

7.1 Modelling

The *motional averaging* of the light-matter coupling on thermal atomic vapours is important for an efficient mapping of light to spins and vice-versa. The usage of spin-preserving coating on the container walls allows for atoms to move in and out of the interaction with the laser beam, maintaining the phase relation with light. Although not explicitly mentioned, the motional averaging approach has been widely used in atomic ensemble-based continuous variable Quantum Information protocols, see (Hammerer et al., 2010). As described in (Borregaard et al., 2016), this concept can also be extended and applied to discrete variable schemes, with the first experimental results presented in (Zugemaier et al., 2018).

The description presented here follows (Borregaard et al., 2016) closely. The situation is sketched in Figure 7.1. The atoms move across the cell and experience a time-dependent coupling as flying through the Gaussian laser beam. Assuming the atomic motion is classical and that the ensemble is in thermal equilibrium with the cell walls, the atomic velocity distribution should follow

¹Collective effects of light interacting with atoms depend both on the optical mode profile and the relative positioning of the atoms. See (Tanji-Suzuki et al., 2011) for related discussions.

the Maxwell-Boltzmann distribution. For the case of non-interacting atoms, the situation is further simplified as we can describe the atoms as point particles moving within the cell.

In Borregaard et al. (2016), the motion of 5000 independent particles in a microcell sized volume, across a $2w_0 = 110 \mu\text{m}$ Gaussian beam, taking into account the cell walls' randomization and trapping on the spin preserving coating was simulated. Given the randomizing effect of the collisions, the atomic position will be completely uncorrelated from its initial position after collisions with the walls. The ensemble average of the light-matter coupling, nonetheless, does not vanish. In particular, the two-time correlation of coupling $\langle g(0)g(t) \rangle$, which gives us information about the spectral components of the coupling, does not vanish. The simulation results are shown in Figure 7.2 (blue curve). The ensemble average of the two-time correlation function decays rapidly with time to a steady state value. The dynamics of this decay can be approximated by the model

$$\langle g(0)g(t) \rangle = \langle g(0)^2 \rangle e^{-t/t_b} + \langle g(0) \rangle^2 (1 - e^{-t/t_b}), \quad (7.1)$$

with the brackets $\langle \dots \rangle$ representing the ensemble average, involving the trajectories of all atoms in the cell container. Fitting the correlation function with this test model gives the yellow curve in Figure 7.2. The coupling constant of the two-time correlation is time dependent and has two components: the first term describes the fast correlations, with the transit time through the beam as characteristic time constant, and the second contains the long term behaviour, where the correlation happens through the mean values. The fitting presented in Figure 7.2 gives $t_b = 0.26 \mu\text{s}$. In frequency, it is equivalent to a rate of $\gamma_b/2\pi = 1/\pi t_b = 1.24 \text{MHz}$. This rate is quite close to the one observed in the experiments, building up confidence on the simple model given in equation (7.1). According to these results, $t_b \propto v_{Cs}/w_0$, with v_{Cs} as the average thermal velocity of the atoms in the cell and w_0 the Gaussian beam waist.

An alternative description is presented by Shaham et al. (2020). There, the atomic motion is modelled via the diffusion equation for the density operator. In this picture, the observed spin noise is decomposed in spatial dependent modes, being subject to the boundary conditions of the cell wall, collisional decay and evolution due to coupling via the light mode. The initial spatial configuration of atoms is scrambled by the container walls and as the cell is anti-relaxation coated, the atoms return to the area illuminated by the laser beam after a brief period in the dark, coupling again to light with a random spatial phase. Therefore, most of the spatial modes decay rather quickly; the only mode that survives carries no information about atomic position.

The description given by Shaham et al. (2020) complements Borregaard et al. (2016), as it gives insight into a formalism to treat the atomic motion in an analytical fashion. Here, we adopt a qualitative approach that treats the total polarization rotation induced by the spin ensemble as composed by two independent spin modes: the so called *narrow mode*, the long lived mode of interest, and the *broad mode*, which contains all other atomic responses. An approach similar to this has also been experimentally tested by Tang et al. (2020).

We move now to introducing the effect of atomic motion in our input-output relations. The interaction of light with the spins is given in Chapter 3. Here, we rewrite the main results, in the light of the language introduced above. A spin mode is coupled both to the optical mode \hat{X}_{LS} and to its thermal environment \hat{F}_S . In the limit of high spin polarization, the transverse spin components are mapped to the harmonic variables \hat{X}_S . As described by the equation (3.42), the response of the spin mode to the optical and thermal forces is written as

$$\hat{X}_S = 2\sqrt{\Gamma_S} \mathbf{LZ} \hat{X}_{LS}^{\text{in}} + \mathbf{L} \hat{F}_S. \quad (7.2)$$

for the matrices defined in equation (3.43). The effect of the coupling on the light variables is given by equation (3.50)

$$\hat{X}_{LS}^{\text{out}} = \hat{X}_{LS}^{\text{in}} + \sqrt{\Gamma_S} \mathbf{Z} \hat{X}_S = (\mathbf{1}_2 + 2\Gamma_S \mathbf{ZLZ}) \hat{X}_{LS}^{\text{in}} + \sqrt{\Gamma_S} \mathbf{ZL} \hat{F}_S, \quad (7.3)$$

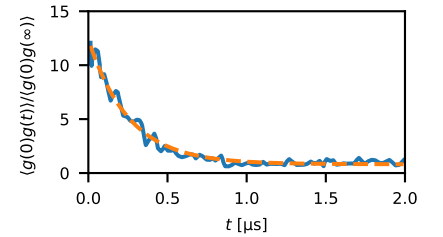


Figure 7.2: Time evolution of the two-time correlation function. Figure is adapted from (Borregaard et al., 2016, SI Fig. 3). Numerically simulated two-time correlation function (blue) for atoms randomly flying through a Gaussian beam with $2w_0 = 110 \mu\text{m}$ in a container with $300 \mu\text{m}$ side length, and averaged over the ensemble. The data is fitted (orange) to the model presented equation (7.1), giving $t_b = 0.26 \mu\text{s}$.

in which in the last step we used (7.2).

We are now in a position to include the broad mode in our description. Assuming that the effective broad mode couples as described by equation (7.2), that is

$$\hat{\mathbf{X}}_{S,b} = 2\sqrt{\Gamma_b}\mathbf{L}_b\mathbf{Z}\hat{\mathbf{X}}_{L,S}^{\text{in}} + \mathbf{L}_b\hat{\mathbf{F}}_{S,b}, \quad (7.4)$$

for \mathbf{L}_b as \mathbf{L} with $\gamma_{S0} \rightarrow \gamma_b$ and $\Gamma_S \rightarrow \Gamma_{S,b}$. Here, we conjecture that the output light field carries information about the total response of the ensemble as

$$\hat{\mathbf{X}}_{L,S}^{\text{out}} = \hat{\mathbf{X}}_{L,S}^{\text{in}} + \sqrt{\Gamma_S}\mathbf{Z}\hat{\mathbf{X}}_S + \sqrt{\Gamma_{S,b}}\mathbf{Z}\hat{\mathbf{X}}_{S,b}. \quad (7.5)$$

In words, the output light reads out two spin modes: the narrow mode $\hat{\mathbf{X}}_S$ with rate Γ_S and the broad mode $\hat{\mathbf{X}}_{S,b}$ with rate $\Gamma_{S,b}$. The broadband response read-out rate, that is, the coupling rate of the light to the fast decaying spatial spin modes is $\Gamma_{S,b}$. We have therefore decomposed the response of the spins to light in a modal basis: $\hat{\mathbf{X}}_S$ contains information about the long lived spin mode, while $\hat{\mathbf{X}}_{S,b}$ contains information about all the other short lived spin modes. Assuming the basis chosen decorrelates the modes, the spin mode cross-correlations will be zero. This feature is specially important when the PSD of the detected light is calculated, later in this chapter.

The matrix \mathbf{L} represents the dynamics of the ensemble on frequency space. While in Chapter 3 we dealt with the near-resonance description, that is for $\Omega \sim \omega_S$, here we are interested in Fourier frequencies far from resonance. We rewrite \mathbf{L} as

$$\mathbf{L} = \begin{pmatrix} \varrho_S(\Omega) & \chi_S(\Omega) \\ -\chi_S(\Omega) & \varrho_S(\Omega) \end{pmatrix}, \quad (7.6)$$

in which the *general spin susceptibility* χ_S and ϱ_S are

$$\chi_S(\Omega) = \frac{\omega_S}{\omega_S^2 - \Omega^2 - i\Omega\gamma_S + (\gamma_S/2)^2} \quad (7.7)$$

$$\varrho_S(\Omega) = \frac{\gamma_S/2 - i\Omega}{\omega_S^2 - \Omega^2 - i\Omega\gamma_S + (\gamma_S/2)^2} \quad (7.8)$$

with $\gamma_S = \gamma_{S0} + 2\zeta_S\Gamma_S$ as the total spin linewidth, including the tensor (dynamical) broadening. The parameter ζ_S is the tensor coupling constant. Given an input force, the matrix \mathbf{L} determines the response of the mode of interest to this disturbance. In the high-Q limit, when only the dynamics around the resonance ($\Omega \sim \omega_S$) are significant, the susceptibility gets the more familiar form

$$\chi_S(\Omega) \sim \frac{1}{2} \frac{1}{\omega_S - \Omega - i\gamma_S/2} \quad (7.9)$$

$$\varrho_S(\Omega) \sim -i\chi_S(\Omega). \quad (7.10)$$

These expressions are satisfied best for the narrow spin mode dynamics, centred around ω_S . The narrow spin mode is commonly a couple of kHz wide. For the broadband mode, whose linewidth $\gamma_{S,b} \sim \omega_S$, the response can, in principle, also be considerable for $\Omega \sim 0$. In the experiments detailed below, we will therefore use different functions to describe the narrow and broad spin noise contributions.

The contributions presented on equation (7.3), in terms of \mathbf{L} , the input optical, and thermal forces are

$$\mathbf{ZLZ}\hat{\mathbf{X}}_{L,S}^{\text{in}} = \begin{pmatrix} -\zeta_S^2\chi_S\hat{P}_{\text{in}} - \zeta_S\varrho_S\hat{X}_{\text{in}} \\ \chi_S\hat{X}_{\text{in}} - \zeta_S\varrho_S\hat{P}_{\text{in}} \end{pmatrix} \quad (7.11)$$

$$\mathbf{ZL}\hat{\mathbf{F}}_S = \begin{pmatrix} \zeta_S\chi_S\hat{F}_S^X - \varrho_S\zeta_S\hat{F}_S^P \\ \chi_S\hat{F}_S^P + \varrho_S\hat{F}_S^X \end{pmatrix}. \quad (7.12)$$

Beam size dependence

The expressions above, along with equation (7.3), give the full model used to describe the spin response in this thesis. The coupling with light is studied in depth in Chapter 8, noise measurements and analysis are presented in Chapter 10 and 11.

In the absence of tensor broadening, $\xi_S = 0$, the PSD of the output phase quadrature, calculated from equation (7.5), is

$$\begin{aligned} \text{PSD}_{\text{out}}^{\text{PP}} = & 1 + (\Gamma_S^2 |\chi_S|^2 + \Gamma_{S,b}^2 |\chi_{S,b}|^2) \\ & + \Gamma_S (|\chi_S|^2 + |q_S|^2) \gamma_{S0} (n_S + \frac{1}{2}) \\ & + \Gamma_{S,b} (|\chi_{S,b}|^2 + |q_{S,b}|^2) \gamma_{S0,b} (n_{S,b} + \frac{1}{2}), \end{aligned} \quad (7.13)$$

assuming a lossless detection. The contributions, line by line, are the probe shot noise and back action noise, the narrow mode thermal noise, and the broad mode thermal noise. Note that we assume both modes having the same effective occupation n_S , as we assume the optical pumping preparing all atoms with the same internal state density matrix. The functions $\chi_{S,b}$ and $q_{S,b}$ are the broad spin mode susceptibilities.

For the analysis of the detected light noise, we detect the phase quadrature of light and use the model from equation (7.13). We also set the tensor contribution to zero, for clarity. To simplify the data visualization, we divide the spectrum in two regions, according to the spin mode: (i) close to resonance $\Omega \sim \omega_S$ for observing the dynamics of the narrow mode, and (ii) wide range, excluding the signal close to resonance, for the broad spin modes. The fitting functions used are derived from equation (7.13). Its near-resonance approximation, for the broad and narrow frequency regions, respectively, are

$$\text{PSD}_{\text{narrow}} = 1 + A \frac{(\gamma/2)^2}{(\omega_S - \Omega)^2 + (\gamma/2)^2} \quad (7.14)$$

$$\text{PSD}_{\text{broad}} = 1 + A \frac{(\gamma/2)^2 + \omega_S^2 + \Omega^2}{(\omega_S^2 - \Omega^2 + (\gamma/2)^2)^2 + \Omega^2 \gamma}, \quad (7.15)$$

where A is the coupling/scaling constant.

In the next sections we present the experiments and compare the results with the theory predictions.

7.2 Beam size dependence

We start by studying the spin noise dependence on the beam size. A Gaussian laser beam is sent through a microcell with channel dimensions $L \times d \times d$, with length $L = 25$ mm and side length $d = 500$ μm . At some position before the cell, we insert a flip mirror and redirect the light to a waistsmeter, with which the beam profile is characterized as presented in Figure 9.1. The region in grey represents the position in which the cell is positioned. The beam profile is modified by adjusting the lens in an adjustable fiber collimator. Optical transmission through the cell is $\sim 90\%$, dropping by 4% for the largest beam used.

The power spectral density of the phase quadrature for fixed probe power and various beam sizes is shown in Figure 7.5. The probe laser is detuned $\Delta/2\pi = 3$ GHz and the power is set to 1 mW. At first sight, the detected noise spectra are only slightly modified. The width and peak height of the narrow feature are not strongly dependent on the beam size. The mean atomic mode coupling, as described in the section above, only depends on the power and in the cell transverse area. Therefore, on the limit of high probe power, the peak height and width do not change with beam size.

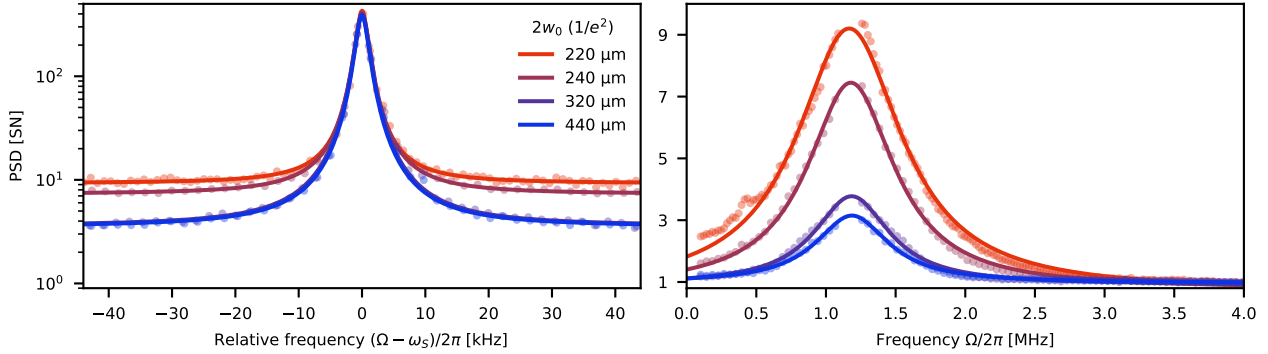


Figure 7.3: Narrow and broadband spin noise versus beam size. The analysis of signal presented in Fig 7.5 is divided in between the narrow (left) and broad (right) frequency regions. The raw data is cut out in two sections and analyzed separately. Data has been normalized to shot noise and detection efficiency. See text for discussion about fits (solid lines).

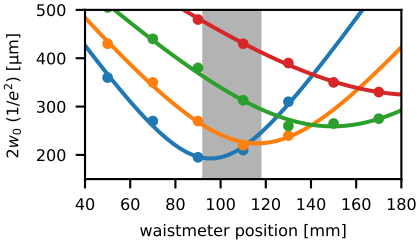


Figure 7.4: Beam profiling for studying the spin broadband noise. Region in grey represents the vapour cell position. Fitted waist beam diameters are 190 μm , 220 μm , 260 μm and 320 μm .

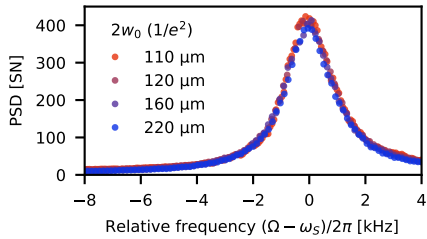


Figure 7.5: Spectral density of the light noise. A 1 mW probe beam with variable beam profile interacts with the spin ensemble. The PSD is normalized to detection efficiency and shot noise (SN).

In Figure 7.3 we show the data already presented in Figure 7.5, for a different frequency range. The detected noise is separated in two parts: a ± 50 kHz cut around the narrow feature (left) and the remaining range (right), here shown up to 4 MHz. This perspective, along with the fitted widths and heights presented in Figure 7.7, makes clear that the broad feature depends on the beam size. In other words, the coupling to the rapidly decohering spin noise modes is highly dependent on the coupling inhomogeneities.

To first order, the motional averaging theory and the model presented in equation (7.13) correctly reproduces the shape and width of the fast decaying mode seen from Figure 7.3. Nonetheless, as can be seen in Figure 7.3 (right), the theory deviates from the data in the feature's wings. The model described here is not the complete answer to the problem. The feature seems to decay faster than a Lorentzian in the wings.

The extracted width of the broad feature in Figure 7.7 (left) shows that the width tends to saturate for increasing beam size; the scaling predicted from motional averaging theory, $t_b \propto v_{Cs}/w_0$, does not follow the fitted results, as shown by the blue line. As the width seems to saturate with increasing beam size, adding a constant offset reproduces the qualitative behaviour more closely; for reference, the constant value is ~ 500 kHz. The readout rate of the broad mode, scales linearly with power (Figure 7.7 (right)); experiments varying the atomic density (not shown) also showed a linear scaling for $\Gamma_{S,b}$. Effectively, we can say that $\Gamma_{S,b}$ scales the same way as Γ_S .

The dependence on power shown on Fig.7.7 (right), shows that increasing the beam size does not only change the width of the broad feature, but also the height. In other words, the total noise area decreases. Increasing the probe transverse area by a factor of ~ 4 decreased the area by a factor of ~ 8 . Nonetheless, the incremental noise reduction per increased probe area decreases as the beam is made bigger, indicating that the remaining noise is for a bigger beam is increasingly difficult to get rid of.

7.3 Power dependence

We proceed to study the noise dependence with power, for a fixed beam size $2w_0 = 440 \mu\text{m}$. We measure two different optical quadratures: one very close to $\phi = 0$ —the phase quadrature —and the other very close to $\phi = \pi/2$ —the amplitude quadrature —in Figure 7.8 (left) and (right), respectively. The total photodetection efficiency, including propagation and photodiode losses,

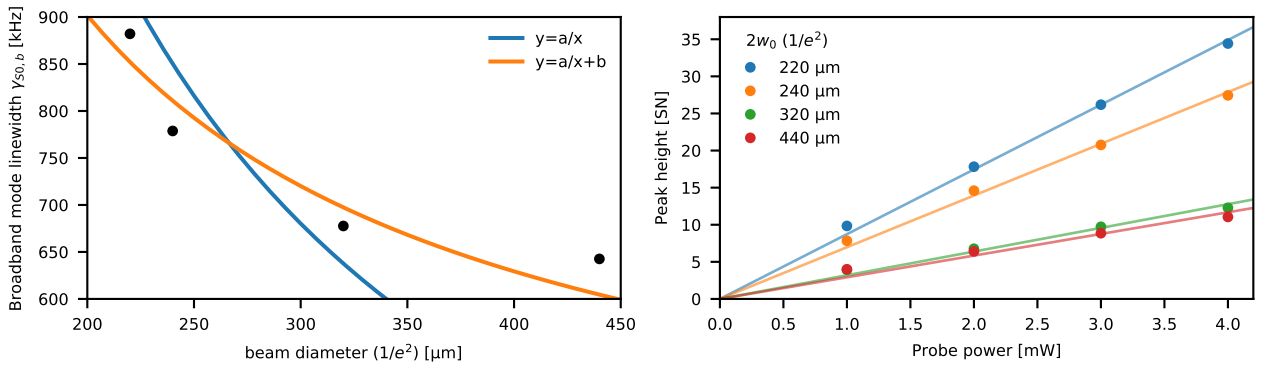


Figure 7.7: Broadband spin noise linewidth and peak height versus beam size. As the beam is enlarged, the fly-through time of the spins through the beam increases, decreasing the width of the broadband spin noise (left); fitting to qualitative two models, with a and b as free parameters, shows that best agreement is for model with constant independent of the beam size. The peak height of feature increases linearly with power; lines show a linear fit to the various datasets.

is 87%. The peak value and width dependence of this feature were already presented in Chapter 3, see Figure 7.6.

The phase quadrature measurements show that an increased power, leads to a bigger readout rate and spin noise contribution. The height and width of the narrow response, presented in Figure 7.6, show that for highest probe power the spin readout is already saturated, that is, the optical read out is performed faster than the decoherence processes. The increased power also requires adjustments of the linear input polarization from compensating the tensor Stark shifts, as described in Chapter 3. The adjustment leads to an optical shift to the resonant frequency, as expected from the tensor Stark shift contributions —see Chapter 3.

The amplitude quadrature measurements, on the other hand, show the characteristic frequency dependent squeezing of the light fluctuations below the shot noise limit. The increase in power, nonetheless, leads to a degradation of the squeezing; for the highest value used, the sub-shot noise feature disappears completely, as extra atomic noise dominates the baseline of the detected fluctuations. From the perspective of light coupling to multiple spin modes in the vapour cell, given that most of the modes decays much faster than the

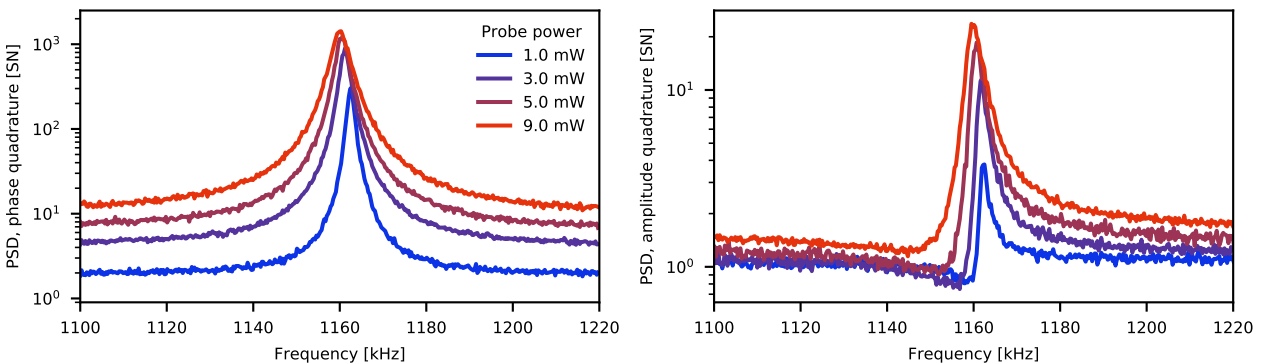


Figure 7.8: Spin noise scaling with probe power. Probe power is increased from 1-9 mW, from blue to red. Power spectral density of the detected phase (left) and approximately amplitude (right) quadrature are shown.

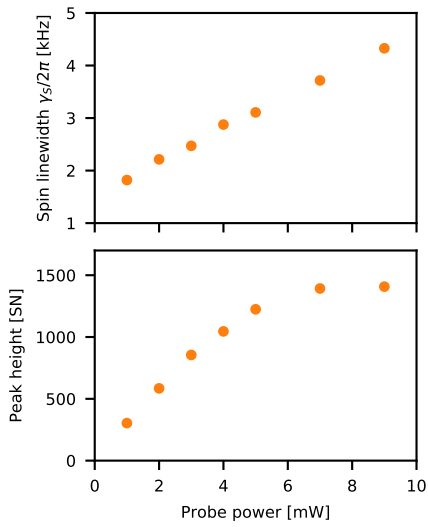


Figure 7.6: Peak height and width of the narrow response versus power. Increasing the probe power leads to a higher Γ_S and γ_S . For high enough probe power, the peak height saturates, indicating that the probing laser dominates the spin oscillator dynamics.

narrow mode, the noise induced by the different contributions adds incoherently. While we only discuss in Chapter 11 the implications of the added noise, we note that it is particularly harmful in protocols that rely on discerning the narrow mode from other noise sources with high efficiency, as the conditional entanglement presented in Chapter 11.

7.4 Conclusions

In this chapter we studied the broadband spin response dependency on power and transverse laser beam profile. The experimental results show that, for a given detuning from the atomic resonance, if the broad response area is to be minimized, a beam with the maximum size and smallest photon flux must be used.

The theory of motional averaging, along with the insights given by diffusion equation, while successfully qualitatively explaining most of the observed features, fails to give precise quantitative predictions about the spectral shape and coupling. Further studies are required to identify a more precise description of the broadband noise.

Chapter 8

Coherently Induced Faraday Rotation

In this chapter, we present a spin readout rate Γ_S calibration method. In the Coherently Induced Faraday Rotation (CIFAR), an optical polarization modulation coherent tone couples to the spins, interferes with spin response and reveals information about the readout rate Γ_S . The signal is also sensitive to the tensor coupling parameter ξ_S , spin linewidth γ_S and to the broad spin mode dynamics. The technique has been developed as complementary method to the presented in Chapter D, which itself gives information about the ratio of quantum back-action to thermal noise (QBA/TH).

We start by describing the basic idea, the signal modeling, and finish the chapter discussing experimental results.

8.1 Introduction

Estimating the spin-light interaction strength allows us to determine the effect of the light in the spin dynamics. For minimizing systematic errors, an ideal calibration technique would provide the measurement in a disturbance free and self-calibrated manner. From the practical point of view, it would also only involve marginal change in the experimental setup.

Our spin ensemble, in the hybrid experiment, is operated in conditions rather different from the previous setups in QUANTOP (Sherson, 2006; Krauter, 2011). Operating the experiments in a continuous wave fashion makes most of the techniques historically employed for calibrating spin-light interaction inapplicable.

In Møller et al. (2017), we have used a calibrated amount of classical optical polarization noise to drive the spins and estimate QBA/TH. The necessity of calibrating the amount of added noise is the essential crux of the problem, as it relies in determining the quantum efficiency of the detection path. Essentially, as the interaction strength increases, the fractional error in detection efficiency will generate an increased uncertainty in the estimate of QBA/TH. As we aim to work in the regime in which quantum back-action dominates the spin response, we would therefore like to use a method that does not rely on knowing the photon detection efficiency.

With a closer look on the similarities the spin and mechanical systems share, we drew inspiration from the *Optomechanically-Induced Transparency* (OMIT) experiments (Weis et al., 2010), widely used in the optomechanics community as a calibration technique —see its usage in (Nielsen et al., 2017), for example.

The original OMIT experiment can be described as follows. A phase modulated input drive is sent to the optomechanical cavity; this cavity, being operated with a non-zero detuning, converts the phase into amplitude modulation, quadrature which couples to the mechanical oscillator. The modulated drive is swept in frequency around the mechanical resonance. For a given detuning, the response of this drive then interferes with the input, generating a characteristic dispersive signal. Most importantly, the interference pattern does not depend

on photo-detector quantum efficiency and its shape is independent of driving power.

For the case of our free-space spin ensemble, there is no cavity to reference the response of the oscillator to its own the drive. Nonetheless, using a suitable EOM we can make arbitrary combinations of input quadratures. Due to the QND nature the coupling, the drive would then be unaffected by the interaction, serving as reference for the process.

Let us consider the signal modeling. Starting from the QND input-output relations presented in Chapter 3, the steady state response of the spin system, in the frequency space is, from equations (3.38) and (3.39)

$$X_L^{\text{out}} = X_L^{\text{in}} \quad (8.1)$$

$$P_L^{\text{out}} = P_L^{\text{in}} + 2\Gamma_S \chi_S X_L^{\text{in}}, \quad (8.2)$$

in which $\{X^{\text{in}}, P^{\text{in}}\}$ and $\{X^{\text{out}}, P^{\text{out}}\}$ are the optical quadratures of the input and output light field, respectively. The coupling to the thermal bath is neglected, as the classical drive dominates the response. We have also dropped the operator notation and the tensor coupling, for simplicity. Choosing, for example, an input modulation satisfying $X^{\text{in}} = P^{\text{in}} = G$, the output phase quadrature becomes

$$P_L^{\text{out}} = (1 + 2\Gamma_S \chi_S) G. \quad (8.3)$$

Notably, drive and response interfere independently of the input amplitude G —as we were wishing for. In particular, the absolute square of (8.3), for the spin susceptibility in the high-Q limit $\chi_S \sim \frac{1}{2}(\delta - i\gamma_S/2)^{-1}$, we have

$$|P_L^{\text{out}}|^2 \equiv \text{CIFAR} \propto 1 + 4\Gamma_S^2 |\chi_S|^2 + 4\Gamma_S \text{Re}\chi_S = 1 + \frac{\Gamma_S^2 + 2\Gamma_S \delta}{\delta^2 + (\gamma_S/2)^2},$$

for δ as relative frequency between the spin resonance and the input modulation tone. The CIFAR signal for a set of spin parameters is presented in Figure 8.1 (left), with $\theta_{\text{in}} = -\pi/4$ the input drive satisfying $X^{\text{in}} = P^{\text{in}} = G$. The definition of θ_{in} will be presented in the next section. Notice that the signal is a combination of a constant, a lorentzian, and a dispersive term. The minimum and maximum of the signal are at the frequencies

$$\delta_{\text{min}} = \frac{1}{2} \left(-\sqrt{\gamma_S^2 + \Gamma_S^2} - \Gamma_S \right) \quad (8.4)$$

$$\delta_{\text{max}} = \frac{1}{2} \left(\sqrt{\gamma_S^2 + \Gamma_S^2} - \Gamma_S \right), \quad (8.5)$$

being separated by

$$\delta_{\text{min}} - \delta_{\text{max}} = \sqrt{\Gamma_S^2 + \gamma_S^2} \sim \Gamma_S,$$

in the limit high coupling, $\Gamma_S \gg \gamma_S$. Therefore, one can readily know the readout rate just by noting this frequency difference, directly from the sweep figure. In Figure 8.1 (right), we show the CIFAR signal for various readout rates.

With this, we finish the introduction to the CIFAR signal. Comparing CIFAR with the calibration technique presented in Chapter D, we see that in CIFAR we do not need to precisely know the detection efficiency to estimate the coupling rate. The sensitivity to the thermal occupation of the ensemble, nonetheless, is lost when using CIFAR. In a sense, both techniques can work in parallel, giving information about more parameters.

We now move on to the more detailed model, which includes the effects of tensor coupling, and arbitrary input and detection quadratures.

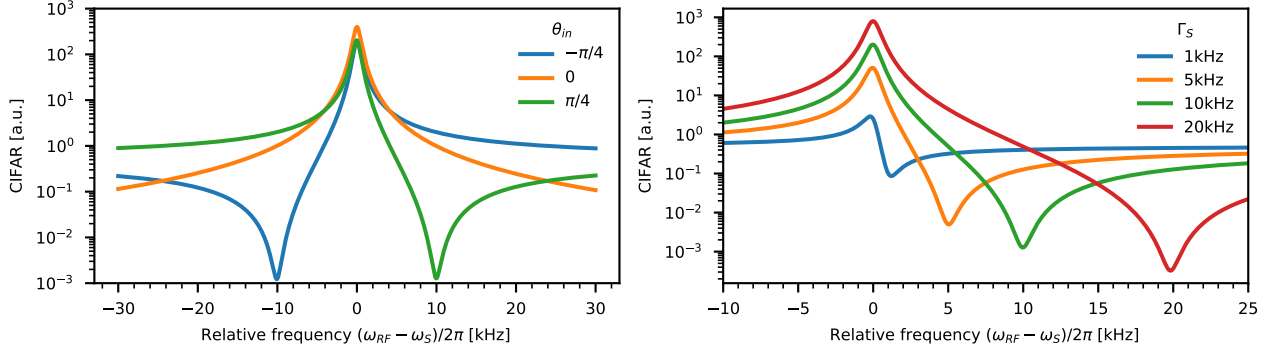


Figure 8.1: CIFAR signal and readout rate estimation. Driving the spins with different types of polarization modulation, parametrized by θ_{in} , leads to interference of the input field with the response. The tensor interaction parameter is set to zero, $\zeta_S = 0$. (left) By detecting the phase quadrature of light P^{out} and driving the spins with $\theta_{in} \pm \pi/4$, leads to a dip at ± 10 kHz, which is the readout rate Γ_S in the limit of $\Gamma_S \ll \gamma_S$. Setting the driving modulation and increasing the readout rate (right), leads to a dip shifting accordingly. Other parameters for this figure are $\gamma_S/2\pi = 1$ kHz, $\omega_S/2\pi = 1$ MHz.

8.2 General CIFAR expression

A general CIFAR modelling relies on using the precise input-output relations. We point to Chapter 3 for the discussions on the matter. Here, we reproduce some of the steps, with emphasis on the CIFAR context.

The steady state response of the spin system to an optical field, in the matrix notation, is given by equations (3.42) and (3.50). Dropping the term referring to the thermal environment coupling, we have

$$\hat{\chi}_S = 2\sqrt{\Gamma_S}\mathbf{LZ}\hat{\chi}_L^{in} \quad (8.6)$$

for the spin system, and

$$\hat{\chi}_L^{out} = \hat{\chi}_L^{in} + \sqrt{\Gamma_S}\mathbf{Z}\hat{\chi}_S = (\mathbf{1}_2 + 2\Gamma_S\mathbf{ZLZ})\hat{\chi}_L^{in}, \quad (8.7)$$

for the light field, where $\mathbf{1}_2$ is the 2×2 identity matrix. The matrices \mathbf{Z} , $\hat{\chi}_L^{in}$, $\hat{\chi}_L^{out}$, $\hat{\chi}_S$, and \mathbf{L} are given in the sidebar¹, for reference.

The input driving field $\hat{\chi}_L^{in}$ can be generated by an EOM that is capable of producing polarization modulation, as a free space EOM, as shown by Sherson (2006). An alternative method is to use a polarization sensitive interferometer. A standard phase modulator in one of the arms, modulates the phase of a weak laser tone. This tone is subsequently mixed it with a the strong local oscillator already in use in a polarization beam splitter. If the beams are mixed with orthogonal polarizations, the laser at the output of the interferometer will have its polarization modulated. Controlling the relative path length in the interferometer allows for selecting arbitrary polarization ellipticity or, in the quadratures language, an arbitrary combination of X_L^{in} and P_L^{in} .

In any case, the effect of the arbitrary control is done by choosing θ_{in} as

$$\begin{aligned} \begin{pmatrix} X_L^{in} \\ P_L^{in} \end{pmatrix} &= \begin{pmatrix} \cos \theta_{in} & -\sin \theta_{in} \\ \sin \theta_{in} & \cos \theta_{in} \end{pmatrix} \begin{pmatrix} 0 \\ G \end{pmatrix} \\ &= \begin{pmatrix} -\sin \theta_{in} \\ \cos \theta_{in} \end{pmatrix} G, \end{aligned}$$

$$\mathbf{Z} = \begin{pmatrix} 0 & -\zeta_S \\ 1 & 0 \end{pmatrix}$$

$$\mathbf{L} = \begin{pmatrix} \gamma_{S0}/2 + \zeta_S\Gamma_S - i\Omega & -\omega_S \\ \omega_S & \gamma_{S0}/2 + \zeta_S\Gamma_S - i\Omega \end{pmatrix}^{-1}$$

$$\hat{\chi}_L^{in} = \begin{pmatrix} \hat{X}_L^{in} \\ \hat{P}_L^{in} \end{pmatrix}, \quad \hat{\chi}_L^{out} = \begin{pmatrix} \hat{X}_L^{out} \\ \hat{P}_L^{out} \end{pmatrix}$$

$$\hat{\chi}_S = \begin{pmatrix} \hat{X}_S \\ \hat{P}_S \end{pmatrix}$$

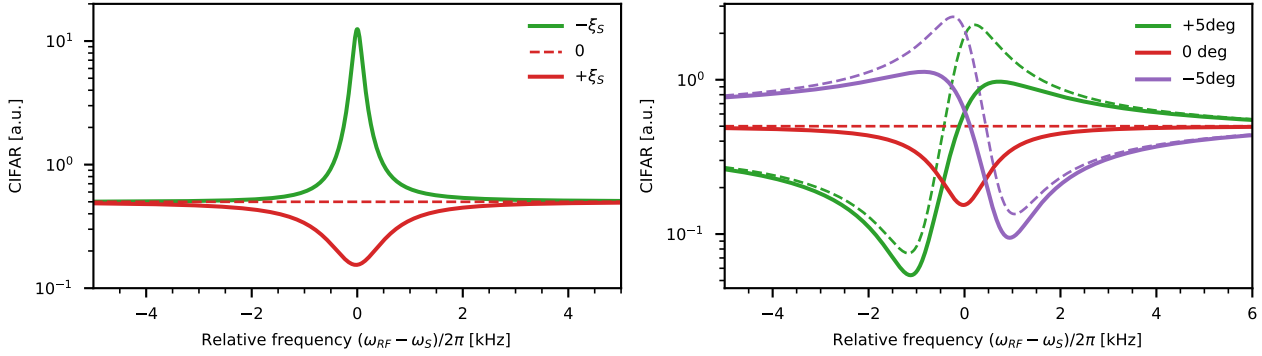


Figure 8.2: Tensor effects in the CIFAR signal. The presence of tensor effects, $\zeta_S = 0.04$, leads to a non-zero spin response when detecting the amplitude quadrature X^{det} of light. (left) The sign of ζ_S determines if the response observed will be a dip or a peak. (right) Detecting an optical quadrature away from the ideal value by $\pm 10^\circ$ leads to mixing with the phase quadrature response, resulting in a dispersive feature; dashed curves are for $\zeta_S = 0$ and solid curves have $\zeta_S = 0.04$. Other parameters for this figure are $\gamma_S/2\pi = 1$ kHz, $\Gamma_S/2\pi = 10$ kHz and $\omega_S/2\pi = 1$ MHz.

for a modulation with amplitude G . The detection quadrature, by the same line of thought, can be chosen by its ϕ value

$$\begin{pmatrix} X^{\text{det}} \\ P^{\text{det}} \end{pmatrix} = \begin{pmatrix} \cos \phi & -\sin \phi \\ \sin \phi & \cos \phi \end{pmatrix} \begin{pmatrix} X_L^{\text{out}} \\ P_L^{\text{out}} \end{pmatrix}.$$

If $\phi = 0$, the detected quadratures are identical to the output from the spin ensemble. We remind the reader that the quadratures $\{X^{\text{det}}, P^{\text{det}}\}$ are measured using balanced polarimetry and that the output quadratures are related to the Stokes parameters $X_L^{\text{out}} \propto S_z$ and $P_L^{\text{out}} \propto S_y$.

Finally, by plugging in all the matrices in equation (8.7), we get to the general expressions

$$\begin{aligned} X_L^{\text{out}} &= \frac{2P_L^{\text{in}}\Gamma_S\zeta_S^2\omega_S}{\omega_S^2 + \left(\frac{\gamma_S}{2} + \Gamma_S\zeta_S + i\Omega\right)^2} + X_L^{\text{in}} \left(1 - \frac{2\Gamma_S\zeta_S \left(\frac{\gamma_S}{2} + \Gamma_S\zeta_S + i\Omega\right)}{\omega_S^2 + \left(\frac{\gamma_S}{2} + \Gamma_S\zeta_S + i\Omega\right)^2}\right) \\ P_L^{\text{out}} &= P_L^{\text{in}} \left(1 - \frac{2\Gamma_S\zeta_S \left(\frac{\gamma_S}{2} + \Gamma_S\zeta_S + i\Omega\right)}{\omega_S^2 + \left(\frac{\gamma_S}{2} + \Gamma_S\zeta_S + i\Omega\right)^2}\right) - \frac{2X_L^{\text{in}}\Gamma_S\omega_S}{\omega_S^2 + \left(\frac{\gamma_S}{2} + \Gamma_S\zeta_S + i\Omega\right)^2}, \end{aligned} \quad (8.8)$$

which are used throughout this chapter.

In particular, we can see the complexities added by the tensor interaction. In Figure 8.2 (left), we plot the CIFAR signal for measuring the amplitude quadrature, $\phi = \pi/2$, and driving at $\theta_{\text{in}} = \pi/4$. The amplitude quadrature, which contains no spin response in the QND regime, as per equation (8.1), gets a Lorentzian feature that adds (subtracts) from the constant background for (negative) positive ζ_S . The different width features represents the dynamical cooling induced by the optical probe. When slightly deviating from the ideal amplitude quadrature detection, a situation often encountered experimentally, there is an interference with spin response present in the phase quadrature, see Figure 8.2 (right).

We now move to discussing the experimental realization of CIFAR.

8.3 Experiments

In this section, we present a collection of experimental results accumulated over the period of approximately 1 year. Being so, the measurements were

taken in different experimental conditions of probe power, atomic density and Larmor frequency, and must not be directly compared to each other. We aim to show the capabilities and sensitivities of the probing scheme.

For all measurements shown here, we have generated the polarization modulation using the scheme of a phase modulator within a polarization sensitive interferometer, as shown in Figure 8.3. In simple terms, at an initial PBS the local oscillator and the modulation light are split. The EOM modulates the phase of the modulation light. At the output of the interferometer, the beams are recombined in another PBS, leading to polarization modulation of the output field. One of the output arms ports of the interferometer is aligned to the spin ensemble and the other to phase stabilization.

The interferometric visibility between the modulation and local oscillator beams is usually on the order of 90%. We can easily select the type of polarization modulation by changing the interferometer locking point. On the other hand, the quality of the path length difference control is very important to control the type of polarization modulation, needing to be stabilized via a feedback control of a piezo installed in one of the interferometer's arm.

As it can be seen from the theory curves from Figure 8.1 (right), the dip of the detected signal will get more pronounced with larger spin readout rates. Therefore, in this frequency region, in which the drive and the spin response interfere destructively, the signal is the most sensitive to electronic pick-ups and other technical imperfections. Having the collected the data, the fitting procedure used for extracting the various parameters works best if educated guesses are set as input.

In Figure 8.4 (left), we show the results for various drive amplitudes. We have set the driving and detection angles such that $\phi = 0$, measuring P_L^{out} , and driving at $\theta_{\text{in}} = \pi/4$. Increasing the voltage drive leads to a mere scaling of the detected signal, as described in Section 8.1.

The dependence of the signal on the tensor interaction strength ζ_S is shown in Figure 8.4 (right). As presented in Figure 8.2, the tensor coupling leads to a frequency dependent change in the CIFAR response. We have controlled $\zeta_S = -14 \frac{a_2}{a_1} \cos 2\alpha$ by the angle α of the linearly polarized strong probe with respect to the DC magnetic field. Measuring both $\{X_L^{\text{det}}, P_L^{\text{det}}\}$ output light quadrature for a drive with $\theta_{\text{in}} = \pi/4$. We show that the tensor interaction can be turned off at $\alpha = \pi/4$. For $\alpha = \{0, \pi/2\}$, a feature similar to the shown in Figure 8.2(left) appears in the measurement of X_L^{meas} . The frequency shift is due to

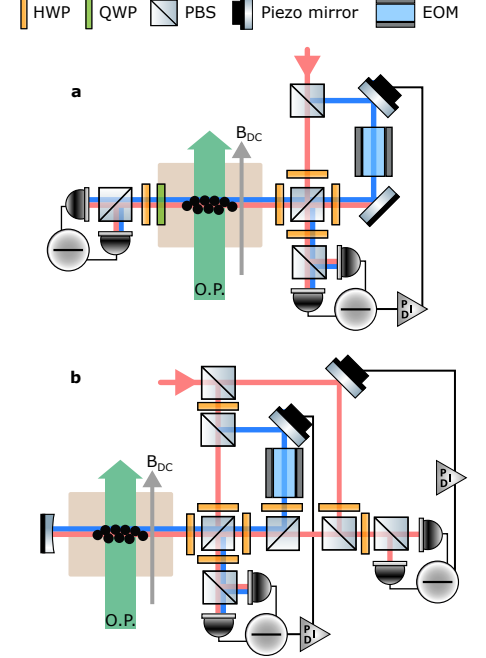


Figure 8.3: Experimental setup. The single pass **a** and double pass setups for the CIFAR experiments. The EOM's arm optical path is marked in blue for reference. The spin ensemble is positioned in a constant magnetic field B_{DC} within a magnetically shielded volume. Optical pumping (O.P.) is marked by the green arrow.

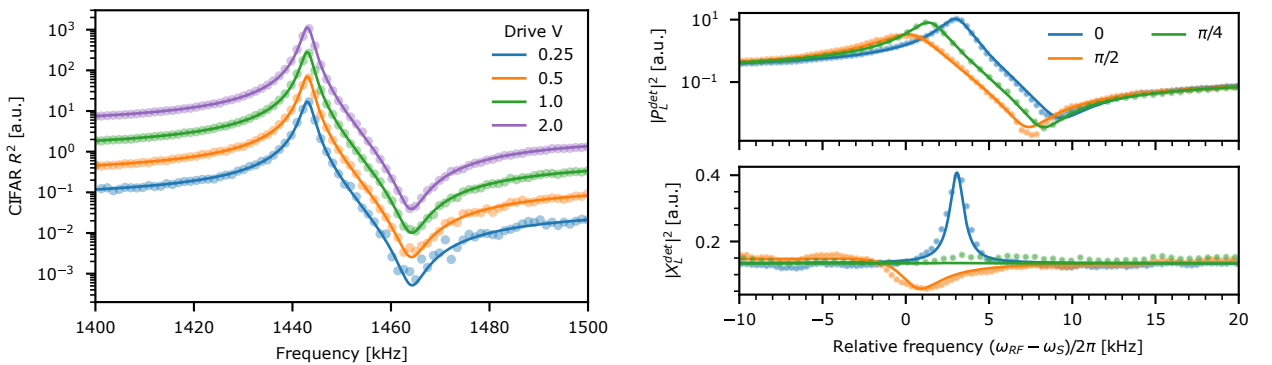


Figure 8.4: CIFAR signal for various drive amplitudes and tensor couplings ζ_S . The shape of the detected signal is not dependent on the EOM drive voltage V (left), with detected power scaling linearly with the input drive power $\propto V^2$. The CIFAR signal is sensitive to the tensor couplings parameter ζ_S (right). By choosing different angles of the linearly polarized strong probe with respect to the DC magnetic field and measuring both $\{X_L^{\text{det}}, P_L^{\text{det}}\}$ output light quadratures, we can set $\zeta_S = 0$ (in green), $\zeta_S = 0.05$ (in orange), and $\zeta_S = -0.05$ (in blue). Other parameters for this figure are $\omega_S/2\pi = 340$ kHz.

the static terms of tensor interaction, neglected in the Hamiltonian derivation in Chapter 3.

8.3.1 Broadband spin noise

The modulation of the input polarization, mimicking an enhanced optical coupling rate, couples to the spins in the same manner the quantum noise fluctuations. Being so, both narrow and broad spin contributions will appear in the CIFAR response, equation (8.7). The effect of the narrow and broadband noise contribution, as discussed in Chapter 7, can be modeled as given in equation (7.5)

$$\hat{\chi}_{L,S}^{\text{out}} = \hat{\chi}_{L,S}^{\text{in}} + \sqrt{\Gamma_S} \mathbf{Z} \hat{\chi}_S + \sqrt{\Gamma_{S,b}} \mathbf{Z} \hat{\chi}_{S,b}. \quad (8.9)$$

with the broad spin mode dynamics as

$$\hat{\chi}_{S,b} = 2\sqrt{\Gamma_b} \mathbf{L}_b \mathbf{Z} \hat{\chi}_{L,S}^{\text{in}}, \quad (8.10)$$

where \mathbf{L}_b is \mathbf{L} with $\gamma_{S0} \rightarrow \gamma_b$, and $\Gamma_S \rightarrow \Gamma_{S,b}$. $\Gamma_{S,b}$ is the broadband spin mode readout rate. According to this model, both responses will be driven by the same light field. By having a common origin, they will interfere with the drive and be present in output light. Given the characteristic broadband mode bandwidth of order MHz, the CIFAR scan must cover a large frequency band.

In Figure 8.6, we show a wideband CIFAR scan for $\phi = 0$ and different θ_{in} . Differently than the figures shown above, we decompose the demodulated signal in the polar form, plotting the amplitude squared R^2 and its phase ϕ . With $\omega_S/2\pi = 1.3$ MHz, we set the scan to cover a ~ 1.1 MHz span. The trace for $\theta_{\text{in}} = \pi/2$ should have a response to light that closely matches the case for a driven harmonic oscillator. The fit to the model given in equation (8.9), for $\Gamma_{S,b} = 0$, is presented as the black curve in Figure 8.5. The extra noise in the wings of Figure 8.5 (top) and the phase of the spin response in Figure 8.5 (bottom) give away the message of coupling to the broadband mode.

The full model fit, now including a non-zero broadband mode coupling rate, is given in Figure 8.6. The presence of the broadband response as modeled above reproduces the detected features rather well, including the electronic phases response. The extracted spin mode coupling rates $\Gamma_S/2\pi = 19$ kHz and $\Gamma_{S,b}/2\pi = 83$ kHz. Although rather well coupled to light, the broad mode quantum cooperativity is $\Gamma_{S,b}/(2\gamma_b(n_S + \frac{1}{2})) \sim 0.02$, for $\gamma_b/2\pi = 1.3$ MHz and $n_S = 0.8$ (assumed to match the narrow mode occupation). Therefore, it is

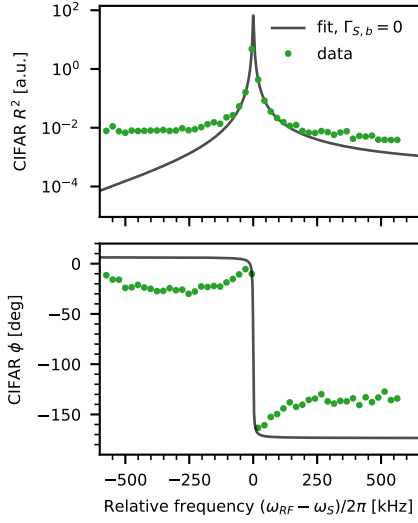


Figure 8.5: Signatures of the broadband spin noise. The polarization modulation drive also couples to the broadband spin modes, altering the wide CIFAR scan. The data for $\theta_{\text{in}} = 0$ presented in 8.6 is shown, along with the fit function for $\Gamma_{S,b} = 0$, demonstrating the expected behaviour for a homogeneous spin-light coupling.

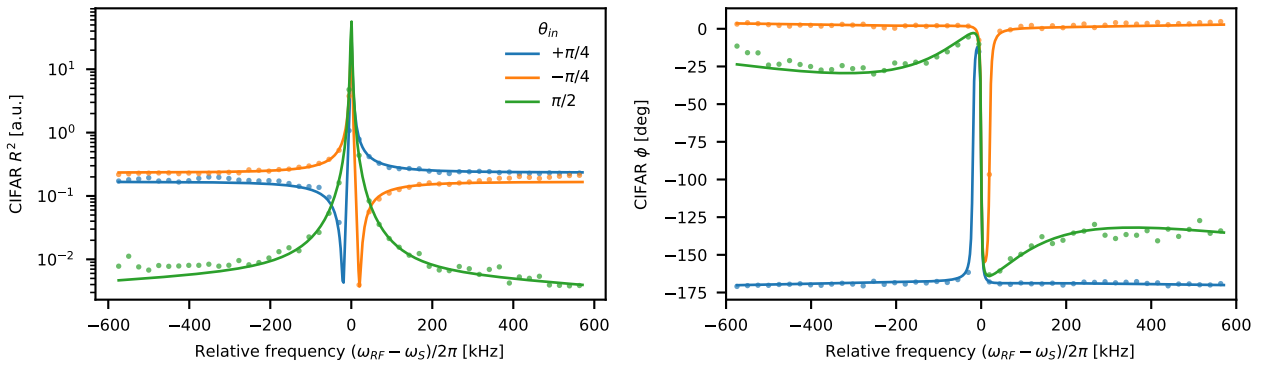


Figure 8.6: Wide CIFAR scan. The CIFAR signal for various input modulation θ_{in} are shown, with detected power (left) and electronic phase (right).

safe to assume that quantum back-action effects on the broad mode are negligible. The narrow mode, for example, shows $C_q^S \sim 5$.

In this chapter, we have shown a polarization modulation calibration technique that gives direct information about light-spins interaction strength. The signal generated by this method is sensitive to the various intricacies of the coupling, including tensor effects and broadband spin modes.

Chapter 9

Spin optodynamics in a warm cesium ensemble

In this chapter we report on the performance of the spin oscillator placed in an optical resonator. The results presented here were part of an effort towards increasing the spin quantum cooperativity, one of the quantities that was a major limitation in the performance of the first implementation of the hybrid experiment (Møller et al., 2017).

Due to coherent build up of the intra-cavity field, the effective optical depth of the ensemble, for a cavity with finesse \mathcal{F} , is increased as $\frac{2}{\pi}\mathcal{F}$ (Ye and Lynn, 2003), leading to a corresponding quantum cooperativity boost. Previous experiences with cavity enhanced warm vapour in the group (Vasilakis et al., 2015), showed that finesse as $\mathcal{F} \sim 17$ were achievable. An astounding $\times 10$ increase in quantum cooperativity was a good reason to study this configuration in more detail. If intra-cavity losses could be made low, the optical link between spin and mechanics would also be efficient. Note how both a high C_q and inter-system losses are important for optimal hybrid system performance.

It did not take long to realize that operating the spins in the of high probing powers, as in the hybrid experiment, the optical resonator introduced drastically different spin oscillator dynamics. In particular, we observed a rather sensitive dependence of the spin response on cavity detuning, effects that resemble the dynamics of an optomechanical system (Brahms and Stamper-Kurn, 2010). The *spin optodynamical* system, in which the mechanical oscillator is replaced by the spin analogous, can exhibit the same phenomena as those explored in the field of quantum optomechanics, as cooling (Gigan et al., 2006) and amplification (Kippenberg et al., 2005), and ponderomotive squeezing of light (Brooks et al., 2012). As we will see in the next pages, we observed all the mentioned effects in our warm spin ensemble implementation. Many of these effects have been observed in a cold spin ensemble cloud (Köhler et al., 2017), also in a spin-mechanics hybrid configuration (Köhler et al., 2018).

As far as the hybrid experiment is concerned, we have not yet implement the cavity-enhanced spin response in the next generation of experiments. The trade-off between finesse enhancement and intra-cavity photons escape efficiency $\kappa_{\text{in}}/\kappa$, the fraction of intra-cavity photons leaking into the optical mode of interest, was not beneficial for the hybrid experiment performance. Due to around 10% vapor cell induced round-trip losses, requiring $\kappa_{\text{in}}/\kappa > 0.9$ would lead to $\mathcal{F} \sim 1$, undermining the C_q improvements.

In this chapter we present a summary of the procedures used for cell cavity characterization and the initial results on the cavity enhanced spin response.

9.1 Cell cavity characterizations

As in the previous cell cavity designs utilized in the group, we positioned the vapor cell in a Fabry-Perot interferometer in an almost concentric mirror

Cell cavity characterizations

configuration. The mirrors M_1 and M_2 , with nominal radius of curvature¹ $R_1 = 110$ mm and $R_2 = 120$ mm. The mirror transmissivities are $r_1 = 99.97\%$ and $r_2 = 80\%$, respectively. We placed the two cavity mirrors just outside the magnetic shielding, at $d \sim 230$ mm distance. With this mirror spacing configuration, we operate with very small beam radius w_0 , required for fitting the light through the $300 \mu\text{m}$ side length cell, but also close to the unstable resonator regime. The beam radius w_0 , the transverse cavity mode frequency ν_{mn} of the TEM_{mn} mode, and the finesse coefficient are (Kogelnik and Li, 1966)

$$w_0^4 = \left(\frac{\lambda}{\pi}\right)^2 \frac{d(R_1 - d)(R_2 - d)(R_1 + R_2 - d)}{(R_1 + R_2 - 2d)^2} \quad (9.1)$$

$$\frac{\nu_{qmn}}{\text{FSR}} = (q + 1) + \frac{1}{\pi}(m + n + 1) \arccos \sqrt{(1 - d/R_1)(1 - d/R_2)} \quad (9.2)$$

$$\mathcal{F} \approx \frac{\pi(r_1 r_2)^{\frac{1}{4}}}{1 - (r_1 r_2)^{\frac{1}{2}}} \quad (9.3)$$

in which λ is the wavelength of light, c the speed of light, d is the cavity length, $\text{FSR} = c/2d$ the free spectral range of the cavity, and q the longitudinal mode number. The typical transmission spectrum of the cell cavity is shown in Figure 9.2 (orange points). Finite mode-matching of the input mode to the fundamental TEM_{00} cavity mode appears as non-zero contributions from the TEM_{10} and TEM_{20} families.

The cavity parameters we are mostly interested in measuring are the cavity beam waist w_0 and the cavity decay rate κ . The beam waist defines the overall interaction with the spins once the vapour cell is aligned to the cavity mode. As discussed in Chapter 7, we are interested in the biggest filling factor of the cell channel, for reducing the broadband spin contribution, entailing in a large w_0 . Nonetheless, we are also interested in achieving the highest possible cavity finesse, which entails using a small w_0 . The compromise is solved by choosing a beam waist whose Rayleigh length $z_R = \pi w_0^2/\lambda$ matches the cell length. For a cell with $L_{\text{cell}} = 10$ mm, it leads to $w_0 \sim 50 - 60 \mu\text{m}$. The cavity decay rate gives us information about the overall losses and can be used to determine the vapor cell induced intra-cavity losses.

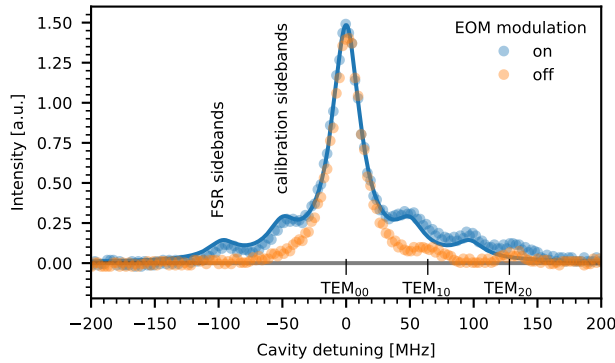


Figure 9.2: FSR, TMS and empty cavity linewidth measurements. By scanning the cavity piezo around resonance, cavity length and waist parameters are calibrated by using phase modulated light. The transmitted light without modulation (yellow) shows the spectral decomposition of the input mode in the cavity mode basis. We aim to match the input to the TEM_{00} mode. Finite mode-matching appears as non-zero contributions from the TEM_{10} and TEM_{20} families. The sidebands are set for calibrating the frequency axis and the cavity FSR.

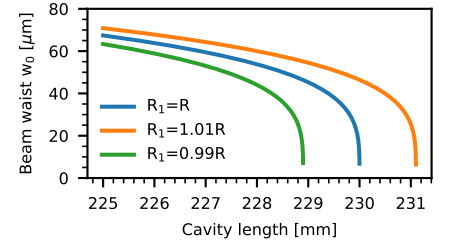


Figure 9.1: Beam waist sensitivity on the cavity length. Percent scale uncertainties in the mirror curvatures lead to a large uncertainty on the beam waist, if calculated using equation (9.1). The mirror radius of curvatures are $R = 110$ mm and $R_2 = 120$ mm.

¹We chose mirrors with radius of curvature such that there was a ~ 10 mm gap for placing a small mirror inside the cavity, for free space-like characterizations of the system.

The beam waist can be estimated by measuring the using cavity length d and mirror curvatures R_1, R_2 , as given in equation 9.1. In Figure 9.1, we show the beam waist as a function of the cavity length. Note the sensitivity to the cavity length and in the mirror curvature R_1 . The manufacturer specifies the curvatures with a $\pm 5\%$ margin.

A trustworthy method for estimating the beam size is using the frequency of the higher order transverse modes TEM_{mn} . As the different modes will pick up different overall phases per cavity round trip, the frequency of the modes is sensitive to the radius of curvature and to the total cavity length as given in equation (9.2). We define the transverse mode splitting ν_{TMS} as

$$\nu_{\text{TMS}} \equiv \nu_{q10} - \nu_{q00} = \frac{\text{FSR}}{\pi} \arccos \sqrt{(1 - d/R_1)(1 - d/R_2)}. \quad (9.4)$$

In Figure 9.3 we show how the transverse mode splitting measurement gives a much more precise estimate of the beam waist, even considering the manufacturer mirror specs. The sensitivity of this method is about $2.5 \text{ MHz } \mu\text{m}^{-1}$.

Given the sensitivity of the cavity waist estimation on the mirror's radius of curvature and cavity length, we proceed to characterize the cavity parameters in an all optical method. We use an EOM to generate phase modulation sidebands around the laser carrier. By scanning the cavity length around resonance, the transmission signal will give rise to transmission peaks allowing for estimating the cavity decay rate κ and the transverse mode splitting ν_{TMS} . Finally, we estimate the free spectral range by driving the EOM with a frequency close to the longitudinal mode spacing, here $\sim 560 \text{ MHz}$.

With the aid of calibration sidebands ($\omega_{\text{cal}}/2\pi = 50 \text{ MHz}$). We determine the FSR is $\sim 660 \text{ MHz}$. The calibration sidebands allow extraction of the cavity decay rate and transversal mode spacing, here $\kappa/2\pi = 26 \text{ MHz}$ and $\nu_{\text{TMS}} = 63 \text{ MHz}$, respectively. The beam waist for this given cavity setting is $65(2) \mu\text{m}$.

We proceed to align the cell to the resonator optical mode. Placing the cell in the cavity will enlarge the optical length by $\sim 4 \text{ mm}$ due to the glass cell windows, therefore reducing the beam size to approximately $55 \mu\text{m}$.

Placing the cell J18 in the resonator brings the cavity linewidth to $\kappa/2\pi = 33 \text{ MHz}$, corresponding to a $\mathcal{L} = 7\%$ of round trip added losses. The photon escape efficiency through the mirror M_2 , here defined as

$$\eta_{\text{cav}} = \frac{T_2}{T_1 + T_2 + \mathcal{L}} \quad (9.5)$$

goes from ~ 0.9 to ~ 0.67 for the cell cavity with the aligned cell. Correspondingly, the finesse \mathcal{F} goes from 26 to 19. Although the promising cavity finesse, η_{cav} is prohibitively low. In the current hybrid experiments, the cell induced losses should not exceed 5%, otherwise the spin system itself becomes the limiting factor in quantum efficiency.

Overall, despite the low efficiency of the photon detection, a parameter which the hybrid experiment is quite sensitive to, the enhancement of the spin-light interaction is potentially substantial. In the next two sections we will present some experimental results and provide some theoretical background to the findings.

9.2 Experiments

We have set up the spin cavity as shown in Figure 9.4. The mirrors M_1 and M_2 are mounted to $\text{\O}1.5''$ posts. The cavity is read out in transmission, with the polarimetry detection set up after mirror M_2 . The probe laser frequency is set to 852.3700 nm , approximately -6 GHz from the $F = 4 \rightarrow F' = 5$ electronic transition in the D_2 line. The cavity path length is stabilized by dither locking. The cavity resonance can be tuned and modulated via piezoelectric action. We lock the cavity in reflection, with dither frequency $\omega_{\text{dither}}/2\pi = 100 \text{ kHz}$.

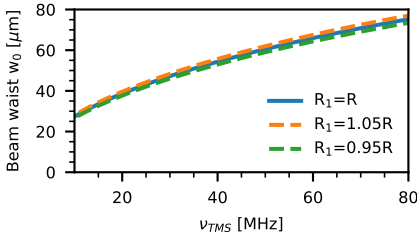


Figure 9.3: Beam waist sensitivity on the transverse mode splitting. The TEM_{00} beam waist plotted versus the transverse mode splitting. The mirror radius of curvatures are $R = 110 \text{ mm}$ and $R_2 = 120 \text{ mm}$. Note how the dashed curves represent a $\times 5$ larger uncertainty than in Figure 9.1.

The experiment is ran in the continuous mode, with the optical pumping performed by a repump beam only. The photo-detection is set up in transmission, allowing us to freely choose the optical quadrature of interest. The different optical quadratures are set adjusting the HWP and QWP used in the polarimetric measurements.

We start by showing the results with the optical cavity tuned to resonance, $\Delta = 0$. The effects of a considerable C_q in the optical signal are very similar to the ones discussed in Chapter 3. In Figure 9.5 we show the power spectral density of two different optical quadratures, with $\varphi \sim 0$ deg (left) and $\varphi \sim 90$ deg. The quantum cooperativity was estimated by the white noise method, described in Appendix D, being in the range of 0.5-1.5 for the experiments shown in this section.

As discussed in Section 3.3, the probing beam induces light shifts due to the non-zero tensor coupling. The initial Zeeman level splitting, set by the quadratic component $\omega_{qzs}/2\pi = 0.6$ kHz, is further enhanced to approximately 1.9 kHz by the probe laser with linear polarization along B_{DC} ($\alpha = 0$ deg) in Figure 9.5 (left, orange curve). By setting the probe polarization to $\alpha \sim 56$ deg, we cancel the shifts via light, recovering the effective single spin mode description (blue curve). Having set α , we rotate the detection waveplates to observe an optical quadrature with $\varphi \sim 90$ deg. We fine tune the phase to mostly observe the drive optical quadrature, to observe the optical correlations induced by the spins. Notice the rather large broadband spin noise component, which is approximately 6 shot noise units. In Figure 9.5 (right) we observe frequency dependent squeezing of light, a quite remarkable feat as the overall detection efficiency was measured to be $\eta = 0.55$. The detection efficiency is mainly limited by the intra-cavity losses, as the empty cavity $\kappa_{in}/\kappa = 0.91$ are decreased to $(\kappa_{in} + \kappa_{ex})/\kappa = 0.65$.

By detuning the optical cavity from resonance, substantially different effects than those explored in the free space case can be explored. In particular, the dynamical effects described in Section 9.3.

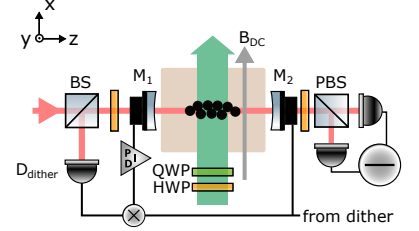


Figure 9.4: Sketch of the cell cavity setup. A cavity is assembled around the magnetic shielding (beige shaded area). The spin ensemble pumping, probing, and detection are similar to the described in Chapter 3. A sinusoidal drive with frequency $\omega_{dither}/2\pi = 100$ kHz drives the cavity resonance via a piezo-electric actuator. The locking signal is fed back to a second piezo. The output light from the cavity is detected in balanced polarimetry.

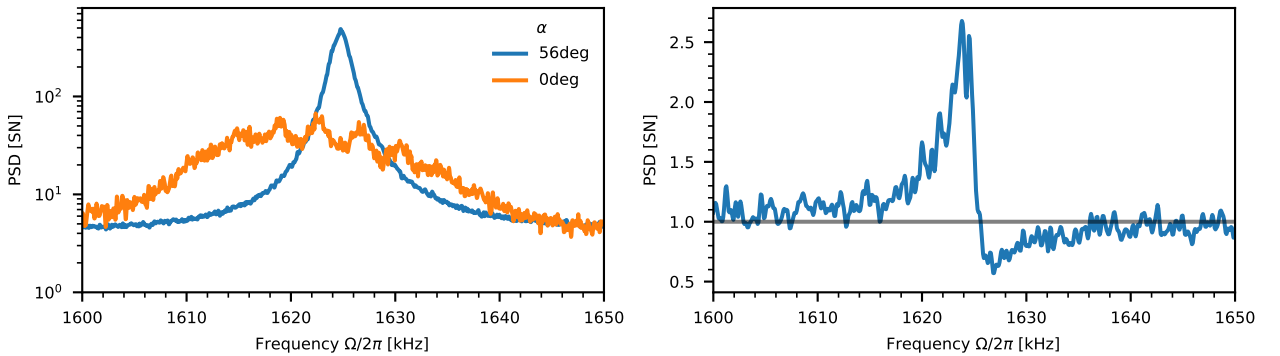


Figure 9.5: Cavity-enhanced spin noise in the phase and amplitude quadratures. (left) The PSD of cavity output phase noise ($\varphi = 0$ deg) exhibiting the spin response for a probe laser with linear polarization at $\alpha = 0$ deg (in orange) and $\alpha \sim 56$ deg (in blue). The latter light polarization leads to tensor Stark shifts that cancel the quadratic Zeeman splitting. (right) The PSD of the optical quadrature with $\varphi \sim 90$ deg, showing squeezing of the light fluctuations.

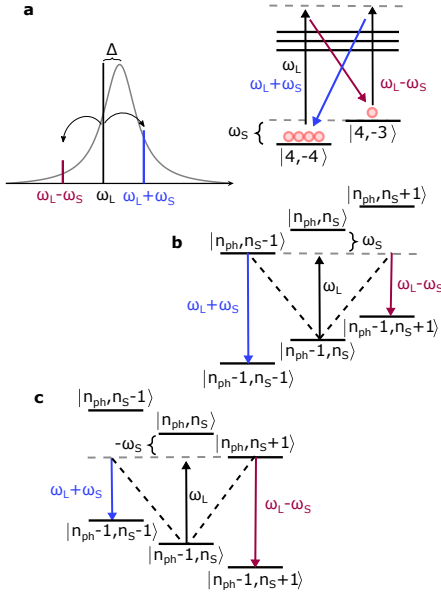


Figure 9.6: Cavity assisted spin heating and cooling. (a) The spin ensemble exchanges energy with the laser beam. Detuning the laser from the cavity allows for suppressing one of the Stokes scattering processes. (b) For a positive mass oscillator in a red detuned cavity, photons will predominantly scatter at $\omega_L + \omega_S$, removing a spin excitation n_S in the process. The states $|n_{\text{ph}}, n_S\rangle$ describe the number excitations in the light and spin oscillators. (c) Switching the effective mass of the oscillator, for the same cavity detuning, leads to preferential scattering at $\omega_L - \omega_S$, adding a spin excitation n_S in the process. Figure adapted from Nielsen (2016).

In a new experimental run, we set the spin system as an effective positive mass oscillator, resembling a *true* mechanical oscillator. In Figure 9.7 (left) we detune the cavity by $\Delta/2\pi = \pm 3$ MHz and observe the power spectral density for $\varphi = 0^\circ$. The full lines are fits to Lorentzian functions. By detuning the cavity to $\Delta < 0$ ($\Delta > 0$), we observe a downshift (upshift) of the oscillator frequency and optical broadening (narrowing) of the spin response. The spin linewidth increases from $\gamma_S/2\pi = 1.5$ kHz. For the resonant probing, to $\gamma_S/2\pi = 1.8$ kHz for the red detuned cavity (red curve). In the case of blue detuning, the spin response narrows, becoming $\gamma_S/2\pi = 1.2$ kHz wide.

By reversing the effective mass sign, the same cavity detuning leads to the opposite shift and broadening. For this configuration the cavity output power is higher than the negative mass case, being $150 \mu\text{W}$. The spin linewidth increases from $\gamma_S/2\pi = 2.1$ kHz, for the resonant probing, to $\gamma_S/2\pi = 2.4$ kHz for the blue detuned cavity (blue curve). In the opposite detuning, the spin response narrows to $\gamma_S/2\pi = 1.0$ kHz.

The principles of the cavity induced cooling and heating can be better understood by considering energy conservation arguments (Schliefer, 2009). The atoms exchange energy with the laser beam, promoting excitations and de-excitations of the spin ensemble, as depicted in Figure 9.6 (a). For a laser beam far detuned from the excited state electronic states F' , the interaction with light leads to the balanced Stokes ($\omega_L - \omega_S$) and anti-Stokes scattering ($\omega_L + \omega_S$) processes. Placing the ensemble inside a resonator and setting the laser frequency away from the resonance will unbalance the rates of the processes, favoring one of them, as seen in Figure 9.6 (b and c). In the case of a red detuned cavity ($\Delta < 0$), scattering higher frequency photons $\omega_L + \omega_S$ happens with higher rate. The oscillator will provide the required energy difference. In the case of a positive (negative) mass oscillator, a spin excitation will be removed (added) from the spin system.

The dynamical effects induced by the cavity can be further enhanced when increasing the intra-cavity power. If the cavity detuning is set in a way the Stokes process scatters atoms away from the ground state level, these photons will parametrically drive the ensemble (Brahms and Stamper-Kurn, 2010). When the rate of the Stokes scattering introduced by the probe overcomes the intrinsic decay rates, the spin system is parametrically driven out of its initial state. In the same way as in the AC Faraday angle experiments, the spin is set to coherently oscillate around the Bloch sphere pumped by the optical field.

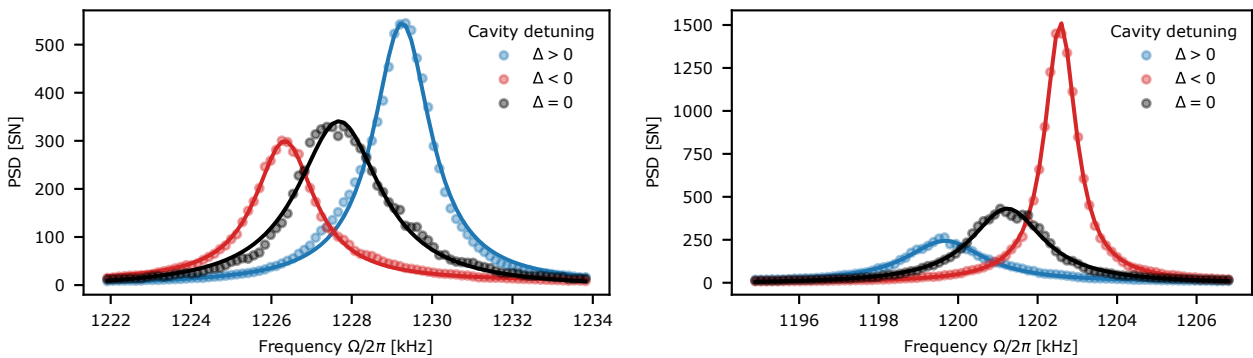


Figure 9.7: Spin oscillator exhibiting dynamical heating and cooling. The effects of the cavity detuning resemble cavity optomechanics: detuning the cavity to the red (blue) leads to a downshift (upshift) of the oscillator frequency and optical broadening (narrowing) for an effective positive mass spin oscillator (left). Switching the mass sign leads to the opposite frequency shift and broadening behaviour. For these sets, the cavity output power is $100 \mu\text{W}$ (left) and $150 \mu\text{W}$ (right). Detuned traces have $\Delta/2\pi = \pm 3$ MHz. The difference in spin frequency ω_S is due to slight change in B_{DC} .

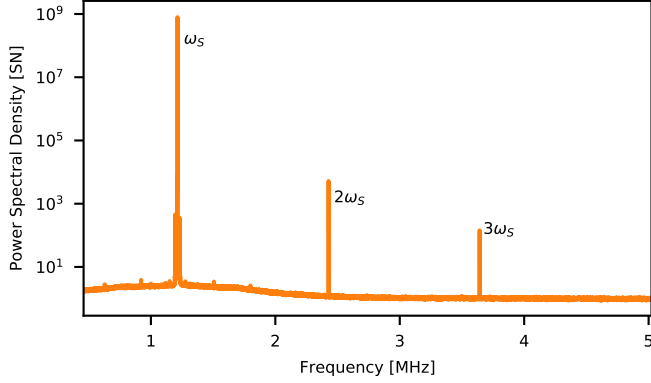


Figure 9.8: Spectrum of the signal exhibiting steady state coherent oscillations. By tuning the input power and blue detuning, the positive mass spin oscillator is put in a self-oscillator regime. We show the spectrum of the output light in shot noise units. The features linewidth is limited by the resolution bandwidth of the spectrum analyzer (< 50 Hz). Up to the 3rd harmonic are observable.

Spectrally, the output cavity field has its polarization modulated at the Larmor frequency ω_S with the amplitude determined by the effective coupling. In our experiments, the optical spectrum we observe is presented in Figure 9.8. The various narrow peaks are the harmonics of the 1.3 MHz Larmor frequency. The width of the features is narrower than the natural spin linewidth, a consequence of the parametric pumping.

9.3 Spin dynamics in a cavity

The optodynamical effects of the spin ensemble in an optical resonator have been studied in depth, including experimental, in Kohler et al. (2017). For more general aspects of the interaction, see (Brahms and Stamper-Kurn, 2010). Here, we will describe the cavity input-output relations and the dynamical cooling effects.

As described in Chapter 3, a probe beam far detuned from the $F = 4 \rightarrow F' = 5$ in the D_2 line, interacts with the ensemble via the scalar and vector light polarizability as

$$\hat{H}_{\text{eff}}/\hbar = \Delta \hat{S}_0 + \omega_S \hat{F}_x + 2g_{\text{eff}} (\hat{F}_0 \hat{S}_0 + \hat{F}_z \hat{S}_z) \quad (9.6)$$

with $g_{\text{eff}} \sim 1/\Delta_{La}$, in which $\Delta_{La} \equiv \omega_L - \omega_a$, the frequency detuning in between the light and the atomic transition. The interaction, as well as operators \hat{F}_i and \hat{S}_i , have been introduced in Chapter 3, with the extra detail that the optical field operators are now related to the intra-cavity field. We disregard tensor effects for simplicity. The detuning $\Delta \equiv \omega_L - \omega_c$, is the frequency difference of the input laser field with respect to the cavity resonance.

From here on, we will assume a strong, classical \hat{x} -polarized drive field and a \hat{y} -polarized quantum field, that is, $\hat{a}_x \rightarrow \alpha_x e^{i\phi}$ and $\hat{a}_y \rightarrow \hat{a}_y$, in which $\phi = \arctan(2\Delta/\kappa)$ is the phase of the intracavity carrier field with respect to the incoming field. This choice is such that the language here utilized and the one in Chapter 2 match in the functional form. We proceed to linearize the Hamiltonian (9.6) as

$$\hat{H}_{\text{eff}}/\hbar \sim -(\Delta - g_{\text{eff}} \bar{F}_0) \hat{a}_y^\dagger \hat{a}_y + \omega_S \hat{F}_x - i\alpha_x g_{\text{eff}} \hat{F}_z (\hat{a}_y e^{-i\phi} - \hat{a}_y^\dagger e^{i\phi}), \quad (9.7)$$

in which we have also assumed a constant number of atoms $\hat{F}_0 \rightarrow \bar{F}_0$. We also assume, *a priori*, that the steady state exists and is stable. We have disregarded static terms (as $\propto |\alpha_x|^2$). The spin ensemble shifts the cavity frequency according to the total number of atoms $\bar{F}_0 \sim N_a$, a shift that can be compensated by tuning the cavity back to resonance.

From this hamiltonian, using the Heisenberg-Langevin formalism, we calculate the equations of motion for the light and spin variables

$$\begin{aligned}
\frac{d}{dt}\hat{a}_y &= (i\Delta - \kappa/2)\hat{a}_y + g_{\text{eff}}\alpha_x e^{i\phi}\hat{F}_z + \sqrt{\kappa/2}\hat{a}_{y,\text{in}} \\
\frac{d}{dt}\hat{F}_x &= ig_{\text{eff}}\alpha_x(\hat{a}_y e^{-i\phi} - \hat{a}_y^\dagger e^{i\phi})\hat{F}_y - \gamma_{\text{S0}}\hat{F}_x/2 \\
\frac{d}{dt}\hat{F}_y &= -\omega_S\hat{F}_z - ig_{\text{eff}}\alpha_x\hat{F}_x(\hat{a}_y e^{-i\phi} - \hat{a}_y^\dagger e^{i\phi}) - \gamma_{\text{S0}}\hat{F}_y/2 \\
\frac{d}{dt}\hat{F}_z &= \omega_S\hat{F}_y - \gamma_{\text{S0}}\hat{F}_z/2.
\end{aligned} \tag{9.8}$$

The equations look rather similar to the free space coupling, given in equations (3.28). As in Chapter 3, we have added all the decay effects, induced by light and other dephasing processes, via γ_{S0} .

A crucial difference is that the spin components now can be driven by a different optical quadrature, set by the phase ϕ . We can gain more intuition about the evolution by re-writing the field in terms of the more familiar Stokes operators \hat{S}_y and \hat{S}_z , as given in Section A.3, and setting $\hat{F}_x \rightarrow \bar{F}_x$. This limit is valid for small deviations from the unperturbed spin components, that is, without coupling to light. With the transformation to the polarization operators, we have

$$\begin{aligned}
\frac{d}{dt}\hat{S}_y &= -\Delta\hat{S}_z - \kappa\hat{S}_y/2 + g_{\text{eff}}|\alpha_x|^2\hat{F}_z \cos \phi \\
\frac{d}{dt}\hat{S}_z &= \Delta\hat{S}_y - \kappa\hat{S}_z/2 + g_{\text{eff}}|\alpha_x|^2\hat{F}_z \sin \phi \\
\frac{d}{dt}\hat{F}_y &= -\omega_S\hat{F}_z + g_{\text{eff}}\bar{F}_x(\cos \phi\hat{S}_z - \sin \phi\hat{S}_y) - \gamma_{\text{S0}}\hat{F}_y/2 \\
\frac{d}{dt}\hat{F}_z &= \omega_S\hat{F}_y - \gamma_{\text{S0}}\hat{F}_z/2.
\end{aligned} \tag{9.9}$$

From this perspective, we see that the spin-cavity system rotates the polarization of light. The birefringence induced by the spins into the cavity, as well as the rotation induced by light into the spins, is cavity detuning dependent. The cavity detuning plays the role of a trigger to the feedback dynamics. If

- $\Delta = 0$, then $\phi = 0$, and the cavity plays no role in the dynamics of the ensemble (apart from boosting the coupling constant), that is, the atomic response contained in \hat{S}_y does not couple to the spin dynamics.
- $\Delta \neq 0$, the intracavity quadrature that drives the oscillator gets a contribution from the spins response. As \hat{S}_y is modulated by the sine function, which is odd around $\phi = 0$, the spin system will be acted upon by an optical force either in or out-of-phase with respect to the motion, effectively dampening or amplifying the response depending in the sign of the detuning Δ .

Let us now study the dynamical effects of the cavity in the spin susceptibility. For that, we go to the Fourier space and solve for the evolution of the spin variables disregarding the input field fluctuations. We look for how an external force \hat{F} acts on \hat{F}_z . From equations (9.8), for a constant mean spin, $\hat{F}_x \rightarrow \bar{F}_x$, we

Spin dynamics in a cavity

have²

$$\begin{aligned}\hat{a}_y(\Omega) &= \frac{\alpha_x g_{\text{eff}} \hat{F}_z(\Omega)}{i(\Omega - \Delta) + \kappa/2} \\ \hat{a}_y^\dagger(\Omega) &= [\hat{a}_y(-\Omega)]^\dagger = \frac{\alpha_x g_{\text{eff}} \hat{F}_z(\Omega)}{i(\Omega + \Delta) + \kappa/2} \\ (i\Omega + \gamma_{S0}/2) \hat{F}_z &= \frac{\omega_S}{i\Omega + \gamma_{S0}/2} \left[-\omega_S \hat{F}_z - i g_{\text{eff}} \alpha_x \bar{F}_x (\hat{a}_y(\Omega) - \hat{a}_y^\dagger(\Omega)) \right] + \hat{F}.\end{aligned}$$

Solving for \hat{F}_z , for a given input force \hat{F} , will give us the cavity enhanced spin susceptibility

$$\begin{aligned}\chi_S^{-1} &\equiv \frac{\hat{F}}{\hat{F}_z} \\ &= (i\Omega + \gamma_{S0}/2)^2 + \omega_S^2 + i\omega_S g_{\text{eff}}^2 \alpha_x^2 \bar{F}_x \left[\frac{1}{i(\Omega - \Delta) + \kappa/2} - \frac{1}{i(\Omega + \Delta) + \kappa/2} \right].\end{aligned}\quad (9.10)$$

The first three terms make the natural spin susceptibility in the absence of coupling to the cavity. The term $\Sigma(\omega)$ contains the cavity induced feedback, a Fourier frequency and cavity dependent contribution. Note that the overall scaling goes as approximately the readout rate $\Gamma_S \propto g_{\text{eff}}^2 \alpha_x^2 \bar{F}_x$.

The susceptibility (9.10) resembles the dynamical broadened mechanical analogous, given in equation (2.22). It is not a surprise, as we have been going on our way to approximate the spin system as an oscillator. From equation (9.10), we can simplify the susceptibility to contain the dependencies on the optical damping/excitation and frequency shift

$$\chi_S^{-1} = \omega_S^2 + 2\Omega\delta\omega_S - \Omega^2 - i\Omega\gamma_S, \quad (9.11)$$

for $\gamma_S = \gamma_{S0} + \delta\gamma_S$. For spin coupling rates satisfying $g_{\text{eff}}^2 \alpha_x^2 \bar{F}_x \ll \kappa$, the cavity effects can be approximated to their values at the spin resonance ω_S , such that

$$\begin{aligned}\delta\omega_{\text{opt}} &\equiv \frac{\text{Re}\Sigma(\omega_S)}{2\omega_S} \\ &= -\frac{2g_{\text{eff}}^2 \alpha_x^2 \bar{F}_x}{\kappa} \left[\frac{(\Delta + \omega_S)\kappa/2}{(\Delta + \omega_S)^2 + (\kappa/2)^2} + \frac{(\Delta - \omega_S)\kappa/2}{(\Delta - \omega_S)^2 + (\kappa/2)^2} \right]\end{aligned}\quad (9.12)$$

$$\begin{aligned}\gamma_{\text{opt}} &\equiv -\frac{\text{Im}\Sigma(\omega_S)}{\omega_S} \\ &= -\frac{2g_{\text{eff}}^2 \alpha_x^2 \bar{F}_x}{\kappa} \left[\frac{(\kappa/2)^2}{(\omega_S - \Delta)^2 + (\kappa/2)^2} - \frac{(\kappa/2)^2}{(\omega_S + \Delta)^2 + (\kappa/2)^2} \right],\end{aligned}\quad (9.13)$$

the frequency shift and dynamical broadening. The small coupling approximations entailed substituting $\Omega = \omega_S$. The functional dependence of these expressions was already shown in Figure 2.8, in connection to the optomechanical readout rate and sideband asymmetry parameters. An important feature of the spin oscillator is the dependence of the dynamical effects on the effective mass, here parametrized by \bar{F}_x . A negative mass $\bar{F}_x > 0$ will have frequency shift and broadening opposite to the positive mass $\bar{F}_x < 0$ cases.

²The Fourier transform convention follows the one from Møller et al. (2017).

Part III

Hybrid implementation

Chapter 10

Back-action evasion

In this chapter we describe the back-action evasion experiments performed in our hybrid system. We show that the measurement back-action imposed in each of the constituents can be interfered, destructively or constructively, depending on the choice of spin effective mass. We also show that the mismatch of linewidths, along with the particular light-oscillator couplings, introduce limits and intricacies to the otherwise simple QND interaction.

We start by presenting the full model and then proceed to break down the various effects we encounter in the accessible parameter space, arriving at the ideal models discussed in Chapter 1. With this approach, I hope to present to the reader an accounting of the challenges imposed to recover the simpler expressions and intuition built based on the ideal models.

The second part of the chapter deals with the experimental implementation of our hybrid system. We breakdown the choice of parameters and the daily check-ups followed in a operation run. The first experimental realization of the back-action evasion in the spin-mechanics hybrid configuration is presented in Møller et al. (2017). Further experimental improvements are also featured in Thomas et al. (2020).

10.1 Full model

The intricate details of our hybrid system revolve around transformations that light experiences from the input to photodetection. As shown in Figure 10.1, once the input light has interacted with the spin system, it passes by a series of rotations, encounters lossy elements, interacts with the optomechanical system, to only then be directed to photodetection. All the relevant features are included in our hybrid theory model, which will be discussed in short.

The spin system, interacting with light and its environment has been presented in Chapter 3. A full model must also include the effect of broadband spin noise, discussed in Chapter 7. The mechanical system and its relevant coupling, have been presented in Chapter 2. We start this section by describing the optical link between the systems, fundamental in our hybrid system. We will be writing the formulae in the matrix formalism, as we have done for the individual systems. In this formalism, the hybrid system is reduced to a series of matrix multiplications, linking the input vector states and parameters to a vector output state. At the end of this section, hopefully the reader will be able to simulate the hybrid system performance on their own.

There are two ingredients that will show up in different parts of the hybrid implementation and will to be introduced first: optical losses ν and η , and interferometric rotations φ and ϑ .

Optical losses that do not involve change of the transverse mode profile are modelled as beam splitter-like operations. In this picture, a input mode $\hat{\mathbf{X}}_{\text{L}}^{\text{in}}$ is partially transmitted and admixed with vacuum $\hat{\mathbf{X}}_{\text{L},\eta}$ from its dark port.

Full model

We point out that, in general, the optical quadrature driving the mechanical system will contain a non-zero contribution of the spin oscillator response.

Once the spin output is mode matched to the optical cavity, the light after interaction is described by the cavity input-output relations. Taking account for the acquired phase shift with respect to the input, finite overcoupling and intracavity losses rates κ_{in} and κ_{ex} , respectively, the output field is given by expression (2.32)

$$\hat{\mathbf{X}}_{L,M}^{\text{out}} = \mathbf{O}_{\psi_{\text{out}}}^{\top} (\kappa_{\text{in}} \mathbf{Y}^{-1} - \mathbf{1}_2) \mathbf{O}_{\psi_{\text{in}}}^{\top} \hat{\mathbf{X}}_{L,M}^{\text{in}} \quad (10.8)$$

$$+ \sqrt{\kappa_{\text{in}} \kappa_{\text{ex}}} \mathbf{O}_{\psi_{\text{out}}}^{\top} \mathbf{Y}^{-1} \mathbf{O}_{\psi_{\text{in}}}^{\top} \hat{\mathbf{X}}_{L,\text{ex}}^{\text{in}} \quad (10.9)$$

$$- \sqrt{\kappa_{\text{in}}} \mathbf{O}_{\psi_{\text{out}}}^{\top} \mathbf{Y}^{-1} \mathbf{B} \chi_{M00} \hat{F}_M \quad (10.10)$$

including the effects of the mechanical oscillator⁴ as $\mathbf{Y} = \mathbf{A} - \mathbf{B} \chi_{M00} \mathbf{C}$ and respective coupling to the bath reservoir via the Langevin force \hat{F}_M . The output field from the optomechanical cavity contains effects of the three different drive forces which, line by line, are the input vacuum that contains the spin response $\hat{\mathbf{X}}_{L,M}^{\text{in}}$, the vacuum leaking in the cavity from lossy channels $\hat{\mathbf{X}}_{L,\text{ex}}^{\text{in}}$, and the thermal noise \hat{F}_M from the phonon bath reservoir. Each contribution is transduced in a different way by the mechanical degree of freedom.

The last step in the description is the final homodyning of the joint signal. The output cavity field, on its way to being finally detected, is overlapped with a local oscillator with efficiency η and phase ϑ

$$\hat{\mathbf{X}}_L^{\text{meas}} = \sqrt{\eta} \mathbf{O}_{\vartheta} \hat{\mathbf{X}}_{L,M}^{\text{out}} + \sqrt{1-\eta} \hat{\mathbf{X}}_{L,\eta}. \quad (10.11)$$

Note that the our homodyne measurement only allows us to access one component of $\hat{\mathbf{X}}_L^{\text{meas}}$ for a given choice of ϑ .

The equation (10.11) contains the full information needed to fit the experimental data and quantify correlations among the various constituents. We may now construct a bigger matrix \mathbf{U} in the basis of the optical and thermal forces acting on the systems, namely

$$\mathbf{Q}_{\text{in}} \equiv (\hat{F}_S^X, \hat{F}_S^P, \hat{F}_M, \hat{X}_{L,S}^{\text{in}}, \hat{P}_{L,S}^{\text{in}}, \hat{X}_{L,\nu'}^{\text{in}}, \hat{P}_{L,\nu'}^{\text{in}}, \hat{X}_{L,\text{ex}}^{\text{in}}, \hat{P}_{L,\text{ex}}^{\text{in}}, \hat{X}_{L,\eta'}^{\text{in}}, \hat{P}_{L,\eta'}^{\text{in}})^{\top} \quad (10.12)$$

such that the equation (10.11) is now

$$\mathbf{Q}_{\text{out}} = \mathbf{U} \mathbf{Q}_{\text{in}}, \quad (10.13)$$

with $\mathbf{Q}_{\text{out}} \equiv (\hat{X}_M, \hat{P}_M, \hat{X}_S, \hat{P}_S, \hat{P}_L^{\text{meas}})^{\top}$ as the output vector. The matrix \mathbf{U} is, therefore, rectangular.

To sum up, we have a linear system of equations, in which 5 degrees of freedom are of interest: \hat{P}_L^{meas} , the detected phase light quadratures, and $\hat{X}_S, \hat{P}_S, \hat{X}_M, \hat{P}_M$, the spin/mechanics canonical variables.

To relate the vector \mathbf{Q}_{out} to the measured power spectral density, we take the absolute square of the vector \mathbf{Q}_{out} given the input matrix of spectral densities

$$\bar{\mathbf{S}}_{\text{in}} \delta(\Omega - \Omega') = \frac{1}{2} (\mathbf{Q}_{\text{in}}^{\dagger}(\Omega) [\mathbf{Q}_{\text{in}}(\Omega')]^{\top} + \mathbf{Q}_{\text{in}}(\Omega) [\mathbf{Q}_{\text{in}}^{\dagger}(\Omega')]^{\top}). \quad (10.14)$$

The input spectral density $\bar{\mathbf{S}}_{\text{in}}$ is a square matrix that characterizes the correlation among the various input thermal and vacuum fluctuations. The spin and mechanical thermal baths lead to independent dynamics for each system, as they have independent physical origin. The same applies to the amplitude and phase quadrature terms $\hat{X}_{L,i}^{\text{in}}$. Although all being vacuum noises, they represent different uncorrelated realizations of it. Ultimately, the matrix $\bar{\mathbf{S}}_{\text{in}}$ has diagonal

$$\mathbf{A} = \begin{pmatrix} \kappa/2 - i\Omega & \Delta \\ -\Delta & \kappa/2 - i\Omega \end{pmatrix}$$

$$\mathbf{B} = \begin{pmatrix} 0 \\ -2g \end{pmatrix},$$

$$\mathbf{C} = (-4g \quad 0)$$

entries

$$\text{diag}(\bar{\mathbf{S}}_{\text{in}}) = \left(\bar{S}_{F_S^x F_S^x}, \bar{S}_{F_S^p F_S^p}, \bar{S}_{F_M F_M}, \bar{S}_{X_L X_L}, \bar{S}_{P_L P_L}, \bar{S}_{X_L X_L}, \bar{S}_{P_L P_L} + \frac{\nu}{1-\nu} \bar{S}_{S,bb}, \right. \\ \left. \bar{S}_{X_L X_L}, \bar{S}_{P_L P_L}, \bar{S}_{X_L X_L}, \bar{S}_{P_L P_L} \right), \quad (10.15)$$

and all other elements are equal to zero. The broadband noise $\bar{S}_{S,bb}$ is added via the inter-system loss port in the $\hat{p}_{L,\nu}^{\text{in}}$ field, effectively experiencing the same losses and rotation as the mean spin noise mode. This approach is valid in (i) the narrow-band limit, as the broad spin mode PSD is approximately flat when the frequency band of interest focus in mean spin mode, and (ii) in the limit in which the spin modes do not significantly interfere among themselves. The power spectral densities constituting equation (10.15) are defined in equations (A.7) and (A.8), with Fourier frequency dependencies Ω dropped for brevity. The diagonal entries related to light variables are all vacuum noise, therefore the indistinguishable labelling.

Finally, the spectral densities of the output signal is

$$\bar{\mathbf{S}}_{\text{out}} = \mathbf{U}^\dagger \bar{\mathbf{S}}_{\text{in}} \mathbf{U}. \quad (10.16)$$

This expression contains not only the power spectral densities, but also the cross-correlation of the various variables of interest. In Chapter 11, we will get to use the correlations as calculated above.

Having introduced the full model, in the remaining part of this Chapter we will focus on the light variables captured in Eq. (10.11), breaking down the contributions in more digestible bits. For simplicity, we will take the lossless scenario. We will connect the full model picture given here with the ideas discussed in Chapter 1, showing how the back-action evasion measurement can lead to perfect noise removal.

10.2 QND limit

As described in the section above, many of the modelling complexities arise due to rotations induced by interferometers and the optomechanical cavity, and losses. By setting these contributions to zero, we start recovering the ideal QND picture, presented initially in Chapter 1, language in which back-action evasion is only due to the oscillators opposite relative mass. This is the approach taken in the proposal Hammerer et al. (2009).

The initial point of the analysis is the measured optical quadratures, given in equation (10.11). By setting the phase rotations $\varphi, \vartheta, \psi_{\text{in}}, \psi_{\text{out}}$ and optical losses $\eta, \nu, \kappa_{\text{ex}}$ to zero, also including the contribution from intracavity losses, we obtain

$$\hat{\mathbf{X}}_{\text{L}}^{\text{meas}} = (\kappa \mathbf{Y}^{-1} - \mathbf{1}_2) \hat{\mathbf{X}}_{\text{L},\text{M}}^{\text{in}} + \sqrt{\kappa_{\text{in}}} \mathbf{Y}^{-1} \mathbf{B} \chi_{\text{M}00} \hat{F}_{\text{M}}. \quad (10.17)$$

Note that by setting all phase rotations to zero, we are also setting $\Delta = 0$, which plays in ψ_{in} and ψ_{out} . For an optomechanical readout with zero detuning, the dynamical broadening is also zero. The mechanical response will therefore have a profile that is derived from the natural susceptibility $\chi_{\text{M}00}$.

At this moment, we note that the optical input to the optomechanical system is the output from the spin response, equation (10.5). Inserting this expression in equation (10.17), we have

$$\hat{\mathbf{X}}_{\text{L}}^{\text{meas}} = (\kappa \mathbf{Y}^{-1} - \mathbf{1}_2) ((\mathbf{1}_2 + 2\Gamma_S \mathbf{Z}_0 \mathbf{L} \mathbf{Z}_0) \hat{\mathbf{X}}_{\text{L},\text{S}}^{\text{in}} + \sqrt{\Gamma_S} \mathbf{Z}_0 \mathbf{L} \hat{\mathbf{F}}_S) + \sqrt{\kappa_{\text{in}}} \mathbf{Y}^{-1} \mathbf{B} \chi_{\text{M}00} \hat{F}_{\text{M}} \quad (10.18)$$

in which \mathbf{Z}_0 is \mathbf{Z}_S for $\xi_S = 0$ and shown in the sidebar⁵. Equation (10.18) shows that the spin response is filtered by the optomechanical system and added to the mechanical response driven by its thermal bath.

⁵ $\mathbf{Z}_0 = \begin{pmatrix} 0 & 0 \\ 1 & 0 \end{pmatrix}$

QND limit

We proceed by evaluating the matrix \mathbf{Y} , which accounts for the optomechanical coupling with light and thermal forces. For $\Delta = 0$, we have

$$\begin{aligned} \kappa \mathbf{Y}^{-1} - \mathbf{1}_2 &= \frac{\kappa/2 + i\Omega}{\kappa/2 - i\Omega} \mathbf{1}_2 + \frac{8\kappa g^2 \chi_{M00}}{(\kappa/2 - i\Omega)^2} \mathbf{Z}_0 \\ \sqrt{\kappa} \mathbf{Y}^{-1} \mathbf{B} \chi_{M00} \hat{F}_M &= -\frac{2g\sqrt{\kappa} \chi_{M00}}{\kappa/2 - i\Omega}, \end{aligned} \quad (10.19)$$

in which we have also used the matrix \mathbf{Z}_0 for the optomechanical mapping.

Let us assume that the optomechanical read out is done far into the unresolved regime, $\kappa \gg \omega_M$, and in the weak coupling regime, $g \ll \kappa$. We can expand the equation (10.17) in powers of Ω/κ , to the zeroth-order, such that the optomechanical interaction, without the contribution from the spins

$$\hat{\mathbf{X}}_L^{\text{meas}} = (\mathbf{1}_2 + 2\Gamma_M \chi_{M00} \mathbf{Z}_0) \hat{\mathbf{X}}_{L,M}^{\text{in}} - \sqrt{\Gamma_M \chi_{M00}} \hat{F}_M \mathbf{v}_2, \quad (10.20)$$

for the column vector $\mathbf{v}_2 = (0, 1)^\top$. The equation (10.20) has a functional dependence similar to the spin response in the QND regime. Plugging in the equations (10.19) in equation (10.18), we arrive at our final expression, the QND limit of the hybrid system

$$\hat{\mathbf{X}}_L^{\text{meas}} = (\mathbf{1}_2 + 2(\Gamma_M \chi_{M00} + \Gamma_S \chi_S) \mathbf{Z}_0) \hat{\mathbf{X}}_{L,S}^{\text{in}} - (\sqrt{\Gamma_M \chi_{M00}} \hat{F}_M - \sqrt{\Gamma_S \chi_S} \hat{F}_S) \mathbf{v}_2, \quad (10.21)$$

in which we have also approximated the spin response according to its high-Q limit. The first term in the right hand side of the equation above contains the input light quantum fluctuations and the system's response induced by them, the quantum back-action. The second and third terms are the thermal contributions from the mechanical and spin system, respectively.

In the QND case, both systems susceptibilities appear via the matrices \mathbf{Z}_0 , which guarantee the multiple responses and forces do not couple directly to each other. Although in abstract terms, the mapping via \mathbf{Z}_0 guarantees the intuition that if no optical quadrature rotation happens between the systems, both systems will interact with the same input vacuum fluctuations. We can see this easier by writing the vector (10.21) term by term

$$\hat{\mathbf{X}}_L^{\text{meas}} = \hat{\mathbf{X}}_{L,S}^{\text{in}} \quad (10.22)$$

$$\hat{P}_L^{\text{meas}} = \hat{P}_{L,S}^{\text{in}} + 2(\Gamma_M \chi_{M00} + \Gamma_S \chi_S) \hat{\mathbf{X}}_{L,S}^{\text{in}} - \sqrt{\Gamma_M \chi_{M00}} \hat{F}_M + \sqrt{\Gamma_S \chi_S} \hat{F}_S. \quad (10.23)$$

Therefore, for removing the back-action induced noise, the susceptibility matching condition must be fulfilled

$$\Gamma_M \chi_{M00} = -\Gamma_S \chi_S. \quad (10.24)$$

If this condition is fulfilled, the quantum back-action noise will be completely removed, in all frequency components. The fulfilment of the condition requires

1. *susceptibilities χ_i matching*. It is important to notice that this quantity is Fourier frequency dependent. The two parameters available for matching are the resonant frequencies ω_S and ω_{M0} , and the natural linewidths γ_S and γ_{M0} .
2. *readout rate matching*. Under the current approximations, the mechanical readout rate Γ_M depends on the intracavity photon number \bar{n} and single photon coupling rate g_{M0} ; the spin readout rate Γ_S , on the other hand, can be adjusted by the atomic density.

Matching our spin and mechanical systems in the QND regime is a very difficult task, mainly due to the linewidths (in the absence of dynamical processes)

being mismatched by approximately 6 orders of magnitude. For the results presented later in this chapter, we have $\gamma_{M0}/2\pi \sim \text{mHz}$ and $\gamma_{S0}/2\pi \sim \text{kHz}$.

Our scheme also contains an intrinsic noise penalty factor. Matching the spin and mechanics responses leads to the addition of uncorrelated spin thermal response. The relative contribution of this penalty is nonetheless decreased in the limit of high C_q 's, in which quantum back-action dominates over the thermal contribution. In this limit, the total noise cancellation is bigger than the added uncorrelated contribution and our scheme offers better noise performance.

As a last point, we note that our scheme also allows for back-action cancellation in the regime of two oscillators with the same effective mass, although only in a given Fourier frequency range. If we detune the matched oscillators by $\delta_{MS} \gg \{\gamma_S, \gamma_M\}$, the quantum back-action induced responses will interfere in the frequency range in between the two resonances.

In the next section, we discuss how to match the systems linewidths via dynamical broadening the mechanical system, and also some of the effects of rotating the quadratures in between the systems.

10.3 Non-QND noise interference

In the last section, we saw that the susceptibilities in the QND readout of the hybrid system are highly mismatched in linewidth. Given that reducing the spins natural linewidth in our cell geometry to the level of the mechanics natural linewidth is much beyond the current state of the art⁶, we will take the approach of broadening the mechanical response via dynamical cooling, achieved by detuning the probe laser from the cavity resonance, as discussed in Chapter 2. Dynamical broadening is a rather standard effect, requiring only a red detuned laser and some degree of sideband resolution.

This section is divided in three semi-independent parts. The first involves . The second part follows the derivations also encountered in the methods section of Møller (2018), in which the effects of a non-QND readout of the mechanical system in the hybrid experiment are considered.

We start by rewriting equation (10.11). In the lossless case, but now including the effects of $\Delta \neq 0$

$$\mathbf{O}_\varphi^{-1} \hat{\mathbf{X}}_L^{\text{meas}} = \mathbf{O}_{\psi_{\text{out}}}^\top (\kappa \mathbf{Y}^{-1} - \mathbf{1}_2) \mathbf{O}_{\psi_{\text{in}}}^\top \hat{\mathbf{X}}_{L,M}^{\text{in}}, \quad (10.25)$$

neglecting the thermal noise contribution, which will be discussed in the next section. Before including the spin response, we choose a inter-system phase rotation φ such that

$$\mathbf{O}_{\psi_{\text{in}}}^\top \mathbf{O}_\varphi = \mathbf{1}_2, \quad (10.26)$$

for $\varphi - \psi_{\text{in}} = \varphi - \arctan(2\Delta/\kappa) = m\pi$, for an integer m . With this, we undo the input cavity induced rotations. On the same hand, choosing the detection phase as $\varphi - \psi_{\text{out}} = m\pi$ will allow us writing, from equations (10.5) and (10.25)

$$\hat{\mathbf{X}}_L^{\text{meas}} = (\kappa \mathbf{Y}^{-1} - \mathbf{1}_2) (\mathbf{1}_2 + 2\Gamma_S \mathbf{Z}_S \mathbf{LZ}_S) \hat{\mathbf{X}}_{L,S}^{\text{in}} \quad (10.27)$$

On this way, the phase rotations induced by a non-zero cavity detuning in the input and output fields can be compensated by a appropriate choice of input and output phases. The matrix \mathbf{Y} , nonetheless, also contains cavity detuning sensitive dynamics. In fact, as $\mathbf{Y} = \mathbf{A} - \mathbf{B}\chi_{M00}\mathbf{C}$, it contains the dynamical cooling effects.

For the case when the optomechanical broadening dominates the mechanical damping, $\gamma_M \gg \gamma_{M0}$, and in the sideband unresolved limit, $\omega_M \ll \kappa/2$, an analytical expression can be extracted. The power spectral density of the quantum back-action contribution of the hybrid system can be written as (Møller, 2018)

$$\frac{\bar{S}_{P_{L,\text{meas}}}(\Omega)}{\bar{S}_{X_{L,\text{in}}}(\Omega)} = \frac{(\Gamma_M \delta_S \pm \Gamma_S \delta_M)^2 + \Gamma_M^2 \gamma_S^2}{(\delta_M^2 + \gamma_M^2)(\delta_S^2 + \gamma_S^2)}, \quad (10.28)$$

⁶The narrowest Zeeman spin linewidth ever reported, to the knowledge of the writer, is $\gamma_S/2\pi = 4 \text{ mHz}$, reported in Balabas et al. (2010b), for an spherical vapor cell with 30 mm diameter, at room temperature.

Losses

for $\delta_{M,S} = \Omega - \omega_{M,S}$, $S_{X_{L,in}}$ being the power spectral density of the input light amplitude fluctuations, and \pm for the spin oscillator effective mass sign. In particular, the on-resonance matched hybrid response, with $\omega_M = \omega_S$, $\gamma_S = \gamma_M$, and $\Gamma_S = \Gamma_M$, the expression (10.28), for the negative mass case becomes

$$\frac{\bar{S}_{P_{L,meas}}(\Omega)}{\bar{S}_{X_{L,in}}(\Omega)} \sim \frac{\Gamma^2 \gamma^2}{(\delta^2 + \gamma^2)^2}. \quad (10.29)$$

This expression is to be compared with the quantum back-action noise for mechanical oscillator only

$$\frac{\bar{S}_{P_{L,meas}}(\Omega)}{\bar{S}_{X_{L,in}}(\Omega)} \sim \frac{\Gamma_M^2 \gamma_M^2}{\delta_M^2 + \gamma_M^2}. \quad (10.30)$$

The two expressions coincide for $\Omega = \omega_M$, revealing that no back-action interference happens on resonance for the matched oscillators. Note the stark contrast to the QND case, in which the reduction of the light-induced noise happens for all Fourier frequencies. Nonetheless, we also note that the validity of the expression (10.28), apart from not including the ever present optical losses, depends on an unresolved sideband limit approximation. We will see that for $\omega_M/\kappa/2 \sim 0.3$, approximate regime for the 2020, there is significant back-action reduction on resonance.

The non-QND noise interference terms also affect the spin thermal noise contribution. As shown in Huang et al. (2018), mismatched interactions between the systems and light, characterized by $\chi_M \neq \chi_S$, lead to efficient destructive interference of the spin response for $\chi_M > \chi_S$.

10.4 Losses

The last stop in the description of our model is adding the effect of optical losses. The optical losses will add uncorrelated vacuum to the the oscillator drive, reducing the total noise cancellation observed. We divide them in three categories: inter-system, intra-cavity, and detection.

The intra-cavity losses, happening due to a non-unity cavity escape efficiency $\kappa_{ex} \neq 0$, will induce vacuum fluctuations that couples to the mechanical oscillator as

$$\sqrt{\kappa_{in}\kappa_{ex}} \mathbf{O}_{\psi_{out}}^T \mathbf{Y}^{-1} \mathbf{O}_{\psi_{in}}^T \hat{\mathbf{X}}_{L,ex}^{in}. \quad (10.31)$$

As importantly, they also affect the phase rotation ψ_{out} , which needs to be further compensated by the detection phase ϑ .

The inter-system losses happen anywhere in between the spin system and the cavity mode-matching. Apart from reducing the back-action interference, the vacuum fluctuations introduced by this loss channel will drive the mechanical system as

$$\sqrt{1-\nu} \mathbf{O}_{\psi_{out}}^T (\kappa_{in} \mathbf{Y}^{-1} - \mathbf{1}_2) \mathbf{O}_{\psi_{in}}^T \hat{\mathbf{X}}_{L,\nu}. \quad (10.32)$$

spectrally mimicking the effects of $\hat{\mathbf{X}}_{L,S}^{in}$.

The detection losses are due to finite homodyning mode-matching and non-unity power transmission. This loss channel will determine the ratio of the hybrid signal to shot noise.

Having discussed the matching conditions and reasoning behind the various phase rotations and loss channels, we move to the experimental implementation.

10.5 Running the experiment

The basics of the implementation were already laid out in Hammerer et al. (2009). There, although in the reverse order of the described in this thesis, the conditions for transforming the polarization rotation signal induced by the spin oscillator into the single-polarization amplitude and phase quadratures are described as

- LO_1 must be perfectly removed from the optical path. Nonetheless, as the joint measurement involves only homodyning of the hybrid signal, even finite LO extinction ratio in the order of part-per-thousand level is sufficient.
- the signal/sidebands generated by the spin system must be mode matched to LO_2 with unity efficiency;
- the phase of the spin signal in respect to the local oscillator must be freely adjustable.

Therefore, regardless of the spin-mechanics system ordering, that is, regardless of which experiment is first in order of interaction with light, the filtering conditions are the same. We have chosen the configuration “spins first, mechanics second”, due to the possibility of filtering the first system local oscillator and addition of the second local oscillator using polarization optics only. The same level of control in the opposite orientation would require narrow auxiliary cavities for the same role⁷.

Over the course of the hybrid experiment’s 2015-2020 period, the setup has been in constant evolution. In Figure 10.2a, we show the setup used in the experiments that culminated with the results presented in Møller et al. (2017); in Figure 10.2b, the setup put together for the work Thomas et al. (2020). In the latter experiments, the spin is read out in double pass, that is, the light travels through the ensemble twice before heading out towards the mechanical oscillator. The single-to-double pass update sparked a complete rebuilt in the experimental layout in the spin-mechanics direction.

The knowledge gained in controlling the optomechanical system in the early years also triggered a change in the cavity locking scheme. While in the 2020 experiments the cavity is locked via a fringe lock, in the 2017 experiments, the cavity was locked using the *Pound-Drever-Hall* (PDH) technique (Black, 2001) in a frequency detuned lock beam⁸. Getting rid of the modulators and lock beam greatly simplified the daily operation of the optomechanical system. It also removed the various spurious interferences between the two counter-propagating beams in the setup.

The spin local oscillator, LO_1 , is linearly polarized at an angle α in respect to the DC magnetic field B_{DC} . After the interaction with the spin ensemble, the local oscillator is filtered out of the optical path. In the single pass configuration, a set of quarter and half wave plates can be used for maximal extinction. For the double pass case, the LO will be automatically re-directed to its original direction; in this scenario, the LO extinction ratio is set by the performance of the optical elements in the optical path, being in the order of 1 : 500 for the experiments here described.

After its extinction, the spin signal is spatially overlapped with a intense beam on a polarizing beam splitter and directed to the optical cavity for mode matching. The combined beam is ready to interface with the optomechanical system after being projected in the same polarization mode at the polarization beam splitter 1. Most of the intense beam is rejected at this splitter, as the waveplate prior to the splitter 1 is for minimal loss of spin signal (usually on the order of %).

In the next pages, we will go through a set of points followed in a standard hybrid experiment operation. They are here to give an introductory idea of how the experiment *actually* works. Most of the points are general enough to be applied in both setups from Figure 10.2.

⁷It is debatable if the same level of control is actually needed. For the current experimental conditions, as the ratio of powers in the local oscillators LO_1/LO_2 is about 100, perhaps it is not strictly necessary to strip off the mechanics oscillator.

⁸The science light and locking light were shifted in frequency by independent *acousto-optical modulators* (AOM). With the RF fields driving each AOM frequency shifted by ~ 5 MHz, selecting the same AOM diffraction order means that the two beams are detuned by the RF frequency difference. The locking beam is then sent through a phase modulating EOM, generating the tone required by the PDH technique.

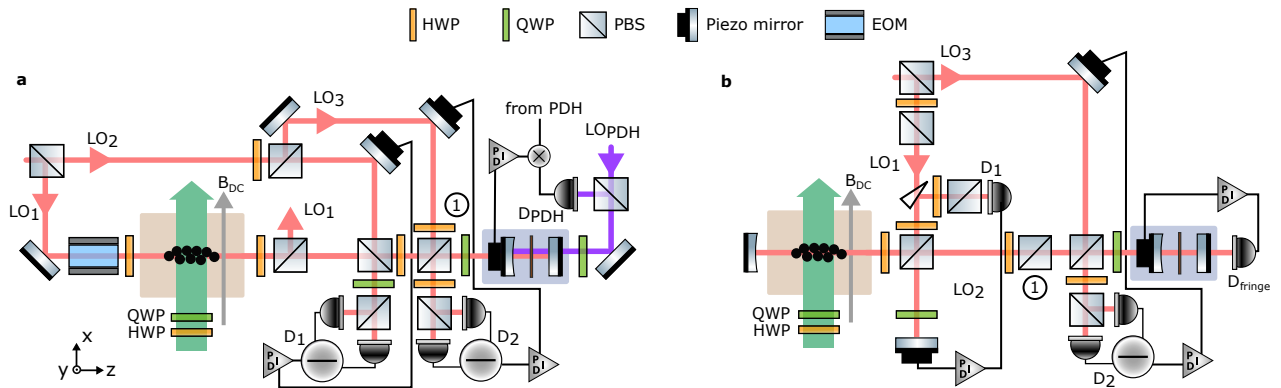


Figure 10.2: Experimental setups. This figure has been presented in Chapter 4 and is reproduced here once more for convenience. The simplified representation of the hybrid experiment, including, local oscillators, polarization/power control, and detection. The piezo mirrors are the actuators for relative path length control. The setup in **a** was used in Møller et al. (2017), while **b** was implemented for Thomas et al. (2020). The numbered PBS 1 marks the element in which the spin response and LO_2 are projected into the same polarization mode. The purple line in **a** marks the cavity locking optical path.

We have already discussed some features and procedures in Chapter 4. We refer to that chapter for details on laser debugging, vapor cell alignment, optical pumping power levels, optical cavity losses, mechanical Q , and light-mechanics coupling.

Given the basic checks are done, or assumed to be good enough to move on, we proceed to the operation points

1. The cryostat temperature must be stable, for order 30 min, at nominal $T = 4.3$ K. The temperature is responsible for setting the whole cryostat construction at a given horizontal and vertical position in respect to the optics. A drift will eventually lead to a decrease in cavity mode matching, which is rather detrimental to the hybrid system performance.
2. The optical power getting to the experimental island must be stable and about 20-25 mW in total, measured right before the $LO_1/LO_2/LO_3$ splitter. About 15 mW must be reserved for LO_3 . The homodyning beam requires such high proportion of power as the optical path involves a series of free-space to optical fiber conversions (not shown in the experiment sketch), amounting to ~ 3 mW of available power at the detector.

The remaining optical power is used for LO_1 and LO_2 , with LO_2 taking a big proportion of it. LO_1 power levels are on the 0.3-1 mW range. LO_2 uses 2-5 mW as most of it is dumped when projecting the spin signal and the to-be local oscillator in the same polarization, at the element 1, see Figure 10.2. On the double pass setup, the EOM for spin readout readout rate calibration requires only about 50 μ W of laser power.

3. On the spin double pass setup, the power split at the Michelson interferometer input polarization beam splitter, used for LO_1 and for the to-be LO_2 , will also effectively set the LO_1 polarization, as a consequence of the finite extinction ratio and polarization leakage present in PBS. Commonly, about 1-2 μ W of LO_1 power leak down the path in the double pass configuration; for the single pass, a set of waveplates is used for optimally removing the carrier, with only 0.1-0.5 μ W leaking. The half waveplate angle in the spin arm of the interferometer must be set to cancel the quadratic Zeeman splitting, as discussed in Chapter 3, commonly being in the range 55-60° with respect to the DC magnetic field. We cancel the quadratic Zeeman splitting for restoring the single mode description of the spin ensemble.

4. LO₁ and LO₂ must be spatially and polarization overlapped. The visibility of such interference is typically $\sim 90\%$, being fine tuned by the cavity mode matching. We recommend aligning LO₁ first, using as many knobs as necessary. After alignment, these knobs must not be touched. The LO₂ adjustment is done by using the mirrors only coupled to this local oscillator, with matching being $\sim 80\%$. Finite cavity coupling is not critical for this beam, as it will only boost the intracavity photon number.
5. The modematching of LO₁ and LO₃ should be as high as possible, reaching $> 92\%$. This step finishes all the alignments.
6. Lock LO₁-LO₂ phase. This should stabilize total power sent to the mechanics
7. Measure input power to the mechanics. Preferably, for avoiding miscalibrations, it should be done right before the cavity input mirror. This power should be somewhere in the range 5-20 μW .
8. Find the amplitude quadrature for the atoms by sending signal from atoms (including leakage) with LO₂ onto a single diode photodetector. Observe the power spectral density of the detected signal around the known Larmor frequency range. The signal should look like one of the spin noise spectra shown in Chapter 7. Adjust the LO₁-LO₂ phase until minimal response is observed, that is, until the observed noise is the closest to the shot noise level. As discussed earlier in this chapter, the selected interferometric phase is the one that puts the atomic response on the orthogonal light quadrature. Cavity induced rotations can therefore be counter-acted by small changes around the initial value.

Although presented in a numbered fashion, we emphasize that many points can be switched in order or skipped without altering the final product.

10.6 Calibrations

Once the experiment is up and running, it is time to calibrate the light-system interaction. Over the years, a series of calibration tools that suit our working setup have been developed. Given the drifts and shifts experienced by both spins and mechanics throughout a measurement series, we are particularly interested in techniques that allow the parameters estimation in experimental conditions, with minimal modifications to the hybrid setup. All calibrations rely in one way or another in the full model presented earlier in this chapter, and in the discussions in Chapter 2 and 3. We present the list of parameters, whose roles are shown in Figure 10.1. Some of the calibration procedures, nonetheless, require a more careful approach than others.

Take the optomechanical bath temperature T estimation, for example. Although there is a thermostat reading out the cryostat's cold finger temperature, which is itself firmly connected to the sample holder and membrane chip, we can not rely in this reading for estimating the temperature of the mechanical mode of interest (Nielsen, 2016; Møller, 2018).

Here, we follow the procedure described in (Møller et al., 2017), detailed in (Møller, 2018), and briefly discussed here. As pointed out throughout this work, the optical coupling to the mechanical degree of freedom acts not only as a probe of the mechanical dynamics, but also as a force that induces motion. As the measurement rate Γ_M is cranked up, back-action effects start to induce correlations between the optical and mechanical degrees of freedom. When Γ_M is on the same order of magnitude as the decoherence rate γ_M^{MM} , the optical fluctuations of a detuned probe beam will start to effectively interact with themselves via the mechanical mode susceptibility, leading to a frequency dependent feature that has total noise below the shot noise level.

In the limit of $\Gamma_M \gg \gamma_M^{\text{MM}}$, the maximum squeezing attainable will be limited by the ratio $\Gamma_M/\gamma_M^{\text{MM}}$ and detection losses (Nielsen et al., 2017). For

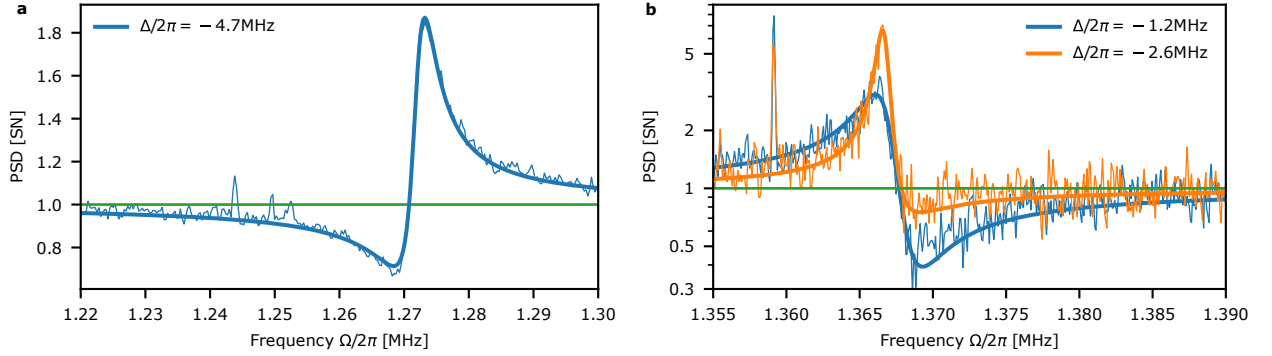


Figure 10.3: Optical estimation of the bath temperature. For a given set of known optomechanical interaction parameters $\{\Delta, \kappa_1, \kappa, \eta\}$, the detected optical spectrum gives access to mechanical mode temperature. The mechanical device used in **a** has a 2D phononic bandgap structure, while in **b** employs the soft-clamping technique. The fitting procedure outputs $T = 7$ K (left), and $T = 11$ K (right).

a known measurement rate, set by the parameters $\{\Delta, \kappa_1, \kappa\}$, and photon detection efficiency η , the amplitude noise spectrum has a frequency dependent shape that is sensitive to the bath temperature. Alternatively, we have measured spectra for different parameters, as cavity detunings Δ , and globally fitted them to the equation (10.16) using the known values of Δ and a common set of parameters.

In Figure 10.3 we show the temperature calibration for the 2017 and 2020 experiments. As the Figure 10.3(a) was measured in reflection, while Figure 10.3(b) was measured in transmission, the output cavity field will interfere with the reflected input beam and alter the resulting spectrum of fluctuations (Møller, 2018).

On the spins side, the quantum cooperativity C_q^S and readout rate Γ_S are measured via polarization modulation induced by an EOM. The readout rate calibration method is described at length in Chapter 8. Here we only present the calibration result, shown in Figure 10.4(b). There, we show the CIFAR result for three different types of input modulation. The curves have been fitted simultaneously, leading to $\Gamma_S/2\pi = 19$ kHz.

An alternative spin calibration was used in Møller et al. (2017) and is described in Chapter D. There, the EOM was to produce circular polarization modulation $S_z \propto X_L$, polarization quadrature which couples to the spin oscillator via Faraday rotation. Driving the EOM with white noise will induced extra polarization rotation noise. By applying a known amount of this modulation, and recording the driving and the respective response signal, we can estimate the amount of noise induced by the shot noise limited readout via the procedure described on Appendix D. In Figure 10.4(a), $C_q^S = 1.1$.

10.7 Results

Given a hybrid experiment aligned and calibrated, we can start discussing the back-action interference studies. We will cover the results presented in 2017 and 2020 in a chronological manner, highlighting the relevant updates and important numbers.

10.7.1 The 2017 experiments

The first quantum back-action evasion results of the hybrid were presented in 2017. The experimental findings there reported concluded the first years of intense characterization, debugging and modeling the physics involved in

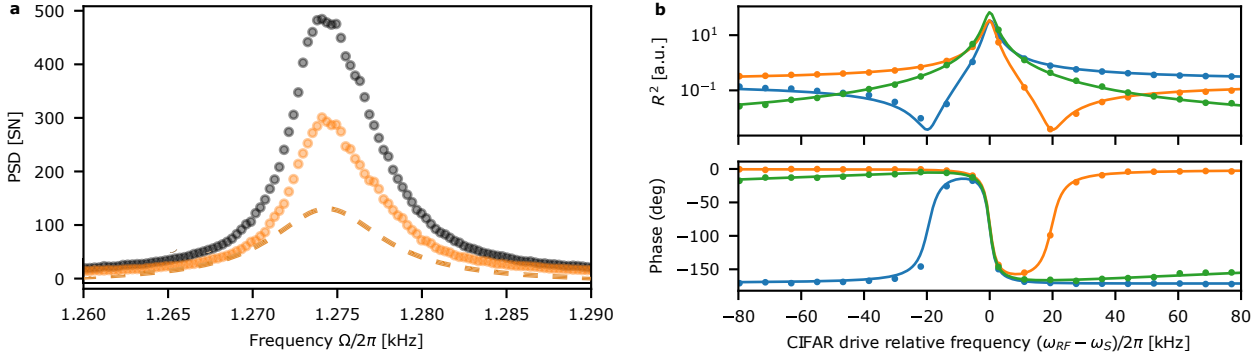


Figure 10.4: Light-spin oscillator coupling calibration. The **a** quantum cooperativity calibration measurements for the 2017 experiments. Orange dots is the spin noise for the shot noise driven probe beam. Black dots are for added 1.2 classical noise to the optical driving quadrature. From the input-output relations, we extract the spin thermal noise contribution (orange dashed line). In **b**, the readout rate measurements for the 2020 experiments. The blue, green and orange curves are for θ_{in} as $\pi/4, 0$ and $-\pi/4$, respectively.

the experiment. For storytelling purposes, we will navigate through some of the non-trivial features of the experimental results. Given the intricate model, discussed in length earlier in this chapter, we strived for seeing back action interference in a rather calibration independent fashion.

We start by matching the systems bandwidths, $\gamma_M \sim \gamma_S$, by selecting a suitable local oscillator power and cavity detuning. The readout rates of the systems $\{\Gamma_M, \Gamma_S\}$ are also affected by such choice. The spin readout rate can be further adjusted by the number of atoms in the vapor cell, which has been pushed to the maximum possible for this experiment. We also set the phase $\varphi = 0$, such that the amplitude quadrature to the optomechanical cavity contains no spin response; with this, we guarantee that, apart from cavity rotations, both systems will see the same vacuum. This condition allows us to have the description presented in Section 10.3 as reference. The spectral responses of the individual systems are presented in Figure 10.5, with the spin response frequency shifted (in post-processing) to match the mechanical resonance, for clarity.

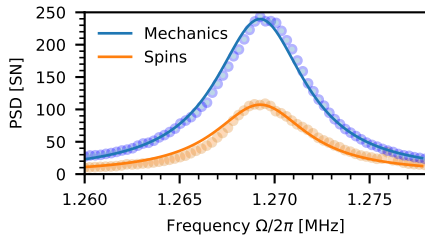


Figure 10.5: Mechanical and spin noise in the 2017 implementation. Power spectral density of the optical readout of the individual systems in the final homodyning. The spin oscillator, with resonant frequency $\omega_S/2\pi = 1.52$ MHz, has been shifted down in post-processing for easier visual comparison. See Figure 10.6 for the associated hybrid signal.

The systems are then brought to resonance, $\omega_M \sim \omega_S$, by tuning the magnetic field that controls the spin resonant frequency. The noise spectra, both for spins with positive and negative mass, are presented in Figure 10.6. Note that the negative mass hybrid spectrum is very similar to the mechanics only. The positive mass case shows added extra noise at frequencies $\Omega \neq \omega_M$. Given that the only parameter that changed is the sign of the spin oscillator effective mass, we claim that the difference in noise is due to the interference of the back-action contributions. Notice that trustworthy modeling of the hybrid signal is vital for all claims here presented.

Further evidence of the back-action interference is gained when breaking down the noise spectra. In Figure 10.6, given the system parameters extracted from fits and summarized in Appendix I, we color the detected noise in respect to system and origin. The filled areas represent the thermal noise; the remaining contribution is related to shot noise, light induced fluctuations and their respective interferences. The correlation between shot noise and induced fluctuations happen due to the non-QND type of system-light interactions and the various phase rotations induced by the interferometers and optical cavity.

The non-Lorentzian spin thermal contribution demonstrates that the spin response is being filtered by the optomechanical interaction, regardless of the spin mass. This is an experimental signature of the non-local dynamical cooling discussed in Section 10.3. The slight asymmetry around the peak response is due to imperfect frequency matching and input phase adjustment. As the

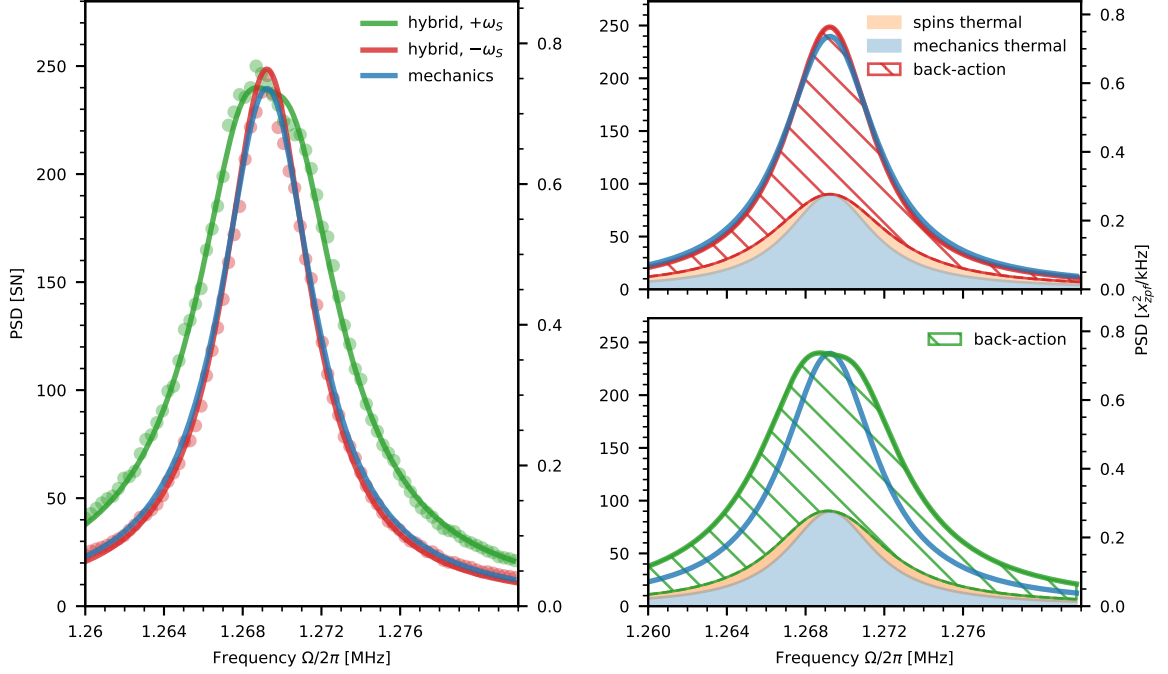


Figure 10.6: Back-action interference in the resonant hybrid system. We match the individual systems linewidths and readout rates, and tune the spin oscillator such that $\omega_S = \omega_M$. In the left panel, we show the joint system noise for negative (red) and positive (green) effective mass. The fit of the mechanical noise is shown in blue. In Figures right column panels, we show the noise breakdown for the two mass configurations. Filled blue (yellow) area represents the mechanics (spins) thermal noise contribution for parameters extracted from fitting. Vertical figure axis are presented both in shot noise units (SN) and in displacement.

total noise area for spins with negative mass similar to the mechanics case only, the back-action evasion is evident as the hybrid signal contains the uncorrelated spin noise, reaching 24% reduction in respect to the mechanics only back-action noise. For spins with positive mass, the constructive interference leads to additional 53% of back-action noise. For a summary of the results extracted from the resonant hybrid system, see Table 10.1.

Although the light-induced noise is indeed reduced in the $\omega_M \sim \omega_S$ case, our next step is to detune the oscillators and use the input phases to find the biggest noise reduction. In this regime, we go away from the simpler picture described in Section 10.3. By detuning the oscillators by ~ 4 kHz and adding a interferometer rotation φ of 6° we partially add the spin response to the input amplitude quadrature. Now, the input to the mechanical system is squeezed as shown in Figure 10.7, with overall shape determined by the spin effective mass.

The hybrid signals are presented in Figure 10.8. As in the resonant case, the shape of the positive and negative mass cases are rather different. Most importantly, there is a calibration independent overall noise reduction over a couple of kHz bandwidth, as we initially wished.

The noise breakdown allows us to learn some more about the hybrid system. The noise area numbers are presented in Table 10.2. The back-action cancellation is improved to 34%, while when positive mass, the spins contribute to adding 73% of the mechanics only noise.

Parameter	QBA area	% of mechanics
mechanics	$2.0x_{zpf}^2$	—
hybrid, $+\omega_S$	$3.1x_{zpf}^2$	$(53 \pm 8)\%$
hybrid, $-\omega_S$	$1.5x_{zpf}^2$	$(-24 \pm 5)\%$

Table 10.1: Noise breakdown for the data presented in Figure 10.6. Summary of the back-action noise areas for the resonant hybrid system. Error bars come from fit uncertainties.

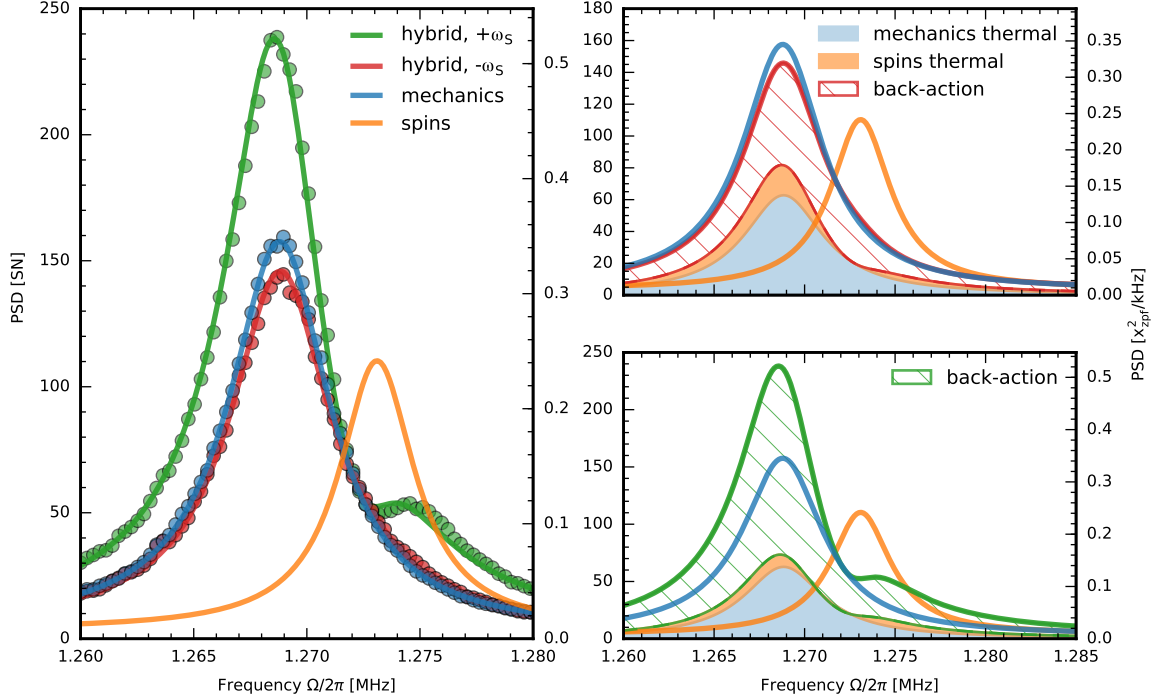


Figure 10.8: Back-action interference in the detuned hybrid system. For readout rates and linewidths similar to the ones presented in Figure 10.6, we set the spin oscillator frequency such that $\omega_S - \omega_M \sim \gamma_S$. In the left panel, we show the joint system noise for negative (red) and positive (green) effective mass. The mechanical noise and respective model fit are shown in blue. In Figures right column panels, we show the noise breakdown for the two mass configurations. Filled blue (yellow) area represents the mechanics (spins) thermal noise contribution, for parameters extracted from fitting. Vertical figure axis are presented both in shot noise units (SN) and in displacement.

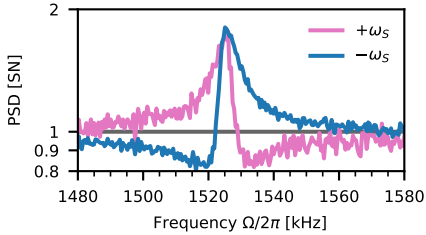


Figure 10.7: Amplitude quadrature PSD before the optomechanical cavity. The hybrid data presented in Figure 10.8, the amplitude quadrature fluctuations of the input light to the optomechanical cavity present a frequency dependent spectrum due to the spin-light interaction. For the choice of phase φ , the light is squeezed below (above) resonance for negative (positive) effective spin mass, shown in blue (pink).

With this, we finish the first incarnation of the hybrid experiment. At this stage, the overall performance was limited by a range of parameters

- losses: with a inter-system power transmission efficiency of $\nu_P = 0.6$ and cavity mode matching on the order of $\nu_{cav} \sim 0.9$, about half of the spin fluctuations are replaced with uncorrelated vacuum. From the cavity to photo-detection, the efficiency was in the order of $\eta \sim 0.6$, including cavity out-coupling, propagation losses, homodyning visibility and photo-detector quantum efficiency.
- coupling strengths: the light-system interaction parameters, the C_q 's, need to be further increased to remove a bigger fraction of the total hybrid noise. With quantum cooperativities in the order unity, the thermal noises make a considerable part of the detection noise.

10.7.2 The 2020 experiments

Going beyond the levels of back-action evasion reported in the 2017 experiments required a major rebuild period from us. Many of the constituent parts of the hybrid experiment were drastically changed from the Autumn of 2017 to early Spring 2019. The finished updated setups can be compared in Figure 10.2.

The experimental challenges to tackle the limitations encountered in the previous iterations are plentiful. Changing the membrane design, for devices with

higher Q factor but also with a smaller central defect, made us more sensitive to membrane induced losses, which triggered the cavity design update described in Chapter 4. With a fully controllable membrane in the middle setup we didn't need to rely on luck to achieve optimum $2kz$ position, sensibly improving the operational time at cryogenic temperatures.

On the spins side, we have changed for a better performing microcell, with significantly lower losses (7% to 2% per window) and better anti-relaxation coating performance (natural linewidth decreasing from 1 kHz to 450 Hz). Given the hybrid linewidth matching conditions, a narrower spin natural linewidth gives more room for the broadening induced by probing and optical pumping. In our case, it allows for adding a pump beam, which increases the spin polarization at the cost of line broadening. The spin polarization increased from $p = 0.65$ to $p = 0.8$, further reducing the extra thermal spin noise. This noise reduction is particularly important for the entanglement experiments, discussed in Chapter 11.

The spins readout rate and quantum cooperativity was boosted by employing a double pass probing scheme, see Chapter 3. While the quantum cooperativity scales with the cell length, therefore doubling in the double pass scheme, the double pass scheme also leads to an extra effective power enhancement. The light back propagating over its incoming path leads to a spatial standing wave pattern (with $\lambda/2$ periodicity), modulating the local laser intensity from zero to four times the input value in the ideal lossless case. Atomic motion averages out the intensity, leading to a twice bigger effective intensity at the vapor cell. Therefore, for a given input power, the readout rate Γ_S quadruples and the spin linewidth γ_S doubles, when in comparison to the single pass ensemble with the same single pass length and input power. The optical losses in the double pass scenario are analyzed in Appendix B

By using a new cell and improving the optical pumping, the ratio of back-action to thermal noise increased from ~ 1 to ~ 5 . We have also considered inserting the cell in an optical cavity, as discussed and shown in Chapter 9. Nonetheless, the intra-cavity losses were a too high for that particular implementation.

The inter-system power losses were decreased, from $\nu = 0.4$ to $\nu = 0.2$. Nonetheless, with the double pass implementation we became sensitive to back reflections from the optomechanical to the spin system. Due to imperfect polarization control, a small leakage from cavity output, travels upstream towards the spin system. There, the leakage is boosted by LO_1 , drastically affecting the spin performance. Further isolation was granted by using a Faraday isolator, nonetheless adding 5% to the inter-system losses.

On the mechanics side, we moved from the 2D silicon bandgap membranes to the improved ultra-soft clamped devices. The new design, particularly for membranes with a reduced thickness, routinely exhibits Q-factors $> 500 \times 10^6$ at cryogenic temperatures. The reduced coupling to the environment allows for a more efficient readout via light, amounting to higher quantum cooperativities. In our case, the quality factor increased from 12×10^6 to 650×10^6 . The ratio of back-action to thermal noise increased from ~ 2 to ~ 20 .

The individual systems noise, according to our calibrations, can be seen in Figure 10.9. This figure can be directly compared to Figure 10.5. Both systems QBA/TH ratio have clearly improved, demonstrating the quantum back-action dominated readout. We have also matched the readout rates according $\Gamma_M \sim \nu \Gamma_S$, where ν is the transmission efficiency between the systems. This choice of readout rate matching allows for canceling the back-action induced by the input vacuum fluctuations.

The performance of the updated hybrid performance can be seen in Figure 10.11. The spin oscillator, set with negative mass, has resonant frequency ω_S is scanned around the mechanical resonance, showing the frequency dependent noise spectrum. Particularly, on panels *c* and *d*, the hybrid signal is significantly reduced in comparison to the mechanics only.

The noise breakdown of the measurement noise in Figure 10.11 *d*, in which

Parameter	QBA area	of mechanics
mechanics	$1.7x_{zpf}^2$	—
hybrid, $+\omega_S$	$3.0x_{zpf}^2$	$(73 \pm 10)\%$
hybrid, $-\omega_S$	$1.1x_{zpf}^2$	$(-34 \pm 5)\%$

Table 10.2: Noise breakdown for the data presented in Figure 10.8. Summary of the back-action noise areas for the off-resonant hybrid system. Error bars come from fit uncertainties.

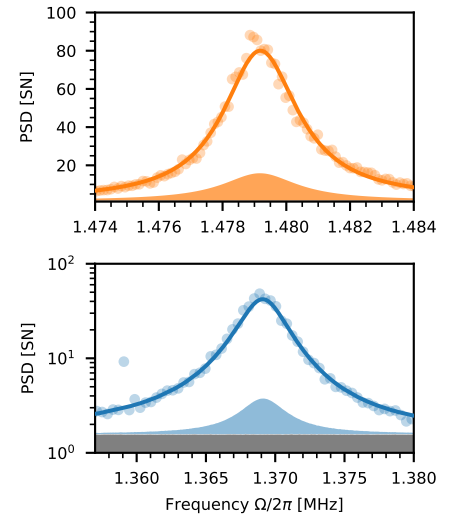


Figure 10.9: Spin and mechanical noise in the 2020 implementation. Power spectral density of the optical readout of the individual systems in the final homodyning. Spin noise is presented in the top panel. Mechanical noise in the bottom panel. The shaded orange and blue areas represents the thermal noise contribution from spins and mechanics, respectively. See Figure 10.10 for the associated hybrid signal.

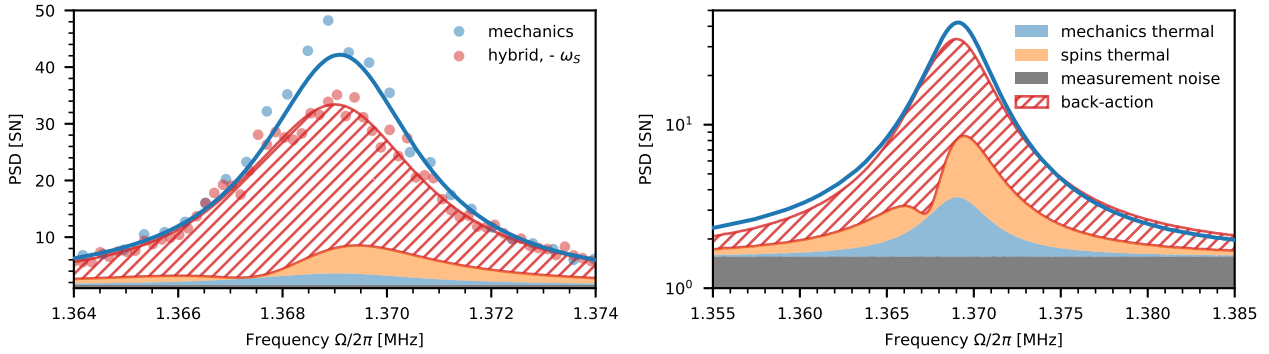


Figure 10.10: Back-action interference in the 2020 implementation of the hybrid system. The spin oscillator with negative effective mass is set on resonance with the mechanical oscillator and $\varphi \sim 0$. Data and fits are shown in linear scale (left). The fits are also shown in log scale (right). Filled areas stand for the different noise contributions.

the spins and mechanics are resonant and φ are adjusted to zero, is presented in Figure 10.10. The back action noise of the hybrid system in respect to the mechanics only has been reduced by $\sim 45\%$, significantly improved in respect to the previous experiment. In Figure 10.10 (right), we can also see that the measurement is bigger than 1SN, demonstrating the broadband spin noise contribution is a current limit factor.

We point out that in the data here presented, we have optimized the system performance for entanglement generation. The entanglement experiment requires a high detection quantum efficiency, quantity which is a function of broadband spin noise as $\eta \propto 1/\bar{S}_{\text{bb}}$. As presented on Chapter 7, the broadband spin noise power spectral density is reduced by decreasing the probe power and atomic density. We have tweaked both parameters, reducing the spins readout rate from initial $\Gamma_S/2\pi = 28$ kHz, when at maximum operating temperature (60°C).

Going forward, improving the back-action evasion performance while keeping extraneous noise sources at a low level, will require further improvement on the inter-system efficiency and coupling strengths. These requirements, already discussed at the 2017 experiments, put significant limitations to the hybrid system operation. In particular, the cavity-mode matching contribution of the inter-system losses requires further understanding. With overlap on the order of $\nu_{\text{cav}} \sim 0.9$, it makes about half of the contribution.

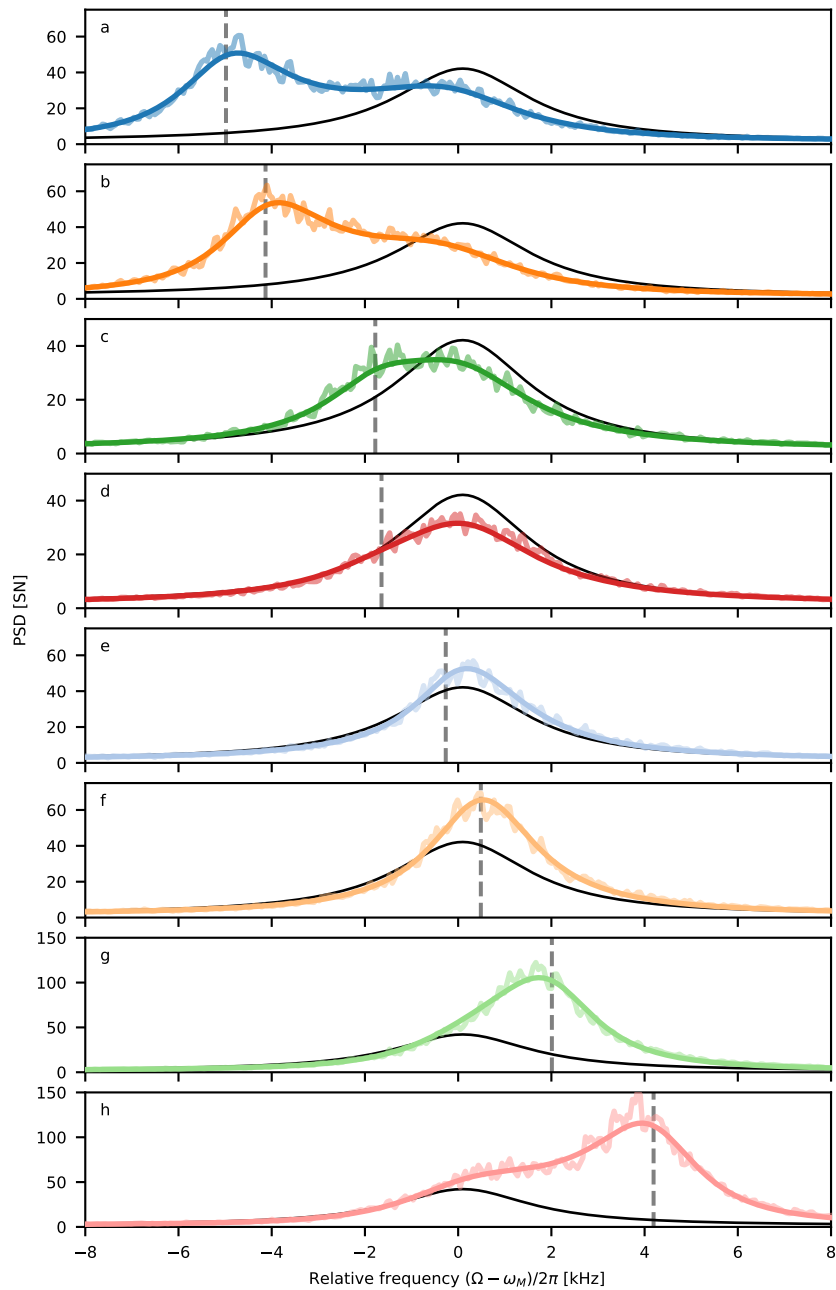


Figure 10.11: Back-action evasion detuning series. The negative spin oscillator resonant frequency ω_S is scanned around the mechanical resonance ω_M (black curve). The colored lines are the data (lighter shade) and the full model fit (darker shade). The phases ϑ and φ have been adjusted such that the $\omega_S \sim \omega_M$ hybrid signal shows maximum noise reduction. The dashed line stands for the spin oscillator resonance frequency.

Chapter 11

Hybrid entanglement

In this chapter, we present the preparation of the spin-mechanics system in an Einstein-Podolsky-Rosen state. We focus the presentation on the description of the signal conditioning, the usage of the Wiener filter and the entanglement error estimation.

In this chapter, we focus on the individual system with respect to the ground state variances. This is different than the approach taken in Chapter 10, in which the approach was based mostly on the optical degrees of freedom. In the conditional entanglement procedure, we are also interested in estimating the the hybrid system state with the highest possible measurement and detection efficiency.

11.1 Background

Quantum entanglement has long attracted attention due to its seemingly *spooky* features (Einstein et al., 1935) and connections to the foundations of quantum mechanics (Bohr, 1935). The transition from *gedanken* to laboratory experiments had to wait for a couple of decades (Bell, 1964) until more experimentally friendly criteria appeared (Clauser and Shimony, 1978). In the ensuing decades, increasingly sophisticated methods testing the validity and limits of the quantum theory have been explored.

The entanglement between photonic variables, such as the polarization of single photons, has been studied since the 60's (Clauser et al., 1969). Early works mostly use atoms as sources of entangled photons (Fry and Thompson, 1976), with a shift towards parametric down conversion in non-linear crystals in the 90's (Kwiat et al., 1995).

In the 1990's, key discoveries in the of quantum states for cryptography (Ekert, 1991) and teleportation (Bennett et al., 1993) ushered the fields of quantum information and computation (Feynman, 1982). Entanglement can nowadays be manipulated, controlled and broadcast by a variety of experimental implementations and to a multitude of protocols (Zeilinger, 1999; Horodecki et al., 2009).

The understanding that a large collection of atoms could also offer an efficient platform for quantum optics experiments and related applications in quantum information experiments brought a new approach to the interfacing of light and matter. Since then, in a non-extensive list, entanglement between separate ensembles has been generated in the continuous variables (Julsgaard et al., 2001; Krauter et al., 2011) and discrete variables (Chou et al., 2005) regimes. due to its weak coupling with the environment, atomic ensembles are viewed as good candidates for quantum-enabled memories. Proposals (Kozhokin et al., 2000) and experiments using coherent states (Julsgaard et al., 2004) and entangled states (Jensen et al., 2011) have demonstrated memory times on the order ms .

As for mechanical degrees of freedom, rapid developments have been happening in the last decade. The advances in the fabrication of miniaturized electronic, optical, and mechanical structures, along with respective theoretical understandings, pushed the boundaries in the experimental optomechanics research. As far as entanglement goes, it has been generated between two micromechanical oscillators in a common microwave cavity (Ockeloen-Korppi et al., 2018) in the continuous variable regime and between two distant mechanical oscillators at the single photon level (Riedinger et al., 2018). There has also been work in using a mechanical device as a non-linear optical medium, entangling different optical modes (Chen et al., 2020).

The entanglement between disparate degrees of freedom has been mostly limited to single ion systems (Lo et al., 2015), in which the interaction between motion and spin is short-range, at micron-scale distances, with motional and spin degrees of freedom associated with the same atoms.

Our hybrid entanglement occurs in a very different regime. Our method allows generation of long-range macroscopic entanglement between the motion of one object and the spin of another. The initial proposal was presented by Hammerer et al. (2009), in which the key point is to invoke a negative-mass oscillator. We prepare this oscillator in ground state levels of an atomic spin ensemble, which is subsequently coupled by a traveling optical field to a distant mechanical oscillator. Back-action-evading measurement allows generating entanglement between the two objects.

The procedure presented by Hammerer et al. (2009) differs from the procedure used in our experiments in many ways. First and foremost, the 2009 proposal uses the hybrid measurement result to generate a feedback that stabilizes the spin-mechanics in the EPR state. It also does not include dynamical effects in the light interaction with the individual systems, which are a vital part of our current implementation.

Important developments in the fabrication of mechanical devices allowed for realizing the challenging parameter requirements. One of the basic experimental requirements for the establishing entanglement is performing the measurement within a time scale $\tau \ll 1/\gamma(n + \frac{1}{2})$, with γ being the system decay rate and n as the bath thermal occupancy. The timescale τ must therefore be much smaller than the average time it takes for the system to experience coupling to the surrounding thermal environment. While for the spin system $n = n_S < 1$ and $\gamma_S/2\pi \sim 0.5$ kHz are typical for encapsulated microcells, in the mechanical system $n = n_M \sim k_B T / \hbar \omega_M$ and $\gamma_M/2\pi \sim \omega/2\pi Q$, entailing the requirement $\tau \ll \hbar Q / k_B T$.

The initial proposal considered the membrane-in-the-middle design with a $\omega_M/2\pi = 30$ MHz mechanical mode with $Q = 10^5$ at dilution refrigerator temperatures $T = 40$ mK. Achieving high in-and-out optical coupling efficiencies using dilution refrigerators is specially hard as the device requires complete shielding to achieve the design base temperature. Operating flow cryostats with free space optical access sets the temperature at about 4 K, requiring a $\sim \times 100$ improvement in mechanical Q for constant mechanical coherence times. The development of a phononic bandgap (Tsaturyan et al., 2014) and carefully designed mechanical device boundaries (Tsaturyan et al., 2017) allowed the required improvement. Our mechanical devices operates at $\omega_M/2\pi \sim 1.5$ MHz, with $Q \sim 0.5 \times 10^9$ at $T = 10$ K. For these parameters, $\hbar Q / k_B T \sim 1$ ms, enough time to perform measurements.

In the next section, we start studying the entanglement generation scheme and the various properties of the implementation.

11.2 Hybrid entanglement

We start by discussing the hybrid state we create by our measurement procedure. In Figure 11.1, we show the simplified interaction scheme. The spin system, prepared as an effective negative mass oscillator, is read out via light.

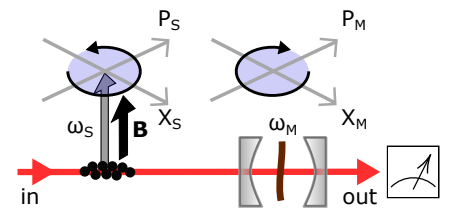


Figure 11.1: Schematic of the entanglement scheme. The input traveling field couples the distant atomic ensemble and the mechanical system embedded in a cavity. The output light is then directed to photo-detection. Note that the spin oscillator rotates in the opposite direction in the phase-space representation, as a consequence of the negative effective spin mass. Shaded circle in the \hat{X}, \hat{P} plane represents the ground state variance of the system. Figure adapted from Hammerer et al. (2009).

The output of the spin system is fed as input to the optomechanical system. After interaction with the mechanical degrees of freedom, the light leaks from the cavity towards a homodyne measurement setup.

The optical readout allows us to access the position and momentum variables of both systems. After treating the light according to our full model and calibrations, we construct generalized coordinates \hat{X}_{EPR} and \hat{P}_{EPR} , defined as

$$\hat{X}_{\text{EPR}} = (\hat{X}_{\text{M}} - a\hat{X}_{\text{S}}^{\beta}) / \sqrt{1 + a^2} \quad (11.1)$$

$$\hat{P}_{\text{EPR}} = (\hat{P}_{\text{M}} + a\hat{P}_{\text{S}}^{\beta}) / \sqrt{1 + a^2}, \quad (11.2)$$

where a as an arbitrary weight scalar parameter and

$$\hat{X}_{\text{S}}^{\beta} = \hat{X}_{\text{S}} \cos \beta + \hat{P}_{\text{S}} \sin \beta \quad (11.3)$$

$$\hat{P}_{\text{S}}^{\beta} = \hat{P}_{\text{S}} \cos \beta - \hat{X}_{\text{S}} \sin \beta, \quad (11.4)$$

are generalized spin operators, accounting for a phase rotation β . Such variables are a mere generalization of the original EPR states presented by Einstein et al., and is also featured in Bohr's reply. By choosing $a = -1$ we arrive at a re-scaled version of the variable discussed in Hammerer et al. (2009). Commonly, we will also write a superscript c in the EPR variables, e- g. \hat{X}_{EPR}^c , to define the conditional state analogue.

The statistics of the states we deal with, being of light as well as the individual oscillators, is Gaussian. Being so, the full statistical information can be expressed from the first and second statistical moments, that is, the average and the variances. The interaction between light and systems preserves the Gaussianity, as it involves at most products of field operators. The inseparability criterion for Gaussian systems and EPR-type operators was given in Duan et al. (2000). For any separable state, i.e. non-entangled, the total variance of the general EPR variables obeys

$$V = \text{Var}[\hat{X}_{\text{EPR}}] + \text{Var}[\hat{P}_{\text{EPR}}] \geq 1. \quad (11.5)$$

Therefore, achieving $V < 1$ demonstrates that the total quantum state of the system can not be written in a product form and therefore that the spin and mechanical oscillators are entangled. For conditional variances, we have $V_c < 1$. For Gaussian systems, this criterion is a necessary and sufficient condition for inseparability between the two parties.

Let us now discuss how light carries information about both systems. For simplicity, we will disregard losses and other imperfections discussed in connection with the full model in Chapter 10, such as the broadband noise contribution. We will also assume that the dynamics and coupling rates are much smaller than the natural oscillation frequencies, setting the systems well within the rotating wave approximations (RWA). In the RWA limit, we only need to track the variance of one of the canonical variables, here \hat{X} , as the variances of the position and momentum variables becomes equal (Huang et al., 2018).

As discussed in Chapter 3, the spin system is coupled to the input light fluctuations $\hat{X}_{\text{L,S}}^{\text{in}}$ and to its own effective spin thermal bath \hat{F}_{S} , as

$$\hat{X}_{\text{S}} = \chi_{\text{S}} \left[2\sqrt{\Gamma_{\text{S}}} \begin{pmatrix} 1 \\ -i\zeta_{\text{S}} \end{pmatrix}^{\text{T}} \hat{X}_{\text{L,S}}^{\text{in}} + \hat{F}_{\text{S}} \right], \quad (11.6)$$

with χ_{S} being the spin susceptibility, and Γ_{S} and ζ_{S} as the readout rate and tensor coupling, respectively. The momentum variable can be directly obtained from the Fourier-domain relation $\hat{P}_{\text{S}} \approx -\text{sign}(\omega_{\text{S}0})i\hat{X}_{\text{S}}$. The light carrying the information of the spin oscillator has the form

$$\mathbf{X}_{\text{L,S}}^{\text{out}} = \mathbf{X}_{\text{L,S}}^{\text{in}} + \sqrt{\Gamma_{\text{S}}} \begin{pmatrix} -i\zeta_{\text{S}} \\ 1 \end{pmatrix} \hat{X}_{\text{S}}. \quad (11.7)$$

Hybrid entanglement

As discussed in Chapter 2, the mechanical variables evolve as

$$\hat{X}_M \sim \chi_M \left[2\sqrt{\Gamma_M} \begin{pmatrix} 1 \\ i\zeta_M \end{pmatrix}^\top \hat{X}_{L,M}^{\text{in}'} + \hat{F}_M \right] \quad (11.8)$$

with χ_M as the spin susceptibility, and Γ_M and ζ_M being the readout rate and sideband asymmetry parameter, respectively. By analogy with the equations for the spin oscillator, ζ_M is the mechanical analogue of the tensor interaction strength. The output from the optomechanical cavity is

$$\mathbf{X}_{L,M}^{\text{out}'} = \mathbf{X}_{L,M}^{\text{in}'} + \sqrt{\Gamma_M} \begin{pmatrix} i\zeta_M \\ 1 \end{pmatrix} \hat{X}_M. \quad (11.9)$$

As the hybrid system goes, the output light from the spin system is coupled as input to the mechanical system. By choosing the appropriate phase rotations, we can input equation (11.7) in equation (11.8), such that the mechanical variable is

$$\hat{X}_M \sim \chi_M \left[2\sqrt{\Gamma_M} \begin{pmatrix} 1 \\ i\zeta_M \end{pmatrix}^\top \left[\hat{X}_{L,S}^{\text{in}} + \sqrt{\Gamma_S} \begin{pmatrix} -i\zeta_S \\ 1 \end{pmatrix} \hat{X}_S \right] + \hat{F}_M \right]. \quad (11.10)$$

Therefore, given the hybrid matching, the mechanical oscillator is not only coupled to light and its own thermal bath. Multiplying the matrices, it can be shown that for $\zeta_M \neq 0$, the input phase quadrature also affects the motion. For $\zeta_M \neq \zeta_S$ the mechanics effectively also couples to the spin oscillator. The dynamics of the mechanical driving optical force is therefore getting correlated with the spins via light.

Let us return to the output light from the hybrid system for a moment. Plugging equation (11.10) in (11.9), along with the spin equations (11.7) and (11.6), we get the output phase quadrature

$$\begin{aligned} \hat{P}_{L,M}^{\text{out}'} &\propto [\Gamma_S \chi_S + \Gamma_M \chi_M] 2\hat{X}_{L,S}^{\text{in}} \\ &+ 2i\Gamma_M \chi_M \chi_S \left[2\Gamma_S [\zeta_M - \zeta_S] \hat{X}_{L,S}^{\text{in}} + \sqrt{\Gamma_S} [\zeta_M - \zeta_S] \hat{F}_S \right] \\ &+ \sqrt{\Gamma_S} \chi_S \hat{F}_S + \sqrt{\Gamma_M} \chi_M \hat{F}_M, \end{aligned} \quad (11.11)$$

in which we have disregarded second order terms in ζ and terms proportional to $\hat{P}_{L,S}^{\text{in}}$. The equation (11.11) shows the interplay between the types of interaction and the interference of the input light fluctuations. It also features the spin thermal force being processed by the mechanical system.

In the last chapter we mentioned the importance of detuning the optomechanical cavity, therefore making $\zeta_M > 0$, to match the mechanical and the spin susceptibility and improve the back-action evasion. We also mentioned that in our parameter regime, $\zeta_S > 0$. Therefore, in our case we have $\zeta_M \neq \zeta_S$, and the spin-mechanics correlations might become important.

The connection between back-action evasion and entanglement is subtle and involves defining the method by which the quantum states and dynamics are engineered. It also involves acknowledging that the decoherence induced by the optical field is related to the acquisition of information, as in the measurement process. As is common in the literature (Vasilyev et al., 2013), we divide the schemes into the conditional and unconditional/dissipative categories.

In the unconditional entanglement generation schemes, the dynamics of the systems are engineered in such a way that the decoherence induced by the probing light is the feature that allows generating the non-classical state (Verstraete et al., 2009), without the need of any active feedback or state preparation stages. In the case of atomic spin ensembles, it has been proposed in Muschik et al. (2011) and realized in Krauter et al. (2011). In the case of our spin-mechanics interface, it has been theoretically studied in Huang et al. (2018).

In the conditional entanglement generation schemes, the state or dynamics of the system is conditioned upon a measurement performed on the light. Here,

the measurement updates the knowledge about the system. The measurement result may be used to control the dynamics via feedback, if that is desired. Entanglement (Julsgaard et al., 2001) and a variety of quantum information protocols have been performed using atomic spin ensembles (Hammerer et al., 2010).

Let us imagine the spin and the mechanical system had identical susceptibilities and were both interacting in a QND fashion with light, that is, $\zeta_M = \zeta_S = 0$, such that $\chi_S = \chi_M = \chi_{S00}$. As discussed in Chapter 10 and displayed in equation (11.11) the back-action interference would be perfect in the case of a negative mass spin oscillator. The unconditional variance of the EPR state V_u , nonetheless, would not go below the inseparability limit, but would reach $V_u = 1$ for $n_S = n_M = 0$. Including measurement and/or feedback, as shown in (Vasilyev et al., 2013), the conditional variance of the EPR state V_c can be made arbitrarily close to zero for high Γ/γ .

In our hybrid implementation, the system's natural susceptibilities are mismatched, $\gamma_{S0}/2\pi = 1$ kHz and $\gamma_{M0}/2\pi = 5$ mHz. Furthermore, the mostly QND light-spins interaction $\zeta_S \sim 0.03$ is also different from the light-mechanics in which the red detuned laser induces important cooling/beam-splitter interaction $\zeta_M \sim 0.15$. It has been shown (Huang et al., 2018) that the mismatches actually allow for improved unconditional entanglement performance over matched system situations, as long as the readout rates can be appropriately matched $\Gamma_S \sim \Gamma_M$. Due to the mismatch in interaction types, part of the spin response written into light will couple to the mechanical oscillator, which in its turn, will generate a response that interferes with the input. For $\zeta_M > \zeta_S$, the interference will be destructive, reducing the overall system noise even for the highly asymmetric sub-systems we have.

While the negative mass spin oscillator and the related quantum back-action cancellation is necessary to go below the inseparability limit, it is not sufficient. Unless dynamical processes are present, the inevitable coupling to the thermal bath \hat{F} and the ground state noise will always bring the total unconditional variance to or above the inseparability limit. The thermal fluctuations, along with eventually residual un-canceled quantum back-action, can be suppressed by conditioning the measurement results.

Our entanglement generation scheme, therefore, employs quantum back-action evasion, additional interference induced by mismatched systems, and conditioning/filtering of the detected light. In the next section we discuss the filtering used.

11.3 Filtering

Estimating the knowledge of the present state based on existing information is a problem we deal with daily. The estimation is usually a hard task due to the measurement noise in measuring the current state of the system, blurring the prediction's effectiveness. Fortunately, in some tasks, the uncertainties are either regular or have patterns that make the predictions work very precisely. Commonly, some noise sources are stationary processes, in which the noise statistics does not change when shifted in time. For this very type of processes the Wiener filter was developed in the 1940's by Norbert Wiener, in connection to war related position estimation tasks. Happily, in our case we deal with inoffensive low energy photons and vacuum fluctuations.

Estimating a quantum state or the evolution of a quantum system is a fundamental task, as quantum mechanics sets probabilistic rules on the possible measurement outcomes. According to the Copenhagen interpretation of quantum mechanics, an isolated quantum state can be represented by a wave function, a mathematical object that contains the knowledge about the system. Most commonly, the system inevitably couples to its surroundings, losing information irreversibly and evolving into a statistical mixture of states described via the density matrix ρ .

Let us consider the case we deal with in our experiments. An oscillator is prepared in the atomic spin ensemble, for example. The oscillator is coupled

to its thermal bath, which over time leads to damping/decoherence and diffusion/fluctuations in the canonical variables of the system. Furthermore, a light field also couples to the system, interacting and extracting information about its dynamics. The stronger the coupling, the stronger is the back-action effect of light onto the spin oscillator and the more disturbed the oscillator becomes.

The measurement back-action is, nonetheless, an information extraction process. Due to the light-spin coupling, the information about the system dynamics is written into light. If the measurement is efficient, that is, if the back-action dominates over other decoherence processes, the state of the oscillator can be extracted with high fidelity from the measurements of light.

The full quantum dynamics of systems open to interactions with environments is usually treated via stochastic master equations (Carmichael, 1993) or the Monte Carlo method (Mølmer et al., 1993). For the conditional density matrix master equation of a harmonic oscillator coupled to environments with uncorrelated measurement noise and constant measurement strength, see (Müller-Ebhardt et al., 2009).

For our particular case, our system and respective interactions have Gaussian statistics. Operating our oscillators at MHz frequencies are acted only by the quantum fluctuations of the light and the coupling to the thermal bath, both following wide-sense stationary-noise statistics (Broersen, 2006). In this limit, the conditional density matrix approach, the Kalman filter, and the Wiener filter have identical estimating power for incorporating the information recorded at previous times $t' < t$ in the current time conditional quantum state $\rho_c(t)$. The application of Wiener filter to quantum state preparation tasks has been discussed in Müller-Ebhardt et al. (2008), in Müller-Ebhardt et al. (2009), and in Miao (2010).

As described by Buonanno and Chen (2002), the measurement of the quadrature of light, here \hat{P}_L^{out} , follows two “classical” properties

- the operators associated with the measurement current obtained at different times t and t' commute, $[\hat{P}_L^{\text{out}}(t), \hat{P}_L^{\text{out}}(t')] = 0$, implying their simultaneous measurability;
- causality enforces $[\hat{P}_L^{\text{out}}(t), \hat{X}(t')] = 0$, $t' > t$, with \hat{X} being any quadrature of a hybrid spin-mechanics system, that is, the detection of the probe light does not influence the future state of system of interest.

Therefore, quantum mechanics enforces only the presence of amplitude and phase quantum noise in the optical probing field. However, the fundamental origin of the noise in the system is not important for the Wiener filtering theory.

Our approach focuses on the Wiener filter technique, for a number of reasons. First of all, the Wiener filter does not require including the dynamics of undesired noise sources in the modelling, contrary to the Kalman filter (Wieczorek et al., 2015). In the steady state, as we will see below, all required by the Wiener filter—on top of the conditions given in the paragraph above—is a precise estimation of the dynamics of interest in the measured signal, along with the statistical properties of the measurement noise. Second of all, there is an efficient numerical procedure to efficiently calculate the optimal Wiener filter.

For completeness, we stress that other approaches could have been taken. The conditional master equation and Kalman filtering has been explored in Lammers (2018) and in Rossi et al. (2019), respectively. If data from before and after the moment of the time state estimation is available, the theory of past quantum states (Gammelmark et al., 2013), which has been applied in Bao et al. (2020), is also a possibility.

11.4 Wiener Filtering

To clarify the Wiener filtering procedure, we will first study an example with a single variable. In the next subsection we will consider a situation closer to

that of the experiment, in which we wish to extract multiple variables from the light field.

Consider a general¹ system with noisy output signal $\hat{y}(t)$ which we can separate into the signal of interest, $\hat{x}(t)$, and the measurement noise, $\hat{n}(t)$, as

$$\hat{y}(t) = \hat{x}(t) + \hat{n}(t). \quad (11.12)$$

The Wiener filter $K(t)$ allows for obtaining the conditional signal estimate as

$$\tilde{\hat{x}}(t) = \int_{-\infty}^t K(t-t')\hat{y}(t')dt'. \quad (11.13)$$

We decompose the signal as

$$\hat{x}(t) = \tilde{\hat{x}}(t) + \hat{R}(t), \quad (11.14)$$

where $\hat{R}(t)$ is the residual noise operator. If we want to estimate the signal $\hat{x}(t)$ using the output $\hat{y}(t)$, the optimal filter $K(t)$ is found by requiring that $\hat{R}(t)$ must be uncorrelated with the past output such that

$$\langle \hat{R}(t)\hat{y}(t') + \hat{y}(t')\hat{R}(t) \rangle = 0 \quad \forall t' < t. \quad (11.15)$$

To find the optimal filter function $K(t)$ we solve the Wiener-Hopf equation (which results from the above requirement)

$$C_{xy}(t) - \int_0^{\infty} dt' K(t')C_{yy}(t-t') = 0 \quad \forall t > 0 \quad (11.16)$$

where $C_{xy}(\tau)$ is the cross-correlation function between signal and measurement output, and $C_{yy}(\tau)$ is the auto-correlation function of the measurement output. We demand $K(t) = 0$ for $t < 0$, in order to obtain a causal filter, and that $K(t)$ will be a decaying function ($K(t) \rightarrow 0$ as $t \rightarrow \infty$). The proofs and more detailed derivations are given in Müller-Ebhardt et al. (2009).

In the hybrid experiment we deal with spectral densities. Formally, we have (Clerk et al., 2010)

$$\bar{S}_{XY}(\Omega) = \int_{-\infty}^{\infty} \frac{d\Omega'}{2\pi} \frac{1}{2} \langle \{ \hat{X}(\Omega'), \hat{Y}^\dagger(\Omega) \} \rangle, \quad (11.17)$$

where $\{ \cdot, \cdot \}$ is an anti-commutator, which satisfies

$$\bar{S}_{XY}(-\Omega) = \bar{S}_{XY}^*(\Omega) \quad (11.18)$$

$$\bar{S}_{YX}(\Omega) = \bar{S}_{XY}^*(\Omega) \quad (11.19)$$

From the power spectral density, we can get the two-point temporal correlation function via the Wiener-Khinchin theorem (Clerk et al., 2010)

$$C_{XY}(\tau) = \int_{-\infty}^{\infty} \frac{d\Omega}{2\pi} \bar{S}_{XY}(\Omega) e^{i\Omega\tau} = 2 \int_0^{\infty} \frac{d\Omega}{2\pi} \bar{S}_{XY}(\Omega) e^{i\Omega\tau}. \quad (11.20)$$

The variance of a given variable is defined as

$$\text{Var}(X) = C_{XX}(0) = \int_{-\infty}^{\infty} \frac{d\Omega}{2\pi} \bar{S}_{XX}(\Omega) = 2 \int_0^{\infty} \frac{d\Omega}{2\pi} \bar{S}_{XX}(\Omega). \quad (11.21)$$

Now we go on to calculate the conditional variance. It can be shown using equations (11.14) and (11.15) that

$$V_c = \langle \hat{R}(0)^2 \rangle = \langle \hat{x}(0)^2 \rangle - \langle \hat{\tilde{x}}(0)^2 \rangle = V_u - \langle \hat{\tilde{x}}(0)^2 \rangle, \quad (11.22)$$

¹We mark the signals as operators for the sake of our own specific problem involving noise of quantum origin. The same reasoning apply for classical signals.

the conditional variance is equal to unconditional variance minus the variance of the best estimate. Note that this equation is only true for an optimal estimator (predictor), as otherwise equation 11.14 is not satisfied.

The conditional variance requires knowing the variance of the best estimate, which is

$$\langle \hat{x}(0)^2 \rangle = \int_0^\infty ds K(s) C_{xy}(s) \quad (11.23)$$

We will be using this to calculate the variance of the best estimate in the discrete cases, also in the practical analysis.

Overall, solving the Wiener-Hopf equations to obtain the analytical expressions for the Wiener filter and conditional variance, the two most important quantities for our applications, is rather challenging. As for the full hybrid model, we will rely on a numerical routine.

In the next section, we will provide the solution for the QND read out of a single oscillator, and the case of matched oscillators in the quantum back-action evasion configuration.

11.5 Filtering, QND readout

As an example that we can solve analytically, we will consider the QND readout of the hybrid system. We start with the Hamiltonian

$$\hat{H} = \frac{\omega_M}{2} (\hat{X}_M^2 + \hat{P}_M^2) \pm \frac{\omega_S}{2} (\hat{X}_S^2 + \hat{P}_S^2) + 2\sqrt{\Gamma_M} \hat{X}_L \hat{X}_M + 2\sqrt{\Gamma_S} \hat{X}_L \hat{X}_S, \quad (11.24)$$

for ω_M, ω_S as the resonant frequencies, and Γ_M, Γ_S as the readout rate of the spin and mechanics system.

We proceed to write equation (11.24) in a rotating frame at ω_M . We will also set $\omega_M = -\omega_S = \omega_0$ and match the readout rates $\Gamma = \Gamma_M = \Gamma_S$. The rotating frame transformation is described in Appendix F

$$\hat{H}_{\text{int}} = 2\sqrt{\Gamma} \hat{X}_L [(\hat{X}_S + \hat{X}_M) \cos \omega_0 t + (\hat{P}_M - \hat{P}_S) \sin \omega_0 t] \quad (11.25)$$

In time, we will also assume identical thermal occupation for both oscillators, that is, $n = n_S = n_M$.

Having the Hamiltonian, the time evolution² of the operators can easily be calculated.

11.5.1 Single oscillator

We will first study the case of a single oscillator, developing an intuition about the behaviour of the Wiener filter.

For the spin operators, for example, the dynamics for the variables is

$$\frac{d}{dt} \hat{\mathbf{R}}_S = -\gamma_{S0} \hat{\mathbf{R}}_S / 2 + 2\sqrt{\Gamma_S} \mathbf{M}(t) \hat{\mathbf{R}}_L + \hat{\mathbf{F}}_{S,\text{th}}, \quad (11.26)$$

for the matrices

$$\hat{\mathbf{R}}_S = \begin{pmatrix} \hat{X}_S \\ \hat{P}_S \end{pmatrix} \quad \mathbf{M}(t) = \begin{pmatrix} \pm \sin \omega_0 t & 0 \\ -\cos \omega_0 t & 0 \end{pmatrix} \quad \hat{\mathbf{R}}_L = \begin{pmatrix} \hat{X}_L \\ \hat{P}_L \end{pmatrix} \quad \hat{\mathbf{F}}_{S,\text{th}} = \begin{pmatrix} \hat{F}_{X,S} \\ \hat{F}_{P,S} \end{pmatrix}. \quad (11.27)$$

In the steady state limit, that is $t \rightarrow \infty$, the spin variables respond as

$$\hat{\mathbf{R}}_S(t) = \int_{-\infty}^t d\tau e^{\gamma_{S0}(\tau-t)/2} (2\sqrt{\Gamma_S} \mathbf{M}(\tau) \hat{\mathbf{R}}_L(\tau) + \hat{\mathbf{F}}_{S,\text{th}}(\tau)) \quad (11.28)$$

²We will follow the definitions

$[\hat{X}_i, \hat{P}_i] = i \quad [\hat{X}_L, \hat{P}_L] = i/2.$

The relations for the light variables can be written as

$$\begin{aligned}\hat{X}_{L,S}^{\text{out}} &= \hat{X}_{L,S}^{\text{in}} \\ \hat{P}_{L,S}^{\text{out}} &= \hat{P}_{L,S}^{\text{in}} + \sqrt{\Gamma_S} (\hat{X}_S \cos \omega_0 t \pm \hat{P}_S \sin \omega_0 t)\end{aligned}\quad (11.29)$$

Therefore, demodulation will give access to spin oscillator variables in the in and out-of-phase electronic quadratures.

We will measure the \hat{P}_L light quadrature. In the rotating frame, the dynamics are the same for both electronic quadratures, thus we may consider only one of them. Furthermore, including detection efficiency η , the readout of the position quadrature \hat{X}_S is

$$\hat{P}_{L,S}^{\text{out}} = \hat{P}_{L,S}^{\text{in}} + \sqrt{\eta\Gamma_S} \hat{X}_S. \quad (11.30)$$

We compare the equation above to the equation (11.14), equation from which the Wiener filter derivation starts. We map

$$\hat{x} \rightarrow \sqrt{\eta\Gamma_S} \hat{X}_S \quad (11.31)$$

$$\hat{n} \rightarrow \hat{P}_{L,S}^{\text{in}}, \quad (11.32)$$

such that $\hat{y} = \hat{x} + \hat{n}$.

We can now state the power spectral densities of the measurement current \hat{y} and signal \hat{x} . Being white-noise forces convolved by decaying exponentials in equation (11.28), the PSD for \hat{y} and \hat{x} are

$$\bar{S}_{yy}(\Omega) = \frac{1 + \bar{S}_b}{2} + \frac{1}{2} \frac{\eta\Gamma_S}{(\gamma_{S0}/2)^2 + \Omega^2} \left(\Gamma_S + 2\gamma_{S0}(n_S + \frac{1}{2}) \right) \quad (11.33a)$$

$$\bar{S}_{xx}(\Omega) = \frac{1}{2} \frac{\eta\Gamma_S}{(\gamma_{S0}/2)^2 + \Omega^2} \left(\Gamma_S + 2\gamma_{S0}(n_S + \frac{1}{2}) \right). \quad (11.33b)$$

The three terms in \bar{S}_{xx} are the quantum back-action, ground state and thermal noises contributions. The extra term in \bar{S}_{yy} is the detection shot noise.

We now make use of equation (11.20) to calculate the two-time auto-correlation functions in the time domain

$$C_{yy}(\tau) = \frac{1 + \bar{S}_b}{2} \delta(\tau) + \frac{\eta\Gamma_S e^{-\frac{1}{2}\gamma_{S0}\tau}}{2\gamma_{S0}} [\theta(-\tau)e^{\gamma_{S0}\tau} + \theta(\tau)] \left(\Gamma_S + 2\gamma_{S0}(n_S + \frac{1}{2}) \right) \quad (11.34a)$$

$$C_{xx}(\tau) = \frac{\eta\Gamma_S e^{-\frac{1}{2}\gamma_{S0}\tau}}{2\gamma_{S0}} [\theta(-\tau)e^{\gamma_{S0}\tau} + \theta(\tau)] \left(\Gamma_S + 2\gamma_{S0}(n_S + \frac{1}{2}) \right), \quad (11.34b)$$

where $\delta(\tau)$ and $\theta(\tau)$ are the Dirac delta and the Heaviside functions, respectively. For $\tau = 0$, we have the auto-correlation function

$$C_{xx}(0) = \eta\Gamma_S \left(n_S + \frac{1}{2} + \frac{\Gamma_S}{2\gamma_{S0}} \right) = \eta\Gamma_S V_u = \eta\Gamma_S \langle \hat{X}_S^2 \rangle, \quad (11.35)$$

showing that the total (unconditional) noise variance is proportional to the total occupancy of the oscillator.

We proceed to calculate the optimal filter function and the conditional variance related to such filtering. The Wiener-Hopf equation, defined in (11.16), can be solved by plugging in a test filter function of the form

$$K(t) = \Lambda e^{\lambda t} \theta(t), \quad (11.36)$$

in which Λ and λ are parameters to be determined. Inserting equations (11.34) and (11.36) in (11.16), we find

$$\Lambda = \frac{1}{2} \left(\frac{\sqrt{(\bar{S}_b + 1)\gamma_{S0}^2 + 4\gamma_{S0}\Gamma_S\eta + 4\Gamma_S^2\eta + 8\gamma_{S0}\Gamma_S\eta n_S}}{\sqrt{\bar{S}_b + 1}} - \gamma_{S0} \right) \quad (11.37)$$

$$\lambda = -\frac{\sqrt{(\bar{S}_b + 1)\gamma_{S0}^2 + 4\gamma_{S0}\Gamma_S\eta + 4\Gamma_S^2\eta + 8\gamma_{S0}\Gamma_S\eta n_S}}{2\sqrt{\bar{S}_b + 1}}. \quad (11.38)$$

Important insights in the filtering dynamics can be extracted from the parameters above. Let us first consider the lossless and shot-noise limited case, in which $\eta = 1$ and $\bar{S}_b = 0$. We will also set the effective thermal occupation to zero, $n_S = 0$.

In the limit of strong optical readout $\Gamma_S/2\gamma_{S0}(n_S + \frac{1}{2}) \gg 1$, the filter reduces to

$$K(t) \sim \Gamma_S e^{-\Gamma_S t}, \quad (11.39)$$

simplify determined the readout rate Γ_S . Equivalently, in frequency space the filter is a Lorentzian with linewidth $\Gamma_S/2\pi$ (FWHM), which narrows as the readout rate increases towards infinity. This demonstrates that in the limit of system dynamics dominates by the optical readout, the output light signal and state of the oscillator are as correlated as possible.

In the opposite limit, $\Gamma_S/\gamma_{S0} \ll 1$, the filter becomes

$$K(t) \sim \Gamma_S e^{-\gamma_{S0} t/2}. \quad (11.40)$$

The optimal state estimation is done when taking into account the whole envelope decay of the system dynamics, extracting all the information from the optical measurement.

The broadband spin noise contribution alters the Wiener filter parameters. In the limit of $\Gamma_S \gg \gamma_{S0}$, a non-zero \bar{S}_b makes the filtering time scale shorter and reduces the absolute weight of the estimator, effectively broadening the filter in frequency space.

The variance of the best estimate is calculated using equation (11.22). We use the unconditional variance V_u from equation (11.35) and the best estimate variance $\langle \hat{x}(0)^2 \rangle$ and Wiener filter from equations (11.23) and (11.36), respectively, to calculate the conditional variance

$$V_c^X = \frac{\sqrt{\gamma_{S0}^2 + 4\gamma_{S0}\Gamma_S\eta'(\Gamma_S/\gamma_{S0} + 2n_S + 1)} - \gamma_{S0}}{4\Gamma_S\eta'} \quad (11.41)$$

for $\eta' = \eta/(\bar{S}_b + 1)$. Therefore, the broadband spin noise contribution reduces the detection efficiency of the conditional state preparation, increasing the final variance. In the strong read out limit, for $\eta' = 1$, the conditional variance tends to

$$V_c^X \rightarrow \frac{1}{2}. \quad (11.42)$$

Therefore, the conditioning procedure can remove all the back-action noise induced by the measurement and thermal noise induced bath the thermal bath. The remaining variance is due to the ground state noise energy. The back-action noise is, after all, a signature of the light field carrying information about the oscillator dynamics.

The total conditional variance, in the rotating wave approximation limit, is obtained by summing with the conditional variance for the \hat{P}_S spin variable, such that

$$V_c^X + V_c^P = 1, \quad (11.43)$$

in the perfect measurement limit.

11.5.2 Hybrid system

For the matched hybrid configuration, the procedure for finding the Wiener filter and conditional variance is basically the same. Nonetheless, now we have the optical quadratures carrying information about the hybrid system

$$\begin{aligned}\hat{X}_L^{\text{out}} &= \hat{X}_L^{\text{in}} \\ \hat{P}_L^{\text{out}} &= \hat{P}_L^{\text{in}} + \sqrt{\Gamma_S} ((\hat{X}_S + \hat{X}_M) \cos \omega_0 t + (\hat{P}_M - \hat{P}_S) \sin \omega_0 t).\end{aligned}\quad (11.44)$$

As in the previous section, we will calculate the Wiener filtering for the cosine component of \hat{P}_L^{out} , which will give access to $\sqrt{2}\hat{X}_{\text{EPR}} = \hat{X}_S + \hat{X}_M$. Due to the symmetry of the problem, the sine component will have the same variance.

As for the spin and mechanical system variables, the power spectral densities $\bar{S}_{ij}(\Omega)$ and respective auto-correlation functions in the time domain $C_{ij}(\tau)$, for i, j as general indices, will not have the quantum back-action and ground state contributions, that is

$$\bar{S}_{yy}(\Omega) = \frac{1}{2} + \frac{1}{2} \frac{\eta\Gamma}{(\gamma_{S0}/2)^2 + \Omega^2} (4\gamma_{S0}(n + \frac{1}{2})) \quad (11.45a)$$

$$\bar{S}_{xx}(\Omega) = \frac{1}{2} \frac{\eta\Gamma}{(\gamma_{S0}/2)^2 + \Omega^2} (4\gamma_{S0}(n + \frac{1}{2})), \quad (11.45b)$$

for the power spectral densities, and

$$C_{yy}(\tau) = \frac{1}{2} \delta(\tau) + \frac{\eta\Gamma e^{-\frac{1}{2}\gamma_{S0}\tau}}{2\gamma_{S0}} [\theta(-\tau)e^{\gamma_{S0}\tau} + \theta(\tau)] (4\gamma_{S0}(n + \frac{1}{2})) \quad (11.46a)$$

$$C_{xx}(\tau) = \frac{\eta\Gamma e^{-\frac{1}{2}\gamma_{S0}\tau}}{2\gamma_{S0}} [\theta(-\tau)e^{\gamma_{S0}\tau} + \theta(\tau)] (4\gamma_{S0}(n + \frac{1}{2})), \quad (11.46b)$$

for the auto-correlation functions. We have disregarded the broadband spin noise contribution, for simplicity.

We proceed to find solutions for the Wiener-Hopf equation following the same test function as in equation (11.36). We believe the decaying exponential is a good test function because with both oscillators matched in all parameters, spectrally we will only see a single feature, with Lorentzian shape. The Λ and λ , and V_c parameters are modified relative to single-oscillator case akin to the PSDs and auto-correlations, with no quantum back-action but double thermal noise terms. Overall, they are found to be

$$\begin{aligned}\Lambda &= \frac{1}{2} \left(\sqrt{\gamma_{S0}^2 + 4\gamma_{S0}\Gamma_S\eta + 8\gamma_{S0}\Gamma_S\eta n} - \gamma_{S0} \right) \\ \lambda &= - \frac{\sqrt{\gamma_{S0}^2 + 4\gamma_{S0}\Gamma_S\eta + 8\gamma_{S0}\Gamma_S\eta n}}{2} \\ V_c^{\text{XepR}} &= \frac{1}{2} \frac{\sqrt{\gamma_{S0}^2 + 8\gamma_{S0}\Gamma\eta(2n+1)} - \gamma_{S0}}{4\Gamma\eta}.\end{aligned}\quad (11.47)$$

Let us focus on the conditional variance V_c . In the limit of infinitely strong readout, $\Gamma/\gamma \gg 1$, we have the remarkable result

$$V_c^{\text{XepR}} \rightarrow 0, \quad (11.48)$$

which, when compared to the single oscillator variance, equation (11.42), reveals that the variance is not bounded from below. This is a direct consequence of the collective Hamiltonian (11.25), which decouples \hat{X}_{EPR} from the dynamical evolution. As $[\hat{X}_{\text{EPR}}, \hat{P}_{\text{EPR}}] = 0$, the measurement does not lead to the accumulation of measurement back-action.

A vanishing variance indicates we can have a perfect estimate of the collective \hat{X}_{EPR} variable. As the same conclusion applies for the \hat{P}_{EPR} , the total conditional variance lower bound goes to zero, as

$$V_c^{\text{Xepr}} + V_c^{\text{Pepr}} \rightarrow 0, \quad (11.49)$$

indicating the generation of a perfectly quantum-correlated EPR state.

In this section we have shown that an ideal conditional measurement of the matched hybrid system can generate a certified quantum state with variance below the inseparability limit $V_c < 1$. As we will see in the coming sections, although the current status of experimental realization sets limitations in detection efficiencies and oscillators matching, the frequency dependence of the Wiener filter, for example, qualitatively agrees with the filter constructed from the full hybrid model and measured noise spectra for the resonant $\omega_S \sim \omega_M$ cases.

11.5.3 A discrete Wiener filter

In the experiments, the detected photo-current is sampled with a finite rate, that is, we have access to a new measured after a certain amount of time Δt . The continuous description presented in the sections above, requiring integrals over the continuously varying time variable, must be adapted for the our experimental needs.

A discrete Wiener filter can be derived from purely discrete considerations (Wiener, 1964). Here, however, we choose to discretize the Wiener-Hopf equation, equation (11.16). For a discrete time from $t = 0$ to t_n , we have $t_0 = 0, t_n = n\Delta t$. This yields, for example

$$\begin{aligned} C_{xy}(t_0) &= K(t_0)C_{yy}(t_0) + K(t_1)C_{yy}(-t_1) + K(t_2)C_{yy}(-t_2) + \dots \\ C_{xy}(t_1) &= K(t_0)C_{yy}(-t_1) + K(t_1)C_{yy}(-t_2) + K(t_2)C_{yy}(-t_3) + \dots \\ C_{xy}(t_2) &= K(t_0)C_{yy}(-t_2) + K(t_1)C_{yy}(-t_3) + K(t_2)C_{yy}(-t_4) + \dots \end{aligned} \quad (11.50)$$

We now notice that given the symmetry of the measured power spectral density we have $C_{yy}(-t) = C_{yy}(t)$. Given a finite correlation time, we can always truncate the detected signal as $C_{y(x)y}(\tau) \rightarrow 0$ as $\tau \rightarrow \infty$. We may then rewrite the system of equations (11.50) as a matrix equation

$$\begin{pmatrix} C_{yy}(t_0) & C_{yy}(t_1) & C_{yy}(t_2) & \dots & C_{yy}(t_N) \\ C_{yy}(t_1) & C_{yy}(t_0) & C_{yy}(t_1) & \dots & C_{yy}(t_{N-1}) \\ C_{yy}(t_2) & C_{yy}(t_1) & C_{yy}(t_0) & \dots & C_{yy}(t_{N-2}) \\ \vdots & \vdots & \vdots & \ddots & \vdots \\ C_{yy}(t_N) & C_{yy}(t_{N-1}) & C_{yy}(t_{N-2}) & \dots & C_{yy}(t_0) \end{pmatrix} \begin{pmatrix} K(t_0) \\ K(t_1) \\ K(t_2) \\ \vdots \\ K(t_N) \end{pmatrix} = \begin{pmatrix} C_{xy}(t_0) \\ C_{xy}(t_1) \\ C_{xy}(t_2) \\ \vdots \\ C_{xy}(t_N) \end{pmatrix}, \quad (11.51)$$

as

$$\mathbf{C}_{yy}\mathbf{K} = \mathbf{C}_{xy}, \quad (11.52)$$

which constitutes a set of linear equations for the optimal filter \mathbf{K} . It can be efficiently solved, as C_{yy} is a so-called Toeplitz matrix via the Levinson-Durbin algorithm (Durbin, 1960).

As in equation (11.22), the conditional variance can be numerically calculated as

$$V_c = \mathbf{C}_{xx}[0] - \mathbf{K}^T \mathbf{C}_{xy}. \quad (11.53)$$

This relation is very important, as it gives a simple way to calculate the variance of interest by just multiplying matrices.

11.6 Experiments

The hybrid system and the experimental configuration have already been discussed in Chapter 10, Section 10.7.2. In fact, the spectra presented and discussed there are further studied in this section, with the analysis viewed from the perspective of conditional measurements.

We start by presenting the procedure for estimating the conditional variances, being

1. the digitized photo-current of the hybrid homodyning signal is either directly saved as time traces (for the time evolution analysis) or it is averaged after being converted into power spectral densities. In any case, the shot-noise and electronic noise levels must also be recorded for normalization of the homodyning PSD and subtraction from the normalized PSD, respectively.
2. the full model is fitted to the averaged PSDs for extracting the system parameters. It can be done using the MCMC procedure described in Section 11.7, or just a standard least-square minimization procedure. In general, fitting is necessary for extracting the system parameters that best reproduce the experimental results.
3. from the fitted parameters, using the full model, we calculate $\bar{C}_{XX}(t)$ and $\bar{C}_{XY}(t)$, the time domain auto-correlation of the oscillator variable of interest and the variable-optical quadrature cross-correlation function, respectively, as described in Section 11.4.

The steady-state unconditional variance of the spin, mechanical, and hybrid system can be calculated from covariance matrix in the spin-mechanics subspace. From the full model presented in Chapter 10, we define the submatrix of $\bar{\mathbf{S}}_{\text{out}}$ containing the first 4 rows and columns as $\bar{\mathbf{S}}_{\text{MS}}$. The unconditional covariances and covariances are calculated as

$$\mathbf{V}_u = \int_{-\infty}^{\infty} \frac{d\Omega}{2\pi} \bar{\mathbf{S}}_{\text{MS}}(\Omega). \quad (11.54)$$

4. we calculate the optical quadrature time-domain auto-correlation function $\bar{C}_{YY}(t)$ from the detected PSD or from the full model fitted with the system parameters.
5. given the time-dependent correlation functions \bar{C}_{XX} , \bar{C}_{XY} and \bar{C}_{YY} , we can solve the Wiener-Hopf equations by arranging the matrices according to the Toeplitz form and using the Levinson algorithm³ to find the Wiener filter.
6. finally, the conditional variance is calculated using equation (11.53), that is, by subtracting the convolution of the signal-measurement current cross-correlation with the extracted Wiener filter from the unconditional variance.

Having the procedure for estimating the conditional variance of the hybrid system, we move on to discussing the experiments. A table with a summary of the experimental parameters is presented in Appendix I.

We start by analyzing the hybrid system in the time domain. During its time evolution, the individual oscillators evolve according to the random fluctuations induced by the coupling to light and the respective thermal baths. The hybrid system, being composed of the spin and mechanical oscillators, will evolve accordingly.

We record and apply the state estimation procedure to independent realizations of the hybrid homodyne photo-current, with the resonant frequencies satisfying $|\omega_S| - \omega_M \sim -\gamma_M/2$. Subsequently, we obtain the slowly varying

³Using the Python package `scipy.linalg.solve_toeplitz`.

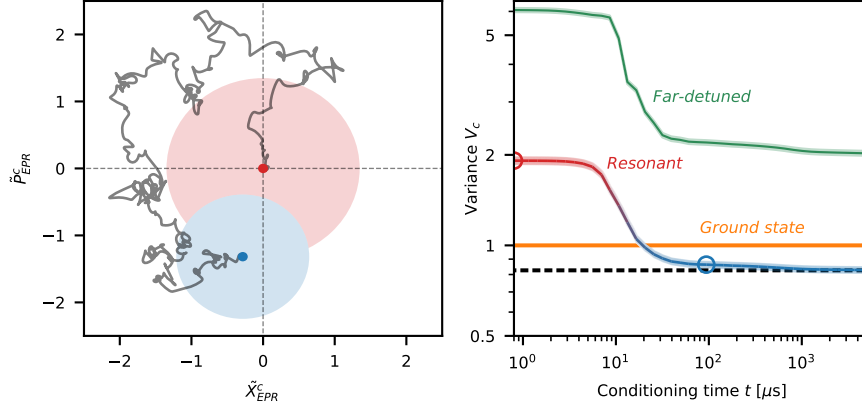


Figure 11.2: Time resolved tracking of the EPR oscillator. (left) A single realization (gray curve) of the conditional trajectory over time of the resonant ($\omega_M \sim \omega_S$) EPR oscillator in the phase space from $t = 0$ (red dot) to $t = 110 \mu\text{s}$ (blue dot). The red (blue) shaded area represents the mean unconditional (conditional) variance $V_u = 1.91$ ($V_c = 0.83$), averaged over 1000 realizations. (right) The conditional variance as a function of conditioning time. With the gradual accumulation of information over time, the resonant EPR system variance (red to blue line) goes below the EPR ground state variance ($V_c = 1$, orange shaded area). When the spin-mechanics resonant frequency detuning is ~ 110 kHz (green line), the conditioning does not lead to the preparation of an entangled state.

conditional EPR position and momentum variables, \tilde{x}_{EPR}^c and \tilde{p}_{EPR}^c , by demodulating the EPR variables with frequency $\omega/2\pi = 1.37$ MHz. The demodulation frequency is rather arbitrary, as the individual oscillators have different resonant frequencies. The demodulation allows us to extract the trajectory of the hybrid system in phase space.

We present one of the trajectories (gray line) in Figure 11.2 (left). The random dynamics of the hybrid oscillator is seen in the diffusion-like trajectory from $t = 0$ (red dot) to $t = 110 \mu\text{s}$ (blue dot). The red shaded circle represents the unconditional state variance, the variance before without applying the Wiener filter. The blue shaded circle represents the conditional state variance, after filtering the measured photo-current to estimate the system state. The radius of the red (blue) circle is given by $\sqrt{V_u}$ ($\sqrt{V_c}$). The variance of the hybrid state is reduced, showing the effectiveness of the filtering procedure.

In Figure 11.2 (right) we show the dynamics of the conditional variance V_c with conditioning time. Additionally to the approximately resonant hybrid system (in the red to blue line), we also show the case of the oscillators detuned by ~ 110 kHz (green line).

Let us first focus on the conditional variance for small conditioning times, when the system variance is still rather unconditional. At $t = 1 \mu\text{s}$, we see that the variance of the system decreases from 6.07 to 1.91 when bringing the systems close to resonance. This indicates that the back-action-evading measurement, along with the non-local dynamical cooling of the spin thermal noise by the mechanical oscillator, brings the variance of the EPR oscillator down by 5 dB, which is a major factor considering the goal is to go below the classical limit $V_c = 1$.

We now let the conditioning evolve. As the conditioning time increases, we obtain a more precise estimate of the conditional state of the hybrid system, observing the dynamics of the accumulated knowledge extracted from the optical probe. The V_c decays approximately exponentially in the range of 10-20 μs , when it goes below the classical limit, establishing that the spin-mechanics system is indeed entangled. In the next 100 μs it basically reaches the steady state

value of $V_c = 0.83 \pm 0.03$. The far-detuned case also has a reduced variance at the end of the conditioning procedure.

We can repeat the filtering procedure for different spin-mechanics detunings $|\omega_S| - \omega_M$. Differently than the case discussed above, now we are interested in the steady state conditional state preparation. The spectra are presented in Figure 11.3 panels, each for a different spin-mechanics detuning. The spin resonant frequency is marked by the gray dashed lines. The homodyne spectra, normalized to SN, are presented as colors. The full model fittings to the spectra were already shown in Figure 10.11. In black, we present the respective Wiener filters, extracted from the conditioning procedure.

The Wiener filters have a double-peak structure for the cases in which the oscillators' detuning can be resolved over their respective linewidths. For the resonant cases, in panels **d** to **g**, the filter has a Lorentzian shape with width ~ 20 kHz, on the order of the average oscillator's readout rate.

The full modeling of the system, along with the conditioning procedure, allows rejecting spurious noise contributions. In Figure 11.3, for example, the narrow peak at $\Omega - \omega_M \sim -2\pi \times 10$ kHz. Note that the Wiener filter has a notch-like feature at that particular frequency, which indicates that the conditional variance will reject the extra noise component.

The data presented in Figure 11.4 (top), shown as a wider Fourier frequency range of the panel **d** from Figure 11.3 (also Figure 10.10), gives a clearer picture of the noise sources presented in a hybrid experiment. First of all, we see that the phononic bandgap created by the periodic patterning of holes in the membrane leads to a significant noise density reduction at the 1.32-1.53 MHz range. Apart from the laser phase noise peak at approximately 1.36 MHz, the mirror mode at 1.45 MHz is the only other large noise structure due to a motion not associated directly with a membrane mode. There are four other membrane modes present in the bandgap, associated with higher order vibrations. For completeness, we include the better coupled membrane modes to the joint system modelling, whose fit to the full model is shown as the blue line. We also show the joint system noise breakdown, the mechanical thermal noise (blue shaded area), spin thermal noise (green shaded area) and quantum back-action (striped area). The orange shaded baseline defines the measurement noise, which accounts for the detection shot noise and the broadband spin noise component.

In Figure 11.4 (bottom), we show the polar representation of the associated Wiener filter, used for the conditional variance estimation. The absolute square of the filter envelope normalized to its maximum (blue line), has a bandpass like shape, centered at the joint system resonant frequency. It gives the central feature with the largest weight and rejects all other noise components.

The contributions of the unwanted noise in the conditioning procedure, although on the percent scale in the Wiener filter, decrease V_c as seen in Figure 11.5. The dots correspond to the conditional variance calculated for the experimental data. The gray curve is the conditional variance calculated from the theoretical spectra, which includes only the variables included in the modelling. The smallest variance occurs around zero atomic detuning from the mechanical resonance, increasing towards the entanglement boundary as the detuning is increased. Note that the influence of the spurious noise contributions increases with the atomic detuning, as the Wiener filter needs a bigger frequency range to estimate the signal. The error bar estimation is discussed in the next section.

11.7 Estimation of uncertainties

Establishing meaningful uncertainty levels to the conditional variances is central to claiming entanglement. For that, we require trustworthy calibrations of the system parameters. The spectra associated with conditional variances presented in Figure 11.5 —shown in Figure 10.11 or in Figure 11.3—are collectively fit to the full hybrid model, discussed in Chapter 10, Section 10.1. A

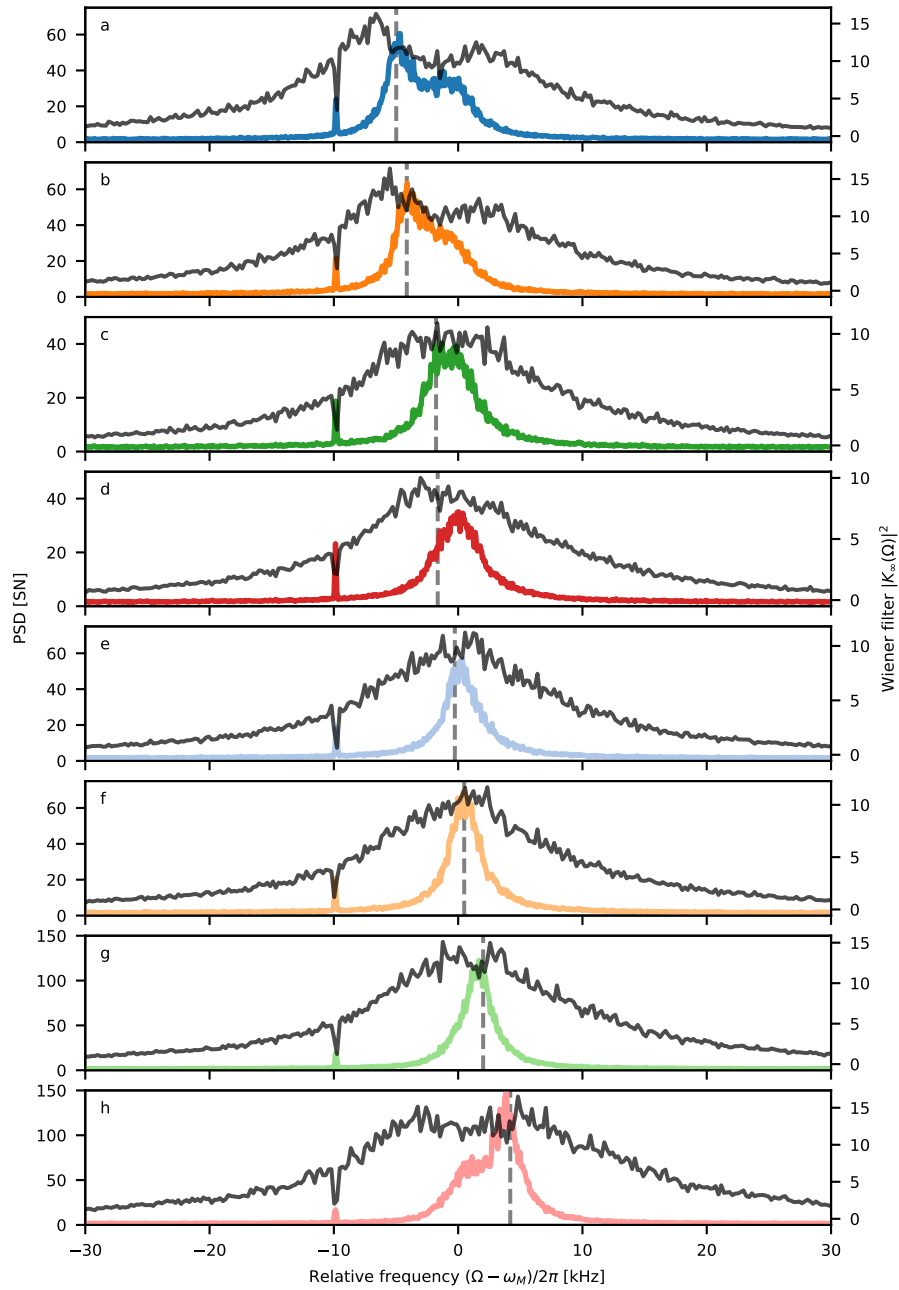


Figure 11.3: Light noise and Wiener filter spectra. The hybrid system spectra for different spin-mechanics detunings (colored), already presented along with the respective model fittings in Figure 10.11, are now presented along with its steady state Wiener filter $|K_\infty(\Omega)|^2$ (black curves). Figure in panel **d** is also shown in Figure 11.4. Dashed lines stand for the resonant frequency of the spin oscillator

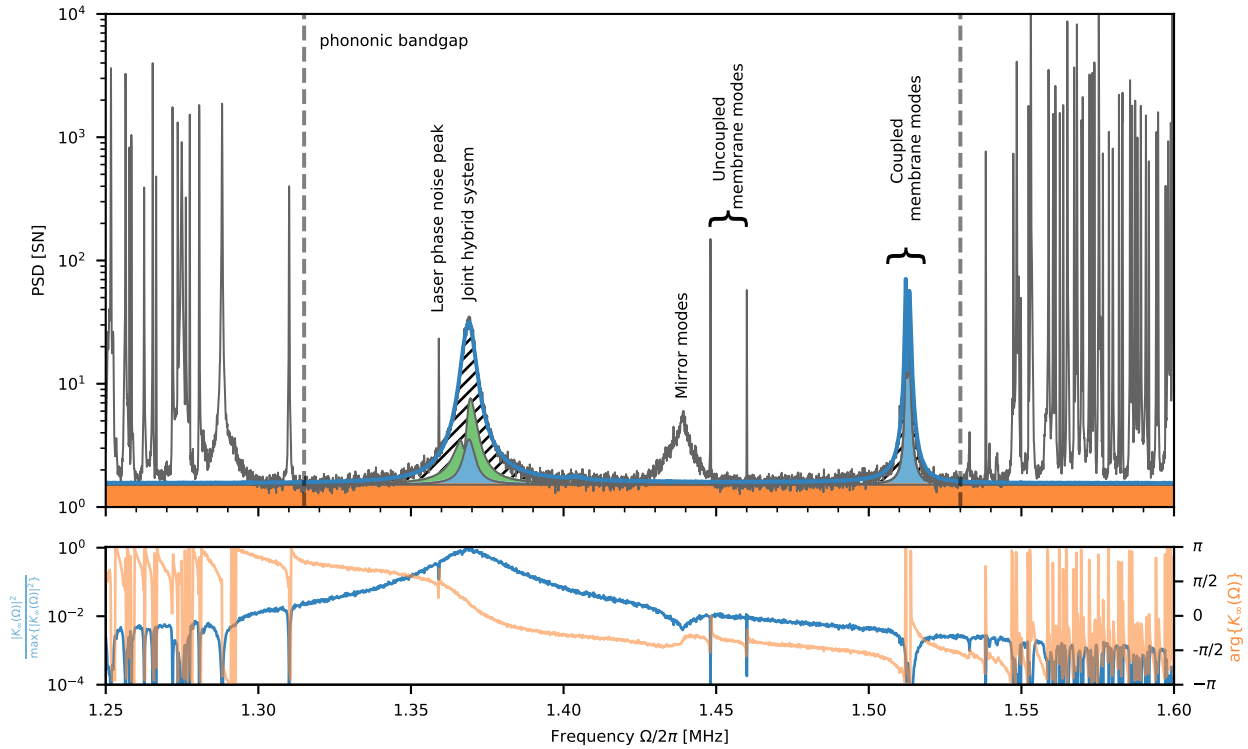


Figure 11.4: Light noise and Wiener filter spectra in a wider range. (top) A wide range power spectral density of the joint system phase fluctuations and the various noise contributions. The orange, blue and green shaded areas are the measurement noise (including shot-noise and broadband spin noise contributions), mechanical thermal noise, and spin thermal noise, respectively. The frequency band protected by the phononic bandgap is populated by laser, mirror and other weakly coupled membrane modes, apart from the joint hybrid system signal of interest. (bottom) The polar decomposition of the steady state filter. The normalized amplitude squared and phase are shown in blue and orange, respectively. Given the system correlations in the detected signal, the Wiener filter rejects all other components.

subset of the parameters is shared in between all spectra, while a small fraction of the parameters are allowed to vary from point to point, accounting for small fluctuations while the data acquisition was being performed.

The major source of run-to-run fluctuations is the LO₁-LO₂ phase φ stability due to spurious back reflections in the double pass spin readout and finite rejection of LO₁. The effects of a time dependent φ are plentiful. First of all, drifts and fluctuations of the phase φ lead to a change in the overall LO₂ power. Due to changes in LO₂ power, the cavity locking point will lead to a different detuning Δ from the optomechanical cavity. With a drifting detuning, the intra-cavity power and optomechanical coupling g change. Overall, typical drifts of $\varphi \sim 3^\circ$ are present in a experiment lasting a couple of minutes. Given the cascaded effect of the LO₁-LO₂ phase, we allow φ , Δ , and g to vary between plots.

Given the importance of the parameter values for the entanglement estimation, we use Markov Chain Monte Carlo (MCMC) simulations for estimating the values of the shared and not-shared fit parameters⁴. We establish priors for all experimental parameters from independent measurements. By using MCMC together with the fitting procedure, we aim to extracting a set of parameters that reproduces the experimental curves with best certainty given prior parameter knowledge.

Overall, the MCMC fitting procedure operates in a parameter space of up to 17 variables per entanglement data point. We run 150 independent processes

⁴The procedure is implemented in Python using the package *emcee*.

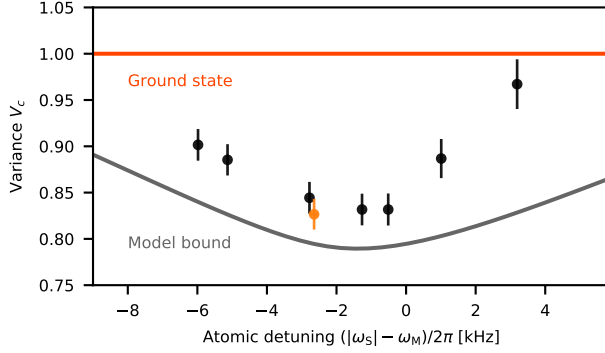


Figure 11.5: Conditional EPR variances versus atomic detuning. The steady-state conditional variance (points) depends rather weakly on the detuning of the spin and mechanical systems, all being below the ground state level (orange line) over a ~ 15 kHz range. The colored orange point has spectrum shown in Figure 11.4. The model bound stands for the conditional variance calculated from the model given parameters extracted from fit in orange.

exploring the parameter space, discarding the initial 4000 steps as the procedure reaches steady state operation. From there, each walker evolves for 6000 sampling steps. From the $150 \times 6000 = 9 \times 10^5$ possible sets of fitting variables, the posteriors, we perform the conditional variance procedure for 1000 of them. The results of the calculations are presented in Figure 11.6. The variances of the distributions are all rather similar, at the level of ± 0.03 .

The posteriors of the MCMC routine, that is, the output parameters from the fitting procedure, agree mostly rather well with the priors. The fitting curves for the hybrid spectra related to this hybrid run are all done using the average posterior values. The prior-posterior discrepancies mostly happens for the parameters related to transmission efficiencies of the quantum signal. The main discrepancy is inter-system quantum efficiency ν . The prior $\nu_{\text{prior}} = 0.65 \pm 0.03$ differs significantly from the posterior $\nu_{\text{posterior}} = 0.53$. The extra losses, not accounted for the priors, can be due to polarization dependent losses and/or to bad estimation of the cavity mode-matching. Other parameters that slightly deviate from the priors are the detection efficiencies $\eta = 0.77$, $\eta_{\text{prior}} = 0.80 \pm 0.03$, and cavity over-coupling $(\kappa_{\text{in}}/\kappa) = 0.925(5)$, $(\kappa_{\text{in}}/\kappa)_{\text{prior}} = 0.91 \pm 0.01$. On the spins side, $\Gamma_{\text{S,prior}}/2\pi = 18(1)$ kHz and posterior $\Gamma_{\text{S}}/2\pi = 20.3(4)$ kHz as well as $n_{\text{S,prior}} = 0.72 \pm 0.05$ and posterior $n_{\text{S}} = 0.81 \pm 0.05$.

11.8 Conclusions

We have demonstrated long-range entanglement between a mechanical oscillator and an atomic spin ensemble via light, showing that the conditional Einstein-Podolsky-Rosen variance goes below the inseparability limit, with variance $V_c = 0.83 \pm 0.02 < 1$. This result sets a new milestone for macroscopic entanglement between disparate systems, showing the versatility of the negative-mass reference frame in quantum information protocols and in measuring noiseless trajectories in the negative-mass reference frame.

Improving the performance requires further reduction of experimental imperfections. Our modeling shows that by reducing the broadband spin noise by a factor of 3 and the improvement of the fractional coherent spin read-out $\Gamma_{\text{S}}/\gamma_{\text{S0}}$ by another factor of 3, along with reduction of the optical losses down to 10% and improvement of cavity over-coupling to $\kappa_{\text{in}}/\kappa = 0.98$, can bring the conditional variance down to $V_c \approx 0.3$ (-5 dB).

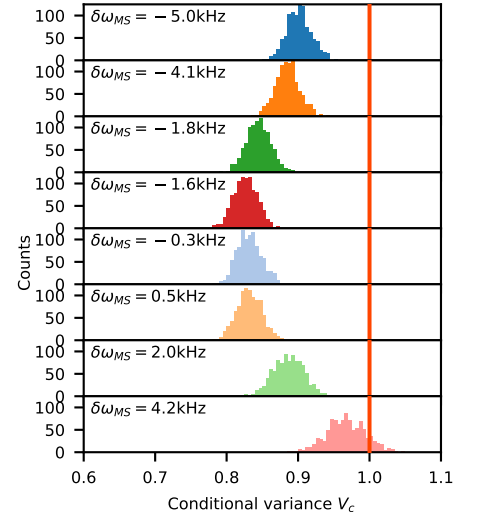


Figure 11.6: Error estimation of the conditional variance. The MCMC routine optimizes the fitting routine given the prior set of parameters and respective uncertainties. We select a random sample ($N = 1000$) of the output parameters from the MCMC simulations, extract the corresponding Wiener filter and calculate the conditional variances. The distributions' average and standard deviations are shown in Figure 11.5.

Chapter 12

Conclusions and Outlook

In this thesis, we have described the experimental realization of an optical interface between a room temperature spin ensemble and a mechanical oscillator to the quantum limits and beyond, preparing the joint system in an entangled Einstein-Podolsky-Rosen state (Thomas et al., 2020). This result, building up from the quantum back-action evasion results (Møller et al., 2017), demonstrates that our hybrid platform has potential applications that range from the sensing of minute forces and accelerations, to quantum information processing protocols by providing a quantum link between vastly different systems.

As discussed in Chapter 11, the broadband spin noise, a consequence stemming from an inhomogeneous spins-light interaction, adds significant noise to the light output from the spin ensemble, limiting the EPR variables detection efficiency. Reducing the broadband noise contribution can be done by making the laser intensity more homogeneous across the transverse section of the cell using a top-hat beam profiler, for example. In the spin-mechanics configuration studied in this thesis, with spins interacting with light first, such transformation would have to be undone for coupling to the optomechanical cavity fundamental TEM₀₀ mode. As we will discuss below, by inverting the spin-mechanics order we can avoid the top-hat-to-gaussian beam transformation. Regardless of the order, tailoring the beam must be done with smallest possible added losses.

Achieving a higher spin quantum cooperativity requires a higher spin read-out rate and better spin state preparation. Due to the unavoidable laser beam divergence, optimally filling a longer cell also requires a larger transverse area which leads to a lower spin natural linewidth γ_{S0} . As discussed in Chapter 10 and 11, reducing the total spin linewidth—a sizeable part of it composed by the natural linewidth—facilitates working on the regime of $\gamma_S \ll \gamma_M$, enhancing the effects of dynamical noise cancellation by the mechanical oscillator, therefore improving the performance of the hybrid experiment.

For improving the vapor cells optical performance, careful assembling of the parts is required. Although a highly trained craftsmen can perform glass-blowing with great precision, several applications still suffer from the common imperfections. The smallest attainable flame size, on the order of a couple of millimetres, sets a lower limit on the spot size that will be most affected by the heating. Therefore, glass-blowing is not a good option cells that minimize volume or require an interferometrically flat windows over the full area of the cell. For our applications, an ideal vapour cell is a sturdy vacuum tight container with uniformly transparent windows. Preferably, the fabrication procedure should allow for arbitrary choice of shapes and volumes. While glass-blowing performs well for volumes down to the order of 1 cm³, further miniaturization is hard to achieve.

During my PhD, we have tried employing two different bonding techniques, anodic and CO₂ laser bonding, to substitute it. Recently¹, we have managed to produce vacuum tight laser bonded cells, with an example shown in Figure 12.1. While still in its early stages, this technique is shown to be much less

¹As part of Erik Belhage's Master's project

invasive as it only significantly distorts the glass volume in the bonded section, the outer rim of the glass tubing. If the optical quality promises become true, a laser beam shaped to the fill the cell transverse area would experience minimal loss.

A low optical loss vapor cell, altogether with a suited optical cavity, is a direct way for improving spin readout rate, further increasing the quantum cooperativity and quantum efficiency of the spin measurement. For efficiently reducing the broadband contribution, the optical mode must fill the transverse section of the vapor cell. Fabry-Perot resonators of the confocal and/or the concentric type allow for match all higher order TEM_{mn} modes along with the fundamental Gaussian mode, tailoring the effective cavity mode to the desired one.

Another avenue to continue improving the experiment is reducing the inter-system losses. The mode matching of the spin's output to the optomechanical cavity is currently limited at $\nu_{\text{cav}} \sim 90\%$, for reasons that are not completely understood to the moment. We currently also have $\sim 10\%$ of extra optical losses, pointed out by our parameter estimation routine, which need further understanding. The current leads point that this losses could be coming directly from the spin ensemble cell.

On the mechanics side, removing mirror noise, the thermal vibrations of the mirror structure itself, would be beneficial. As seen in the entanglement discussion, the extra noise added by mirror modes has as non-negligible contribution. As our mirrors don't have phononic bandgaps, the modes that happen to lie in the membrane bandgap further reduce the shot-noise limited frequency band. Further increasing the mechanical readout rates, would broaden the Wiener filter, making the contribution relatively more important. On a different note, improving the thermal stability of the cryostat housing the optomechanical system would make the experimental runs more stable and alignment free.

As for future hybrid experiments, having already shown the preparation of the system in an entangled state, the complexity of the protocols can be increased. As noted in Hammerer et al. (2009), one of the exciting advantages of a hybrid interface is the possibility of increasing the toolbox of available preparation and measurement schemes from one system to another. Take, for example, the preparation of a mechanical state with quantum fluctuations below the zero-point level, that is, a mechanical squeezed state. Preparing a mode of a macroscopic system in a quantum state offers studying the limits of quantum mechanics on the quantum-to-classical limit and, possibly, its interconnections with the quantum aspects of gravity. In our hybrid system, we could, for example, prepare the spin ensemble in a squeezed state via measurement (Fernholz et al., 2008; Vasilakis et al., 2015) and teleport it (Krauter et al., 2013) to the mechanical system. Our hybrid entanglement could also allow propagating the quantum link forward to, for example, mechanical degrees of freedom electromechanically coupled superconducting qubits Higginbotham et al. (2018); Mirhosseini et al. (2020).

Moreover, as the constituent parts of the entangled state respond to very different perturbations, the entanglement could facilitate measurements of motion and fields, as off-resonant continuous force detection in gravitational wave interferometers Khalili and Polzik (2018); Zeuthen et al. (2019), and resonant pulsed measurements based on state preparation and retrodiction Wasilewski et al. (2010).

The results presented in this work are part of an ongoing progress towards better understanding and control of our mechanical and spins systems at their quantum limits. Hopefully, this is just the beginning of a journey highlighted by many pioneering experiments.

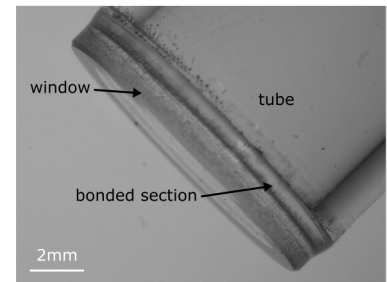


Figure 12.1: Side view of the glass-to-glass laser bonding. A 1/2" glass window is laser bonded to 13 mm diameter glass tube. The laser beam heats the window-tube interface (bonded section), fusing the parts together. Notice that glass 1 mm away from the bonded section is not visibly affected by the heating.

Part IV

Supplementary Information

Appendix A

Mathematical Methods

In this chapter, we summarize some of the useful relations used throughout the main text. Although most of the results can be found in various textbooks, it is handy to have them bunched together—even more for an experimentalist.

A.1 Commutators and power spectral densities

For a function in the time domain $\hat{f}(t)$, we use the Fourier transform sign convention and property

$$\hat{f}(\Omega) = \mathcal{F}\{\hat{f}(t)\} = \int_{-\infty}^{\infty} \hat{f}(t)e^{i\Omega t} dt, \quad \mathcal{F}\left\{\frac{d}{dt}\hat{f}(t)\right\} = -i\Omega\hat{f}(\Omega). \quad (\text{A.1})$$

For the localised optical cavity mode, we introduce the photon annihilation and creation operators obeying the commutation relation $[\hat{a}, \hat{a}^\dagger] = 1$, and, in turn, the light amplitude and phase quadratures (suppressing the time/Fourier-frequency dependence for brevity)

$$\hat{X}_L = \frac{\hat{a} + \hat{a}^\dagger}{2} \quad \hat{P}_L = \frac{\hat{a} - \hat{a}^\dagger}{2i}, \quad (\text{A.2})$$

which obey the same-time commutation relation $[\hat{X}_L(t), \hat{P}_L(t)] = i/2$. In Figure A.1 we present the relationship between the time and frequency version of a general position operator $\hat{X}(t)$. Note how the conjugate of the position operator in frequency space related to the a different Fourier frequency, $[\hat{X}(\Omega)]^\dagger = \hat{X}^\dagger(-\Omega)$.

All travelling optical fields, including additional (vacuum) noise fields introduced by optical losses, are described by amplitude and phase quadratures

$$\hat{X}_L^{\text{in(out)}} = \frac{\hat{a}_{\text{in(out)}} + \hat{a}_{\text{in(out)}}^\dagger}{2} \quad \hat{P}_L^{\text{in(out)}} = \frac{\hat{a}_{\text{in(out)}} - \hat{a}_{\text{in(out)}}^\dagger}{2i}, \quad (\text{A.3})$$

$$\begin{array}{ccc} \hat{X}(t) = \frac{1}{2}(\hat{a}(t) + \hat{a}^\dagger(t)) & \xrightarrow{\dagger} & [\hat{X}(t)]^\dagger = \hat{X}(t) = \frac{1}{2}(\hat{a}^\dagger(t) + \hat{a}(t)) \\ \mathcal{F} \downarrow & & \downarrow \mathcal{F} \\ \hat{X}(\Omega) = \frac{1}{2}(\hat{a}(\Omega) + \hat{a}^\dagger(-\Omega)) & \xrightarrow{\dagger} & [\hat{X}(\Omega)]^\dagger = \hat{X}^\dagger(-\Omega) = \frac{1}{2}(\hat{a}(\Omega) + \hat{a}^\dagger(-\Omega)) \end{array}$$

Figure A.1: Fourier transform relations. The action of the Fourier transformations and the conjugation of the generalized position operator $\hat{X}(t)$.

defined in terms of the quantum amplitudes

$$\hat{a}_{\text{in(out)}}(t) = \frac{1}{2\pi} \int_{-\infty}^{\infty} d\Omega e^{-i\Omega t} \hat{a}_{\text{in(out)}}(\Omega) \quad (\text{A.4})$$

$$\hat{a}_{\text{in(out)}}^\dagger(t) = \frac{1}{2\pi} \int_{-\infty}^{\infty} d\Omega e^{+i\Omega t} \hat{a}_{\text{in(out)}}^\dagger(\Omega) \quad (\text{A.5})$$

where $\hat{a}_{\text{in(out)}}$ is the field in a rotating frame with respect to the relevant optical carrier frequency ω_{laser} , so that $\hat{a}_{\text{in(out)}}(\Omega)$ represents the field at absolute frequency $\Omega + \omega_{\text{laser}}$. This expression is valid for Fourier frequencies close to the optical carrier, $|\Omega| \ll \omega_{\text{laser}}$. According to the above considerations the Fourier transforms of the rotating-frame operators $\hat{a}_{\text{in(out)}}(t)$ and $\hat{a}_{\text{in(out)}}^\dagger(t)$ (see Eqs. (A.4)), using the convention in Eq. (A.1), are

$$\mathcal{F}\{\hat{a}_{\text{in(out)}}(t)\} = \hat{a}_{\text{in(out)}}(\Omega), \quad \mathcal{F}\{\hat{a}_{\text{in(out)}}^\dagger(t)\} = \hat{a}_{\text{in(out)}}^\dagger(-\Omega). \quad (\text{A.6})$$

The non-vanishing commutation relations of the travelling field operators are $[\hat{X}_{\text{L}}^{\text{in(out)}}(t), \hat{P}_{\text{L}}^{\text{in(out)}}(t')] = (i/2)\delta(t - t')$. Accordingly, the symmetrised power spectral densities of the incoming vacuum light fields are

$$\bar{S}_{X_{\text{L}}X_{\text{L}}}(\Omega)\delta(\Omega - \Omega') = \frac{1}{2} \langle \hat{X}_{\text{L},j}^{\text{in}\dagger}(\Omega) \hat{X}_{\text{L},j}^{\text{in}}(\Omega') + \hat{X}_{\text{L},j}^{\text{in}}(\Omega') \hat{X}_{\text{L},j}^{\text{in}\dagger}(\Omega) \rangle = \frac{1}{4} \delta(\Omega - \Omega') \quad (\text{A.7a})$$

$$\bar{S}_{P_{\text{L}}P_{\text{L}}}(\Omega)\delta(\Omega - \Omega') = \frac{1}{2} \langle \hat{P}_{\text{L},j}^{\text{in}\dagger}(\Omega) \hat{P}_{\text{L},j}^{\text{in}}(\Omega') + \hat{P}_{\text{L},j}^{\text{in}}(\Omega') \hat{P}_{\text{L},j}^{\text{in}\dagger}(\Omega) \rangle = \frac{1}{4} \delta(\Omega - \Omega'). \quad (\text{A.7b})$$

For the mechanical (M) and spin (S) oscillators, we follow the commutation relation $[\hat{X}_j, \hat{P}_j] = i$ for ($j = \text{M, S}$); the effect of the thermal reservoirs \hat{F}_j with mean thermal occupancy n_j is captured by the symmetrised correlation functions

$$\begin{aligned} \bar{S}_{F_{\text{S}}^X F_{\text{S}}^X}(\Omega)\delta(\Omega - \Omega') &\equiv \frac{1}{2} \langle \hat{F}_{\text{S}}^{X,\dagger}(\Omega) \hat{F}_{\text{S}}^X(\Omega') + \hat{F}_{\text{S}}^X(\Omega') \hat{F}_{\text{S}}^{X,\dagger}(\Omega) \rangle \\ &= \gamma_{\text{S}0}(n_{\text{S}} + 1/2)\delta(\Omega - \Omega') \\ \bar{S}_{F_{\text{S}}^P F_{\text{S}}^P}(\Omega)\delta(\Omega - \Omega') &\equiv \frac{1}{2} \langle \hat{F}_{\text{S}}^{P,\dagger}(\Omega) \hat{F}_{\text{S}}^P(\Omega') + \hat{F}_{\text{S}}^P(\Omega') \hat{F}_{\text{S}}^{P,\dagger}(\Omega) \rangle \\ &= \gamma_{\text{S}0}(n_{\text{S}} + 1/2)\delta(\Omega - \Omega') \\ \bar{S}_{F_{\text{M}} F_{\text{M}}}(\Omega)\delta(\Omega - \Omega') &\equiv \frac{1}{2} \langle \hat{F}_{\text{M}}^\dagger(\Omega) \hat{F}_{\text{M}}(\Omega') + \hat{F}_{\text{M}}(\Omega') \hat{F}_{\text{M}}^\dagger(\Omega) \rangle \\ &= 2\gamma_{\text{M}0}(n_{\text{M}} + 1/2)\delta(\Omega - \Omega'). \end{aligned} \quad (\text{A.8})$$

A.2 Angular momentum operators

When dealing with atomic physics experiments, choosing a *good* quantization axis can simplify and clarify many physical aspects of the process under study. In the description of optical pumping, for example, light-matter coupling follows selection rules which can be tailored according to the polarization of the photon. Historically, QUANTOP related works have been following the non-trivial school of quantization axis along the x -axis.

In the x -basis, we have

$$\begin{aligned}\hat{F}_x &= \sum_m m A_{mm} \\ \hat{F}_y &= \frac{1}{2} \sum_m c(J, m) (A_{m+1, m} + A_{m, m+1}) \\ \hat{F}_z &= \frac{1}{2i} \sum_m c(J, m) (A_{m+1, m} - A_{m, m+1}) \\ \hat{F}_0 &= \sum_m A_{mm},\end{aligned}$$

in which $c(J, m) = \sqrt{J(J+1) - m(m+1)}$ and $A_{a,b} \equiv |a\rangle\langle b| = |J, a\rangle\langle J, b|$ are the atomic operators; these definitions are useful as they fulfill the standard commutation relations $[\hat{F}_i, \hat{F}_j] = i\epsilon_{ijk}\hat{F}_k$. It is also important to note that the angular momentum operators can be constructed from the ladder operators

$$\begin{aligned}\hat{F}_+ &= \hat{F}_y + i\hat{F}_z & \hat{F}_y &= \frac{1}{2}(\hat{F}_+ + \hat{F}_-) \\ \hat{F}_- &= \hat{F}_y - i\hat{F}_z & \hat{F}_z &= \frac{1}{2i}(\hat{F}_+ - \hat{F}_-)\end{aligned}$$

in which

$$\begin{aligned}\hat{F}_+ &= \sum_m c(J, m) A_{m+1, m} \\ \hat{F}_- &= \sum_m c(J, m) A_{m, m+1}.\end{aligned}$$

Products of these operators will be particularly useful in the calculation of the noise terms

$$\begin{aligned}\hat{F}_x^2 &= \sum_m m^2 A_{mm} \\ \hat{F}_y^2 &= \frac{1}{4}(\hat{F}_+ \hat{F}_+ + \hat{F}_- \hat{F}_- + \hat{F}_+ \hat{F}_- + \hat{F}_- \hat{F}_+) \\ \hat{F}_z^2 &= -\frac{1}{4}(\hat{F}_+ \hat{F}_+ + \hat{F}_- \hat{F}_- - \hat{F}_+ \hat{F}_- - \hat{F}_- \hat{F}_+) \quad (\text{A.9}) \\ \hat{F}_y \hat{F}_z &= \frac{1}{4i}(\hat{F}_+ \hat{F}_+ + \hat{F}_- \hat{F}_- - 2\hat{F}_x) \\ \hat{F}_z \hat{F}_y &= \frac{1}{4i}(\hat{F}_+ \hat{F}_+ + \hat{F}_- \hat{F}_- + 2\hat{F}_x)\end{aligned}$$

A.3 Stokes operators

It is convenient to define the Stokes operators in a matrix form. By using the Pauli matrices

$$\begin{aligned}\sigma_x &= \begin{pmatrix} 0 & 1 \\ 1 & 0 \end{pmatrix} \\ \sigma_y &= i \begin{pmatrix} 0 & -1 \\ 1 & 0 \end{pmatrix} \\ \sigma_z &= \begin{pmatrix} 1 & 0 \\ 0 & -1 \end{pmatrix}\end{aligned} \quad (\text{A.10})$$

and its commutation relations $[\sigma_a, \sigma_b] = 2\epsilon_{abc}\sigma_c$, we can define the Stokes operators as

$$\begin{aligned}\hat{S}_x &= \frac{1}{2}\hat{\mathbf{a}}^\dagger\sigma_x\hat{\mathbf{a}} = \frac{1}{2}(\hat{a}_R^\dagger\hat{a}_L + \hat{a}_L^\dagger\hat{a}_R) \\ \hat{S}_y &= \frac{1}{2}\hat{\mathbf{a}}^\dagger\sigma_y\hat{\mathbf{a}} = \frac{i}{2}(-\hat{a}_R^\dagger\hat{a}_L + \hat{a}_L^\dagger\hat{a}_R) \\ \hat{S}_z &= \frac{1}{2}\hat{\mathbf{a}}^\dagger\sigma_z\hat{\mathbf{a}} = \frac{1}{2}(\hat{a}_R^\dagger\hat{a}_R - \hat{a}_L^\dagger\hat{a}_L) \\ \hat{S}_0 &= \frac{1}{2}\hat{\mathbf{a}}^\dagger\hat{\mathbf{1}}\hat{\mathbf{a}} = \frac{1}{2}(\hat{a}_R^\dagger\hat{a}_R + \hat{a}_L^\dagger\hat{a}_L),\end{aligned}\tag{A.11}$$

with $\hat{\mathbf{1}}$ being the identity matrix of order 2. The commutation relations for these operators are given by $[\hat{S}_a, \hat{S}_b] = i\epsilon_{abc}\hat{S}_c$. In the linear basis, the relations above are rewritten as

$$\begin{aligned}\hat{S}_x &= \frac{1}{2}\hat{\mathbf{a}}^\dagger\sigma_x\hat{\mathbf{a}} = \frac{1}{2}(\hat{a}_x^\dagger\hat{a}_x - \hat{a}_y^\dagger\hat{a}_y) \\ \hat{S}_y &= \frac{1}{2}\hat{\mathbf{a}}^\dagger\sigma_y\hat{\mathbf{a}} = \frac{1}{2}(\hat{a}_x^\dagger\hat{a}_y + \hat{a}_y^\dagger\hat{a}_x) \\ \hat{S}_z &= \frac{1}{2}\hat{\mathbf{a}}^\dagger\sigma_z\hat{\mathbf{a}} = \frac{i}{2}(-\hat{a}_x^\dagger\hat{a}_y + \hat{a}_y^\dagger\hat{a}_x) \\ \hat{S}_0 &= \frac{1}{2}\hat{\mathbf{a}}^\dagger\hat{\mathbf{1}}\hat{\mathbf{a}} = \frac{1}{2}(\hat{a}_x^\dagger\hat{a}_x + \hat{a}_y^\dagger\hat{a}_y).\end{aligned}\tag{A.12}$$

In a more mundane language, the point behind the Stokes parameters – the usefulness and the reason why going through all this mathematical trouble makes any sense – is that all parameters can be accessed by measuring light intensities and intensities differences. Remembering that $\hat{n}_i \equiv \hat{a}_i^\dagger\hat{a}_i$, the number operator for photons, we can already notice in \hat{S}_z at (A.11) and \hat{S}_x at (A.12) that the the Stokes parameters can be generally written as

$$\begin{aligned}\hat{S}_x &= \frac{1}{2}(\hat{n}_x - \hat{n}_y) \\ \hat{S}_y &= \frac{1}{2}(\hat{n}_{45} - \hat{n}_{-45}) \\ \hat{S}_z &= \frac{1}{2}(\hat{n}_R - \hat{n}_L) \\ \hat{S}_0 &= \frac{1}{2}(\hat{n}_i + \hat{n}_j),\end{aligned}\tag{A.13}$$

in which, in the last equation, i, j are the two components of a given basis.

A given optical power P gives rise to a mean voltage V at the photo-detector. The mean flux of photons per unit second, is proportional to the optical power P . Therefore, the mean number of photons, being proportional to the Stokes parameters, is proportional to the voltage V .

A.4 1st order non-homogeneous differential equation

A non-homogeneous, constant coefficients, first order linear differential equations (or a system of)

$$\frac{d}{dt}R(t) = MR(t) + F(t),$$

can be solved using the Integrating Factor technique. Its solution is

$$R(t) = e^{Mt}R(t_0) + e^{Mt}\int_{t_0}^t e^{-Ms}F(s)ds\tag{A.14}$$

Appendix B

Losses in the double-pass atomic readout

In this chapter, we calculate and compare the input-output relations for the atomic readout in single pass and double pass, including optical power losses (adding to L) at the vapor cell windows. We find that the losses introduced in between the two passes are not as bad they would naively be. We show that for a cell with transmission $T = 1 - L$, in the limit $L \ll 1$, the added losses due to the second pass is $L_{\text{add}} 4(1 - 1/\sqrt{2}) \sim 1.17$ the single pass scenario. The readout rate Γ_S , which would double in a lossless scenario (scaling with the effective cell length), also suffers a penalty $\Gamma_{\text{loss}} = 1 - L/2$.

We start by reminding ourselves about the input-output relation of a beam splitter with power transmittivity $\eta = 1 - R$, R being the power reflectivity, following the convention of Figure B.1 (a), such that

$$X_{\text{out}} = \sqrt{\eta}X_1 + \sqrt{1 - \eta}X_2 \quad (\text{B.1})$$

$$\sim (1 - R/2)X_1 + \sqrt{R}X_2, \quad (\text{B.2})$$

in which $\{X_1, X_2\}$ are the optical fields of interest; for notational simplicity, we don't include the hats for the light operators. The second line in (B.1) is obtained from the first in the limit of $R \ll 1$, to the first order. In the matrix form, for the vector $\mathbf{X}_i \equiv (X_i, P_i)^T$ with the amplitude and phase quadrature of the field as components, we have

$$\mathbf{X}_{\text{out}} = (1 - R/2)\mathbf{X}_1 + \sqrt{R}\mathbf{X}_2. \quad (\text{B.3})$$

For a vapor cell with total power losses adding to L , we assume losses equally divided over the two windows. This is not a restricting assumption, any other factorization of losses is possible. For the symmetric case, each window behaves as a beam splitter with loss of $\eta = 1 - R/2$; equivalently, (B.3) for $R = L/2$

$$\mathbf{X}_0 = (1 - L/4)\mathbf{X}_1 + \sqrt{L/2}\mathbf{X}_2. \quad (\text{B.4})$$

Another important definition is the input-output relations for the light-atoms interaction. As discussed in Chapter 3, for QND coupling, disregarding decoherence and extra noise

$$X_L^{\text{out}} = X_L^{\text{out}} \quad (\text{B.5a})$$

$$P_L^{\text{out}} = P_L^{\text{out}} + \sqrt{\Gamma_S}X_L^{\text{in}}, \quad (\text{B.5b})$$

in which $\Gamma_S \propto L_{\text{cell}}$ is the light-matter coupling parameter, proportional to the length L_{cell} of the spin ensemble. In the matrix form

$$\mathbf{X}_L^{\text{out}} = (\mathbf{1}_2 + \sqrt{\Gamma_S}\mathbf{Z}_0)\mathbf{X}_L^{\text{in}}, \quad (\text{B.6})$$

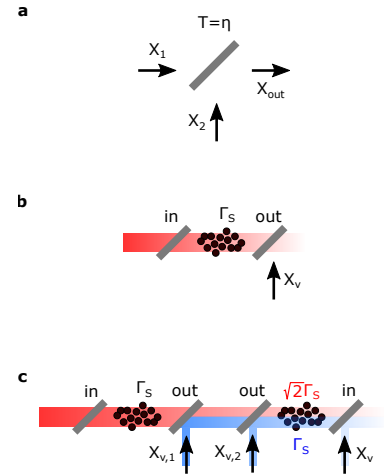


Figure B.1: Notation for lossy beam splitter and corresponding vacuum admixture. a beam splitter input-output, b a single pass, and c an unfolded double pass interaction scheme.

After the interaction with the atomic ensemble, but before crossing the exit window, the light vector is given by (B.6). Nonetheless, as the atomic output is mixed with vacuum at the output interface, shown in Figure B.1 (b), we apply the relation (B.4) with \mathbf{X}_1 as the atomic output and \mathbf{X}_2 as the admixed vacuum,

$$\mathbf{X}_L^{\text{out, single pass}} = (1 - L/4)(\mathbf{1} + \sqrt{d}\mathbf{T})\mathbf{X}_L^{\text{in}} + \sqrt{L/2}\mathbf{X}_v. \quad (\text{B.7})$$

In the double pass case, unsurprisingly, light sees the ensemble twice. We can unfold the retro-reflection as shown in Figure B.1 (c). In this case, as the lossy output window will count twice, fresh vacuum will also interact with the spins. The fraction of light that didn't get lost after the first trip through the vapor will experience an ensemble effectively twice longer, ie, $\sqrt{\Gamma_S} \rightarrow \sqrt{2\Gamma_S}$ (in red). The fraction that leaked in will also interact with the system, but with strength $\sqrt{\Gamma_S}$ (in blue). It is the two spin contributions to the propagating field that makes this description non-trivial.

In the double pass case, the transmission through the two lossy output windows is equivalent to a single loss with $L \rightarrow 2L$, that is,

$$\mathbf{X}_L^{\text{out}} \sim (1 - L/2)\mathbf{X}_L^{\text{in}} + \sqrt{L}\mathbf{X}_v, \quad (\text{B.8})$$

in which $\mathbf{X}_v = (\mathbf{X}_{v,1} + \mathbf{X}_{v,2})/\sqrt{2}$ is the normalized added vacuum field.

Including the interaction, the field after the first trip through the ensemble and the twice the output window is, from (B.6) and (B.8)

$$\mathbf{X}_L^{\text{out, single pass, two windows}} \sim (1 - L/2)(\mathbf{1} + \sqrt{\Gamma_S}\mathbf{Z}_0)\mathbf{X}_L^{\text{in}} + \sqrt{L}\mathbf{X}_v;$$

we proceed by serving this field as input to the final interaction round

$$\mathbf{X}_L^{\text{out, double pass}} = (\mathbf{1} + \sqrt{\Gamma_S}\mathbf{Z}_0)\mathbf{X}_L^{\text{out, single pass, two windows}} \quad (\text{B.9})$$

$$\sim (1 - L/2)(\mathbf{1} + \sqrt{2\Gamma_S}\mathbf{T})\mathbf{X}_L^{\text{in}} + \sqrt{L}(\mathbf{1} + \sqrt{\Gamma_S}\mathbf{Z}_0)\mathbf{X}_v \quad (\text{B.10})$$

$$= (1 - L/2)\mathbf{X}_L^{\text{in}} + \sqrt{L}\mathbf{X}_v + \sqrt{\Gamma_S}\mathbf{Z}_0 \left[\sqrt{2}(1 - L/2)\mathbf{X}_L^{\text{in}} + \sqrt{L}\mathbf{X}_v \right]. \quad (\text{B.11})$$

In the second line we have made the substitution $\sqrt{\Gamma_S} + \sqrt{\Gamma_S} \rightarrow \sqrt{2\Gamma_S}$, as a consequence of renormalizing the commutation relations for the new total spin length, maintaining the canonical form for the spin commutation relations. Breaking down the equation (B.11) by quadratures

$$\begin{aligned} X_L^{\text{out}} &= (1 - L/2)X_L^{\text{in}} + \sqrt{L}X_v \\ P_L^{\text{out}} &= (1 - L/2)P_L^{\text{in}} + \sqrt{L}P_v + \sqrt{\Gamma_S} \left[\sqrt{2}(1 - L/2)X_L^{\text{in}} + \sqrt{L}X_v \right], \end{aligned} \quad (\text{B.12})$$

we note that both output amplitude and phase quadratures have two vacuum contributions. Before propagating this field through the final window, we would like to rewrite the equations above in the same form as (B.5), making it easier to compare the single and double pass scenarios. To do so, we are required to redefine the driving vacuum quadrature, ie, the term that multiplies $\sqrt{\Gamma_S}$ in (B.5a); nonetheless, in the double pass case, this quantity is not the same as (B.5b).

Effectively, one needs to define a new basis, here X_{\parallel} and X_{\perp} , to recover the case of (B.5). The term in square brackets in equation (B.12) is defined as

$$\begin{aligned} X_{\parallel} &\equiv \sqrt{2}(1 - L/2)X_L^{\text{in}} + \sqrt{L}X_v \\ |X_{\parallel}| &\sim \sqrt{2(1 - L) + L} = \sqrt{2 - L} \sim \sqrt{2}(1 - L/4) \\ \hat{X}_{\parallel} &= \frac{X_{\parallel}}{|X_{\parallel}|} = \frac{\sqrt{2}(1 - L/2)X_L^{\text{in}} + \sqrt{L}X_v}{\sqrt{2}(1 - L/4)} \sim (1 - L/4)X_L^{\text{in}} + \sqrt{L/2}X_v. \end{aligned}$$

The vector X_{\perp} is calculated by noticing that its overlap with X_{\parallel} must be zero, $X_{\perp} \cdot X_{\parallel} = 0$; for $X_{\perp} = aX_{\perp}^{\text{in}} + bX_{\text{v}}$, with $a^2 + b^2 = 1$, we find

$$X_{\perp} = \sqrt{L/2}X_{\perp}^{\text{in}} + \sqrt{1 - L/2}X_{\text{v}}.$$

The following step in the exercise is to rewrite (B.12) in this new basis; the overlap of X_{\perp}^{out} and \hat{X}_{\parallel} , for example

$$X_{\perp}^{\text{out}} \cdot \hat{X}_{\parallel} = 1 - L(3/4 - 1/\sqrt{2}).$$

Applying the same procedure for the overlap with \hat{X}_{\perp} , leads us to

$$\begin{aligned} X_{\perp}^{\text{out}} &= [1 - L(3/4 - 1/\sqrt{2})]\hat{X}_{\parallel} + \sqrt{L/2}[1 - \sqrt{1 - L/2}]\hat{X}_{\perp} \\ P_{\perp}^{\text{out}} &= (1 - L/2)P_{\perp}^{\text{in}} + \sqrt{L}P_{\text{v}} + \sqrt{2\Gamma_{\text{S}}}(1 - L/4)\hat{X}_{\parallel}, \end{aligned} \quad (\text{B.13})$$

or

$$\begin{aligned} X_{\perp}^{\text{out}} &= [1 - L(3/4 - 1/\sqrt{2})]\hat{X}_{\parallel} + \text{orthogonal quadrature} \\ P_{\perp}^{\text{out}} &= \text{input phase noise} + \sqrt{2\Gamma_{\text{S}}}(1 - L/4)\hat{X}_{\parallel}, \end{aligned}$$

to compare with (B.5).

The last step is to propagate this field through the final window. Using (B.4)

$$\begin{aligned} X_{\perp}^{\text{out}} &= [1 - L_{\text{add}}L/4]\hat{X}_{\parallel} + \text{orthogonal quadrature} \\ P_{\perp}^{\text{out}} &= \text{input phase noise} + d_{\text{loss}}\sqrt{2\Gamma_{\text{S}}}\hat{X}_{\parallel}, \end{aligned}$$

in which $L_{\text{add}} = 4(1 - 1/\sqrt{2}) \sim 1.17$, the added losses of the double pass case in respect to the single pass, to compare with (B.7); $\Gamma_{\text{loss}} = (1 - L/2)$ is the loss factor on the expected coupling strength.

Appendix C

Effective hamiltonian evolution and decay

In this chapter we comment on the adiabatic elimination procedure by Reiter and Sørensen (2012). The procedure has been used in Chapter 3 for calculating the dynamics of the spin ensemble interacting with light.

Consider an atomic system composed of g ground and e excited states. The excited states are short-lived, due to radiative coupling to the environment; therefore, after a short amount of time, the atoms are back to the assumed long-lived states. The energy levels can be coupled to each other in arbitrary ways within ground and excited manifolds. A complete atomic basis allows us to structure the total Hilbert space according to subspaces, $1 = \hat{P}_g + \hat{P}_e$. \hat{P}_i are projector operators, that is, given a general atomic state, \hat{P}_i will decompose such state in the basis of the i manifold. Therefore, in general, the total system Hamiltonian \hat{H} can be written as

$$\hat{H} = \hat{H}_g + \hat{H}_e + \hat{V}_+ + \hat{V}_-, \quad (\text{C.1})$$

in which $\hat{H}_g = \hat{P}_g \hat{H} \hat{P}_g$ and $\hat{V}_+ = \hat{P}_e \hat{H} \hat{P}_g$, for example. Apart from the unitary hamiltonian processes, there are also the effects of coupling the system to its reservoir, which are denoted by \hat{L}_k , for the k -th channel. With all the tools and decompositions discussed, we present master equation for the density operator in the Lindblad form

$$\frac{d}{dt}\rho = -i[\hat{H}, \rho] + \sum_k \left[\hat{L}_k \rho \hat{L}_k^\dagger - \frac{1}{2} \left(\hat{L}_k^\dagger \hat{L}_k \rho + \rho \hat{L}_k^\dagger \hat{L}_k \right) \right], \quad (\text{C.2})$$

as a starting point for the adiabatic elimination. In summary, it is shown in ? that if the coupling rate of the ground to excited states is small, its effect in the ground state evolution can be treated perturbatively. Furthermore, the populations of the excited state are eliminated if negligible, leading to the effective master equation

$$\frac{d}{dt}\rho = -i[\hat{H}_{\text{eff}}, \rho] + \sum_k \left[\hat{L}_{k,\text{eff}} \rho \hat{L}_{k,\text{eff}}^\dagger - \frac{1}{2} \left(\hat{L}_{k,\text{eff}}^\dagger \hat{L}_{k,\text{eff}} \rho + \rho \hat{L}_{k,\text{eff}}^\dagger \hat{L}_{k,\text{eff}} \right) \right], \quad (\text{C.3})$$

for the ground state dynamics, in which

$$\hat{H}_{\text{eff}} = -\frac{1}{2} \hat{V}_- \left(\hat{H}_{\text{NH}}^{-1} + \hat{H}_{\text{NH}}^{-1,\dagger} \right) \hat{V}_+ + \hat{H}_g \quad (\text{C.4a})$$

$$\hat{L}_{k,\text{eff}} = \hat{L}_k \hat{H}_{\text{NH}}^{-1} \hat{V}_+ \quad (\text{C.4b})$$

$$\hat{H}_{\text{NH}} = \hat{H}_e - \frac{i}{2} \sum_k \hat{L}_k^\dagger \hat{L}_k, \quad (\text{C.4c})$$

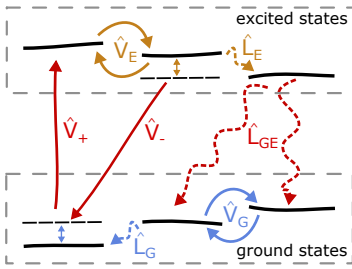


Figure C.1: Breakdown of subspaces, couplings and decay processes. A variety of processes happen within a given subspace (grey dashed areas): couplings (solid lines), energy offsets and decay (dashed lines). Processes in red (\hat{V}_+ , \hat{V}_- , \hat{L}_{GE}) connect the two subspaces.

are the effective Hamiltonian, effective decay terms and non-hermitian “hamiltonian”. In physical terms, \hat{H}_{eff} is capturing the effect of coherent coupling between the ground state levels via the excited manifold: the right hand side of (C.4a), for $\hat{H}_g = 0$, shows that an initial ground state will be transferred to its excited part, evolve, then return to the ground state via \hat{V}_- . \hat{L}_{eff} , on the other hand, describes processes the incoherent effect of photons that reached the excited state, but decay spontaneously back to the lower energy levels. Similar reasoning can be made for this process, only with the decay process happening due to spontaneous emission.

It can also be shown that summing over the no-jump processes

$$\sum_k \hat{L}_{k,\text{eff}}^\dagger \hat{L}_{k,\text{eff}} = -i\hat{V}_- \left(\hat{H}_{\text{NH}}^{-1} - \hat{H}_{\text{NH}}^{-1,\dagger} \right) \hat{V}_+, \quad (\text{C.5})$$

which will be very useful when considering specific level structures. As shown in the toy model sections, to be presented below, the similarities with (C.4a) show that coherent hamiltonian evolution and decay are intimately connected.

Before diving in the specifics of the formalism, it is important to point out that we prefer using the Heisenberg-Langevin equivalent of Eq. (C.3). Namely, for an operator \hat{A} , the evolution is given by

$$\frac{d}{dt} \hat{A} = i[\hat{H}_{\text{eff}}, \hat{A}] + \sum_k \left[\hat{L}_k^\dagger \hat{A} \hat{L}_k - \frac{1}{2} \{ \hat{L}_k^\dagger \hat{L}_k, \hat{A} \} \right] + \sum_k \left[\hat{F}^\dagger [\hat{A}, \hat{L}_k] - [\hat{A}, \hat{L}_k^\dagger] \hat{F} \right], \quad (\text{C.6})$$

for the Langevin noise forces \hat{F} .

Applying this formalism will give a mathematically consistent description of the effects of light on the atomic system dynamics. In the next sections a few examples will be presented, building up in complexity to the full accounting on the dynamics of Cesium ground state. The toy models will be useful for introducing some of the key aspects of the light-matter interaction¹, such as the Faraday interaction and power broadening for the spin-1/2 case and tensor light shifts in the case of spin-1.

¹This description would be somewhat suitable for the $F = 1/2 \rightarrow F' = 1/2$ transition in ⁶Li atoms (Gehm, 2003).

Appendix D

Quantum cooperativity calibration via white noise drive

In this chapter, we present the spin quantum cooperativity calibration used in (Møller et al., 2017). This method requires modulating the circular polarization of light, input to the spins, with Gaussian white noise. As this polarization component drives the spins via Faraday rotation, the spin response is going to be enhanced proportionally to the input added. If the amount of added noise is known, we show that the ratio of quantum back-action to thermal noise can be estimated in the shot-noise driven case, without the added drive.

As shown in Chapter 3, the power spectral density of the spin response is¹

$$S_{PP}^{\text{out}} = S_{PP}^{\text{in}} + 4\Gamma_S^2 |\chi_S|^2 S_{XX}^{\text{in}} + \Gamma_S |\chi_S|^2 \langle \hat{F}_S^\dagger \hat{F}_S \rangle,$$

for S_{ii} as the power spectral density of the optical quadrature $i = \{X, P\}$. When the susceptibility χ_S evaluated at the Larmor frequency ω_S , becomes

$$S_{PP}^{\text{out}} @ \omega_0 = S_{PP}^{\text{in}} + \frac{4\Gamma_S^2}{\gamma_S^2} S_{XX}^{\text{in}} + \frac{2\Gamma_S}{\gamma_S} (n_S + 1/2), \quad (\text{D.1})$$

in which we have used $\langle \hat{F}_S^\dagger \hat{F}_S \rangle = 2\gamma_S (n_S + 1/2)$. The three contributions for the equation above are shot noise, back-action, and thermal noise, respectively. Furthermore, one also arrives to the standard definition of the quantum cooperativity C_q^S by taking the ratio of the back-action and thermal noise components

$$\frac{\text{BA}}{\text{TH}} \equiv C_q^S = \frac{\Gamma_S}{2\gamma_S (n_S + 1/2)}.$$

Experimentally, in this calibration technique, one drives the spin system with a known amount of added light noise. From the input-output relations (D.1), the resonant response of the spin system shows that the back action contribution can be enhanced via increased light noise. The form of the equation (D.1) is

$$\text{peak height} = a \times S_{XX}^{\text{in}} + b,$$

for unknown a, b back action and thermal contributions. Therefore, scaling a will increase the peak height proportionally. The quantum cooperativity C_q^S is the ratio a/b .

More precisely, we can use equation (D.1) and compare the change of response noise for the shot noise limited drive and for a known amount of S_{XX}^{in} , hereby n_{wn} , at spin resonance. Namely, the peak height of the spin response, normalized to the shot noise

$$S_{PP}^{\text{out,wn}} - S_{PP}^{\text{in}} \equiv \beta = \text{BA}(n_{\text{wn}} + 1) + \text{TH} \quad (\text{D.2})$$

$$S_{PP}^{\text{out}} - S_{PP}^{\text{in}} \equiv \alpha = \text{BA} + \text{TH}. \quad (\text{D.3})$$

¹Note that we disregard the tensor probing contribution and the effects of classical spin noise. We only consider the narrow spin mode dynamics.

and the desired ratio is found by solving the equations above for BA and TH, as

$$\frac{\text{BA}}{\text{TH}} = \frac{\beta - \alpha}{(n_{\text{wn}} + 1)\alpha - \beta}. \quad (\text{D.4})$$

This technique relies in knowing n_{wn} at the atomic ensemble. Therefore, is crucial to accurately determine the detection efficiency from the ensemble until the detector, hereby η , and update n_{wn} according to the measured $n_{\text{wn}}^{\text{det}}$

$$n_{\text{wn}}^{\text{det}} = \eta n_{\text{wn}} + (1 - \eta) S_{XX}^{\text{v}}, \quad (\text{D.5})$$

in which $S_{XX}^{\text{v}} = 1$ is the power spectral density of the admixed vacuum.

Appendix E

Doppler broadening and two-level system absorption

In this chapter we connect the absorption of a motionless two-level to a Doppler broadened ensemble. We derive, in a semi-classical fashion, the absorption lineshape and connect it to the optical depth and the absorption cross-section formulae.

We will work with the level structure depicted in Figure E.1. We assume the atomic ensemble to be confined to a volume of dimensions $L_x \times L_y \times L_z$ and being initialized in $|a\rangle$. From there, a laser with frequency ω_L couples this level to $|b\rangle$; the difference between the laser and the transition frequency is $\Delta = \omega_L - \omega_b$. The spontaneous decay rate is γ .

The light-matter coupling is characterized by a coupling rate g , this being the product of the single-photon and single photon coupling g_0 and a spatial profile, ie, a mode function. For the case of free-space ensembles, the longitudinal mode functions are travelling waves, $\propto e^{i\mathbf{k}\cdot\mathbf{r}(t)}$, with $\mathbf{r}(t)$ as the position of a given atom. For the case of a Fabry-Perot resonator, the mode functions are standing waves, $\propto \sin(\mathbf{k}\cdot\mathbf{r}(t))$. The longitudinal mode functions account for the spatial variations of the coupling along the light propagation direction. The position time dependence $\mathbf{r}(t) = \mathbf{x}_0 + \mathbf{v}_0 t$ accounts for the atomic motion. The transverse profile of the laser beam is a Gaussian with $1/e^2$ (intensity) radius w_0 , $\propto e^{-(x^2(t)+y^2(t))/w_0^2}$. After all, we will write the atom-light coupling as

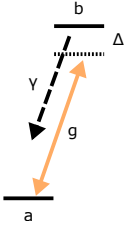


Figure E.1: The general two level system under consideration. $|0\rangle \equiv |4,4\rangle$ and $|s\rangle$ are in the ground state manifolds of Cs; $|e\rangle \equiv |5,5\rangle$ is the excited state which can be electrically dipole excited.

$$\begin{aligned} g(\mathbf{r}, \mathbf{v}, t) &= g_0 e^{-(x^2(t)+y^2(t))/w_0^2} e^{i\mathbf{k}\cdot\mathbf{r}(t)} \\ &= g_0 g_{xy}(t) g_z(t). \end{aligned} \quad (\text{E.1})$$

As the ensemble is an extended object, composed of many moving bodies, interacting with light also calls for considering the coupling over external degrees of freedom, being space (x, y, z) and velocities (v_x, v_y, v_z) . Moving atoms along the laser propagation direction will lead to Doppler shifts of the resonance frequency, spreading the absorption over a wide range of frequencies. For an ensemble at thermal equilibrium at temperature T , the Doppler width of the transition is Γ_D .

Finally, the light-matter hamiltonian, derived in (Julsgaard, 2003, Appendix C) is

$$\hat{H} = - \int_0^{L_z} dz \rho L_x L_y [\Delta \hat{A}_{ee}(z, v_z, t) + g(\mathbf{r}, \mathbf{v}, t) \hat{a}(z, t) \hat{A}_{e0}(z, v_z, t) + \text{h.c.}], \quad (\text{E.2})$$

for $A_{ij}(z, v_z, t) \equiv |i\rangle\langle j|$ as the dimensionless density operator and $\hat{a}(z, t)$ ($\hat{a}^\dagger(z, t)$) the photon's destruction (creation) operator, having units $1/\sqrt{m}$; $g(\mathbf{r}, \mathbf{v}, t)$ has units of \sqrt{m}/s and ρ is the vapor density per unit volume. This hamiltonian

¹The photon ladder operators have such units due to the travelling wave quantization of the field, see (Julsgaard, 2003, Appendix C). Due to this quantization choice, $\hat{a}^\dagger(z, t) \hat{a}(z, t) dz$ is the photon number in between z and $z + dz$. For the atomic operators, $\langle A_{ij}(z, v_z, t) \rangle \rho L_x L_y dz$ is the number of atoms in the level j between z and $z + dz$.

captures the dynamics of the atoms having velocities in the range $[v_z, v_z + dv_z]$; the integration over all the velocity classes is done further down in this notes.

The evolution of the coherences and field amplitude, including the effects of decay is given by the Heisenberg-Langevin equation

$$\begin{aligned} c \frac{d}{dz} \hat{a} &= i[\hat{H}, \hat{a}] = i\rho l_x l_y g^* \hat{A}_{0e} \\ \frac{d}{dt} \hat{A}_{0e} &= i[\hat{H}, \hat{A}_{0e}] - \gamma \hat{A}_{0e}/2 = i\Delta \hat{A}_{0e} - ig\hat{a}(\hat{A}_{ee} - A_{00}) - \gamma \hat{A}_{0e}/2, \end{aligned} \quad (\text{E.3})$$

in which the explicit time dependencies of the variables is implicitly assumed to be the same as the ones in Equation (E.2); the notation will be only revived when explicitly needed. To arrive on the equations above, we used the following commutators

$$\begin{aligned} [\hat{a}(z, t), \hat{a}^\dagger(z', t)] &= \delta(z - z') \\ [\hat{A}_{ab}(z, v_z, t), \hat{A}_{cd}(z', v_z, t)] &= \frac{1}{\rho L_x L_y} (\hat{A}_{ad}(z, v_z, t) \delta_{bc} - \hat{A}_{ad}(z, v_z, t) \delta_{da}) \delta(z - z'). \end{aligned}$$

In equation (E.3), we have neglected the fluctuation part of the dynamics. As we will only deal with average values, the fluctuations of the light and atomic variables will not play fundamental role.

From here on start solving (E.3). We proceed by taking the average value of the variables, noting them as $\langle \hat{A}_{ij} \rangle = A_{ij}$ and $\langle \hat{a} \rangle = a$. Assuming that we work far from saturation, most of the atomic population will be at the ground state, therefore $A_{ee} \sim 0$ and $A_{00} \sim 1$. With this, (E.3) becomes

$$\frac{d}{dt} \hat{A}_{0e} = (i\Delta - \gamma/2) A_{0e} + ig a. \quad (\text{E.4})$$

For $A_{0e}(0) = 0$, the solution of this differential equation is given by

$$A_{0e}(t) = i \int_0^t ds g(\mathbf{r}, \mathbf{v}, s) a(z, s) e^{(i\Delta - \gamma/2)(t-s)}. \quad (\text{E.5})$$

The coherence in between the ground and excited state is a convolution of the field amplitude (modulated by the coupling constant) with the atomic dynamics as the kernel. Over the characteristic timescale, given by $|i\Delta + \gamma/2|^{-1}$ and in the order of ns, the field $a(s)$ and the transverse coupling² are constant and can be taken out of the integral, leaving us with

$$A_{0e}(t) = ig_0 g_{xy}(t) a(z, t) e^{(i\Delta - \gamma/2)t} \int_0^t ds e^{ik(z_0 + v_{z0}s)} e^{-(i\Delta - \gamma/2)s}. \quad (\text{E.6})$$

The integral is solved as

$$\begin{aligned} \int_0^t ds e^{ik(z_0 + v_{z0}s)} e^{-(i\Delta - \gamma/2)s} &= e^{ikz_0} \int_0^t ds e^{ikv_{z0}s} e^{-(i\Delta - \gamma/2)s} \\ &= \frac{e^{ikz_0}}{i(kv_{z0} - \Delta) + \gamma/2} \left[e^{ikv_{z0}t} e^{-(i\Delta - \gamma/2)t} - 1 \right]. \end{aligned} \quad (\text{E.7})$$

$$(\text{E.8})$$

With this, (E.6) becomes

$$\begin{aligned} A_{0e}(t) &= ig_0 g_{xy}(t) a(z, t) e^{(i\Delta - \gamma/2)t} \frac{e^{ikz_0} (e^{ikv_{z0}t} e^{-(i\Delta - \gamma/2)t} - 1)}{i(kv_{z0} - \Delta) + \gamma/2} \\ &= ig_0 g_{xy}(t) a(z, t) \frac{e^{ikz(t)} - e^{ikz_0} e^{(i\Delta - \gamma/2)t}}{i(kv_{z0} - \Delta) + \gamma/2}. \end{aligned} \quad (\text{E.9})$$

²In the nanosecond timescale, room temperature atoms, travelling at $v \sim 100 \text{ m s}^{-1}$, have moved $\Delta r \sim 0.1 \mu\text{s} \ll w_0$.

For the field, (E.3) is written as

$$c \frac{d}{dz} a = i \rho l_x l_y g^* A_0 e \quad (\text{E.10})$$

$$= -\rho l_x l_y g_0^2 g_{xy}^2(t) g_z^*(t) \frac{e^{ikz(t)} - e^{ikz_0} e^{i(\Delta - \gamma/2)t}}{i(kv_{z0} - \Delta) + \gamma/2} a. \quad (\text{E.11})$$

The $g_z^*(t) A_0 e(s)$ term can be further simplified before solving the differential equation

$$\begin{aligned} e^{-ik(z_0 + v_{z0}s)} A_0 e(s) &\propto e^{-ikz(s)} \frac{e^{ikz(s)} - e^{ikz_0} e^{i(\Delta - \gamma/2)s}}{i(kv_{z0} - \Delta) + \gamma/2} \\ &\sim \frac{1}{i(kv_{z0} - \Delta) + \gamma/2}, \end{aligned} \quad (\text{E.12})$$

in which we have neglected the fast evolving phases proportional to γ , as equation (16) at the SI from (Borregaard et al., 2016). Furthermore, we take the ensemble average, averaging the position of the atoms over the cell volume, leading to

$$\langle g_{xy}^2(t) \rangle_e = \frac{1}{L_x L_y L_z} \iiint dx dy dz e^{-2(x^2(t) + y^2(t))/w_0^2} \quad (\text{E.13})$$

$$= \frac{\pi w_0^2}{2L_x L_y} \operatorname{erf}\left(\frac{l_x}{\sqrt{2}w_0}\right) \operatorname{erf}\left(\frac{l_y}{\sqrt{2}w_0}\right) \quad (\text{E.14})$$

$$\sim \frac{A_B}{L_x L_y}, \quad (\text{E.15})$$

in which the limits of the integrals are $[-L_i/2, L_i/2]$, for $i = x, y, z$, and $A_B = \pi w_0^2/2$. We proceed now by combining the results derived above in the equation for the field operator

$$c \frac{d}{dz} a = -\rho g_0^2 A_B \frac{1}{i(kv_{z0} - \Delta) + \gamma/2} a. \quad (\text{E.16})$$

The last step we need to cover is to integrate over the velocity distribution. Assuming the atomic ensemble to be thermalized at temperature T , we can use the Maxwell-Boltzmann distribution to describe the allowed velocities. Therefore, we multiply the result above by the weight factor, sum over all the possibilities and normalize to 1 —meaning that the probability of finding an atom within the assigned probability distribution is unity—such that

$$\sqrt{\frac{m}{2\pi k_B T}} \int_{-\infty}^{+\infty} dv_z \frac{e^{-mv_z^2/2k_B T}}{i(kv_z - \Delta) + \gamma/2}. \quad (\text{E.17})$$

To align this choice with the common definition of a Gaussian process, we define the standard deviation as $\sigma \equiv \sqrt{k_B T/m}$, obtaining the from equation above

$$\frac{1}{\sqrt{2\pi}\sigma} \int_{-\infty}^{+\infty} dv_z \frac{e^{-v_z^2/2\sigma^2}}{i(kv_z - \Delta) + \gamma/2}. \quad (\text{E.18})$$

We proceed by defining $\mu = v_z/\sqrt{2}\sigma$, consequently having $d\mu = dv_z/\sqrt{2}\sigma$. Defining the Doppler standard deviation as $\sigma_D \equiv k\sigma\sqrt{2} = k\sqrt{2k_B T/m}$, we can write the expression above as

$$\begin{aligned} \frac{1}{\sqrt{\pi}} \int_{-\infty}^{+\infty} d\mu \frac{e^{-\mu^2}}{i(\sqrt{2}k\mu\sigma - \Delta) + \gamma/2} &= \frac{i}{\sigma_D \sqrt{\pi}} \int_{-\infty}^{+\infty} d\mu \frac{e^{-\mu^2}}{-\mu + (\Delta + i\gamma/2)/\sigma_D} \\ &= \frac{\sqrt{\pi}}{\sigma_D} \frac{i}{\pi} \int_{-\infty}^{+\infty} d\mu \frac{e^{-\mu^2}}{-\mu + (\Delta + i\gamma/2)/\sigma_D}. \end{aligned}$$

The integral above is related to the Faddeeva function¹

$$\begin{aligned} w(b) &= \frac{i}{\pi} \int_{-\infty}^{+\infty} d\mu \frac{e^{-\mu^2}}{-\mu + b} = \frac{ie^{-b^2}}{\pi} \left(\pi \operatorname{erfi}(b) - \ln\left(-\frac{1}{b}\right) - \ln(b) \right) \\ &= e^{-b^2} (1 + i \operatorname{erfi}(b)) \\ &= e^{-b^2} \left(1 + \frac{2i}{\sqrt{\pi}} e^{b^2} D_+(b) \right), \end{aligned}$$

in which $\operatorname{erfi}(b)$ is the imaginary error function and $D(b)$ is the Dawson function. The latter, in the very useful asymptotic limits is

$$D_+(b) \sim b, \text{ for } |b| \ll 1 \quad (\text{E.19})$$

$$D_+(b) \sim \frac{1}{2b}, \text{ for } |b| \gg 1 \quad (\text{E.20})$$

With this result, we finish the derivation. The final expression for the field amplitude, for $b = (\Delta + i\gamma/2)/\sigma_D$, is

$$c \frac{d}{dz} a = -\rho g_0^2 A_B \frac{\sqrt{\pi}}{\sigma_D} \left(e^{-b^2} + \frac{2i}{\sqrt{\pi}} D_+(b) \right) a \quad (\text{E.21})$$

We start studying (E.21). First we will consider the case of resonant probing, $\Delta = 0$. For

1. *non-moving atoms*, the integration of the velocities distribution is not necessary, as all atoms have the same speed ($v_z = 0$). We come back to equation (E.16), namely

$$\begin{aligned} c \frac{d}{dz} a &= -\frac{2\rho g_0^2 A_B}{\gamma} a \\ a(z) &= e^{\frac{2\rho g_0^2 A_B}{c\gamma} z} a(0) \rightarrow \frac{n(L_z)}{n(0)} = e^{-\text{od}}, \end{aligned}$$

in which the *optical depth* is defined as

$$\text{od} = \frac{4\rho g_0^2 A_B L_z}{c\gamma}. \quad (\text{E.22})$$

2. *moving atoms*, in the limit of $\sigma_D \gg \gamma$, the Voigt profile is approximately Gaussian. In equation (E.21), we therefore treat b as a real number; in this case, the contribution from the Dawson function drop and

$$\begin{aligned} c \frac{d}{dz} a &= -\rho g_0^2 A_B \frac{\sqrt{\pi}}{\sigma_D} e^{-\Delta^2/\sigma_D^2} a \\ a(z) &= e^{-\rho g_0^2 \frac{A_B}{c} z} \frac{\sqrt{\pi}}{\sigma_D} z e^{-\Delta^2/\sigma_D^2} a(0) \xrightarrow{\Delta=0} \frac{n(L_z)}{n(0)} = e^{-\text{od}_{\text{hot}}} \end{aligned} \quad (\text{E.23})$$

for

$$\text{od}_{\text{hot}} = \frac{2\rho g_0^2 A_B L_z}{c} \frac{\sqrt{\pi}}{\sigma_D}. \quad (\text{E.24})$$

¹For relations and approximations of this function, check (Abrarov and Quine, 2014)

Therefore, we comparing the absorption of light by moving to stationary atoms, the ratio of optical depths is

$$\frac{\text{od}}{\text{od}_{\text{hot}}} = \frac{2}{\sqrt{\pi}} \frac{\sigma_D}{\gamma} = \frac{2}{\sqrt{\pi}} \frac{\sqrt{2k\sigma}}{\gamma} = \frac{1}{\sqrt{\pi \ln 2}} \frac{\Gamma_D}{\gamma} \sim \frac{2}{3} \frac{\Gamma_D}{\gamma}, \quad (\text{E.25})$$

for $\Gamma_D/2\pi = 2\sqrt{2\ln 2}k\sigma$ as the Doppler width. For a cesium ensemble at room temperature and at zero temperature, the ratio of optical depths is ~ 48 .

Further insight on the expression for the optical depth can be achieved when writing the coupling and decay rate in terms of fundamental parameters of the interaction. From the definitions found in (Steck, 2019, eq. 38), applied to a closed transition, as the $F = 4 \rightarrow F' = 5$ in cesium

$$g_0 = \sqrt{\frac{\omega_L}{2\hbar\epsilon_0 A_B}} d_{0e}$$

$$\gamma = \frac{\omega_{0e}^3 d_{0e}^2}{3\pi c^3 \epsilon_0 \hbar}$$

for A_B being the laser beam transverse area. Plugging in these results in (E.22), we get

$$\text{od} = 4 \frac{\rho g_0^2 A_B}{c\gamma} l_z = \rho \frac{3\lambda^2}{2\pi} l_z = \rho \sigma_{\text{Cs}} l_z,$$

with $\sigma_{\text{Cs}} = 3\lambda^2/(2\pi)$ agreeing with the standard definitions from (Jackson, 1999, Sec. 17.8, eq. 17.66) and (Steck, 2007, Sec. 4.3.1) as the resonant scattering cross-section for a cyclic transition. More importantly, the equation above fully agrees with the standard definition of optical depth (Hammerer et al., 2010, Sec. C.1).

Another very interesting case is the absorption in the off-resonant limit, $\Delta \gg \gamma, \gamma_D$. For

1. **cold, non-moving atoms.** From equation (E.16), for $v_z = 0$

$$c \frac{d}{dz} a = -\rho g_0^2 A_B \frac{1}{-i\Delta + \gamma/2} a$$

$$\frac{a(l_z)}{a(0)} = e^{-\frac{\text{od}}{4} \frac{\gamma}{-i\Delta + \gamma/2}} \rightarrow \frac{n(l_z)}{n(0)} = e^{-\text{od} L(\Delta)}, \quad (\text{E.26})$$

for which we have defined the Lorentzian function $L(\Delta)$

$$L(\Delta) = \frac{(\gamma/2)^2}{\Delta^2 + (\gamma/2)^2}.$$

Applying the same procedure as in (E.22) to define the optical depth, here in the limit of $\Delta \gg \gamma$

$$\text{od}_{\text{cold, far detuned}} \sim \text{od} \frac{(\gamma/2)^2}{\Delta^2} \quad (\text{E.27})$$

2. **hot, moving atoms.** Defining $z \rightarrow (\Delta + i\gamma/2)/\sigma_D$, using the approximation (E.20), to the first order in γ/Δ we have

$$D_+(z) \sim \frac{1}{2z}.$$

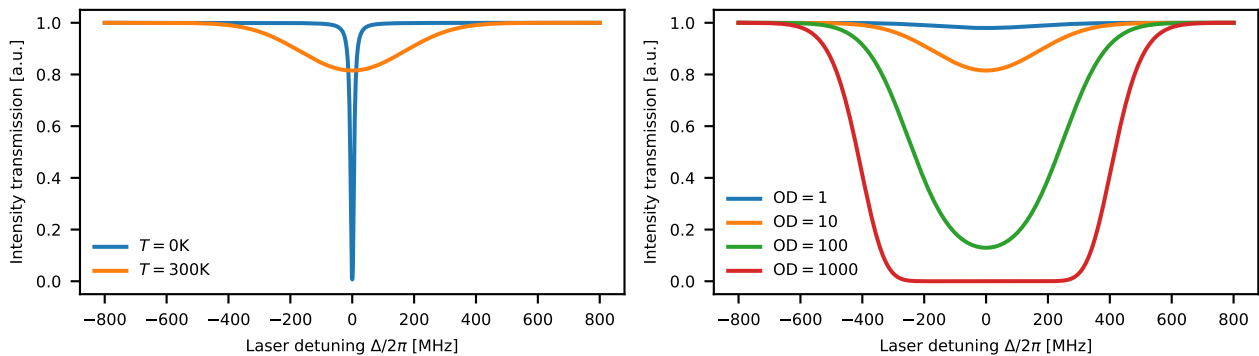


Figure E.2: Optical absorption spectrum. The absorption profile for an ensemble with $od = 10$, and $T = 0\text{K}$ and $T = 300\text{K}$ (left); the blue curve reaches $\sim 7 \times 10^{-3}$ at $\Delta = 0$. The transmission profile for Doppler broadened atomic ensemble of various od 's (right). We have used $\gamma/2\pi = 5.2\text{MHz}$ and $\Gamma_D/2\pi = 376\text{MHz}$.

The optical field, as given in equation (E.21), becomes

$$\begin{aligned} c \frac{d}{dz} a &\sim -\rho g_0^2 A_B \frac{2i}{\sigma_D} D_+(b) a \\ &\sim -\rho g_0^2 A_B \frac{i}{\Delta + i\gamma/2} a \\ &\sim -\rho g_0^2 A_B \frac{\gamma}{\Delta^2} a, \end{aligned}$$

such that the intensity, in the far detuned case, as in the case for non-moving atoms, is attenuated by

$$od_{\text{hot, far detuned}} = od \frac{(\gamma/2)^2}{\Delta^2}. \quad (\text{E.28})$$

Comparing equations (E.27) and (E.28), the far detuned optical depth is equivalent for cold and hot ensembles. Not only that, as we rewrite the expression for the optical depth in terms of the coupling parameters, obtaining

$$od_{\text{far detuned}} = od \frac{(\gamma/2)^2}{\Delta^2} = \rho \frac{(\gamma/2)^2}{\Delta^2} \frac{3\lambda^2}{2\pi} l_z = \rho \sigma_{\text{Cs, far detuned}} l_z$$

which, also matches with (Jackson, 1999) for off-resonant scattering.

Due to motion, the absorption spectrum is a convolution of a Gaussian and a Lorentzian process, as shown in equation (E.18). In the limit of $\Gamma_D \ll \gamma$, limit which our cesium ensemble fulfils, the Gaussian process dominates the absorption lineshape, see Figure E.2. In this figure, we have plotted the equations (E.23) and (E.26)

$$\begin{aligned} \frac{n(L_z)}{n(0)} &= e^{-od L(\Delta)} && \text{for cold atoms} \\ \frac{\hat{n}(L_z)}{\hat{n}(0)} &= e^{-od \frac{\gamma \sqrt{\pi \log^2}}{\gamma_D} G(\Delta)} && \text{for hot atoms,} \end{aligned} \quad (\text{E.29})$$

in which $G(\Delta)$ is the Gaussian profile as

$$G(\Delta) = e^{-4 \log^2(\Delta/\gamma_D)^2}.$$

Note that even significant σ 's do not lead to a strong absorption on resonance for Doppler broadened ensembles.

The results presented above, although using the parameter values for a cesium ensemble, do not contain the various complexities of the alkali atomic structure. We point to (Seltzer, 2008, Chapter 2) for discussing on optical line-shapes of alkali atoms.

Appendix F

Connection with pulsed experiments

Historically, a great part of the experiments realized at QUANTOP was set in quite different manner to the ones described in this document. Apart from the constituent systems — most of the experiments employed two vapour cells, we have substituted one of the cells with a mechanical oscillator — the experimental differences are many: (i) vapour cell geometry, (ii) time scales and (iii) state preparation stage. For comparison, in the historical experiments, the total spin decay rate was on the order $\gamma_S/2\pi \sim 100$ Hz and $\omega_S/2\pi = 325$ kHz. In experiments presented in this thesis, $\gamma_S/2\pi \sim 1$ kHz and $\omega_S/2\pi \sim 1.3$ MHz. On the theory side, the main light-matter coupling strength used the parameter κ^2 (Sherson, 2006; Hammerer, 2006).

In this Appendix, we relate the two approaches, linking κ^2 to the readout rate Γ_S , and κ^2 to the ratio of quantum back action to intrinsic atomic noise.

F.1 Modelling

We focus on the case of QND coupling and disregard losses and atomic motion, for simplicity. As the standard description, we will have the spin ensemble in a transverse magnetic field, probed with a far detuned probing laser via Faraday rotation. The total Hamiltonian is

$$\hat{H} = \frac{\omega_S}{2}(\hat{X}_S^2 + \hat{P}_S^2) + 2a\hat{X}_S\hat{X}_L, \quad (\text{F.1})$$

for $a^2/2\pi = a_1^2 S_x J_x$ as the coupling rate. Notice that the choice of coupling parameter as a is to match the input-output relations defined in (Julsgaard, 2003; Sherson, 2006). The extra factor of 2 is due to the chosen light quadratures commutation relation $[\hat{X}_L, \hat{P}_L] = 1/2$. As the total measured noise does not depend on the definition of commutators, the final result will match. About the sign of ω_S , we are going to deal with only one oscillator and the effective mass of the oscillator plays no fundamental role. It is here assumed to be positive.

We proceed by going to a rotating frame at frequency ω_S . Choosing $\hat{T} = \omega_S(\hat{X}_S^2 + \hat{P}_S^2)/2$ as the rotation kernel according to the procedure described in Appendix A, (F.1) becomes

$$\hat{H}_{\text{int}} = 2a(\hat{X} \cos \omega_S t + \hat{P} \sin \omega_S t)\hat{X}_S. \quad (\text{F.2})$$

The transformation is exact and solely removes the rotation between the canonical variables. In this frame, the time evolution of the spin operators

$$\begin{aligned} \frac{d}{dt}\hat{X}_S &= 2a\hat{X}_L \sin \omega_S t - \gamma_S \hat{X}_S/2 + \hat{F}_X \\ \frac{d}{dt}\hat{P}_S &= -2a\hat{X}_L \cos \omega_S t - \gamma_S \hat{P}_S/2 + \hat{F}_P \end{aligned} \quad (\text{F.3})$$

and quadrature operators

$$\begin{aligned}\frac{d}{dz}\hat{X}_L &= 0 \\ \frac{d}{dz}\hat{P}_L &= a(\hat{X}_S \cos \omega_S t + \hat{P}_S \sin \omega_S t),\end{aligned}\tag{F.4}$$

for γ_S and \hat{F}_X, \hat{F}_P as the decay and associated Langevin forces. In this frame, \hat{X}_S and \hat{P}_S evolve independently from each other and the cosine (sine) light quadratures of the light couple to a given spin component.

To simplify the manipulation of results, one might rewrite the system dynamics in the matrix formalism

$$\frac{d}{dt}\hat{R}_S = -\gamma\hat{R}_S/2 + 2aM\hat{R}_L + \hat{F}_S,\tag{F.5}$$

for the vectors

$$\hat{R}_S = \begin{bmatrix} \hat{X}_S \\ \hat{P}_S \end{bmatrix} \quad M = \begin{bmatrix} \sin \omega_S t & 0 \\ -\cos \omega_S t & 0 \end{bmatrix}\tag{F.6}$$

$$\hat{R}_L = \begin{bmatrix} \hat{X}_L \\ \hat{P}_L \end{bmatrix} \quad \hat{F}_S = \begin{bmatrix} \hat{F}_X \\ \hat{F}_P \end{bmatrix}.\tag{F.7}$$

Solving for the light variables in (F.4), the input-output relations are

$$\begin{aligned}\hat{X}_L^{\text{out}} &= \hat{X}_L^{\text{in}} \\ \hat{P}_L^{\text{out}} &= \hat{P}_L^{\text{in}} + a(\hat{X}_S \cos \omega_S t + \hat{P}_S \sin \omega_S t) = \hat{P}_L^{\text{in}} + aN\hat{R}_S\end{aligned}\tag{F.8}$$

for

$$N = \begin{bmatrix} \cos \omega_S t & \sin \omega_S t \end{bmatrix}.\tag{F.9}$$

From here on we proceed to solve (F.5) and (F.8) on different regimes.

The experiments were ran in a preparation-measurement scheme by implying pulsed laser drive. Given the timescales hierarchy, operating with pulses with duration $T \gg \gamma_S$ was feasible; this case will be discussed first. We will then proceed to include the effects of decoherence, closing the connection with the hybrid experiments. The measurement procedure involves demodulating the detected light and calculating the variance of the recorded results.

F.2 Faster than (bad) decoherence

If experiments are run in a time scale T much faster than any decoherence time scales, we can show that, to the first order, we can set $\gamma = 0$ and disregard the corresponding bath coupling. In this limit, (F.5) is vastly simplified. Given the importance role decoherence plays in a typical experiment, we show in the next section that the results here derived hold in the limit of fast readout ($T \gg \gamma$) and high coupling strength ($\kappa^2 \gg 1$).

Back to derivation. We start by solving (F.5) for zero decay and respective Langevin force

$$\hat{R}_S(t) = \hat{R}_S^{\text{in}} + 2a \int_0^t M(s)\hat{R}_L(s)ds,$$

with $\hat{R}_S^{\text{in}} = \hat{R}_S(0)$ as the initial conditions for the spin variables. Using (F.6), the output phase quadrature of light (F.8) is

$$\hat{P}_L^{\text{out}}(t) = \hat{P}_L^{\text{in}}(t) + aN\hat{R}_S^{\text{in}} + 2a^2 \int_0^t ds \hat{X}_L^{\text{in}}(s) \sin \omega_S(s-t).\tag{F.10}$$

Although in a different form, the detected light field contributions should be familiar at this point; from left to right, they are: detection shot noise, intrinsic atomic noise and light induced noise, respectively.

The detection procedure involves demodulation of the detected signal with a variable frequency ω and phase ϕ , the sometimes called *electronic quadratures*, giving us access to the slowly varying fluctuations \hat{X}_S and \hat{P}_S . As an example, for a detected signal $i(t)$, by demodulating the output phase quadrature we mean

$$\hat{p}_\phi^{\text{out}} \equiv \hat{p}_\phi^{\text{out}}(T) = \sqrt{\frac{2}{T}} \int_0^T dt i(t) \cos(\omega t + \phi), \quad (\text{F.11})$$

that is, the detected signal $i(t) \propto \hat{P}_L^{\text{out}}(t)$ is mixed with a sinusoidal function and integrated for a time T . Importantly, the condition $T\omega_S/2\pi \gg 1$ ensures that only the fluctuations around ω are contributing¹. Given the choice of ϕ , two orthogonal electronic quadratures are possible, \hat{p}_0^{out} and $\hat{p}_{\pi/2}^{\text{out}}$. In the case of $a^2 \ll \omega_0$, the two contributions are identical.

Applying the demodulation procedure to (F.10) for $\omega = \omega_S$ and $\phi = 0$,

$$\begin{aligned} \hat{p}_0^{\text{out}} &= \hat{p}_0^{\text{in}} + a \sqrt{\frac{2}{T}} \int_0^T dt \cos \omega_S t \left(\hat{X}_S^{\text{in}} \cos \omega_S t + \hat{P}_S^{\text{in}} \sin \omega_S t \right) \\ &\quad + 2a^2 \sqrt{\frac{2}{T}} \int_0^T dt \int_0^t ds \hat{X}_L^{\text{in}}(s) \cos \omega_S t \sin \omega_S (s - t) \\ &= \hat{p}_0^{\text{in}} + a \sqrt{\frac{T}{2}} \hat{X}_S^{\text{in}} \\ &\quad + a^2 \sqrt{\frac{2}{T}} \int_0^T ds \hat{X}_L^{\text{in}}(s) (T - s) \sin \omega_S s. \end{aligned} \quad (\text{F.12})$$

In the last passage, in the integral $\propto a^2$, we have interchanged the integration order

$$\int_0^T dt \int_0^t ds \rightarrow \int_0^T ds \int_s^T dt,$$

and integrated over t .

We are interested in the noise power of the detected light, that is, the variance of p_0^{out} . Given the correlation functions for light prepared in its minimum variance state

$$\langle \hat{X}_L^{\text{in}}(t) \hat{X}_L^{\text{in}}(t') \rangle = \langle \hat{P}_L^{\text{in}}(t) \hat{P}_L^{\text{in}}(t') \rangle = \frac{1}{4} \delta(t - t'), \quad (\text{F.13})$$

atoms in a state with initial occupation $\langle (\hat{X}_S^{\text{in}})^2 \rangle = \langle (\hat{P}_S^{\text{in}})^2 \rangle = n_S^{\text{in}} + \frac{1}{2}$, and that all other correlation functions are zero, we can calculate the variance of (F.12). For example, if the mean is null, $\langle p_0^{\text{out}} \rangle = 0$, the contribution of the input light noise \hat{p}_0^{in} is

$$\begin{aligned} \langle (\hat{p}_0^{\text{in}})^2 \rangle &= \left\langle \left(\sqrt{\frac{2}{T}} \int_0^T dt \hat{P}_L^{\text{in}}(t) \cos \omega_S t \right) \left(\sqrt{\frac{2}{T}} \int_0^T dt' \hat{P}_L^{\text{in}}(t') \cos \omega_S t' \right) \right\rangle \\ &= \frac{1}{2T} \int_0^T \cos^2 \omega_S t \sim \frac{1}{4}, \end{aligned}$$

in which we have used the property that input light is delta correlated and $T\omega_S/2\pi \gg 1$. The remaining terms in (F.12) are calculated in similar procedure. The back-action term is

$$\begin{aligned} \left\langle \left(a^2 \sqrt{\frac{2}{T}} \int_0^T ds \hat{X}_L^{\text{in}}(s) (T - s) \sin \omega_S s \right)^2 \right\rangle &= \frac{2a^4}{4T} \int_0^T ds (T - s)^2 \sin^2 \omega_S s \\ &\sim \frac{1}{4} \frac{2a^4 T^2}{6}. \end{aligned}$$

¹The more restrictive condition $T\omega_S/2\pi = m \gg 1$ can also be used to suppress harmonic contributions. Alternatively, for best estimation of the atomic state, different filter functions can be — and certainly are — employed in other scenarios (Krauter, 2011; Jensen, 2011). For simplicity, we comply to the standard choice.

Having calculated all Eq. (F.12) contributions, the total detected noise in the output phase quadrature (F.12), for the oscillator prepared in its ground state $n_S^{\text{in}} = 0$, is

$$\begin{aligned} \langle (p_0^{\text{out}})^2 \rangle &= \frac{1}{4} \left(1 + a^2 T + \frac{a^4 T^2}{3} \right) \\ &= \frac{1}{4} \left(1 + \kappa^2 + \frac{\kappa^4}{3} \right), \end{aligned} \quad (\text{F.14})$$

for $\kappa^2 \equiv a^2 T$ as the dimensionless coupling constant. This classic result shows that the ratio of back-action induced noise to the ground state noise is

$$\frac{\text{QBA}}{\text{PN}} = \frac{\kappa^2}{3}. \quad (\text{F.15})$$

Therefore, comparing to the quantum cooperativity language, a quantum back action to thermal noise ratio of 1, that is $C_q = 1$, corresponds to $\kappa^2 = 3$.

F.3 Including decoherence

We proceed to include the effects of coupling to the environment by considering the effect of decay, γ , and forces, \hat{F} . In this limit, (F.5) is a first order differential equation with constant coefficients (see Appendix A), whose solution is

$$\hat{R}_S(t) = e^{-\gamma t/2} \hat{R}_S^{\text{in}} + \int_0^t ds e^{\gamma(s-t)/2} \left(2aM(s) \hat{R}_L^{\text{in}}(s) + \hat{F}(s) \right). \quad (\text{F.16})$$

This equation points out that as time progresses, the atomic variables convolutes the optical \hat{X}_S^{in} and thermal \hat{F} forces with an exponential kernel; spectrally, forces centred at ω_S are filtered with width γ . The first term in (F.16) shows that the initial atomic state is read out with characteristic rate γ .

The optical signal (F.8), using the definitions (F.6), carries the information about the spin variables (F.16) as

$$P_L^{\text{out}}(t) = P_L^{\text{in}}(t) \quad (\text{F.17})$$

$$+ ae^{-\gamma t/2} \left(\hat{X}_S^{\text{in}} \cos \omega_S t + \hat{P}_S^{\text{in}} \sin \omega_S t \right) \quad (\text{F.18})$$

$$+ 2a^2 \int_0^t ds e^{\gamma(s-t)/2} \hat{X}_L^{\text{in}}(s) \sin \omega_S(s-t) \quad (\text{F.19})$$

$$+ a \int_0^t ds e^{\gamma(s-t)/2} \left(\hat{F}_X(s) \cos \omega_S s + \hat{F}_P(s) \sin \omega_S s \right). \quad (\text{F.20})$$

Although lengthier, this equation is similar to (F.10). The contributions are shot noise, input state noise, light induced and Langevin bath forces, respectively.

As in the previous section, we demodulate P_L^{out} with frequency ω_S and phase ϕ . The correlation for input light and atomic states are defined in (F.13). The inclusion of the Langevin forces requires us to define the bath induced correlations. For an environment with thermal occupation n_S , we have

$$\langle \hat{F}_X(t) \hat{F}_X(t') \rangle = \langle \hat{F}_P(t) \hat{F}_P(t') \rangle = \gamma(n_S + 1/2) \delta(t - t').$$

We proceed to calculate the detected variances. The contributions (F.17) and (F.18) are straightforward when plugging in the corresponding input variances. The effect of backaction and thermal bath, (F.19) and (F.20), respectively, have

the same functional shape. As an example, for the initial state (F.18) and back-action contribution (F.19), multiplying the expression by itself and using the input noise values we get to

$$\begin{aligned} \text{shot noise} &= \frac{1}{4} \\ \text{initial state} &= \frac{2a^2(2n_S^{\text{in}} + \frac{1}{2})}{\gamma} h(\gamma T) \\ \text{back action} &= \frac{a^4}{\gamma^2} g(\gamma T) \\ \text{thermal} &= \frac{2a^2(n_S + \frac{1}{2})}{\gamma} g(\gamma T), \end{aligned}$$

for the envelope functions

$$\begin{aligned} g(x) &= \frac{x + 4e^{-x/2} - e^{-x} - 3}{x} \\ h(x) &= \frac{1 + e^{-x} - 2e^{-x/2}}{x}. \end{aligned}$$

The functional dependence of these expressions is presented in Fig.F.1.

We study the noise contributions in the short and long time limit. For normalized time scale

- $\gamma T \ll 1$: the dynamics of interest are happening faster than the decoherence rate. In this limit (F.17) is reduced to

$$\langle (p_0^{\text{out}})^2 \rangle = \frac{1}{4} \left[1 + 2a^2 T (2n_S^{\text{in}} + 1) + \left(a^4 + a^2 \gamma (2n_S + 1) \right) \frac{T^2}{3} \right].$$

For a bath and initial state with null occupation, $n_S^{\text{in}} = n_S = 0$, in the limit of strong probe induced influence $a^2/\gamma = \Gamma_S/\gamma \gg 1$, we recover (F.14).

- $\gamma T \gg 1$: we get to the steady state limit, that is, when the initial state contribution is forgotten. A close inspection on Fig F.1 shows that this contribution is negligible for $\gamma^{-1} \sim T/50$. In this limit, the variance is

$$\langle (p_0^{\text{out}})^2 \rangle = \frac{1}{4} \left[1 + \frac{4a^2(2n_S + 1)}{\gamma} + \frac{4a^4}{\gamma^2} \right],$$

which looks like the function for the integrated spin noise spectrum. Using $a^2/\gamma = \Gamma_S/\gamma = C_q$, and setting $n_S = 0$, the total noise is

$$\frac{1}{4} \left[1 + 4C_q + 4C_q^2 \right]. \quad (\text{F.21})$$

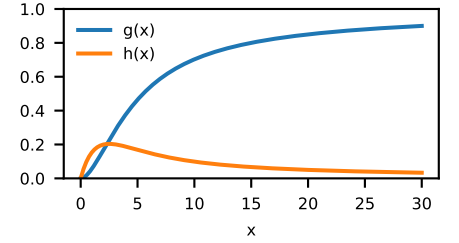


Figure F.1: Temporal dependence of the noise with integration time. (blue) initial condition, (yellow) convoluted forces and (green) sum of the previous curves.

Appendix G

Unshielded measurements

In this chapter we describe the vapor cell characterization measurements performed in unshielded environment, that is, the cell was not positioned inside a magnetically shielded volume. Characterizing the vapor cell outside the shielding makes the whole procedure of alignment and corresponding debugging much easier. More importantly, as we have discussed on Chapter 3, the coherence time performance of small volume encapsulated cells in unaltered, regardless of being measured in a shielded environment or not. Here, we derive the Free Induction Decay (FID) signal, present the coherence time measurement of a cubic vapor cell with sidelength 5 mm and discuss the results.

The transverse coherence time is extracted from the a single-shot Free Induction Decay (FID) signal. Due to environment time dependent magnetic fields, multiple realizations are not phase coherent and the signal averages out to zero; given this uncontrolled variation, the MORS method described in Chapter 5 is not applicable here. We note that although averaging is not possible, the time dependent magnetic field does not, by its own, lead to an increased decoherence rate, as long it is homogenous across the ensemble.

In a FID experiment, we observe the decay of the transverse spin components. On the light of description presented on Chapters 5 and 6, the ensemble is prepared in a state with non-zero spin polarization via optical pumping. A short and weak RF pulse induces a small transverse magnetization, rotating the magnetization vector from its equilibrium position. The spins time evolution after the RF drive, ie for $A = 0$, in the rotating frame at the Larmor frequency, is given by equation (6.5) and reproduced here

$$\frac{d}{dt} \begin{bmatrix} F_x(t) \\ F_y(t) \\ F_z(t) \end{bmatrix} = \begin{bmatrix} -\gamma_1 & & \\ & -\gamma_2 & \\ & & -\gamma_2 \end{bmatrix} \begin{bmatrix} F_x(t) \\ F_y(t) \\ F_z(t) \end{bmatrix}. \quad (\text{G.1})$$

We consider here that the probe laser is weak enough to disregard the effect of power broadening and backaction, that is, γ_2 is limited by decoherence in the dark and $\Gamma_S \ll \gamma_2$. The decay rates $\gamma_1 = \pi/T_1$ and $\gamma_2 = \pi/T_2$ lump all the processes that induce population and coherence damping. We also note that T_2 is intrinsically limited by T_1 , as $1/T_2 = 1/2T_1 + 1/T_\phi$, with T_ϕ as the contribution from dephasing. The weak probe beam measures the spin components as

$$S_y^{\text{out}} \propto g S_x^{\text{in}} (F_z \cos \omega_d t + F_y \sin \omega_d t), \quad (\text{G.2})$$

for g as the light-matter coupling. The spins and the probing polarization are prepared as $\vec{F}(0) = (F_{x0}, 0, F_{z0})$ and $\vec{S}(0) = (S_x^{\text{in}}, 0, 0)$. The equation (G.1), in the matrix form, has solution

$$\frac{d}{dt} \vec{J}(t) = \mathbf{M} \vec{J}(t) \quad (\text{G.3})$$

$$\vec{J}(t) = e^{\mathbf{M}t} \vec{J}(0), \quad (\text{G.4})$$

in which \mathbf{M} is the matrix of coefficients from (G.1). Given the input spin state, the spin components evolve as

$$\begin{bmatrix} F_x(t) \\ F_y(t) \\ F_z(t) \end{bmatrix} = \begin{bmatrix} F_{x0}e^{-\gamma_1 t} \\ 0 \\ F_{z0}e^{-\gamma_2 t} \end{bmatrix}. \quad (\text{G.5})$$

From equation (G.2), the expected optical signal is a sinusoidal function, decaying with an exponential envelope.

The unshielded measurement procedure is similar to the MORS presented in Chapter 5. The cell is positioned in the center of a Helmholtz coil pair; this coil will be generating an oscillating magnetic field close to the natural spin precession frequency. The cell is optically pumped and probed by a far-detuned ($\Delta/2\pi = 3\text{GHz}$), weak probe beam (with $\sim 5\mu\text{W}$). Optimal detection maximizes the signal to noise ratio of the Faraday rotation, which requires aligning the optical pumping direction with the average static magnetic field and probing in a direction orthogonal to that. A section of the detected signal is shown in Figure G.1.

The lasers are run continuously and the RF excitation is turned on for about $\sim 0.5\text{ms}$. The RF magnetic field is a sine wave with frequency ω_d and amplitude A . In our geolocation, the Earth's magnetic field magnitude is $\approx 0.5\text{G}$, leading to a Larmor frequency $\omega_S \sim 175\text{kHz}$; nonetheless, the presence of magnetic materials close by lead to a reduced field, as shown by the $\sim 95\text{kHz}$ observed oscillation frequency, see Figure G.2.

The envelope of the decay signal is an exponential with time constant $T_2 = 15\text{ms}$. The fast oscillations, nonetheless, do not have a single frequency component. Fitting a sine wave to chunks of signal presented in Figure G.1, with amplitude and frequency as free parameters, we can observe the time dependent magnetic field frequency modulating the spin response, see Figure G.2 (left). The $\sim 1\text{kHz}$ frequency swing has a periodic time dependence. In Figure G.2 (right), we show the spectral composition of the measured Larmor frequency. The main components are at 50Hz and harmonics, demonstrating that the spin ensemble is picking up the signal from nearby electronic components.

Finally, notice that the signal to noise ratio on G.2 (left) would allow to use such cell as a sensor for the ambient magnetic field, being able to resolve changes on the order of 0.1kHz or, equivalently, 30nT , within a couple of ms.

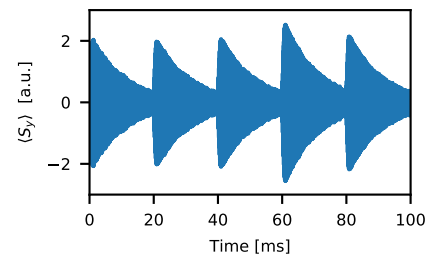


Figure G.1: Single-shot unshielded FID signal. At every 20 ms, a short RF pulse excites the spin ensemble, leading to a non-zero polarimeter $\langle \hat{S}_y \rangle$ signal. The presented signal has not been averaged, only bandpass filtered around 95kHz with 5kHz 3dB width. The coherence time observed is $T_2 = 15\text{ms}$.

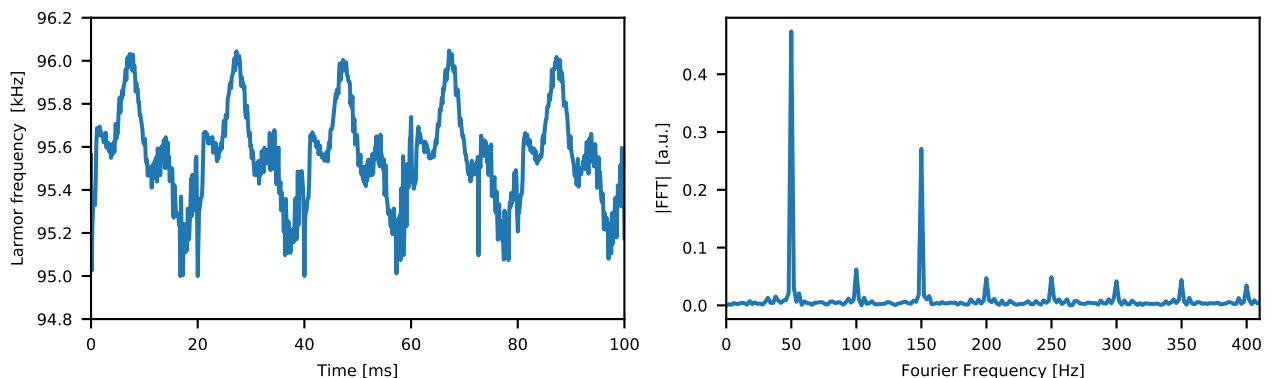


Figure G.2: Time dependent Larmor frequency. We fit a sine wave to 1 ms chunks of signal presented in Figure G.1, extracting the oscillation frequency. The periodic nature tells us that the mean magnetic field is evolving with time. Spectral analysis of the . Contribution of 50Hz and harmonics reveals the effect of magnetic fields from equipments and electrical line.

Appendix H

Cesium vapor density

For estimating the alkali density in a room temperature container, a common procedure is to model the vapor as an ideal gas, following the *ideal gas law*

$$PV = nRT,$$

for a given pressure P in atm, volume V in L and temperature T in K. In this formulation, the ideal gas constant is $R \sim 0.082 \text{ atmLK}^{-1}/\text{mol}$, and the number of particles n is given in mol. With the Avogadro constant, the atomic density n/V (in terms of particles per m^3) is

$$\frac{n}{V} = 7.34 \times 10^{27} \frac{P}{T} \sim 10^{27.866} \frac{P}{T}. \quad (\text{H.1})$$

As described by Alcock et al.¹, the saturated cesium vapor pressure for a temperature T is

$$\begin{aligned} \log_{10} P &= A - BT^{-1} \\ P &= 10^{A-BT^{-1}}. \end{aligned} \quad (\text{H.2})$$

in which the values for A and B are presented in Table H.1, which also depend on the temperature (the solid-liquid transition happens at 28.5°C). The accuracy of the model above is $\pm 5\%$ in the range of temperature $298 - 550 \text{ K}$ (Steck, 2019).

Combining (H.1) and (H.2), the temperature dependence of the Cesium density is given by

$$\rho_{\text{Cs}} = \frac{1}{T} 10^{27.866+A-B/T},$$

and presented in Figure H.1.

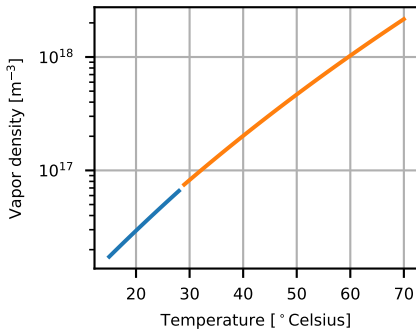


Figure H.1: Cesium density as a function of temperature. Blue (yellow) curve for solid (liquid) cesium phase.

Parameter	State of matter	
	Solid	Liquid
A	4.711	4.165
B	3999	3830

¹A similar expression is presented in (Seltzer, 2008, p. 238)

Table H.1: A and B parameters for Cesium.

Appendix I

Experimental parameters

Here we present a summary of the experimental parameters extracted from modelling the hybrid in the 2017 and in the 2020 runs.

Parameter	Symbol	Value
Atomic spin oscillator		
Decoherence rate in the dark	$\gamma_{S0,\text{dark}}/2\pi$	1 kHz
Intrinsic linewidth	$\gamma_{S0}/2\pi$	4.8/4.2 kHz
Effective dynamical linewidth	$\gamma_{S,\text{dyn}}/2\pi$	0.4 kHz
Total linewidth	$\gamma_S/2\pi$	5.2/4.6 kHz
Tensor contribution	ζ_S	0.02
LO ₁ driving power		1.7-1.5 mW
Readout rate	$\Gamma_S/2\pi$	23-21 kHz
Spin Polarisation	p	0.6
Spin thermal occupancy	n_S	1.7
Microcell single pass optical losses	$\eta_{\text{microcell}}$	13%
Microcell temperature		65°C
Mechanical oscillator and cavity		
Intrinsic mechanical frequency	$\omega_{M0}/2\pi$	1.28 MHz
Intrinsic damping rate	$\gamma_{M0}/2\pi$	100 mHz
Optical damping rate	$\gamma_M/2\pi$	5.6-5.4 kHz
Cavity detuning	$\Delta/2\pi$	-4.7 MHz
Total cavity linewidth	$\kappa/2\pi$	17.4/15.4 MHz
LO ₂ drive power		54/38 μ W
Intracavity photons	N	$5.8 \times 10^6 / 4.4 \times 10^6$
Single photon coupling rate	$g_0/2\pi$	150 Hz
Cavity overcoupling	$\kappa_{\text{in}}/\kappa$	0.96
Thermal bath temperature	T	7 K
Bath occupancy	n_{M0}	114×10^3
Mean occupancy	n_M	2
Quantum cooperativity	C_q^M	2.6/2.2
Hybrid & detection		
Quantum efficiency between systems	ν	0.45
Cavity mode-matching (amplitude)		0.89
Power transmission between systems		0.62
Detection efficiency	η	0.65/0.67
Homodyning visibility		0.89
Power transmission and detector QE		0.74/.76
LO ₁ – LO ₂ phase	φ	0/6°

Table I.1: Summary of notation and experimental parameters for the experiments in (Møller et al., 2017) and discussed in Chapter 10.

Parameter	Symbol	Value
Atomic spin oscillator		
Decoherence rate in the dark	$\gamma_{S0,\text{dark}}/2\pi$	450 Hz
Intrinsic linewidth	$\gamma_{S0}/2\pi$	1.7 kHz
Effective dynamical linewidth	$\gamma_{S,\text{dyn}}/2\pi$	1.2 kHz
Effective linewidth (incl. dynamical damping)	$\gamma_S/2\pi$	2.9 kHz
Tensor contribution	ζ_S	0.028
LO ₁ driving power		350 μ W
Readout rate	$\Gamma_S/2\pi$	20 kHz
Spin Polarisation	p	0.82
Spin thermal occupancy	n_S	0.8
Microcell single pass optical losses	$\eta_{\text{microcell}}$	4%
Microcell temperature		50°C
Mechanical oscillator and cavity		
Intrinsic mechanical frequency	$\omega_{M0}/2\pi$	1.370 MHz
Intrinsic damping rate	$\gamma_{M0}/2\pi$	2.1 mHz
Optical damping rate	$\gamma_M/2\pi$	3.9 kHz
Cavity detuning	$\Delta/2\pi$	-0.7 MHz
Total cavity linewidth	$\kappa/2\pi$	4.2 MHz
LO ₂ drive power		$\sim 8 \mu$ W
Intracavity photons	N	1.6×10^6
Single photon coupling rate	$g_0/2\pi$	6×10^1 Hz
Readout rate	$\Gamma_M/2\pi$	15 kHz
Cavity overcoupling	$\kappa_{\text{in}}/\kappa$	0.93
Thermal bath temperature	T	11 K
Bath occupancy	n_{M0}	173×10^3
Mean occupancy	n_M	~ 2
Quantum cooperativity	C_q^M	15
Hybrid & detection		
Quantum efficiency between systems	ν	0.53
Cavity mode-matching (amplitude)		0.9
Power transmission between systems		0.8
Detection efficiency	η	0.77
Homodyning visibility		0.96
Power transmission and detector QE		0.87
LO ₁ – LO ₂ phase	φ	$\sim 180^\circ$
Detection phase	ϑ	2°

Table I.2: Summary of notation and experimental parameters for the experiments in (Thomas et al., 2020) and discussed in Chapters 10 and 11.

Bibliography

- Abbott, B. P. et al. (2016). Observation of gravitational waves from a binary black hole merger. *Phys. Rev. Lett.*, 116:061102. (page 3).
- Abragam, A. and Proctor, W. G. (1958). Spin temperature. *Phys. Rev.*, 109:1441–1458. (page 55).
- Abrarov, S. and Quine, B. (2014). Accurate approximations for the complex error function with small imaginary argument. *arXiv preprint arXiv:1411.1024*. (page 143).
- Alcock, C., Itkin, V., and Horrigan, M. (1984). Vapour pressure equations for the metallic elements: 298–2500k. *Canadian Metallurgical Quarterly*, 23(3):309–313. (page 154).
- Anderson, L. W. and Ramsey, A. T. (1963). Study of the spin-relaxation times and the effects of spin-exchange collisions in an optically oriented sodium vapor. *Phys. Rev.*, 132:712–723. (page 48).
- Appelt, S., Baranga, A. B.-A., Erickson, C. J., Romalis, M. V., Young, A. R., and Happer, W. (1998). Theory of spin-exchange optical pumping of ^3He and ^{129}Xe . *Phys. Rev. A*, 58:1412–1439. (pages 48, 51, 56).
- Appelt, S., Ben-Amar Baranga, A., Young, A. R., and Happer, W. (1999). Light narrowing of rubidium magnetic-resonance lines in high-pressure optical-pumping cells. *Phys. Rev. A*, 59:2078–2084. (page 51).
- Aspect, A., Grangier, P., and Roger, G. (1981). Experimental tests of realistic local theories via bell’s theorem. *Phys. Rev. Lett.*, 47:460–463. (page 3).
- Aspelmeyer, M., Kippenberg, T. J., and Marquardt, F. (2014). Cavity optomechanics. *Rev. Mod. Phys.*, 86:1391–1452. (pages 4, 11).
- Atoneche, F. and Kastberg, A. (2017). Simplified approach for quantitative calculations of optical pumping. *European Journal of Physics*, 38(4):045703. (page 50).
- Baker, C. G. and Bowen, W. P. (2017). Precision measurement: Sensing past the quantum limit. *Nature*, 547(7662):164–165. (page 9).
- Balabas, M. V., Jensen, K., Wasilewski, W., Krauter, H., Madsen, L. S., Müller, J. H., Fernholz, T., and Polzik, E. S. (2010a). High quality anti-relaxation coating material for alkali atom vapor cells. *Opt. Express*, 18(6):5825–5830. (page 42).
- Balabas, M. V., Karaulanov, T., Ledbetter, M. P., and Budker, D. (2010b). Polarized alkali-metal vapor with minute-long transverse spin-relaxation time. *Phys. Rev. Lett.*, 105:070801. (pages 41, 96).
- Bao, H., Duan, J., Jin, S., Lu, X., Li, P., Qu, W., Wang, M., Novikova, I., Mikhailov, E. E., Zhao, K.-F., et al. (2020). Spin squeezing of 10 11 atoms by prediction and retrodiction measurements. *Nature*, 581(7807):159–163. (page 113).

Bibliography

- Barg, A. (2018). *Optomechanics with soft-clamped silicon nitride membranes and carrier-mediated forces in coupled quantum wells*. PhD thesis, University of Copenhagen. (pages v, 14, 15, 42).
- Bariani, F., Seok, H., Singh, S., Vengalattore, M., and Meystre, P. (2015). Atom-based coherent quantum-noise cancellation in optomechanics. *Phys. Rev. A*, 92:043817. (page 8).
- Bell, J. S. (1964). On the einstein podolsky rosen paradox. *Physics Physique Fizika*, 1:195–200. (page 108).
- Bennett, C. H., Brassard, G., Crépeau, C., Jozsa, R., Peres, A., and Wootters, W. K. (1993). Teleporting an unknown quantum state via dual classical and einstein-podolsky-rosen channels. *Phys. Rev. Lett.*, 70:1895–1899. (page 108).
- Black, E. D. (2001). An introduction to pound–drever–hall laser frequency stabilization. *American journal of physics*, 69(1):79–87. (page 98).
- Bohr, N. (1935). Can quantum-mechanical description of physical reality be considered complete? *Phys. Rev.*, 48:696–702. (pages 108, 110).
- Borregaard, J., Zugenmaier, M., Petersen, J. M., Shen, H., Vasilakis, G., Jensen, K., Polzik, E. S., and Sørensen, A. S. (2016). Scalable photonic network architecture based on motional averaging in room temperature gas. *Nature communications*, 7:11356. (pages 40, 68, 69, 142).
- Bose, S., Mazumdar, A., Morley, G. W., Ulbricht, H., Toroš, M., Paternostro, M., Geraci, A. A., Barker, P. F., Kim, M. S., and Milburn, G. (2017). Spin entanglement witness for quantum gravity. *Phys. Rev. Lett.*, 119:240401. (page 3).
- Bouchiat, M. A. and Brossel, J. (1966). Relaxation of optically pumped rb atoms on paraffin-coated walls. *Phys. Rev.*, 147:41–54. (page 3).
- Bowen, W. P., Schnabel, R., Bachor, H.-A., and Lam, P. K. (2002). Polarization squeezing of continuous variable stokes parameters. *Phys. Rev. Lett.*, 88:093601. (page 34).
- Braginsky, V. B., Khalili, F. Y., and Thorne, K. S. (1992). *Quantum Measurement*. Cambridge University Press. (page 8).
- Braginsky, V. B., Vorontsov, Y. I., and Thorne, K. S. (1980). Quantum nondemolition measurements. *Science*, 209(4456):547–557. (pages 4, 6).
- Brahms, N. and Stamper-Kurn, D. M. (2010). Spin optodynamics analog of cavity optomechanics. *Phys. Rev. A*, 82:041804. (pages 82, 86, 87).
- Broersen, P. M. T. (2006). *Automatic Autocorrelation and Spectral Analysis*. Springer-Verlag, Berlin, Heidelberg. (page 113).
- Brooks, D. W., Botter, T., Schreppler, S., Purdy, T. P., Brahms, N., and Stamper-Kurn, D. M. (2012). Non-classical light generated by quantum-noise-driven cavity optomechanics. *Nature*, 488(7412):476–480. (page 82).
- Brossel, J. and Bitter, F. (1952). A new "double resonance" method for investigating atomic energy levels. application to Hg^3p_1 . *Phys. Rev.*, 86:308–316. (page 3).
- Budker, D., Hollberg, L., Kimball, D. F., Kitching, J., Pustelny, S., and Yashchuk, V. V. (2005). Microwave transitions and nonlinear magneto-optical rotation in anti-relaxation-coated cells. *Phys. Rev. A*, 71:012903. (page 53).
- Buonanno, A. and Chen, Y. (2002). Signal recycled laser-interferometer gravitational-wave detectors as optical springs. *Phys. Rev. D*, 65:042001. (page 113).

- Camerer, S., Korppi, M., Jöckel, A., Hunger, D., Hänsch, T. W., and Treutlein, P. (2011). Realization of an optomechanical interface between ultracold atoms and a membrane. *Phys. Rev. Lett.*, 107:223001. (page 5).
- Carmichael, H. (1993). *An Open Systems Approach to Quantum Optics*. Springer, Berlin, Heidelberg. (page 113).
- Caves, C. M. (1980). Quantum-mechanical radiation-pressure fluctuations in an interferometer. *Phys. Rev. Lett.*, 45:75–79. (page 6).
- Chalupczak, W., Godun, R. M., Anielski, P., Wojciechowski, A., Pustelny, S., and Gawlik, W. (2012). Enhancement of optically pumped spin orientation via spin-exchange collisions at low vapor density. *Phys. Rev. A*, 85:043402. (page 50).
- Chalupczak, W., Josephs-Franks, P., Pustelny, S., and Gawlik, W. (2010). Optical–radio-frequency resonances free from power broadening. *Phys. Rev. A*, 81:013422. (page 42).
- Chan, J., Alegre, T. M., Safavi-Naeini, A. H., Hill, J. T., Krause, A., Gröblacher, S., Aspelmeyer, M., and Painter, O. (2011). Laser cooling of a nanomechanical oscillator into its quantum ground state. *Nature*, 478(7367):89–92. (page 4).
- Chen, J., Rossi, M., Mason, D., and Schliesser, A. (2020). Entanglement of propagating optical modes via a mechanical interface. *Nature communications*, 11(1):1–6. (page 109).
- Chou, C.-W., de Riedmatten, H., Felinto, D., Polyakov, S. V., Van Enk, S. J., and Kimble, H. J. (2005). Measurement-induced entanglement for excitation stored in remote atomic ensembles. *Nature*, 438(7069):828–832. (pages 3, 108).
- Christoph, P., Wagner, T., Zhong, H., Wiesendanger, R., Sengstock, K., Schwarz, A., and Becker, C. (2018). Combined feedback and sympathetic cooling of a mechanical oscillator coupled to ultracold atoms. *New Journal of Physics*, 20(9):093020. (page 5).
- Clauser, J. F., Horne, M. A., Shimony, A., and Holt, R. A. (1969). Proposed experiment to test local hidden-variable theories. *Phys. Rev. Lett.*, 23:880–884. (page 108).
- Clauser, J. F. and Shimony, A. (1978). Bell’s theorem. experimental tests and implications. *Reports on Progress in Physics*, 41(12):1881. (pages 5, 108).
- Clerk, A. A., Devoret, M. H., Girvin, S. M., Marquardt, F., and Schoelkopf, R. J. (2010). Introduction to quantum noise, measurement, and amplification. *Rev. Mod. Phys.*, 82:1155–1208. (page 114).
- Colangelo, G., Sewell, R. J., Behbood, N., Ciurana, F. M., Triginer, G., and Mitchell, M. W. (2013). Quantum atom–light interfaces in the gaussian description for spin-1 systems. *New Journal of Physics*, 15(10):103007. (page 25).
- Corsini, E. P., Karaulanov, T., Balabas, M., and Budker, D. (2013). Hyperfine frequency shift and zeeman relaxation in alkali-metal-vapor cells with antirelaxation alkene coating. *Phys. Rev. A*, 87:022901. (page 48).
- Danilishin, S. L. and Khalili, F. Y. (2012). Quantum measurement theory in gravitational-wave detectors. *Living Reviews in Relativity*, 15(1):5. (page 92).
- Davidovich, L. (1996). Sub-poissonian processes in quantum optics. *Rev. Mod. Phys.*, 68:127–173. (pages 6, 55).
- de Echaniz, S. R., Koschorreck, M., Napolitano, M., Kubasik, M., and Mitchell, M. W. (2008). Hamiltonian design in atom-light interactions with rubidium ensembles: A quantum-information toolbox. *Phys. Rev. A*, 77:032316. (page 31).

Bibliography

- Deutsch, I. H. and Jessen, P. S. (2010). Quantum control and measurement of atomic spins in polarization spectroscopy. *Optics Communications*, 283(5):681–694. (pages 29, 31, 47).
- Di Domenico, G., Bison, G., Groeger, S., Knowles, P., Pazgalev, A. S., Rebetez, M., Saudan, H., and Weis, A. (2006). Experimental study of laser-detected magnetic resonance based on atomic alignment. *Phys. Rev. A*, 74:063415. (page 31).
- Duan, L.-M., Giedke, G., Cirac, J. I., and Zoller, P. (2000). Inseparability criterion for continuous variable systems. *Phys. Rev. Lett.*, 84:2722–2725. (pages 10, 110).
- Duan, L.-M., Lukin, M. D., Cirac, J. I., and Zoller, P. (2001). Long-distance quantum communication with atomic ensembles and linear optics. *Nature*, 414(6862):413–418. (pages 2, 3).
- Dumont, V., Bernard, S., Reinhardt, C., Kato, A., Ruf, M., and Sankey, J. C. (2019). Flexure-tuned membrane-at-the-edge optomechanical system. *Opt. Express*, 27(18):25731–25748. (page 15).
- Durbin, J. (1960). The fitting of time-series models. *Revue de l'Institut International de Statistique*, pages 233–244. (page 119).
- Einstein, A., Podolsky, B., and Rosen, N. (1935). Can quantum-mechanical description of physical reality be considered complete? *Phys. Rev.*, 47:777–780. (pages 5, 10, 108, 110).
- Ekert, A. K. (1991). Quantum cryptography based on bell's theorem. *Phys. Rev. Lett.*, 67:661–663. (page 108).
- Fernholz, T., Krauter, H., Jensen, K., Sherson, J. F., Sørensen, A. S., and Polzik, E. S. (2008). Spin squeezing of atomic ensembles via nuclear-electronic spin entanglement. *Phys. Rev. Lett.*, 101:073601. (page 127).
- Feynman, R. P. (1982). Simulating physics with computers. *International Journal of Theoretical Physics*, 21(6/7). (page 108).
- Foot, C. (2005). *Atomic physics*. Oxford master series in physics. Oxford University Press. (page 29).
- Forward, R. L. (1978). Wideband laser-interferometer gravitational-radiation experiment. *Phys. Rev. D*, 17:379–390. (page 4).
- Franz, F. A. (1966). Relaxation mechanisms in optical pumping. *Phys. Rev.*, 141:105–112. (page 50).
- Franzen, W. and Emslie, A. G. (1957). Atomic orientation by optical pumping. *Phys. Rev.*, 108:1453–1458. (page 3).
- Fry, E. S. and Thompson, R. C. (1976). Experimental test of local hidden-variable theories. *Phys. Rev. Lett.*, 37:465–468. (page 108).
- Gammelmark, S., Julsgaard, B., and Mølmer, K. (2013). Past quantum states of a monitored system. *Phys. Rev. Lett.*, 111:160401. (page 113).
- Gehm, M. E. (2003). Properties of 6li. (page 137).
- Genes, C. and Dantan, A. (2017). Light-matter interactions in multi-element resonators. *Journal of Physics B: Atomic, Molecular and Optical Physics*, 50(10):105502. (page 14).
- Gerry, C. and Knight, P. (2004). *Introductory Quantum Optics*. Cambridge University Press. (page 6).

- Gigan, S., Böhm, H., Paternostro, M., Blaser, F., Langer, G., Hertzberg, J., Schwab, K. C., Bäuerle, D., Aspelmeyer, M., and Zeilinger, A. (2006). Self-cooling of a micromirror by radiation pressure. *Nature*, 444(7115):67–70. (page 82).
- Griffiths, D., Griffiths, P., and College, R. (1999). *Introduction to Electrodynamics*. Prentice Hall. (page 6).
- Hammerer, K. (2006). *Quantum Information Processing with Atomic Ensembles and Light*. PhD thesis, Technische Universität München. (pages 25, 147).
- Hammerer, K., Aspelmeyer, M., Polzik, E. S., and Zoller, P. (2009). Establishing einstein-poldosky-rosen channels between nanomechanics and atomic ensembles. *Phys. Rev. Lett.*, 102:020501. (pages 5, 94, 98, 109, 110, 127).
- Hammerer, K., Sørensen, A. S., and Polzik, E. S. (2010). Quantum interface between light and atomic ensembles. *Rev. Mod. Phys.*, 82:1041–1093. (pages 28, 31, 68, 112, 144).
- Happer, W. (1972). Optical pumping. *Rev. Mod. Phys.*, 44:169–249. (pages 3, 50, 51).
- Happer, W. and Van Wijngaarden, W. (1987). An optical pumping primer. *Hyperfine Interactions*, 38(1-4):435–470. (pages 50, 51).
- Harris, M. L., Adams, C. S., Cornish, S. L., McLeod, I. C., Tarleton, E., and Hughes, I. G. (2006). Polarization spectroscopy in rubidium and cesium. *Phys. Rev. A*, 73:062509. (page 39).
- Higginbotham, A. P., Burns, P. S., Urmev, M. D., Peterson, R. W., Kampel, N. S., Brubaker, B. M., Smith, G., Lehnert, K. W., and Regal, C. A. (2018). Harnessing electro-optic correlations in an efficient mechanical converter. *Nature Physics*, 14(10):1038–1042. (page 127).
- Horodecki, R., Horodecki, P., Horodecki, M., and Horodecki, K. (2009). Quantum entanglement. *Rev. Mod. Phys.*, 81:865–942. (page 108).
- Huang, X., Zeuthen, E., Vasilyev, D. V., He, Q., Hammerer, K., and Polzik, E. S. (2018). Unconditional steady-state entanglement in macroscopic hybrid systems by coherent noise cancellation. *Phys. Rev. Lett.*, 121:103602. (pages 5, 97, 110, 111, 112).
- Jackson, J. D. (1999). *Classical electrodynamics*. Wiley, New York, NY, 3rd ed. edition. (pages 37, 144, 145).
- Jayich, A. M., Sankey, J. C., Zwickl, B. M., Yang, C., Thompson, J. D., Girvin, S. M., Clerk, A. A., Marquardt, F., and Harris, J. G. E. (2008). Dispersive optomechanics: a membrane inside a cavity. *New Journal of Physics*, 10(9):095008. (pages 11, 14).
- Jensen, K. (2011). *Quantum Information, Entanglement and Magnetometry with Macroscopic Gas Samples and Non-Classical light*. PhD thesis, University of Copenhagen. (pages vi, 48, 149).
- Jensen, K., Budvytyte, R., Thomas, R. A., Wang, T., Fuchs, A. M., Balabas, M. V., Vasilakis, G., Mosgaard, L. D., Stærkind, H. C., Müller, J. H., et al. (2016). Non-invasive detection of animal nerve impulses with an atomic magnetometer operating near quantum limited sensitivity. *Scientific reports*, 6(1):1–7. (page v).
- Jensen, K., Wasilewski, W., Krauter, H., Fernholz, T., Nielsen, B. M., Owari, M., Plenio, M. B., Serafini, A., Wolf, M., and Polzik, E. (2011). Quantum memory for entangled continuous-variable states. *Nature Physics*, 7(1):13–16. (page 108).

Bibliography

- Jöckel, A., Faber, A., Kampschulte, T., Korppi, M., Rakher, M. T., and Treutlein, P. (2015). Sympathetic cooling of a membrane oscillator in a hybrid mechanical–atomic system. *Nature Nanotechnology*, 10(1):55–59. (page 5).
- Julsgaard, B. (2003). *Entanglement and Quantum Interactions with Macroscopic Gas Samples*. PhD thesis, University of Aarhus. (pages vi, 25, 26, 27, 29, 30, 31, 34, 48, 49, 66, 140, 147).
- Julsgaard, B., Kozhekin, A., and Polzik, E. S. (2001). Experimental long-lived entanglement of two macroscopic objects. *Nature*, 413(6854):400–403. (pages 3, 5, 108, 112).
- Julsgaard, B., Sherson, J., Cirac, J. I., Fiurášek, J., and Polzik, E. S. (2004). Experimental demonstration of quantum memory for light. *Nature*, 432(7016):482–486. (pages 3, 108).
- Julsgaard, B., Sherson, J., Sørensen, J., and Polzik, E. S. (2003). Characterizing the spin state of an atomic ensemble using the magneto-optical resonance method. *Journal of Optics B: Quantum and Semiclassical Optics*, 6(1):5. (pages 24, 47, 48).
- Jöckel, A., Rakher, M. T., Korppi, M., Camerer, S., Hunger, D., Mader, M., and Treutlein, P. (2011). Spectroscopy of mechanical dissipation in micro-mechanical membranes. *Applied Physics Letters*, 99(14):143109. (page 11).
- Karg, T. M., Gouraud, B., Ngai, C. T., Schmid, G.-L., Hammerer, K., and Treutlein, P. (2020). Light-mediated strong coupling between a mechanical oscillator and atomic spins 1 meter apart. *Science*. (page 5).
- Karg, T. M., Gouraud, B., Treutlein, P., and Hammerer, K. (2019). Remote hamiltonian interactions mediated by light. *Phys. Rev. A*, 99:063829. (page 5).
- Kastler, A. (1954). Les méthodes optiques d’orientation atomique et leurs applications. *Proceedings of the Physical Society. Section A*, 67(10):853. (page 3).
- Khalili, F. Y. and Polzik, E. S. (2018). Overcoming the standard quantum limit in gravitational wave detectors using spin systems with a negative effective mass. *Phys. Rev. Lett.*, 121:031101. (page 127).
- Kimble, H. J. (1998). Strong interactions of single atoms and photons in cavity qed. *Physica Scripta*, 1998(T76):127. (page 3).
- Kimble, H. J. (2008). The quantum internet. *Nature*, 453(7198):1023–1030. (page 2).
- Kimble, H. J., Dagenais, M., and Mandel, L. (1977). Photon antibunching in resonance fluorescence. *Phys. Rev. Lett.*, 39:691–695. (page 3).
- Kimble, H. J., Levin, Y., Matsko, A. B., Thorne, K. S., and Vyatchanin, S. P. (2001). Conversion of conventional gravitational-wave interferometers into quantum nondemolition interferometers by modifying their input and/or output optics. *Phys. Rev. D*, 65:022002. (page 8).
- Kippenberg, T. J., Rokhsari, H., Carmon, T., Scherer, A., and Vahala, K. J. (2005). Analysis of radiation-pressure induced mechanical oscillation of an optical microcavity. *Phys. Rev. Lett.*, 95:033901. (pages 18, 82).
- Kogelnik, H. and Li, T. (1966). Laser beams and resonators. *Applied optics*, 5(10):1550–1567. (page 83).
- Kohler, J., Gerber, J. A., Dowd, E., and Stamper-Kurn, D. M. (2018). Negative-mass instability of the spin and motion of an atomic gas driven by optical cavity backaction. *Phys. Rev. Lett.*, 120:013601. (pages 5, 82).
- Kohler, J., Spethmann, N., Schreppler, S., and Stamper-Kurn, D. M. (2017). Cavity-assisted measurement and coherent control of collective atomic spin oscillators. *Phys. Rev. Lett.*, 118:063604. (pages 82, 87).

- Kohler, J. L. (2018). *Optodynamical Measurement and Coupling of Atomic Motion and Spin*. PhD thesis, University of California. (page 16).
- Kozhakin, A. E., Mølmer, K., and Polzik, E. (2000). Quantum memory for light. *Phys. Rev. A*, 62:033809. (pages 3, 108).
- Krauter, H. (2011). *Generation and application of entanglement of room temperature ensembles of atoms*. PhD thesis, University of Copenhagen. (pages vi, 33, 48, 75, 149).
- Krauter, H., Muschik, C. A., Jensen, K., Wasilewski, W., Petersen, J. M., Cirac, J. I., and Polzik, E. S. (2011). Entanglement generated by dissipation and steady state entanglement of two macroscopic objects. *Phys. Rev. Lett.*, 107:080503. (pages 108, 111).
- Krauter, H., Salart, D., Muschik, C., Petersen, J. M., Shen, H., Fernholz, T., and Polzik, E. S. (2013). Deterministic quantum teleportation between distant atomic objects. *Nature Physics*, 9(7):400–404. (page 127).
- Kurizki, G., Bertet, P., Kubo, Y., Mølmer, K., Petrosyan, D., Rabl, P., and Schmiedmayer, J. (2015). Quantum technologies with hybrid systems. *Proceedings of the National Academy of Sciences*, 112(13):3866–3873. (page 2).
- Kuzmich, A., Bigelow, N., and Mandel, L. (1998). Atomic quantum non-demolition measurements and squeezing. *EPL (Europhysics Letters)*, 42(5):481. (page 3).
- Kuzmich, A., Mølmer, K., and Polzik, E. S. (1997). Spin squeezing in an ensemble of atoms illuminated with squeezed light. *Phys. Rev. Lett.*, 79:4782–4785. (page 3).
- Kwiat, P. G., Mattle, K., Weinfurter, H., Zeilinger, A., Sergienko, A. V., and Shih, Y. (1995). New high-intensity source of polarization-entangled photon pairs. *Phys. Rev. Lett.*, 75:4337–4341. (page 108).
- Lammers, J. (2018). *State preparation and verification in continuously measured quantum systems*. PhD thesis, Leibniz University Hannover. (page 113).
- Lee, J., Almasi, A., and Romalis, M. (2018). Improved limits on spin-mass interactions. *Phys. Rev. Lett.*, 120:161801. (page 3).
- Li, W., Balabas, M., Peng, X., Pustelny, S., Wickenbrock, A., Guo, H., and Budker, D. (2017). Characterization of high-temperature performance of cesium vapor cells with anti-relaxation coating. *Journal of Applied Physics*, 121(6):063104. (page 42).
- Lo, H.-Y., Kienzler, D., de Clercq, L., Marinelli, M., Negnevitsky, V., Keitch, B. C., and Home, J. P. (2015). Spin–motion entanglement and state diagnosis with squeezed oscillator wavepackets. *Nature*, 521(7552):336–339. (page 109).
- MacFarlane, A. G. J., Dowling, J. P., and Milburn, G. J. (2003). Quantum technology: the second quantum revolution. *Philosophical Transactions of the Royal Society of London. Series A: Mathematical, Physical and Engineering Sciences*, 361(1809):1655–1674. (page 2).
- Mansuripur, M. (2011). Solar sails, optical tweezers, and other light-driven machines. In *Tribute to Joseph W. Goodman*, volume 8122, page 81220D. International Society for Optics and Photonics. (page 4).
- Marletto, C. and Vedral, V. (2017). Gravitationally induced entanglement between two massive particles is sufficient evidence of quantum effects in gravity. *Phys. Rev. Lett.*, 119:240402. (page 3).
- Mathiassen, J. B. (2019). Characterising and modelling thermal substrate noise for a membrane in the middle optomechanical cavity. Master’s thesis, University of Copenhagen. (pages 42, 43, 44).

Bibliography

- Meekhof, D. M., Monroe, C., King, B. E., Itano, W. M., and Wineland, D. J. (1996). Generation of nonclassical motional states of a trapped atom. *Phys. Rev. Lett.*, 76:1796–1799. (page 4).
- Miao, H. (2010). *Exploring Macroscopic Quantum Mechanics in Optomechanical Devices*. PhD thesis, University of Western Australia. (page 113).
- Midolo, L., Schliesser, A., and Fiore, A. (2018). Nano-opto-electro-mechanical systems. *Nature nanotechnology*, 13(1):11–18. (page 4).
- Mirhosseini, M., Sipahigil, A., Kalaei, M., and Painter, O. (2020). Quantum transduction of optical photons from a superconducting qubit. *arXiv e-prints*, page arXiv:2004.04838. (page 127).
- Møller, C. B., Thomas, R. A., Vasilakis, G., Zeuthen, E., Tsaturyan, Y., Balabas, M., Jensen, K., Schliesser, A., Hammerer, K., and Polzik, E. S. (2017). Quantum back-action-evading measurement of motion in a negative mass reference frame. *Nature*, 547(7662):191–195. (pages vii, 17, 19, 41, 43, 44, 45, 75, 82, 89, 91, 98, 99, 100, 101, 126, 138, 155, 156).
- Mølmer, K., Castin, Y., and Dalibard, J. (1993). Monte carlo wave-function method in quantum optics. *JOSA B*, 10(3):524–538. (page 113).
- Müller-Ebhardt, H., Rehbein, H., Li, C., Mino, Y., Somiya, K., Schnabel, R., Danzmann, K., and Chen, Y. (2009). Quantum-state preparation and macroscopic entanglement in gravitational-wave detectors. *Phys. Rev. A*, 80:043802. (pages 113, 114).
- Müller-Ebhardt, H., Rehbein, H., Schnabel, R., Danzmann, K., and Chen, Y. (2008). Entanglement of macroscopic test masses and the standard quantum limit in laser interferometry. *Phys. Rev. Lett.*, 100:013601. (page 113).
- Muschik, C. A., Polzik, E. S., and Cirac, J. I. (2011). Dissipatively driven entanglement of two macroscopic atomic ensembles. *Phys. Rev. A*, 83:052312. (page 111).
- Møller, C. B. (2018). *Quantum Back-Action Evasion in a Hybrid Spin-Optomechanical System*. PhD thesis, University of Copenhagen. (pages v, vi, 5, 12, 42, 43, 96, 100, 101).
- Newell, D. B. and Tiesinga, E. (2019). The international system of units (si). Technical report. (page 23).
- Nielsen, W. H. P. (2016). *Quantum cavity optomechanics with phononic bandgap shielded silicon nitride membranes*. PhD thesis, University of Copenhagen. (pages 17, 42, 43, 86, 100).
- Nielsen, W. H. P., Tsaturyan, Y., Møller, C. B., Polzik, E. S., and Schliesser, A. (2017). Multimode optomechanical system in the quantum regime. *Proceedings of the National Academy of Sciences*, 114(1):62–66. (pages 11, 12, 75, 100).
- Ockeloen-Korppi, C. F., Damskägg, E., Pirkkalainen, J.-M., Asjad, M., Clerk, A. A., Massel, F., Woolley, M. J., and Sillanpää, M. A. (2018). Stabilized entanglement of massive mechanical oscillators. *Nature*, 556(7702):478–482. (page 109).
- Ockeloen-Korppi, C. F., Damskägg, E., Pirkkalainen, J.-M., Clerk, A. A., Woolley, M. J., and Sillanpää, M. A. (2016). Quantum backaction evading measurement of collective mechanical modes. *Phys. Rev. Lett.*, 117:140401. (page 8).
- Pearman, C., Adams, C., Cox, S., Griffin, P., Smith, D., and Hughes, I. (2002). Polarization spectroscopy of a closed atomic transition: applications to laser frequency locking. *Journal of Physics B: Atomic, Molecular and Optical Physics*, 35(24):5141. (page 39).

- Polzik, E. S. and Hammerer, K. (2015). Trajectories without quantum uncertainties. *Annalen der Physik*, 527(1-2):A15–A20. (pages 5, 9).
- Purdy, T. P., Peterson, R. W., and Regal, C. A. (2013). Observation of radiation pressure shot noise on a macroscopic object. *Science*, 339(6121):801–804. (page 11).
- Reiter, F. and Sørensen, A. S. (2012). Effective operator formalism for open quantum systems. *Phys. Rev. A*, 85:032111. (pages 26, 27, 28, 136).
- Riedel, M., Kovacs, M., Zoller, P., Mlynek, J., and Calarco, T. (2019). Europe’s quantum flagship initiative. *Quantum Science and Technology*, 4(2):020501. (page 2).
- Riedinger, R., Wallucks, A., Marinkovic, I., Löschnauer, C., Aspelmeyer, M., Hong, S., and Gröblacher, S. (2018). Remote quantum entanglement between two micromechanical oscillators. *Nature*, 556(7702):473–477. (page 109).
- Rossi, M., Mason, D., Chen, J., and Schliesser, A. (2019). Observing and verifying the quantum trajectory of a mechanical resonator. *Phys. Rev. Lett.*, 123:163601. (pages 10, 113).
- Safavi-Naeini, A. H. and Painter, O. (2010). Design of optomechanical cavities and waveguides on a simultaneous bandgap phononic-photon crystal slab. *Opt. Express*, 18(14):14926–14943. (page 12).
- Sankey, J. C., Yang, C., Zwickl, B. M., Jayich, A. M., and Harris, J. G. E. (2010). Strong and tunable nonlinear optomechanical coupling in a low-loss system. *Nature Physics*, 6(9):707–712. (page 44).
- Savukov, I. M. and Romalis, M. V. (2005). Effects of spin-exchange collisions in a high-density alkali-metal vapor in low magnetic fields. *Phys. Rev. A*, 71:023405. (page 48).
- Schließer, A. (2009). *Cavity optomechanics and optical frequency comb generation with silica whispering-gallery-mode microresonators*. PhD thesis, Ludwig-Maximilians-Universität. (page 86).
- Schmieg, R. (2018). Coherent dynamics of atomic vapors. Technical report, University of Copenhagen. (page 42).
- Seltzer, S. J. (2008). *Developments in Alkali-Metal Atomic Magnetometry*. phdthesis, Princeton University. (pages 23, 34, 52, 146, 154).
- Shaham, R., Katz, O., and Firstenberg, O. (2020). Quantum dynamics of collective spin states in a thermal gas. *arxiv preprint*. (page 69).
- Shen, H. (2014). *Spin squeezing and entanglement with room temperature atoms for quantum sensing and communication*. PhD thesis, University of Copenhagen. (page 53).
- Sherson, J. (2006). *Quantum Memory and Teleportation Using Macroscopic Gas Samples*. PhD thesis, University of Aarhus. (pages vi, 27, 28, 30, 48, 59, 75, 77, 147).
- Simon, C., de Riedmatten, H., Afzelius, M., Sangouard, N., Zbinden, H., and Gisin, N. (2007). Quantum repeaters with photon pair sources and multi-mode memories. *Phys. Rev. Lett.*, 98:190503. (page 3).
- Souza, J. A., Cabral, L., Oliveira, R. R., and Villas-Boas, C. J. (2015). Electromagnetically-induced-transparency-related phenomena and their mechanical analogs. *Phys. Rev. A*, 92:023818. (page 33).
- Steck, D. A. (2007). Quantum and atom optics. available online at <http://steck.us/teaching> (revision 0.13.1, 29 April 2020). (pages 37, 144).

Bibliography

- Steck, D. A. (2019). Cesium d line data. available online at <http://steck.us/alkalidata>. (revision 2.2.1). (pages 23, 24, 144, 154).
- Stærkind, H. C. (2016). Optical magnetometry for biomedical applications. Master's thesis, University of Copenhagen. (page 42).
- Tang, Y., Wen, Y., Cai, L., and Zhao, K. (2020). Spin-noise spectrum of hot vapor atoms in an anti-relaxation-coated cell. *Phys. Rev. A*, 101:013821. (page 69).
- Tanji-Suzuki, H., Leroux, I. D., Schleier-Smith, M. H., Cetina, M., Grier, A. T., Simon, J., and Vuletić, V. (2011). Interaction between atomic ensembles and optical resonators: classical description. In *Advances in atomic, molecular, and optical physics*, volume 60, pages 201–237. Elsevier. (page 68).
- Thomas, R. A., Parniak, M., Østfeldt, C., Møller, C. B., Bærentsen, C., Tsaturyan, Y., Schliesser, A., Appel, J., Zeuthen, E., and Polzik, E. S. (2020). Entanglement between distant macroscopic mechanical and spin systems. (pages vii, 5, 19, 41, 43, 45, 91, 97, 98, 99, 101, 126, 155, 157).
- Thompson, J. D., Zwickl, B. M., Jayich, A. M., Marquardt, F., Girvin, S. M., and Harris, J. G. E. (2008). Strong dispersive coupling of a high-finesse cavity to a micromechanical membrane. *Nature*, 452(7183):72–75. (page 11).
- Tsang, M. and Caves, C. M. (2010). Coherent quantum-noise cancellation for optomechanical sensors. *Phys. Rev. Lett.*, 105:123601. (page 8).
- Tsang, M. and Caves, C. M. (2012). Evading quantum mechanics: engineering a classical subsystem within a quantum environment. *Physical Review X*, 2(3):031016. (page 5).
- Tsaturyan, Y. (2019). *Ultracoherent soft-clamped mechanical resonators for quantum cavity optomechanics*. PhD thesis, University of Copenhagen. (pages v, 13, 15, 42).
- Tsaturyan, Y., Barg, A., Polzik, E. S., and Schliesser, A. (2017). Ultracoherent nanomechanical resonators via soft clamping and dissipation dilution. *Nature nanotechnology*, 12(8):776. (pages 12, 13, 109).
- Tsaturyan, Y., Barg, A., Simonsen, A., Villanueva, L. G., Schmid, S., Schliesser, A., and Polzik, E. S. (2014). Demonstration of suppressed phonon tunneling losses in phononic bandgap shielded membrane resonators for high-q optomechanics. *Optics express*, 22(6):6810–6821. (pages 12, 109).
- Tse, M. et al. (2019). Quantum-enhanced advanced ligo detectors in the era of gravitational-wave astronomy. *Phys. Rev. Lett.*, 123:231107. (page 3).
- Vasilakis, G., Shen, H., Jensen, K., Balabas, M., Salart, D., Chen, B., and Polzik, E. S. (2015). Generation of a squeezed state of an oscillator by stroboscopic back-action-evading measurement. *Nature Physics*, 11(5):389–392. (pages 8, 82, 127).
- Vasilyev, D. V., Hammerer, K., Korolev, N., and Sørensen, A. S. (2012). Quantum noise for faraday light-matter interfaces. *Journal of Physics B: Atomic, Molecular and Optical Physics*, 45(12):124007. (pages 29, 31, 55).
- Vasilyev, D. V., Muschik, C. A., and Hammerer, K. (2013). Dissipative versus conditional generation of gaussian entanglement and spin squeezing. *Phys. Rev. A*, 87:053820. (pages 14, 55, 111, 112).
- Verstraete, F., Wolf, M. M., and Cirac, J. I. (2009). Quantum computation and quantum-state engineering driven by dissipation. *Nature physics*, 5(9):633–636. (page 111).
- Vochezer, A., Kampschulte, T., Hammerer, K., and Treutlein, P. (2018). Light-mediated collective atomic motion in an optical lattice coupled to a membrane. *Phys. Rev. Lett.*, 120:073602. (page 5).

- Wallquist, M., Hammerer, K., Rabl, P., Lukin, M., and Zoller, P. (2009). Hybrid quantum devices and quantum engineering. *Physica Scripta*, T137:014001. (page 2).
- Wasilewski, W., Jensen, K., Krauter, H., Renema, J. J., Balabas, M. V., and Polzik, E. S. (2010). Quantum noise limited and entanglement-assisted magnetometry. *Phys. Rev. Lett.*, 104:133601. (page 127).
- Weber, J. (1967). Gravitational radiation. *Phys. Rev. Lett.*, 18:498–501. (page 4).
- Wehner, S., Elkouss, D., and Hanson, R. (2018). Quantum internet: A vision for the road ahead. *Science*, 362(6412). (pages 2, 4).
- Weis, S., Rivière, R., Deléglise, S., Gavartin, E., Arcizet, O., Schliesser, A., and Kippenberg, T. J. (2010). Optomechanically induced transparency. *Science*, 330(6010):1520–1523. (page 75).
- Wieczorek, W., Hofer, S. G., Hoelscher-Obermaier, J., Riedinger, R., Hammerer, K., and Aspelmeyer, M. (2015). Optimal state estimation for cavity optomechanical systems. *Phys. Rev. Lett.*, 114:223601. (page 113).
- Wiener, N. (1964). *Extrapolation, Interpolation, and Smoothing of Stationary Time Series: With Engineering Applications*. Massachusetts Institute of Technology : Paperback series. M.I.T. Press. (pages 112, 119).
- Wilson, D. J. (2012). *Cavity optomechanics with high stress silicon nitride films*. PhD thesis, California Institute of Technology. (pages 13, 14, 15).
- Wilson, D. J., Regal, C. A., Papp, S. B., and Kimble, H. J. (2009). Cavity optomechanics with stoichiometric sin films. *Phys. Rev. Lett.*, 103:207204. (page 11).
- Wilson-Rae, I., Nooshi, N., Zwerger, W., and Kippenberg, T. J. (2007). Theory of ground state cooling of a mechanical oscillator using dynamical backaction. *Phys. Rev. Lett.*, 99:093901. (page 4).
- Woolley, M. J. and Clerk, A. A. (2013). Two-mode back-action-evading measurements in cavity optomechanics. *Phys. Rev. A*, 87:063846. (page 8).
- Ye, J. and Lynn, T. W. (2003). Applications of optical cavities in modern atomic, molecular, and optical physics. In *Advances in Atomic, Molecular, and Optical Physics*, volume 49, pages 1–83. Elsevier. (page 82).
- Yu, P.-L., Cicak, K., Kampel, N. S., Tsaturyan, Y., Purdy, T. P., Simmonds, R. W., and Regal, C. A. (2014). A phononic bandgap shield for high- q membrane microresonators. *Applied Physics Letters*, 104(2):023510. (page 12).
- Yu, P.-L., Purdy, T. P., and Regal, C. A. (2012). Control of material damping in high- q membrane microresonators. *Phys. Rev. Lett.*, 108:083603. (pages 11, 12).
- Zeilinger, A. (1999). Experiment and the foundations of quantum physics. *Rev. Mod. Phys.*, 71:S288–S297. (page 108).
- Zeuthen, E., Polzik, E. S., and Khalili, F. Y. (2019). Gravitational wave detection beyond the standard quantum limit using a negative-mass spin system and virtual rigidity. *Phys. Rev. D*, 100:062004. (page 127).
- Zhang, K., Meystre, P., and Zhang, W. (2013). Back-action-free quantum optomechanics with negative-mass bose-einstein condensates. *Phys. Rev. A*, 88:043632. (page 8).
- Zugenmaier, M. (2018). *Towards a room temperature single photon source based on atomic vapour*. PhD thesis, University of Copenhagen. (page 41).

- Zugenmaier, M., Dideriksen, K. B., Sørensen, A. S., Albrecht, B., and Polzik, E. S. (2018). Long-lived non-classical correlations towards quantum communication at room temperature. *Communications Physics*, 1(1):76. (pages 42, 53, 68).
- Zwickl, B. M., Shanks, W. E., Jayich, A. M., Yang, C., Bleszynski Jayich, A. C., Thompson, J. D., and Harris, J. G. E. (2008). High quality mechanical and optical properties of commercial silicon nitride membranes. *Applied Physics Letters*, 92(10):103125. (page 11).
- Østfeldt, C. (in preparation). PhD thesis, University of Copenhagen. to be published. (page v).